RICE UNIVERSITY

The Development of a Photocrosslinked Biomaterial for Bone Tissue Engineering Applications

by

John Patrick Fisher

A THESIS SUBMITTED
IN PARTIAL FULFILLMENT OF THE
REQUIREMENTS FOR THE DEGREE

Doctor of Philosophy

APPROVED, THESIS COMMITTEE:

Antonios G. Mikos, Professor (Chair)
Bioengineering, Rice University

Kyriacos A. Athanasiou, Professor
Bioengineering, Rice University

Paul S. Engel, Professor
Chemistry, Rice University

John A. Jansen, Professor
Biomaterials, University Medical Center Nijmegen

HOUSTON, TEXAS
OCTOBER, 2002

UMI Number: 3090143

UMI®

UMI Microform 3090143

Copyright 2003 by ProQuest Information and Learning Company.

All rights reserved. This microform edition is protected against unauthorized copying under Title 17, United States Code.

ProQuest Information and Learning Company
300 North Zeeb Road
P.O. Box 1346
Ann Arbor, MI 48106-1346

ABSTRACT

The Development of a Photocrosslinked Biomaterial for

Bone Tissue Engineering Applications

by

John Patrick Fisher

The photocrosslinking of poly(propylene fumarate) (PPF) using the photoinitiator bis(2,4,6-trimethylbenzoyl) phenylphosphine oxide (BAPO) and low levels of ultraviolet light irradiation has been investigated as the basis for a bone tissue engineering scaffold. The photocrosslinking mechanism as well as the final network structure was studied, showing that a single phosphinoyl radical derived from BAPO was primarily responsible for the photoinitiated crosslinking of PPF. A technique to fabricate PPF into porous scaffolds using a photocrosslinking/porogen leaching strategy was developed, with characterization studies showing that the presence of the leachable porogen did not affect the initiation of the PPF crosslinking reaction in this system. An *in vitro* degradation study of both solid PPF networks and porous PPF scaffolds in phosphate buffered-saline was performed. The results indicated that porogen size and content could be selected to formulate the photocrosslinked PPF scaffolds with a degradation rate, porosity, and mechanical properties to match target values for a specific tissue defect. The soft and

hard tissue response to photocrosslinked PPF scaffolds was studied, with the results indicating that the scaffolds were biocompatible within both soft and hard tissue. The ability of these photocrosslinked PPF scaffolds to act as a carrier for an adsorbed protein in order to promote bone formation was also examined. The results indicate that transforming growth factor-β1 did induce significant bone formation in these porous PPF scaffolds. Finally, an *in vivo* study of the effects of a degradable biomaterial upon wound healing and bone formation within a tooth extraction socket was undertaken. The results show that the implantation of the hydrophobic and degradable PPF biomaterial did not significantly alter this process, while the negative control group, a hydrophilic, degradable biomaterial, significantly reduced bone formation. The effect of biomaterial's surface properties upon bone formation most closely parallel the fibroblastic growth factor-2 localization results, indicating its critical role in the initial phases of wound healing to facilitate later bone formation. These results indicate the great potential of photocrosslinked PPF scaffolds in bone tissue engineering applications.

ACKNOWLEDGEMENTS

This work is dedicated to my grandfather, Thompson Willett

I would like to sincerely thank my advisor, Dr. Antonios Mikos, whose wise guidance throughout my doctoral studies will not be soon forgotten. I also greatly appreciate the advice and counsel of my thesis committee, who significantly contributed to the success of this work. Furthermore, I would like to acknowledge my coworkers in the Mikos lab, friends, and family whose support made my studies a happy and enjoyable experience. Finally, to Gail who has made, and will continue to make, life brilliant.

TABLE OF CONTENTS

Title Page	i
Abstract	ii - iii
Acknowledgements	iv
Table of Contents	v - vi
List of Tables	vi
List of Figures	vii - xi
List of Abbreviations	xii - xiii
List of Symbols	xiv
I. Introduction	1 - 3
II. Background: Photoinitiated Polymerization of Biomaterials	4 - 19
A. Abstract	4
B. Photoinitiation	4
C. Photoinitiated Polymerization	7
D. Photoinitiators	9
E. Photoinitiated Biomaterials	11
F. Summary	18
G. Table	19
III. Objective	20 - 21
IV. The Photoinitiated Crosslinking of the Biodegradable Polyester Poly(propylene fumarate): Determination of Network Structure by Contrasting Photoinitiators	22 - 45
A. Abstract	22
B. Introduction	23
C. Materials and Methods	25
D Results	31
E. Discussion	34
F. Conclusions	37
G. Figures	39
V. Synthesis and Properties of Photocrosslinked Poly(Propylene Fumarate) Scaffolds	46 - 69
A. Abstract	46
B. Introduction	47
C. Materials and Methods	49
D Results	55
E. Discussion	59
F. Conclusions	62
G. Tables and Figures	63
VI. *In Vitro* Degradation of Photocrosslinked Poly(Propylene Fumarate) Scaffolds	70 - 95

A. Abstract 70
B. Introduction 71
C. Materials and Methods 73
D Results 80
E. Discussion 82
F. Conclusions 86
G. Tables and Figures 87
VII. Photocrosslinking Characteristics and Mechanical Properties of Diethyl Fumarate/Poly(Propylene Fumarate) Biomaterials 96 - 125
A. Abstract 96
B. Introduction 97
C. Materials and Methods 99
D Results 106
E. Discussion 109
F. Conclusions 113
G. Tables and Figures 115
VIII. Soft and Hard Tissue Response to Photocrosslinked Poly(Propylene Fumarate) Scaffolds in a Rabbit Model 126 - 150
A. Abstract 126
B. Introduction 127
C. Materials and Methods 129
D Results 134
E. Discussion 137
F. Conclusions 140
G. Tables and Figures 142
IX. Bone Formation in Transforming Growth Factor Beta-1-Coated Porous Poly(Propylene Fumarate) Scaffolds 151 - 173
A. Abstract 151
B. Introduction 152
C. Materials and Methods 154
D Results 160
E. Discussion 162
F. Conclusions 166
G. Tables and Figures 167
X. The Effect of Biomaterial Properties on Bone Formation as Characterized by Histomorphometrical Analysis of Wound Healing and Growth Factor Localization in a Rabbit Tooth Extraction Socket Model 174 - 209
A. Abstract 174
B. Introduction 175
C. Materials and Methods 180
D Results 190
E. Discussion 194
F. Conclusions 198
G. Tables and Figures 200
XI. Summary 210 - 214
XII. Literature Cited 215 - 230

LIST OF TABLES

Table 2.1:	Local wavelength of maximum absorption and associated extinction coefficients for typical chromophores found in photolabile compounds.	19
Table 5.1:	The extent of PPF photocrosslinking in solid and porous scaffolds as determined by FTIR.	63
Table 5.2:	Porosity of photocrosslinked PPF scaffolds.	63
Table 5.3:	Compressive mechanical strength of photocrosslinked PPF scaffolds.	63
Table 6.1:	The three photocrosslinked PPF scaffold formulations that were examined in the *in vitro* degradation study.	87
Table 7.1 :	Outline of the three factor, 2x2x4 factorial design for the DEF/PPF biomaterials study.	115
Table 8.1:	The four classes of PPF scaffolds which were investigated in the *in vivo* study.	142
Table 8.2:	Histological grading scale for soft and hard tissue implants.	143
Table 9.1:	Histomorphometrical analysis for PPF-TGF-β1 implants.	167
Table 10.1:	Itemization of the number of repeats for the experimental and control groups within each time point.	200

LIST OF FIGURES

Figure 4.1:	The radical reactions involved in BAPO exposure to UV irradiation (A) and MAPO exposure to UV irradiation (B).	39
Figure 4.2:	^{31}P NMR spectra of BAPO after UV irradiation (Bx) and the UV initiated reaction of BAPO and diethyl fumarate (DxB).	40
Figure 4.3:	The heat release and fumarate conversion of PPF crosslinked with BAPO and MAPO photoinitiators.	41
Figure 4.4:	The fumarate unit conversion and molecular weight between crosslinks of PPF crosslinked with BAPO and MAPO photoinitiators.	42
Figure 4.5:	The sol fraction and swelling degree of PPF crosslinked with BAPO and MAPO photoinitiators.	43
Figure 4.6:	The tensile modulus of PPF crosslinked with BAPO and MAPO photoinitiators.	44
Figure 4.7:	A proposed structure of photocrosslinked PPF using the BAPO initiator.	45
Figure 5.1:	A photograph of a solid and porous photocrosslinked PPF scaffold.	64
Figure 5.2:	Temperature profile during ultraviolet light exposure within samples of PPF and PPF/NaCl composites.	65
Figure 5.3:	The intensity of transmitted ultraviolet light through samples of PPF and PPF/NaCl composites.	66 - 67
Figure 5.4:	The FTIR spectrum of samples extracted from the interior and exterior of porous and solid photocrosslinked PPF.	68
Figure 5.5:	Scanning electron microscopy images of photocrosslinked PPF scaffolds.	69
Figure 6.1:	Scanning electron micrographs of photocrosslinked PPF scaffolds during *in vitro* degradation.	88

Figure 6.2:	Photographs of solid PPF networks at during *in vitro* degradation.	89
Figure 6.3:	Sample mass loss during *in vitro* degradation.	90
Figure 6.4:	Sample length change during *in vitro* degradation.	91
Figure 6.5:	Sample water absorption during *in vitro* degradation.	92
Figure 6.6:	Scaffold porosity during *in vitro* degradation.	93
Figure 6.7:	Sample mechanical properties during *in vitro* degradation.	94 - 95
Figure 7.1 :	A schematic depicting polyaddition reactions that occur between poly(propylene fumarate) and diethyl fumarate.	116
Figure 7.2 :	The effect of PPF molecular weight, BAPO content, and DEF content upon the uncured solution viscosity.	117
Figure 7.3 :	A typical plot of heat flux from the photocrosslinking reaction of DEF/PPF.	118
Figure 7.4 :	The effect of PPF molecular weight, BAPO content, and DEF content upon the photocrosslinking reaction heat release and the time to maximum heat release.	119
Figure 7.5 :	A typical set of temperature profiles for DEF/PPF formulations with varying DEF content.	120
Figure 7.6 :	The effect of PPF molecular weight, BAPO content, and DEF content upon the maximum reaction temperature and the time to maximum reaction temperature.	121
Figure 7.7 :	The effect of PPF molecular weight, BAPO content, and DEF content upon the sol fraction of photocrosslinked cylinders.	122
Figure 7.8 :	The effect of PPF molecular weight, BAPO content, and DEF content upon the swelling degree and sol fraction of photocrosslinked sheets.	123
Figure 7.9 :	The effect of PPF molecular weight, BAPO content, and DEF content upon elastic modulus and strength at fracture.	124

Figure 7.10 :	A schematic describing how the addition of the DEF precursor to the PPF polymer may effect the structure of the formed crosslinked polymer network.	125
Figure 8.1:	Histological sections of PPF scaffolds implanted subcutaneously.	144
Figure 8.2:	Histological sections of PPF scaffolds implanted in cranial defects.	145 -146
Figure 8.3:	Histological scoring results for the soft and hard tissue response to PPF scaffolds at 2 weeks and 8 weeks.	147 -148
Figure 8.4:	The porosity at 2 weeks and 8 weeks of PPF scaffolds implanted subcutaneously and implanted in cranial defects.	149
Figure 8.5:	The amount of bone growth into the pores of PPF scaffolds at 2 weeks and 8 weeks relative to defect area.	150
Figure 9.1:	Pictures depicting the exposure of the skull bone, four cranial defects, and inserted porous PPF scaffolds.	168
Figure 9.2:	Image analysis procedure.	169
Figure 9.3:	Graph showing *in vitro* rhTGF-β1 release.	170
Figure 9.4:	Histological sections of undecalcified specimens containing various PPF scaffolds viewed with a light microscope.	171
Figure 9.5:	Histological sections of undecalcified specimens containing various PPF scaffolds viewed with a fluorescence microscope.	172
Figure 9.6:	The bone surface area, bone area %, pore fill %, and pore area % results for the *in vivo* study.	173
Figure 10.1:	Schematic depicting a typical histological section and the areas imaged for histomorphometrical analysis of bone formation **(A)** and immunohistochemical staining **(B)**.	201
Figure 10.2:	Light microscopy images of empty control sockets stained with H&E or for FGF-2 at 4 days, 1 week, and 2 weeks.	202
Figure 10.3:	The percent area of bone **(A)** and the average trabecular size **(B)**.	203

Figure 10.4: Light microscopy images of empty control sockets stained for the growth factors FGF-2, VEGF, PDGF-A, TGF-β1, and BMP-2. 204

Figure 10.5: The percent area immunohistochemically stained for FGF-2. 205

Figure 10.6: The percent area immunohistochemically stained for VEGF. 206

Figure 10.7: The percent area immunohistochemically stained for PDGF-A. 207

Figure 10.8: The percent area immunohistochemically stained for TGF-β1 208

Figure 10.9: The percent area immunohistochemically stained for BMP-2. 209

List of Abbreviations

AA	ascorbic acid
ABC	avidin-biotin complex
AC	adipose cells
AIBN	2,2'-Azobisisobutyronitrile
ANOVA	analysis of variance
anti-BMP-2	BMP-2 goat polyclonal antibody
anti-FGF-2	FGF-2 goat polyclonal antibody
anti-PDGF-A	PDGF-A mouse monoclonal antibody
anti-TGF-β1	TGF-β1 goat polyclonal antibody
anti-VEGF	VEGF mouse monoclonal antibody
APS	ammonium persulfate
BAPO	bisacylphosphine oxide
BAPO	bis(2,4,6-trimethylbenzoyl) phenylphosphine oxide
bFGF	basic fibroblastic growth factor (also known as FGF-2)
BIC	direct bone - implant contact
bis-GMA	2,2-bis[4-(2'-hydroxy-3'-methacryloyl-oxypropoxy)phenyl]propane
BM	bone marrow-like tissue
BMP	bone morphogentic protein
BMP-2	bone morphogenetic protein-2
BN	blue normalized
BP	benzoyl peroxide
BSA	bone surface area
BSA	bovine serum albumin
BT	bone-like tissue
Bx	UV irradiated BAPO
CHO	Chinese hamster ovary cells
CQ	camphorquinone
CT	connective tissue
DAB	3,3'-diaminobenzidine
DE	defect edge
DEF	diethyl fumarate
DMT	N,N-dimethyl-p-toluidine
DPC	differential photocalorimetry
DxB	photoproduct of DEF and BAPO
EA	erythrocyte accumulation
ELISA	enzyme-linked immunosorbent assay
FGF-2	fibroblastic growth factor-2 (also known as bFGF)
FTIR	fourier transform infrared
Gd	glow discharge
GPC	gel permeation chromatography

HEMA	2-hydroxyethyl methacrylate
HPLC	high performance liquid chromatography
IC	inflammatory cells
IHC	immunohistochemical
MAPO	monoacylphosphine oxide
M_c	average molecular weight between crosslinks
M_n	number average molecular weight
M_w	weight average molecular weight
NMR	nuclear magnetic resonance spectrometry
NVP	N-vinyl pyrrolidinone
OPF	oligo(poly(ethylene glycol) fumarate)
P	PPF scaffold
PBS	phosphate-buffered saline
PDGF-A	platelet derived growth factor-A
PEG	poly(ethylene glycol)
PI	polydispersity index
PG	1,2 propanediol
PLLA	poly(L-lactic acid)
PLP	paraformaldehyde-lysine-phosphate
PPF	poly(propylene fumarate)
PPF-Fn	fibronectin coated PPF
PPF-Gd	radio frequency glow discharge treated PPF
PPF-Pw	prewetted PPF
PPF-TGF-β1	PPF coated with rhTGF-β1
PPF+TGF	PPF coated with rhTGF-β1
PSA	PPF surface area
RF	radio frequency
RN	red normalized
ROI	region of interest
SEM	scanning electron microscopy
TAPO	trisacylphosphine oxide
TGF	transforming growth factor
TGF-β	transforming growth factor-β
TGF-β1	transforming growth factor-β1
TMA	*N,N*,3,5-tetramethyl aniline
UDMA	1,6-bis(2'-methacryloyl-oxyethoxycarbonylamino)-2,4,4-trimethylhexane
UV	ultraviolet
V	vascularization
VEGF	vascular endothelial growth factor
70Ps	PPF scaffolds fabricated with 70wt% 300-500 μm NaCl
80Ps	PPF scaffolds fabricated with 80wt% 300-500 μm NaCl
80Pl	PPF scaffolds fabricated with 80wt% 600-800 μm NaCl
85Ps	PPF scaffolds fabricated with 85wt% 300-500 μm NaCl

LIST OF SYMBOLS

a	absorption
A_w	water absorption
c	speed of light
C	concentration of a species
C_p	PPF content
C_s	NaCl content
E	energy
FB_o	fumarate groups available for crosslinking within PPF polymer
FB_{nox}	unreacted fumarate bonds after crosslinking
FB_x	reacted fumarate bonds after crosslinking
h	Planck's constant
l	light path length
L_d	dry length
L_i	initial length
M_d	dry mass
M_i	initial mass
M_w	wet mass
P_L	percent length
P_M	percent mass
P_P	percent PPF
V	volume
V_{por}	porous volume per gram sample
W_d	dry sample weight
W_i	initial sample weight
W_p	filter paper weight
W_{p+s}	sample weight with filter paper
W_s	swollen sample weight
X_{FB}	conversion of fumarate bonds
ε	molar absorptivity (extinction coefficient)
ε	scaffold porosity
ε_T	theoretical porosity
ρ_s	NaCl density
ρ_p	PPF density
ρ	sample density
λ	wavelength

CHAPTER I

INTRODUCTION

Critical size craniofacial defects may arise from events such as trauma, surgery to correct infection, cancer resection, or congenital abnormalities. The standard clinical treatment for these defects is the transplantation of an autologous bone graft. An autograft typically integrates well with the host tissue as it not associated with an immune response, but it does have the disadvantages of donor site morbidity and limited availability. In contrast, the transplantation of tissue from cadavers or live donors (allografts) eliminates donor site morbidity, but does introduce other disadvantages such as the risk of a significant immune response as well as disease transmission. The lack of donor tissue also often limits treatment. Alternative approaches, such as metal or bone cement implantation are used clinically, but are associated with complications arising from their persistence in the wound site. The inadequacies of the current treatments have led us and others to investigate tissue engineering strategies for the treatment of large, craniofacial defects.

A fundamental component of many tissue engineering strategies is a biodegradable, polymer scaffold that would act as a temporary site for cellular attachment and proliferation while slowly degrading away, eventually leaving a repaired tissue defect. The development of a tissue engineered scaffold material begins with characterization of its chemical and physical properties followed by an investigation of its

in vitro and *in vivo* mechanical strength, degradation rate, and degradation products. Altering scaffold components and fabrication processes affects properties such as surface chemistry, degradability, and strength. Once these relationships are understood, the scaffold may be tailored to meet the needs of a given tissue. For example, scaffolds designed to function within a guided tissue regeneration strategy, where the scaffold promotes the ingrowth of tissue while providing mechanical support and stability, may be designed with local mechanical properties in mind. Alternatively, scaffolds that are meant to act as carriers for growth factors or other inductive agents for bone growth may have optimized release properties. Finally, scaffolds that are being considered as platforms for the implantation of either differentiated or progenitor cells may be altered so that their surface chemistry promotes cell attachment and proliferation. More than likely, many of these properties must be considered in parallel during the development of a tissue engineering device.

The strategy we investigate here for the treatment of large cranial defects focuses upon the development of such a novel tissue engineering scaffold. Specifically, we seek to development a precision fabricated, craniofacial prosthesis in the form of a biodegradable, tissue engineering scaffold. This implant would be constructed using a rapid prototyping, stereolithography apparatus in the following manner. First, the defect site would be imaged using a standard medical imaging technique such as computed tomography (CT) x-ray or magnetic resonance imaging (MRI). This would provide precise, three dimensional data on the defect site boundaries as well as the contour of the defect site. This data would then be transferred to a computer controlled, stereolithography apparatus. Stereolithography involves the ultraviolet laser light curing

of a polymer resin into a three dimensional structure. The strategy investigated here would use stereolithography to fabricate a biodegradable, tissue engineering scaffold. This approach would allow for the construction of an implant which not only precisely fits the defect site, but also one in which the interior scaffold architecture can be controlled so as to regulate scaffold degradation and ultimately facilitate bone tissue regeneration.

The first step towards the stereolithographic fabrication of tissue engineering scaffolds involves the development of a photocrosslinkable polymer system. This system would involve a biodegradable polymer and a photoinitiator which, upon irradiation by ultraviolet light, would cause the polymer to crosslink into a three dimensional polymer network. The subject of this work is the development and characterization of a photocrosslinkable, degradable polymer for tissue engineering applications.

CHAPTER II

BACKGROUND: PHOTOINITIATED POLYMERIZATION OF BIOMATERIALS[†]

ABSTRACT

Photoinitiated polymerization and polymer cross-linking are viable strategies for biomaterial synthesis because of the mild temperatures and neutral pH environments in which these reactions typically take place. This review summarizes the relevant theories as well as current status of photoinitiated polymerizations in biomaterials. Photoinitiation, photoinitiated polymerization, and photoinitiators are discussed with consideration toward the biological nature of the intended application. Recent investigations into biomaterials, including hydrogels, biodegradable materials, and hard tissue resorbable scaffolds are presented. Lastly, studies of cell interactions with photoinitiated biomaterials are discussed. The work herein illustrates the potential use of photoinitiated polymerization in the development of novel biomaterials for tissue engineering.

PHOTOINITIATION

Photochemistry is concerned with chemical reactions induced by optical radiation [1-3]. The radiation is most often ultraviolet (200-400 nm) or visible (400-800 nm) light, but is sometimes infrared (800-2500 nm) light. Photochemistry may be used to induce

---

[†] This chapter was published as the following article: Fisher JP, Dean D, Engel PS, Mikos AG. Photoinitiated polymerization of biomaterials. Ann Rev Mater Res. 2001;31:171-181.

any number of chemical processes, from initiating a chemical reaction to degrading a compound. The focus here is on photoinitiation of polymerization. Two basic steps characterize photoinitiation: the absorption of light to excite a compound and the resulting photochemical reaction of the excited compound [2]. These processes are briefly examined, with following sections considering photoinitiated polymerization of biomaterials.

Absorption of a photon of light by any compound causes electronic excitation. The energy causing excitation, E, is described by $E = hc/\lambda$ where h is Planck's constant, c is the speed of light, and λ is the wavelength of the exciting light. Light absorption is described by $a = \varepsilon Cl$, where ε is the molar absorptivity (extinction coefficient), C is the concentration of the species, and l is the light path length. The extinction coefficient, a constant for a compound at a specific wavelength, is an experimental measure of the probability of absorption at that wavelength. The magnitude of the extinction coefficient depends upon the compound's chromophore, the chemical moiety responsible for the absorption of light. Typical chromophores contain unsaturated functional groups such as C=C, C=O, NO_2, or N=N [2,4]. Table 2.1 lists some chromophores, their wavelength of maximum absorption, and the extinction coefficient at this wavelength [2,4]. These values are qualitative, because chromophore absorption is highly dependent upon neighboring substituents. For example, the absorption maximum and extinction coefficient of conjugated dienes are known to be influenced by the number of conjugated double bonds, alkyl substituents, and ring structure [4]. Knowledge of the absorption characteristics of the individual species aids in the design and development of pre-

fabricated photoinitiated implants, whether of bioinert or tissue-engineered (resorbable) graft materials, by allowing proper choice of initiator concentration and radiation source.

Any wavelength of radiation that falls within the absorption spectrum of a chromophore can effectively excite that chromophore. Excitation is characterized by the promotion of a valence electron from a bonding σ or π orbital or a nonbonding n orbital to an anti-bonding σ^* or π^* orbitals [2,4]. The electronic excitation of photochemical reactions contrasts with thermal reactions, which typically involve translational, rotational, and vibrational excitation [1]. Photochemical reactions often localize their excitation on one chromophore and produce (a) high levels of electronic excitation, (b) alterations in chemical reactivity, and (c) relatively low levels of thermal degradation [1]. Frequently, the result is to allow photochemical reactions to occur at a mild temperature and neutral pH, often ineffective conditions for thermal systems. These features of photochemistry may provide advantages over thermally cured-methods in the production of tissue-engineered scaffolds.

An excited compound (AB*) can dissociate to fragments (A+B), react with another compound to yield a new compound (ABC), isomerize (BA), luminesce (AB + $h\nu$), ionize ($AB^+ + e^-$), or decay without radiation (AB) [1]. All of these processes are rapid, often occurring on the nanosecond time scale. Additionally, the primary photochemical step is often a precursor to secondary processes. For most photoinitiated polymerizations, the excited chromophore dissociates into radicals, these radicals react with monomers to form radical species, which then propagate radical polymerization. A number of different classes of photoinitiatable polymerization reactions as well as photoinitiators are reviewed next.

PHOTOINITIATED POLYMERIZATION

Polymerizations may employ photoinitiation to effectively produce reactive species that initiate polymerization. Specifically, photoinitiated production of a radical is often used to begin radical chain polymerization, whereas photoinitiated production of an ionic monomer may be used in ionic chain polymerizations. In contrast, the photochemically active species can be the monomer itself, leading to polymerization of the monomer alone. Finally, photochemistry can be used in the crosslinking of already formed polymer chains following a radical chain polymerization mechanism. These photoinitiated processes are each briefly examined below.

Photoinitiated radical chain polymerization begins with light irradiation of a properly sensitive compound [2,5]. This activated compound typically fragments into two radicals that attack a monomer, converting it to a radical. The monomer radical attacks a second monomer and this process continues to add monomer units, thereby forming the polymer. The reaction is terminated either by the reaction with another radical (coupling) or by the transfer of a β-hydrogen from one radical to another, producing a saturated and an unsaturated compound (disproportionation). As in thermal polymerizations, the initiator system used in radical photopolymerization may be either a single initiator compound, which dissociates upon light absorption, or an oxidation-reduction reaction that is photoinitiated. The redox strategy within photoinitiated systems involves either (a) excitation of the electron donating or accepting species, which then undergoes electron transfer to form a radical pair, or (b) excitation of the donor-acceptor pair (often referred to as the charge transfer complex) to also yield a radical ion pair. In

either event, redox photopolymerization follows from that radical ion pair, in a solvent separated form or contact ion form [3].

Photoinitiated ionic chain polymerization is similar to radical chain polymerization but is characterized by the propagation of anionic or cationic species [5]. Initiation can be brought about with a single photoinitiator or with a photolabile initiator/co-initiator pair, producing an electron-donating compound (cationic polymerization) or an electron-withdrawing compound (anionic polymerization). Propagation then occurs with the addition of monomers to the initial ion pair. Termination of polymerization can occur by the transfer of the ion pair to a monomer (which terminates the growth of one polymer chain, but starts the growth of another), the transfer of the ion pair to a polymer, combination with a counterion, or by other nonspecific mechanisms. The instability of the ionic species confines ionic chain polymerizations to systems that promote the ion's persistence, such as those run at low temperatures and/or in polar solvents.

Photopolymerization of a pure monomer is restricted to those compounds that are both photolabile and polymerizable. The vinyl monomers styrene, methyl methacrylate, and acrylonitrile meet both criteria, but their polymerization efficiency is low [2]. For example, styrene irradiated at 313 nm produces small amounts of polystyrene in addition to larger amounts of styrene oligomers [2]. Other compounds require surfaces, photoinitiators, impurities, or oxygen to obtain appreciable rates of monomer photopolymerization [2]. Although of interest, photopolymerization of pure monomers severely restricts the choice of components and therefore possible applications.

Photocrosslinking of polymers can be carried out following either radical or ionic polymerization, but is the reaction of polymers instead of monomers. The product of photocrosslinking is ideally a single, three-dimensional, covalently bonded polymer network; this is in contrast to photopolymerization's production of physical entanglements of many discrete polymer chains. Both photocrosslinking and photopolymerization are valuable, but because their product's properties are often different, each has specific applications.

PHOTOINITIATORS

A number of issues must be considered when choosing a photoinitiator for the polymerization of a biomaterial. These concerns are not limited to the photoinitiator but extend to interactions between the available light source and other chemical species within the proposed implant production system. Specifically, the peak absorption wavelength and extinction coefficient of the initiator, the reactivity of the initiator toward the other species within the system, and the kinetics of the photoinitiator all determine the applicability of the system. A few classes of photoinitiators are reviewed that have seen use in biomaterials. [A more complete presentation of photoinitiators can be found in Rabek [2] and Fouassier [6].] The final choice of initiator, however, is often based upon similarly reported systems in the literature or prior experience.

Peroxides (ROOR) are effective photoinitiators that absorb in the ultraviolet region from 200-300 nm, but without a significant absorption peak [2,6]. The absorption of light causes peroxides to degrade by cleavage of the O-O bond, forming alkoxy radicals ($RO^{\bullet}$) [2]. The hydroxyl radicals ($HO^{\bullet}$) formed from hydrogen peroxide has been used to polymerize methyl methacrylate as well as poly(*N*-isopropylacrylamide)

[2,7]. Benzoyl peroxide (C_6H_5-CO-O_2-CO-C_6H_5), a common thermal radical initiator, is also a photoinitiator that has a local wavelength of maximum absorption at 230 and 273 nm. Benzoyl peroxide's benzoyloxy radicals (C_6H_5-CO-$O^{\bullet}$), and the derived phenyl radicals ($C_6H_5^{\bullet}$), have been shown to polymerize methyl methacrylate and styrene [2].

Ketones (RCOR) make up an extremely large class of photoinitiators. Some of the most commonly used ketones are related to acetophenone (C_6H_5-CO-CH_3), which has large absorbance peak at 280 nm and a smaller peak at 330 nm [8-13]. These initiators typically form benzoyl radicals (C_6H_5-$CO^{\bullet}$) after α-cleavage of the C-C bonds; the benzoyl radicals are thought to be primarily responsible for polymerization [6]. Benzoin (C_6H_5-CHOH-CO-C_6H_5), a phenylated derivative, has an absorption peak at approximately 315 nm, which often shifts to higher wavelengths with substitutions [2]. The frequently used 2,2-dimethoxy-2-phenylacetophenone enhances radical polymerization because of both its additional electron-donating groups and its ability to undergo a secondary light absorption and excitation. The result is a more potent initiator because four radical fragments, instead of the typical two, are produced. Acylphosphineoxides (C_6H_5-CO-PO-$(C_6H_5)_2$) have been reported for dental applications while compounds containing sulfur, such as dibenzoyl disulphides ((C_6H_5)-CO-S_2-CO-(C_6H_5)) or diphenyldithiocarbonate ((C_6H_5)-S-CO-S-(C_6H_5)), have been used in methyl methacrylate photopolymerization [2,14].

Azo compounds have found use as photoinitiators, as the azo group (-N=N-) absorbs at approximately 350 nm to produce two reactive carbon centered radicals [2,15]. 2,2'-Azobisisobutyronitrile (AIBN, $(CH_3)_2C(CN)$-N=N-$C(CN)(CH_3)_2$) has been used

with significant success [2]. However, the low absorptivity and associated low polymerization rate are the chief disadvantages of azo compounds [2].

Finally, a number of longer wavelength systems have been developed. The use of quinones, especially camphorquinone, and the dye eosin in the presence of an amine has been reported with regularity in the biomaterials literature. Both systems utilize blue light (420 to 500 nm) and find significant success in dental applications [16].

PHOTOINITIATED BIOMATERIALS

Many investigations into photoinitiated materials have explored strategies to create a biomaterial that attempts to replace a lost function or to add a new function. Examples of the former include dental and cardiovascular materials; the latter include drug delivery systems and biological adhesives. Photochemistry is an attractive strategy in the production of these materials, because it has a controlled reaction initiation and termination, an often short reaction time, and spatial control. Additionally, photochemical reactions are often run at gentle conditions, such as room temperature or under physiologic temperature and pH, allowing both the incorporation of biologically active molecules and *in vivo* reactions without harm. While photochemistry does offer advantages for biomaterial synthesis, a number of issues must be resolved such as the incorporation of degradable elements, the identification of water soluble components, the insurance of nontoxic unpolymerized material or initiator residues, and the optimization of cell viability. In this section investigations into photoinitiated biomaterials are reviewed, with an emphasis on the photochemical aspects of each.

Hydrogels

Considerable work has been devoted to the development of photoinitiated hydrogels. The main difficulty lies in the development of water-soluble components that are both functional and photolabile. Three basic strategies have been followed: (a) the use of photolabile water-soluble polymers, (b) the addition of photolabile groups to hydrophilic polymers, and (c) the use of water-soluble photoinitiators with hydrophilic polymers. The first two strategies would employ a photopolymerization of a pure monomer or photocrosslinking of a pure polymer scheme, whereas the latter would typically follow a radical polymerization or crosslinking scheme.

While for a given polymer multiple strategies may produce a hydrogel, few may be viable for the desired application. For example, poly(*N*-isopropylacrylamide) is photocrosslinkable alone at low wavelengths (<290 nm) but forms hydrogels of significantly lower sol fraction when using a hydrogen peroxide/potassium persulfate system and longer UV wavelengths (>290 nm) [7]. The cross-linking of the pure polymer is an intriguing approach because it may reduce toxicity by simply reducing the number of components required in the system. However, Kubota et al [7] show that this often leads to undesirable properties, such as in this case a large sol content. An alternative to an innately photolabile polymer is a hydrophilic polymer modified by the addition of a photolabile group. Poly(ethylene glycol) (PEG) has been modified with photolabile cinnamylidene acetyl groups that, interestingly, are both photolabile and cross-linkable [17,18]. Thus PEG hydrogels can be formed by cinnamylidene acetyl cross-links. Similarly, chitin has been modified with photolabile azide groups to form a noncytotoxic biological adhesive [15]. Upon UV irradiation, the photolabile azide

groups release N_2 while becoming highly reactive to nitrogen atoms and thus allowing cross-linking of the chitin. Thus with creative chemical approaches, photoinitiated hydrogels can be formed with considerable success without photoinitiators.

In contrast, hydrogel systems that utilize a discrete photoinitiator possess the advantage of allowing the polymer, or in some cases monomer, to be available for modification. PEG-modified systems crosslinked with a photoinitiator, typically an acetophenone/UV light or eosin Y and triethanolamine/visible blue light system, have been extensively investigated for this purpose [11,19-25]. These systems seek to combine the advantageous properties of a hydrophilic polymer and its resulting hydrogel, a functional group that promotes a desired outcome, and a photoinitiated system. Results have shown that modified PEG can be used as a drug-delivery system [19,25], lubricant [11], nonadhesive cell surface [20], and an inhibitor to thrombosis [21-24]. This strategy is also applicable to other hydrophilic polymers. For example, the hydrophilic monomer 2-hydroxyethyl methacrylate (HEMA) is photopolymerized in the production of hydrogel lenses. It has been shown that poly(HEMA) is effectively produced using the photoinitiator 2,2-dimethoxy-2-phenyl acetophenone [8,9]. Photoinitiated polymerization of HEMA and diethylene glycol dimethacrylate has also been reported in the formation of a hydrogel drug-delivery system [26]. Finally, hydrogels have been photoinitiated from modified polymers such as poly(L-lactic acid-*co*-glycolic acid-*co*-L-serine), again using an acetophenone initiator [10]. While any of the three strategies outlined above are possible means for the synthesis of photoinitiated biomaterials, the use of photoinitiators probably allows the greatest versatility and therefore widest application.

Biodegradable Materials

Development of biodegradable, biocompatible, photoinitiated compounds is often difficult for it typically requires the incorporation of a biodegradable polymer, such as poly(lactic acid), poly(glycolic acid), or a polyester, and a photoinitiator. Nevertheless, investigators have recently begun development of these materials with success. Copolymers of the degradable polyesters poly(ethylene glycol), poly(propylene glycol), and poly(tetramethylene glycol) and acrylated oligomers of D,L lactic acid were synthesized with the photoinitiator 2,2 dimethoxy-2-phenylacetophenone in N-vinylpyrrolidinone to form biodegradable networks [11]. Furthermore, Matsuda et al [27] have shown that biodegradable copolymers of ϵ -caprolactone and trimethylene carbonate can be photopolymerized with high-spatial control, allowing stereolithographically prepared surfaces to be synthesized. While a degree of success has been obtained, further work is required to characterize the properties of these materials.

The property many tissue-engineering investigators are often most interested in controlling is the material's degradation rate. The flexibility of photopolymerization offers a variety of schemes to obtain this control. Burkoth et al [12] shows that the degradation rate of photoinitiated biodegradable systems (using the acetophenone photoinitiator 2,2-dimethoxy-2-phenylacetophenone) can be tailored by controlling the hydrophobicity of the crosslinked polymer. Similarly an acetophenone initiator, *N*-vinylpyrrolidinone, and a dimethacrylate monomer can form degradable hydrogels, with degradation controlled by the monomer structure [13]. Finally, Gursel et al [28] controlled the degradation rate of azoisobutyronitrile photopolymerized materials by varying the composition of a degrading polymer (polyhydroxybutyrate-co-

hydroxyvalerate) and a nondegrading polymer (polyhydroxyethyl methacrylate). Although a variety of biodegradable materials have been successfully synthesized using photoinitiation, considerable room for further developments remains.

Hard Tissue Materials

Since the 1960's photopolymerized materials have been extensively used in dental applications because they possess advantageous properties such as low shrinkage, low water absorption, and good adhesion [29-31]. A typical photoinitiated dental material is comprised of four elements: a monomer, a diluent, a photoinitiator, and an inorganic filler [32]. The monomer is often a dimethacrylate, especially 2,2-bis[4-(2'-hydroxy-3'-methacryloyl-oxypropoxy)phenyl]propane (bis-GMA) or 1,6-bis(2'-methacryloyl-oxyethoxycarbonylamino)-2,4,4-trimethylhexane (UDMA) [32]. The dimethacrylate monomer bis-GMA has been used clinically, although it is associated with some degradation owing to its hydroxyl groups. Ahn et al examined the effect of substitution of these groups with methacryloyl groups, showing a 90% reduction of water sorption and therefore a likely reduction in degradation [16]. The photoinitiator system of choice, camphorquinone (CQ) and an amine such as *N,N*,3,5-tetramethyl aniline (TMA), is excited by visible blue light (420-500 nm) [16]. The development of orthopedic photoinitiated materials has largely grown from the dental research. A significant deviation, however, is that recent materials proposed for orthopedic applications have been devised so that they will degrade over time, ideally allowing bone to reclaim the defect area. A competing factor is the mechanical strength required by the material in order to withstand the forces carried within load-bearing sites or placed upon protective/supporting bone. Anseth and her associates have developed methacrylated

anhydride monomers, based upon sebacic acid, 1,6-bis(p-carboxy phenoxy) hexane, or 1,3-bis(p-carboxy phenoxy) propane, that possess mechanical strength and degrade over periods from weeks to a year [33-37]. The methacrylated anhydride monomers may be photopolymerized with a camphorquinone/ethyl-4-N,N-dimethylaminobenzoate system and visible blue light. Degradation rate can be controlled by alterations in the components and composition that make up the methacrylated anhydride monomer. Additionally, it was shown that hydrolytic degradation occurs from the outer surface toward the interior (surface degradation), in contrast to bulk degradation where there is no spatial dependence owing to the hydrophobicity of the network [37]. The development of photopolymerized hard tissue materials may allow for techniques such as *in vivo* curing and stereolithography printing to better match the patient's imaged anatomy [38-40].

Cell Interactions with Photoinitiated Biomaterials

Recent biomaterial research has shown that photoinitiated materials are suitable platforms for cell growth. As an initial toxicity study, Byrant et al [41] investigated the cytocompatibility of a variety of photoinitiators using a fibroblast cell line. Results showed that a fibroblast cell line is viable with not only direct application of ultraviolet radiation but also in the presence and excitation of a number of photoinitiators, including 1-hydroxycyclohexyl phenyl ketone, 2-methyl-1-[4-(methylthio) phenyl]-2-(4-morpholinyl)-1-propanone, and 2-hydroxy-1-[4-(hydroxyethoxy) phenyl]-2-methyl-1-propanone. In another investigation, chitin modified with both azide and lactose groups was photocrosslinked, through UV excitation of the azide groups and shown to permit cell growth adjacent to the material [15]. No cell proliferation, however, was observed

on the material itself. Orban et al [42] has studied acrylate functionalized phospholipids on alkylated supports for cardiovascular applications, showing that the visible light initiator system of eosin Y and triethanolamine had little effect upon cell viability.

In addition to cell viability tests, many have investigated the ability of photoinitiated materials to promote or inhibit cell adhesion. Typically, a hydrophilic polymer such as PEG is incorporated in order to inhibit cell adhesion [20]. This can be further extended by incorporating a hydrophobic copolymer, such as polystyrene, by photoinitiated copolymerization. The hydrophobic polystyrene allows strong bonding of the copolymer to a poly(ethylene terephthalate) surface, wheras the hydrophilic PEG is highly wettable and cell-adhesion resistant [43]. PEG can also be functionalized with bioactive molecules to promote cell adhesion. Hern et al [44] showed that peptide derivitized PEG can be photopolymerized and, depending upon the inclusion of spacer molecules, selective for cell adhesion, as measured by cell spreading. Specifically, PEG without a peptide sequence attached showed little cell spreading, PEG with a peptide attached but without a spacer linkage showed cell spreading nonspecific to the attached peptide sequence, and PEG with a spacer and peptide attached showed cell spreading specific to the peptide sequence. Although the cellular studies discussed to this point have shown that photoinitiated materials can be synthesized to maintain cell viability as well as promote cell adhesion, these studies have not investigated photoinitiated processes in the presence of cells.

Photopolymerized materials for cell encapsulation have been investigated primarily as tissue engineering constructs but have additionally shown the efficacy of photochemistry in biological systems. Islet cell encapsulation for pancreas tissue-

engineering and chondrocyte encapsulation for cartilage tissue-engineering have been reported [45-48]. Studies with islet cells have shown that photopolymerization of polyethylene glycol diacrylate hydrogels with an argon laser, utilizing eosin Y, triethanolamine, and 1-vinyl-2-pyrrolidinone, is sufficiently gentle to allow approximately 90% of the cells to survive 24 h after the cross-linking reaction [47,48]. Furthermore, it was shown that cell viability could be maintained at this level while increasing the rate of cross-linking that, in turn, improves the efficiency at which the cells are encapsulated. In an extremely effective use of photoinitiation techniques, Elisseeff et al [45,46] showed that poly(ethylene oxide) hydrogels containing chondrocytes could be formed via transdermal photoinitiation. Ultraviolet light exposured to the surface of the skin polymerized and encapusulated a subdermally injected-cell/polymer mixture. Their results show that implants at 2, 4, and 7 weeks exhibited collagen and proteoglycan production, indicating that UV exposure not only permits cell viability but also has no deleterious effect on cell function. These works may guide the future of photoinitiated biomaterials toward more tissue-engineering applications.

SUMMARY

A wide range of biomaterials can be synthesized by photoinitiated polymerization. This review has shown that well-defined hydrogels, degradable materials, and hard tissue materials all have been successfully constructed by using photolabile monomers, photolabile polymers, or photoinitiators. Furthermore, recent studies with tissue-engineering constructs have shown that many of these materials provide suitable substrates for cell encapsulation with maintenance of high levels of cell viability.

TABLE 2.1: Local wavelength of maximum absorption and associated extinction coefficients for typical chromophores found in photolabile compounds [2,4].

Chromophore	λ_{max} (nm)	ε_{max}
C=C	195	10,000
C≡C	195	2000
C=C-C=C	215	20,000
Benzene	185	60,000
	200	8000
	255	200
RRC=O	190	900
	280	15
RCOOH	205	60
N=N	345	4.5
NO_2	270	18.6
S=O	210	1500

CHAPTER III

OBJECTIVE

The goal of this work it to develop and characterize a photocrosslinkable, degradable polymer for use in the fabrication of tissue engineering scaffolds. The basic component of this photocrosslinkable material is the biodegradable polyester poly(propylene fumarate) (PPF). PPF was chosen since its repeating unit contains one carbon-carbon double bond that allows for covalent crosslinking as well as two ester groups that allow for hydrolytic degradation. The crosslinking of PPF through its carbon-carbon double bond forms a solid with significant mechanical integrity. The work described here involves the development of a method to initiate this crosslinking reaction using ultraviolet light as well as the characterization of the resulting material. In the course of this work, the following specific objectives were identified and investigated:

- Develop a photocrosslinkable system for poly(propylene fumarate),
- Characterize the mechanism by which PPF is photocrosslinked as well as the final network structure of the crosslinked PPF polymer,
- Form the PPF photocrosslinkable material into porous scaffolds using a porogen leaching technique and characterize the effects of porogen inclusion upon the photocrosslinking mechanism,
- Describe the *in vitro* degradation of photocrosslinked PPF scaffolds and determine the effects of pore inclusion, pore size, and pore volume upon degradation,

- Modify the PPF photocrosslinking strategy so that scaffold fabrication techniques which require the uncured PPF solution to be fluid are feasible,
- Investigate the soft and hard tissue response to photocrosslinked PPF scaffolds and determine any effects of the scaffold pore morphology upon the tissue response,
- Investigate whether photocrosslinked PPF scaffolds may act as a carrier for an adsorbed protein in order to promote bone formation,
- Determine the effect of the photocrosslinked PPF scaffolds upon bone formation as assessed by histomorphometrical analysis of wound healing and growth factor localization.

CHAPTER IV

THE PHOTOINITIATED CROSSLINKING OF THE BIODEGRADABLE POLYESTER POLY(PROPYLENE FUMARATE): DETERMINATION OF NETWORK STRUCTURE BY CONTRASTING PHOTOINITIATORS

ABSTRACT

In this work, we investigate the mechanism involved in the photoinitiated crosslinking of the polyester poly(propylene fumarate) (PPF) using the initiator bis(2,4,6-trimethylbenzoyl) phenylphosphine oxide (BAPO). It was hypothesized that BAPO has the ability to crosslink PPF into solid polymer networks, without the use of a crosslinking monomer, because two pairs of radicals, both involving a fast adding phosphinoyl radical, were formed upon UV irradiation of BAPO. Spectroscopic investigation first confirmed the addition of BAPO derived radicals to the PPF olefin. Investigations of fumarate conversion and bulk network properties were then undertaken, using the BAPO initiator and a monoacylphosphine oxide (MAPO) initiator which contains a single photolabile bond. Results show that a single BAPO phosphinoyl radical was primarily responsible for the formation of a highly crosslinked PPF network and the additional radical pair which may be formed does not dramatically alter fumarate conversion or bulk network properties. From these results, the network structure of BAPO initiated, photocrosslinked PPF may be deduced. Finally, this study demonstrates a method for inferring crosslinked network structures by contrasting properties of bulk materials formed from similar crosslinking initiators.

INTRODUCTION

Some of the most widely investigated synthetic, degradable polymers for tissue engineering applications are based upon polyesters due to the ester bond's ability to undergo slow hydrolysis. For example, polyesters such as poly(L-lactic acid) and poly(lactic-co-glycolic acid) are biocompatible, biodegradable materials that can be formed into tissue engineering scaffolds through a solvent casting/compressive molding technique [49,50]. Another polyester investigated for tissue engineering applications is poly(propylene fumarate) (PPF), which has also been shown to be biocompatible and biodegradable [51-53]. PPF has the inherent advantage of fumarate groups that allow the polymer chains to be covalently crosslinked through its unsaturated carbon-carbon double bond with relatively low levels of heat release [54]. Thus PPF can be fabricated into a three dimensional scaffold *in situ*. Previous investigated methods of crosslinking PPF employ the monomer N-vinyl pyrrolidone (NVP), the radical initiator benzoyl peroxide (BP), and the accelerator N,N dimethyl-p-toluidine (DMT) [54]. The possibility of developing an alternate system for crosslinking of PPF, particularly involving ultraviolet light initiated crosslinking, led to the study of acylphosphine oxides as initiators of PPF crosslinking. A photoinitiated system would be advantageous as it would allow for the use of fewer components, enhancing biocompatibility, as well as allow for scaffold fabrication techniques such as transdermal curing or stereolithography.

Acylphosphine oxides are a class of photoinitiators which include three basic members: monoacylphosphine oxides (MAPO), bisacylphosphine oxides (BAPO), and trisacylphosphine oxides (TAPO) [55]. All of these compounds undergo fast α-cleavage of the benzoyl-phosphinoyl bond upon irradiation, producing a pair of radicals (Figure

4.1A and 4.1B) [56]. Kolczak et al. showed that these radicals can regenerate the initial compound or go on to form solvent cage products and escape products [57]. If an olefin is present, the escaped radicals can add to its double bond. Of the two radicals produced, the phosphinoyl has been shown to be significantly faster in its subsequent addition than the benzoyl radical [55]. For the case of bis(2,4,6-trimethylbenzoyl) phenylphosphine oxide, the phosphinoyl radical has an addition rate constant to n-butyl acrylate of approximately $1x10^7$ $M^{-1}s^{-1}$, compared to $4x10^5$ $M^{-1}s^{-1}$ for the 2,4,6-trimethylbenzoyl radical [55]. In general, BAPO and TAPO are particularly effective crosslinking agents because they absorb at long UV wavelengths with a high extinction coefficient ($\varepsilon \sim 10^4$ at 370 nm), their excited state efficiently generates radicals that rapidly attack olefins, and the initial olefin adducts are themselves photolabile by virtue of their additional acylphosphine groups.

In general, photoinitiated systems have the advantages of a well defined reaction initiation and termination, short reaction times, a wide range of possible scaffold geometries, and use in both prefabricated and *in situ* systems [36,48,58]. Furthermore, while the photochemistry of biomaterials has been extensively studied, few systems involving biodegradable polymers have been reported [33,58]. Recent work has shown that photocrosslinked PPF can be formed into porous, biocompatible tissue engineering scaffolds and, furthermore, that these scaffolds may be used as carriers for growth factors in order to promote bone formation [59-61]. These studies have all utilized the photoinitiator bis(2,4,6-trimethylbenzoyl) phenylphosphine oxide (BAPO), without the need for a crosslinking monomer. The study described here explores the mechanism by

which the photoinitiator BAPO can effectively crosslink PPF without the use of a crosslinking monomer.

It was hypothesized that BAPO has the ability to crosslink PPF into solid polymer networks because two pairs of radicals, both involving the fast adding phosphinoyl radical, were formed upon UV irradiation of BAPO. In order to test this hypothesis, the photoinitiated crosslinking of PPF was studied using the bis(2,4,6-trimethylbenzoyl) phenylphosphine oxide initiator as well as a 2,4,6-trimethylbenzoyldiphenylphosphine oxide (MAPO) initiator (Figure 4.1A and 4.1B). The BAPO initiator forms two pairs of radical products available for PPF crosslinking, in contrast to the MAPO initiator which forms only one pair. While the same 2,4,6-trimethylbenzoyl radical is produced from both initiators, the phosphinoyl radicals differ, with the addition of a phenyl group to the central phosphorous atom in MAPO. By comparing the fumarate conversion and bulk properties of the networks formed from BAPO crosslinked PPF and MAPO crosslinked PPF, we seek to identify the mechanism for effective PPF crosslinking by BAPO as well as its final network structure.

MATERIALS AND METHODS

Poly(propylene fumarate) synthesis

Poly(propylene fumarate) was synthesized following a two step procedure [62]. First, 1 mol diethyl fumarate (Acros Organics, NJ, USA) and 3 mol 1,2 propanediol (Acros) were reacted using 0.01 mol $ZnCl_2$ (Fisher Chemicals, Fair Lawn, NJ, USA) as a catalyst and 0.002 mol hydroquinone (Acros) as a radical inhibitor. The reaction was run for approximately eight hours under a nitrogen blanket, producing a bis(hydroxypropyl) fumarate as the main product and ethanol as a byproduct. The bis(hydroxypropyl)

fumarate was then transesterified, producing poly(propylene fumarate) and 1,2 propanediol as a byproduct. The reaction was run until the product had the desired molecular weight as determined by gel permeation chromatography. This product was dissolved in methylene chloride (Fisher Chemicals) to allow for purification. PPF was first washed with acid (5 wt% HCl in H_2O) to remove the $ZnCl_2$ and then purified with two washes each of both pure water and brine. The organic phase was dried with sodium sulfate. The concentrated product was then precipitated in ethyl ether twice to remove the radical inhibitor. Finally, all solvents were removed from the PPF by rotary evaporation followed by vacuum drying. The number average molecular weight (M_n) increased after purification as lower molecular weight chains were removed by the aqueous washes. The final product was a clear, light yellow viscous liquid with a M_n of 1680 and a polydispersity index (PI) of 1.45, as determined by gel permeation chromatography.

Gel permeation chromatography

The molecular weight distributions of PPF were determined by gel permeation chromatography (GPC). The GPC system consisted of an HPLC pump (Waters, Milford, MA, USA), an autosampler (Waters), a chromatography column (Waters, Styragel HR 4E, 7.8 x 300 mm column [50 – 100,000 Da range]), and a differential refractometer (Waters). The solvent, degassed chloroform, was run at 1.0 ml/min for sample measurement. Polystyrene standards (500, 2630, 5970, and 9100 Da) were used to obtain a calibration curve for calculating molecular weight distributions.

Poly(propylene fumarate) photocrosslinking

Poly(propylene fumarate) was crosslinked with ultraviolet light and the photoinitiators 2,4,6-trimethylbenzoyldiphenylphosphine oxide (MAPO, BASF Dispersions and Paper Chemicals, Mount Olive, NJ, USA) and bis(2,4,6-trimethylbenzoyl) phenylphosphine oxide (BAPO, Ciba Specialty Chemicals, Terrytown, NY, USA) [60]. An initiator solution was made by dissolving the proper amount of initiator in methylene chloride so that the same amount of solvent was added to each PPF formulation; initiator solutions of 0.4, 2.0 and 4.0 mol % were investigated. The PPF was warmed in an oven (approximately 60°C) to reduce viscosity and then mixed with the initiator solution. This solution was heated (60°C), centrifuged (5 minutes at 3000 rpm) to remove any entrapped bubbles, and then cast into a glass mold. All samples were exposed to ultraviolet light for 30 minutes at a distance of approximately 15 cm. The ultraviolet light source used was an Ultralum (Paramount, CA) ultraviolet light box. The UV box was outfitted with four 15W long wavelength UV bulbs. The total light emission covers a range of UV wavelengths, with a peak at 365 nm (320 – 405 nm) and an intensity of 4 mW/cm^2 at 15 cm. MAPO absorbs wavelengths between 450 and 300 nm; BAPO absorbs wavelengths below 400 nm, with a general increase in absorption as the wavelength decreases to 200 nm.

Nuclear magnetic resonance spectrometry

Proton ^{1}H and phosphorous ^{31}P nuclear magnetic resonance spectrometry (NMR) were obtained using a Bruker Avance 400 MHz NMR system (Bruker Analytik GmbH, Rheinstetten, Germany) operated with a Silicon Graphics O2 workstation (Silicon Graphics, Mountain View, CA). Proton spectra were obtained using a 30° pulse angle, 4

s acquisition time, and 3 s delay time. Samples were run in $CDCl_3$ with TMS as the reference. Phosphorous spectra were obtained similarly but using 85% phosphoric acid (H_3PO_4) was used as the external reference.

Differential photocalorimetry

Differential photocalorimetry (DPC) was performed using a differential scanning calorimeter (TA Instruments, New Castle, Delaware) fitted with a DPC module (TA Instruments). The UV light (200 W Hg lamp whose characteristic wavelengths include 313, 366, 405 and 435 nm) was corrected for any uneven distribution over both the sample and reference in the chamber. The reference used for measurements was a cured sample of crosslinked PPF. Heat release was measured during UV exposure under isothermal conditions and after chamber equilibration at 37°C. The heat release due to UV induced crosslinking was calculated as the area under the differential heat release curve divided by PPF weight. Each sample type was run five times; the reported values are the mean values and the associated errors are the standard deviations.

Characterization of crosslinked network structure

The network structure of crosslinked PPF was analyzed by examination of the degradation products. Degradation of the network releases any unreacted fumarate units that were not involved in the crosslinking reaction as its corresponding unsaturated organic acid. Quantification of the released fumaric acid enables an estimate of the double bond conversion, crosslinking density, and molecular weight of chains between crosslinks [63]. Briefly, the crosslinked PPF specimens were ground into a powder and measured amounts were placed into 20 mL of 1N NaOH solution (Fisher). The solution was stirred and heated at 60°C until the polymer had completely degraded. A 1 mL

sample was taken for high performance liquid chromatography (HPLC) analysis in order to quantify the fumaric acid within the degradation solution. The quantities were normalized to the weight of the powder prior to degradation and presented in units of [mmol]/[g of polymer]. Uncrosslinked PPF formulations were degraded in a similar fashion.

The fumarate functional groups available for crosslinking within the PPF polymer (FB_o) were quantified from the degradation products of the uncrosslinked polymer. The unreacted fumarate bonds (FB_{nox}) were obtained from the degraded polymeric networks. The reacted species (FB_x) were then calculated by:

$$FB_x = FB_o - FB_{nox} \tag{1}$$

and defined as moles per unit mass of the polymer network ([mmol]/[g of polymer]). The double bond conversion within the network was then defined as:

$$X_{FB} = \frac{FB_x}{FB_o} \tag{2}$$

where X_{FB} is the conversion of fumarate bonds. The average molecular weight between crosslinks (M_c) was determined knowing that a reacted fumarate bond will have two chains extending from the crosslink. This calculation was based on the assumption that these chains exist between two reacted fumarate bonds and do not form network defects such as dangling chains ends or loops. M_c in units of g/mol was then estimated by:

$$M_c = \frac{1}{FB_x} \tag{3}$$

Network characterization was carried out in triplicate; the reported values are the mean values and the associated errors are the standard deviations.

High performance liquid chromatography (HPLC)

The fumaric acid within the PPF degradation products was separated and quantified by HPLC equipped with a diode array UV/VIS detector (Waters). Analysis was conducted at room temperature with a Nova-Pak C_{18} column (3.9 mm x 150 mm) (Waters) and a mobile phase mixture of 97% 0.02 M ammonium hydrogen phosphate and 3% methanol at a flow rate of 0.5 mL/min. The pH of the mobile phase was adjusted to 2.35 with phosphoric acid and 0.03 M ammonium acetate was added to avoid silanol effects with the column. Chromatographs were acquired at a UV absorption of 200 nm. Fumaric acid standards of 0, 0.3, 0.5, 0.7, and 1.0 mg/ml concentrations in 1N NaOH were used to generate calibration curves for quantification.

Swelling studies

Degree of swelling and sol fraction of all samples were investigated using photocrosslinked flat sheets, approximately 0.15 g in weight and 1.0 mm in thickness. A photocrosslinked sample was weighed (W_i) and placed into capped vials containing 20 ml of toluene for 24 hours. Toluene was used in this study as PPF swells only moderately in this solvent and thus the samples retain their three dimensional structure throughout the experiment. The samples were removed from the toluene, blotted dry with weigh paper, and then weighed (W_s). Finally, the samples were left in a fume hood to dry overnight and subsequently weighed (W_d). The degree of swelling was calculated using the formula:

$$\text{Swelling Degree} = \frac{W_s - W_d}{W_s}. \qquad (4)$$

The sol fraction was calculated using the formula:

$$\text{Sol Fraction (Sheet)} = \frac{W_i - W_d}{W_i} \times 100\%. \quad (5)$$

Each sample type was run five times; the reported values are the mean values and the associated errors are the standard deviations.

Tensile mechanical testing

Tensile testing of the solid PPF constructs was conducted using an Instron testing machine (Instron, Canton, MA). Dogbone shaped samples were fabricated in teflon molds as described above. The size of the narrow portion of the dogbone was 40 mm in length, 6 mm in width, and 4 mm in thickness. Force and displacement were zeroed prior to testing. Samples were placed under tension at a crosshead speed of 1 mm/min while the load and extension were monitored. Testing was halted after sample fracture. The initial slope of the stress - strain curve determined the elastic modulus of the sample. Five trials were run for each sample set. The values and errors reported for each sample are the mean values and standard deviations, respectively.

Statistics

All sets of data were first inspected with a F-test for treatment effects [64]. The null hypothesis (the means of each set were equal) was evaluated with $\alpha = 0.05$. If the null hypothesis was found to be false (i.e., the mean of the sets were not equal), then a Tukey's multiple comparison test was performed to determine pairwise relationships between sets [64].

RESULTS

The chemical structure of BAPO crosslinked PPF was initially investigated by ^{1}H NMR of two samples: (1) diethyl fumarate (DEF, $CH_3CH_2O_2CCH{=}CHCO_2CH_2CH_3$) and

(2) the photoproduct of DEF and BAPO (DxB). In DEF, the area ratios of the CH_3, CH_2, and =CH were 1.000 : 0.661 : 0.314, close to that expected from the chemical structure of DEF. The DxB spectra exhibited nearly the same chemical shifts but with areas of 1.000 : 0.660 : 0.267, respectively. Thus the DEF/BAPO reaction reduced the amount of fumarate double bonds by approximately 15% while the CH_3 and CH_2 groups remained unchanged. Furthermore, peaks at 4.05, 3.28, 3.14, and 2.95 ppm may reflect the presence of methine groups associated with fumarate, phosphinoyl, or benzoyl compounds, as would be expected from the radical attack on the fumarate double bond by BAPO derived molecules.

The ^{31}P spectra of UV irradiated BAPO (Bx) and the photoproduct of DEF and BAPO (DxB) were then examined (Figure 4.2). The Bx spectrum exhibited a large peak at 7.92 ppm due to unreacted BAPO as well as approximately 11 peaks between 60 ppm and 0 ppm, with no peaks outside this range. The DxB spectra exhibited peaks at 24.80, 21.86, and 7.92 ppm, similar to those seen in the Bx spectrum. However, additional peaks between 33 and 15 ppm show the formation of new phosphorous-DEF compounds. These new peaks lie within the range of phosphorous (V) products which would be the expected products of BAPO radicals and DEF.

The fumarate conversion was studied by two methods, differential photocalorimetry and characterization of network degradation products. Differential photocalorimetry was utilized to examine the heat release and fumarate unit conversion during PPF crosslinking reaction with three different molar concentrations of either MAPO or BAPO (Figure 4.3). The heat release was found to generally increase with increasing initiator content. However, no statistical difference was seen between samples

fabricated with either 2.0 or 4.0 mol% initiator. This data can be transformed into percent fumarate bond conversion by dividing by the theoretical heat of polymerization of diethyl fumarate (378 J/g) [65]; the corresponding trend of fumarate conversion is presented in Figure 4.3B. The trends in heat release and fumarate conversion were similar between BAPO crosslinked PPF and MAPO crosslinked PPF, with a significant difference noted in only the 2.0 mol% samples.

Fumarate conversion was also characterized by degrading the crosslinked network and analyzing the resulting degradation products. Using this method, conversion of the fumarate units as well as the molecular weight between crosslinks (M_c) was determined (Figure 4.4A and 4.4B). The conversion results from this study closely parallel the conversion data obtained by differential photocalorimetry, showing a general increase with increasing initiator content but with no change at the highest two initiator contents studied. As expected, the resulting M_c values mirror these data, with higher conversion giving a lower molecular weight between crosslinks value. The results from this study show a significant difference between all BAPO and MAPO samples.

The properties of the formed crosslinked network were studied by swelling degree and mechanical testing. The sol fraction and swelling degree of the BAPO and MAPO crosslinked samples are presented in Figures 4.5A and 4.5B. As expected, sol fraction dramatically decreased and swelling degree significantly decreased with increasing initiator content. The trends were similar between the BAPO and MAPO crosslinked samples. However, significant differences between the two classes of samples were noted in the sol fraction data (2.0 mol% samples) and the swelling degree data (0.4 mol% and 2.0 mol% samples).

The results from the tensile mechanical studies of photocrosslinked PPF are presented in Figure 4.6. All of the samples showed similar mechanical behavior. The initial slope of the load - elongation curve was small, indicating that the material was only slightly elastic. The ability of the crosslinked material to accept a large amount of deformation before fracture changed with initiator content, with samples crosslinked with low initiator content acting in a ductile manner and samples crosslinked with high initiator content behaving in a brittle manner. The effect of initiator content upon the tensile modulus was dramatic. Both BAPO and MAPO samples show a two orders of magnitude increase in tensile modulus as initiator content was increased from 0.4 mol% to 4.0 mol%. There was no significant difference observed in tensile modulus between the BAPO and MAPO crosslinked samples.

DISCUSSION

The objective of this work was to identify why the photoinitiator BAPO can effectively initiate crosslinking of PPF in the absence of a crosslinking monomer. It was hypothesized that BAPO has the ability to crosslink PPF into solid polymer networks because it contains two photolabile groups which after UV irradiation can form two pairs of radicals, particularly two phosphinoyl radicals, that were available for PPF crosslinking.

Two different studies were performed to test this hypothesis. The first study was undertaken to confirm the reaction of the photoinitiated radicals with the PPF olefin. The reaction of the BAPO photoinitiator with a fumarate group was investigated with NMR, using DEF as a model molecule for PPF, as PPF was synthesized from DEF and thus contains the same reactive group. The advantage of using DEF rather than PPF was that

all products were still liquid, as opposed to the solid form of crosslinked PPF, and therefore easily inspected spectroscopically. Furthermore, the mechanism by which the initiator reacts with DEF was likely to be very similar to the PPF crosslinking mechanism. The procedure used for this study was the same as that typically employed in PPF crosslinking, including the use of methylene chloride as an initiator solvent, the amount of initiator per fumarate double bond, and all reaction conditions.

The results of the ^{1}H NMR investigation clearly show that BAPO reacts with the unsaturated carbon-carbon double bond without significant reaction of the methyl and methylene groups of DEF. Furthermore, the ^{31}P NMR investigation showed that the UV light induced reaction of BAPO and DEF produces phosphorous (V) compounds, not seen when BAPO was exposed to UV light in the absence of DEF. These two results suggest that BAPO reacts with DEF under UV irradiation by radical addition to the fumarate double bond to form phosphorous-DEF compounds. The reaction of PPF and BAPO very likely follows the same mechanism as the one described here between DEF and BAPO. However, as further spectroscopic work, including solid state NMR, could not provide additional insight to the photocrosslinking of PPF, a second study was undertaken.

In order to better understand the mechanism of BAPO crosslinked PPF, an alternate strategy to spectroscopy had to be developed. This strategy involved the comparison of the bulk properties of crosslinked networks formed from MAPO initiated and BAPO initiated crosslinked PPF. The concept behind this comparison was that MAPO and BAPO form nearly the same radical species upon UV irradiation, but BAPO forms two pairs of radicals as MAPO forms only one. Thus, if fumarate conversion and

bulk properties of MAPO crosslinked PPF differ significantly from BAPO crosslinked PPF, the number of radical species may be the source of the difference. Alternatively, if the properties of the crosslinked networks were similar, it may be inferred that the second photolabile group contained with BAPO was not significantly involved in the continuation of PPF crosslinking and the primary mechanism involves simply the addition of a single phosphinoyl radical to the PPF carbon-carbon double bond. It should be noted that changes in the concentration of BAPO initiator, to alter the number of radical species within the system, would not sufficiently answer this question because of the manner in which a photoinitiator containing multiple photolabile bonds is expected to function. Specifically, BAPO is thought to form one radical pair, containing a 2,4,6 trimethylbenzoyl radical and a phosphinoyl radical, and then add to the PPF olefin. Subsequently, the phosphinoyl radical would be available for a second UV initiated cleavage, forming a second 2,4,6 trimethylbenzoyl radical which is free in solution as well as a second phosphinoyl radical, which is now bound to the polymer network and available for continuation of PPF crosslinking. Simply increasing the number of BAPO molecules would increase the number of radicals in solution, but would not necessarily increase the number of radicals bound to the network and available for the continuation of PPF crosslinking.

The results from both fumarate conversion studies indicate a statistically significant increase in fumarate conversion, approximately 15%, when BAPO, rather than MAPO, was used as a photoinitiator (Figures 4.3 and 4.4). However, this was only true at low concentrations. It would have been expected that if BAPO's second photolabile bond was critical in the crosslinking of PPF, that the conversion of fumarate would have

been dramatically higher in the BAPO crosslinked PPF than the MAPO crosslinked PPF. With a small increase in conversion, at only low initiator concentrations, it may be concluded that this second photolabile bond, while involved in PPF crosslinking, was not critical for forming highly crosslinked networks, as seen in molecular weight between crosslinks values in Figure 4.4B.

The results from the bulk properties studies seem to support this conclusion. Again, the MAPO crosslinked samples have similar sol fraction, swelling degree, and tensile modulus as the BAPO crosslinked samples (Figures 4.5 and 4.6). Some statistically significant differences were found between the two sample types, but again the differences were low. No statistically significant differences were observed in tensile modulus between the two sample types (Figure 4.6). Thus, the fumarate conversion results seem to accurately reflect the bulk properties of the two classes of crosslinked PPF.

As a whole, the results indicate that highly crosslinked PPF results from the quick addition of the phosphinoyl radical, present in both the MAPO and BAPO samples, to the PPF olefin. As a result, the final crosslinked network structure, formed from BAPO crosslinked PPF, may be inferred (Figure 4.7). This structure depicts a single BAPO radical pair initiating the crosslinking of PPF, but does not show cleavage of the second photolabile bond and its continuation of PPF crosslinking so as to entrap a phosphinoyl group within crosslinked PPF chains.

CONCLUSIONS

The bis(2,4,6-trimethylbenzoyl) phenylphosphine oxide photoinitiated crosslinking of poly(propylene fumarate) was investigated in order to determine the

critical species involved in the crosslinking mechanism. By contrasting the fumarate conversion and bulk properties of BAPO crosslinked PPF with those of a monoacylphosphine oxide initiator, it was concluded that a single phosphinoyl radical derived from BAPO was primarily responsible for the photoinitiated crosslinking of PPF. Furthermore, knowledge of the crosslinking mechanism allowed for a determination of the general network structure of BAPO initiated, photocrosslinked PPF. Finally, this study demonstrates that by contrasting the bulk properties of crosslinked materials formed from similar initiators, the final structure of a crosslinked network may be inferred.

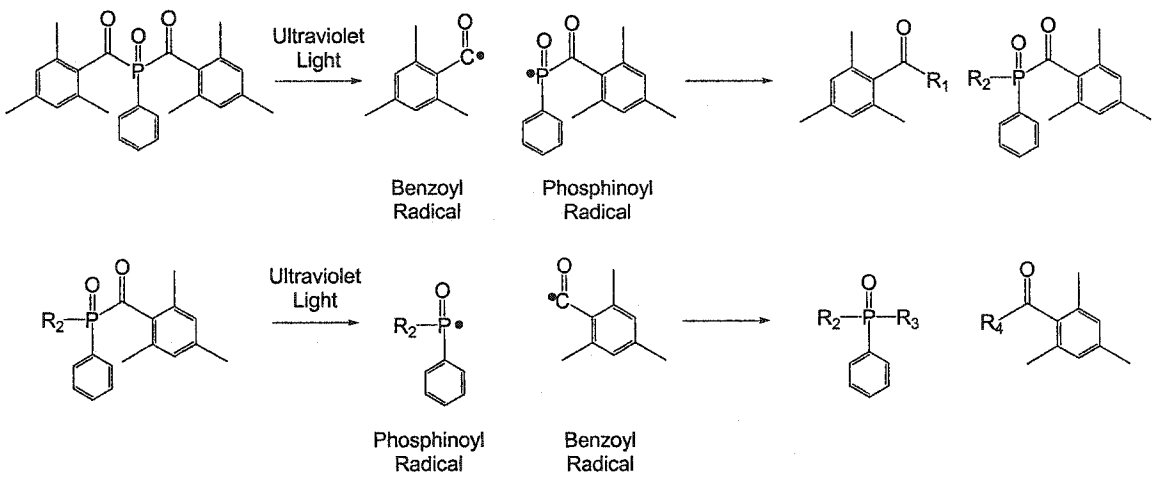

(A)

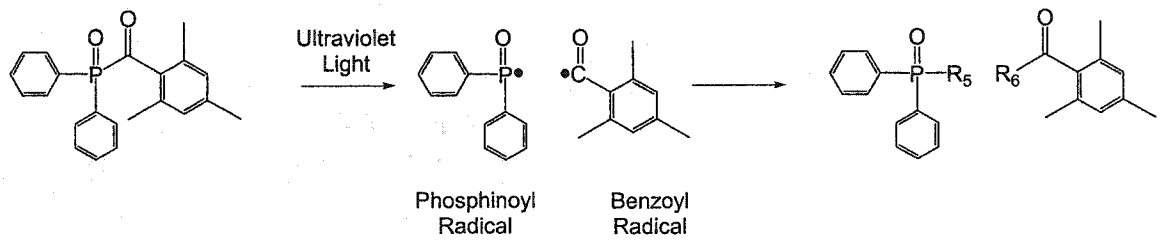

(B)

FIGURE 4.1: The radical reactions involved in BAPO exposure to UV irradiation **(A)** as well as MAPO exposure to UV irradiation **(B)**.

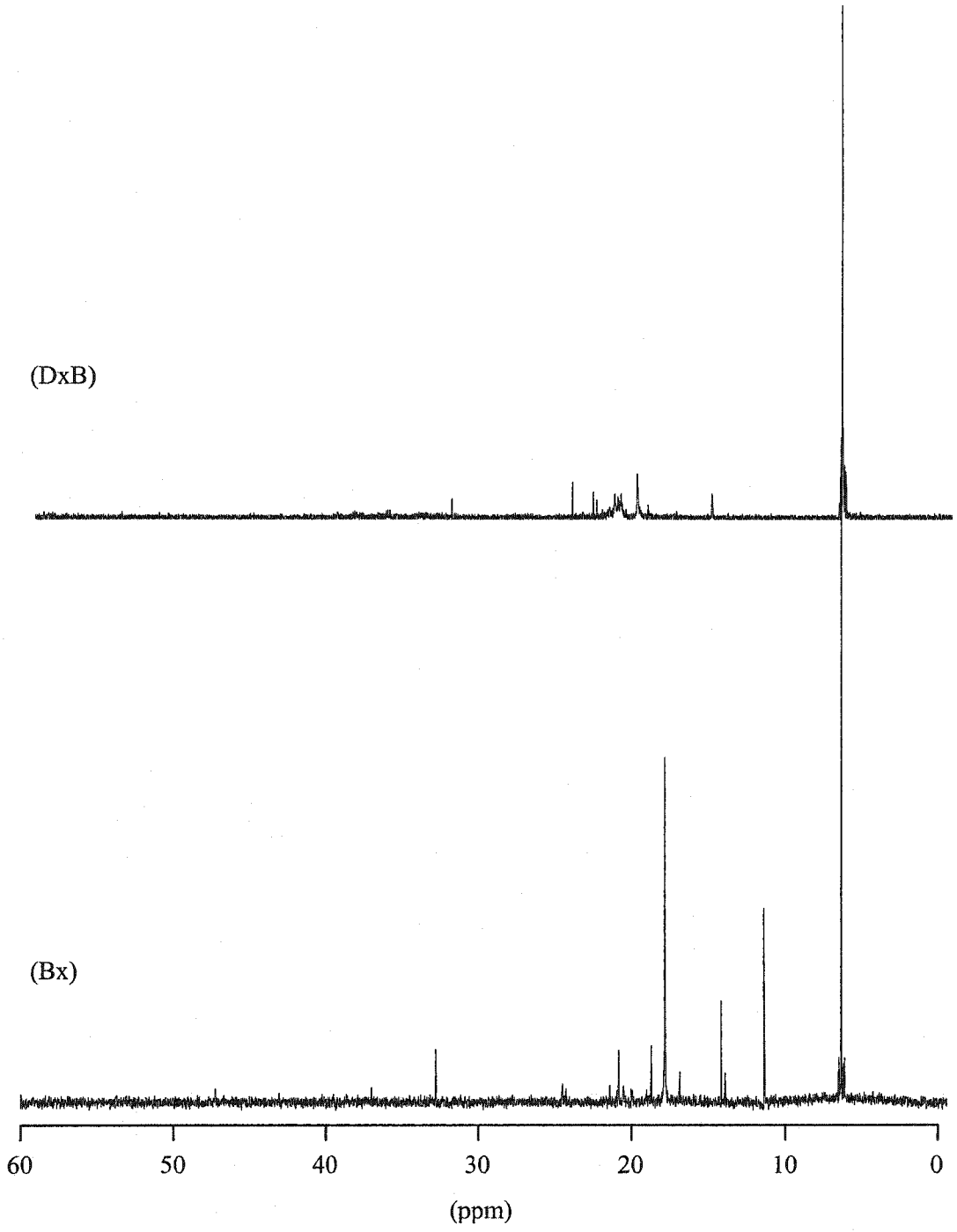

FIGURE 4.2: ^{31}P NMR spectra of BAPO after UV irradiation (Bx) and the UV initiated reaction of BAPO and diethyl fumarate (DxB). The large peak at 7.92 ppm is unreacted BAPO; other peaks identify various radical products of BAPO (Bx) or BAPO and diethyl fumarate (DxB).

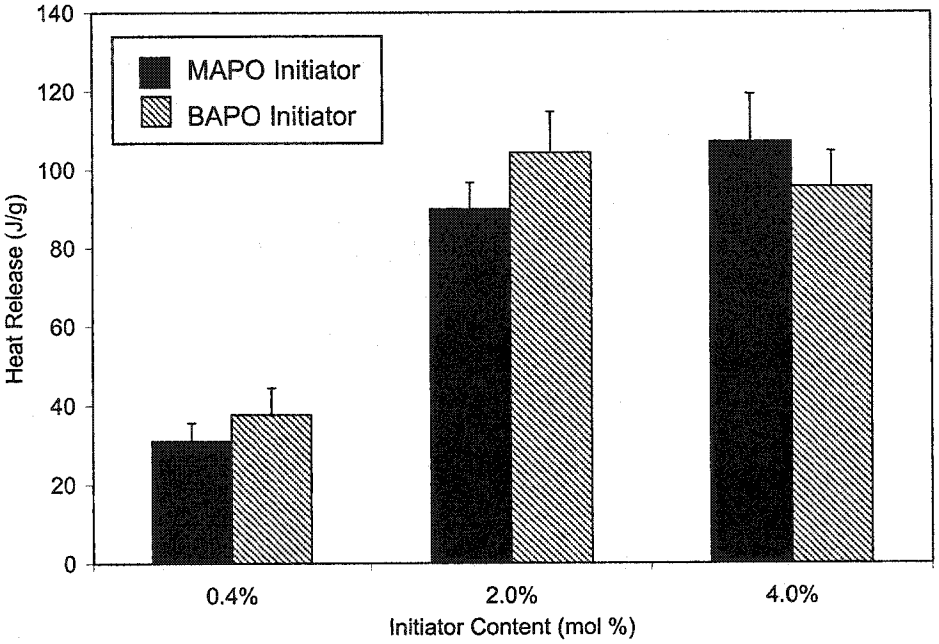

(A)

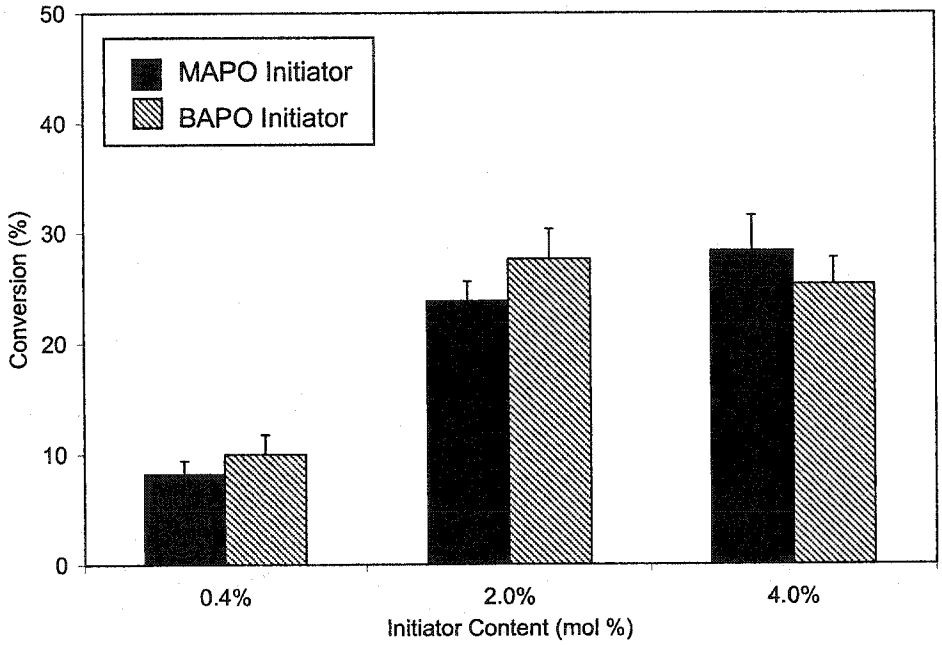

(B)

FIGURE 4.3: The heat release **(A)** and fumarate conversion **(B)** of BAPO and MAPO initiated crosslinking of PPF as measured by differential photocalorimetry. The results of both heat release and fumarate conversion were statistically similar between BAPO crosslinked PPF and MAPO crosslinked PPF, with the exception of the 2.0 mol% samples where a significant difference was found.

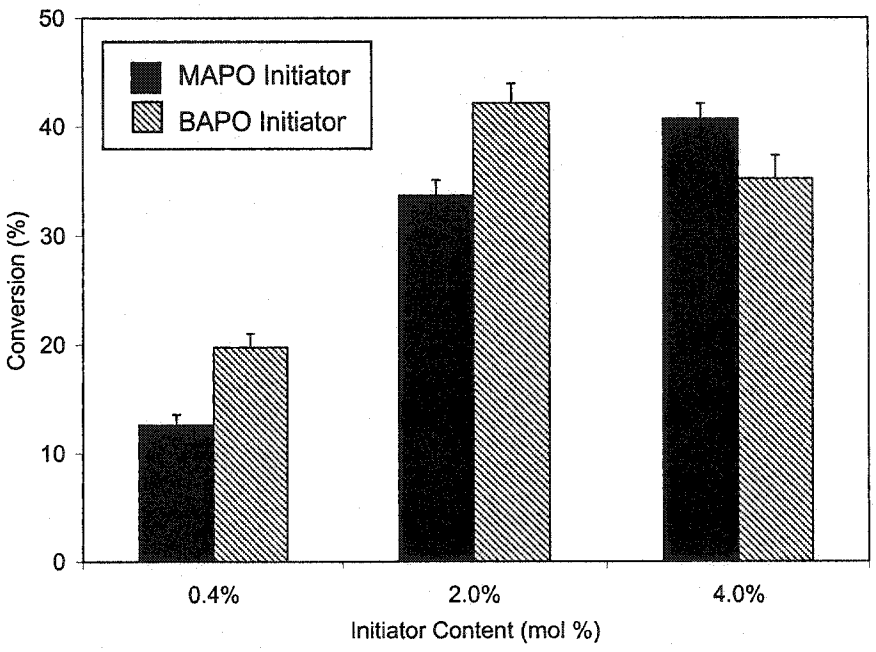

(A)

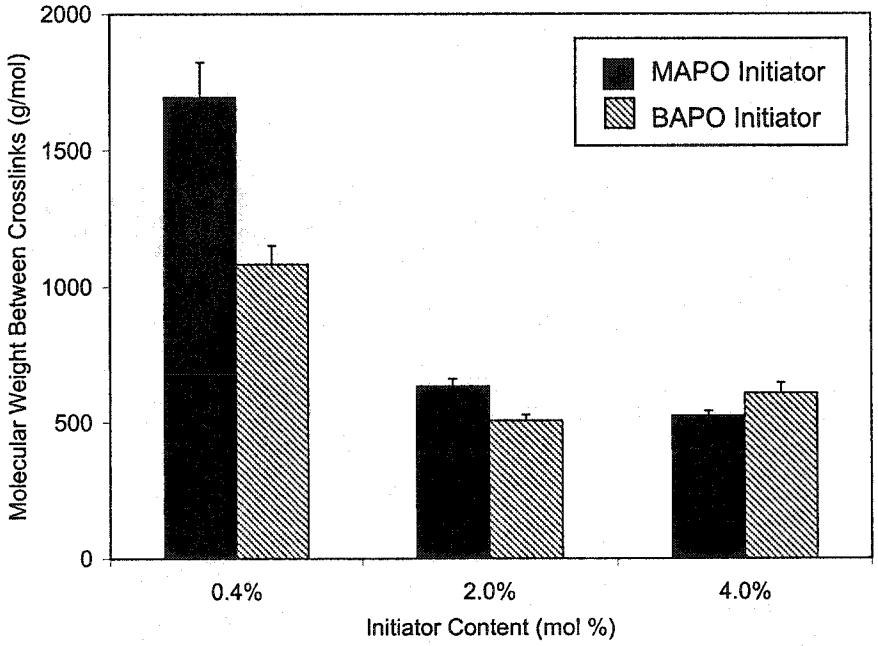

(B)

FIGURE 4.4: The fumarate unit conversion **(A)** and molecular weight between crosslinks **(B)** of PPF crosslinked with BAPO and MAPO photoinitiators, measured by HPLC analysis of network degradation products. The results of both conversion and molecular weight between crosslinks were found to be significantly difference between all BAPO and MAPO samples.

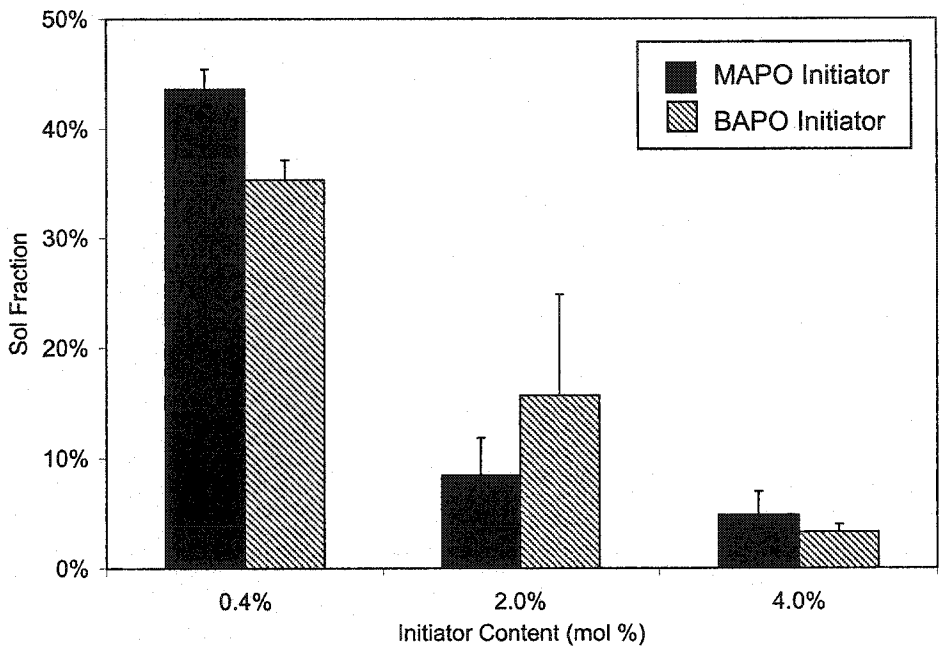

(A)

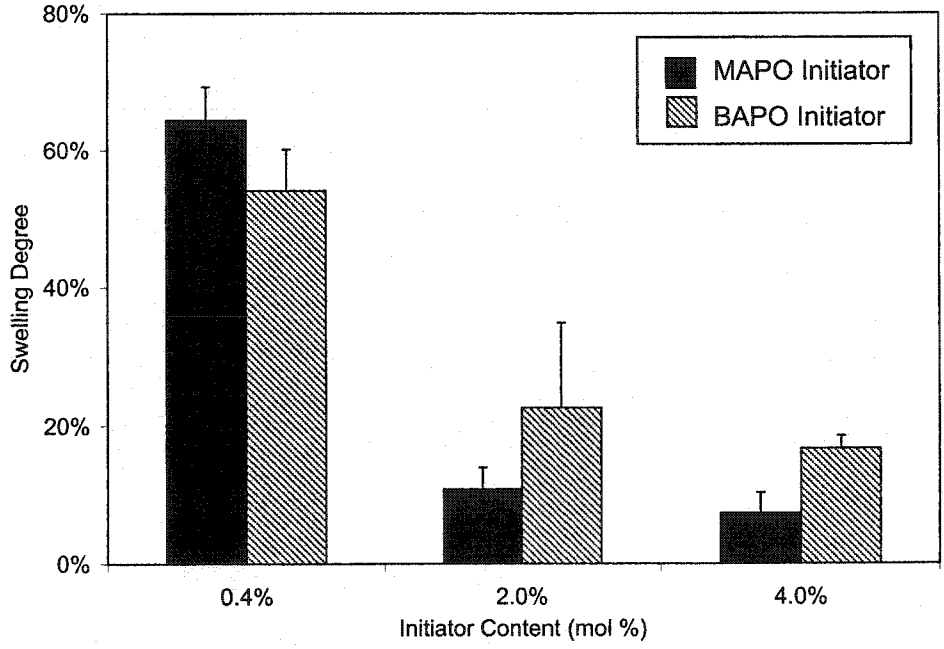

(B)

FIGURE 4.5: The sol fraction **(A)** and swelling degree **(B)** of crosslinked PPF in toluene, using BAPO or MAPO for initiation of PPF photocrosslinking. Significant differences between the BAPO crosslinked PPF and the MAPO crosslinked PPF were found in the sol fraction data (2.0 mol% samples) and the swelling degree data (0.4 mol% and 2.0 mol% samples).

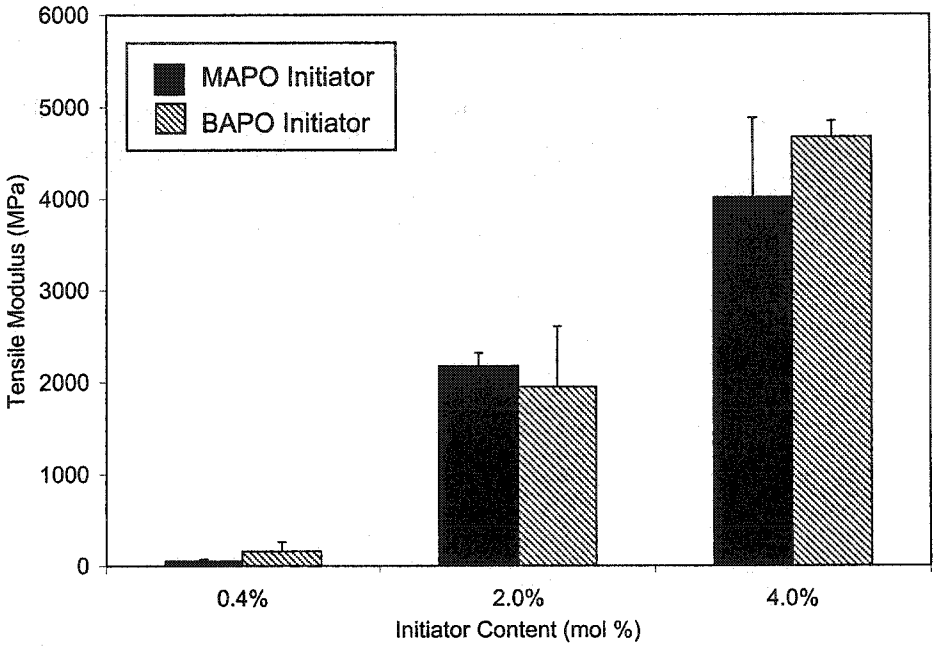

FIGURE 4.6: The tensile modulus of PPF crosslinked with BAPO and MAPO photoinitiators. The tensile modulus was found to be statistically similar between BAPO and MAPO crosslinked PPF for all initiator contents studied.

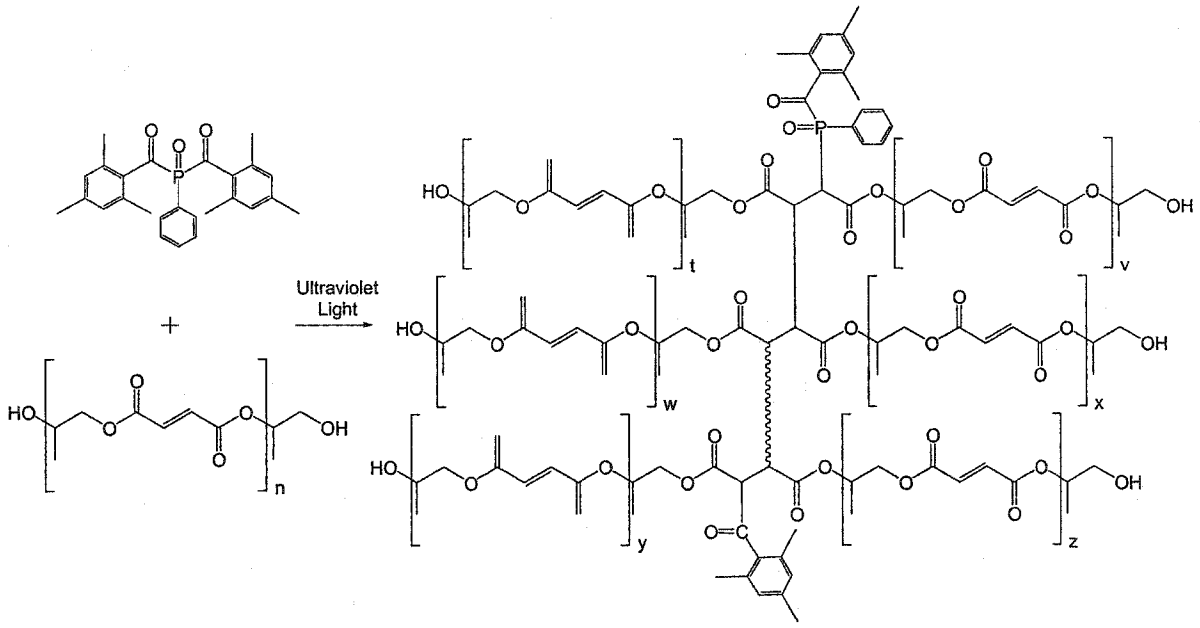

FIGURE 4.7: A proposed structure of photocrosslinked PPF using the BAPO initiator. This structure depicts a single BAPO radical pair initiating PPF crosslinking, without the continuation of crosslinking by the cleavage of the second photolabile bond contained within the BAPO initiator.

CHAPTER V

SYNTHESIS AND PROPERTIES OF PHOTOCROSSLINKED POLY(PROPYLENE FUMARATE) SCAFFOLDS[†]

ABSTRACT

We have investigated the photocrosslinking of poly(propylene fumarate) (PPF) to form porous scaffolds for orthopedic tissue engineering applications. PPF was crosslinked using the photoinitiator bis(2,4,6-trimethylbenzoyl) phenylphosphine oxide (BAPO) and exposure to 30 minutes of long wavelength ultraviolet (UV) light. The porous photocrosslinked PPF scaffolds (6.5 mm diameter cylinders) were synthesized by including a NaCl porogen (70, 80, and 90 wt% at crosslinking) prior to photocrosslinking. After UV exposure, the samples were placed in water to remove the soluble porogen, revealing the porous PPF scaffold. As porogen leaching has not been used often with crosslinked polymers, and even more rarely with photoinitiated crosslinking, a study of the efficacy of this strategy and the properties of the resulting material was required. Results show that the inclusion of a porogen does not significantly alter the photoinitiation process and the resulting scaffolds are homogeneously crosslinked throughout their diameter. It was also shown that porosity can be generally controlled by porogen content and that scaffolds synthesized with at least 80 wt% porogen possess an interconnected pore structure. Compressive mechanical

[†] This chapter was published as the following article: Fisher JP, Dean D, Mikos AG. Synthesis and properties of photo-crosslinked poly(propylene fumarate) scaffolds. J Biomater Sci Polymer Ed. 2001; 12: 673-687.

testing showed scaffold strength to decrease with increasing porogen content. The strongest scaffolds with interconnected pores had an elastic modulus of 2.3 ± 0.5 MPa and compressive strength at 1% yield of 0.11 ± 0.02 MPa. This work has shown that a photocrosslinking/porogen leaching technique is a viable method to form porous scaffolds from photoinitiated materials.

INTRODUCTION

Many strategies for tissue engineering require scaffolds that, by acting as a surrogate extracellular matrix, provide an initial site for cells to anchor, grow, and proliferate. Furthermore, a biodegradable scaffold could be implanted into a defect site, promote regeneration of tissue, and then degrade over time as new tissue reclaims the site [66,67]. Such scaffolds can be cultured with cells prior to implantation (cellular strategy) or alternatively implanted without cells (guided tissue regeneration strategy) [68]. These strategies have been studied for the regeneration of many tissues, including bone [69-72].

Tissue engineering scaffolds have been fabricated from biodegradable polymers using techniques such as freeze drying, phase separation, high pressure CO_2 saturation, and three dimensional printing [68]. An alternate technique involves the incorporation of a porogen into a polymer composite. After polymer processing, the porogen is removed by water leaching to reveal a porous polymer scaffold [68]. A key feature to the porogen leaching method is the processing of the polymer component prior to porogen removal. Previous investigations have used (a) solvent casting of a polymer solution around the porogen, (b) high pressure and temperature molding of the polymer around the porogen, and (c) extrusion of a polymer/porogen composite [68]. All of these strategies, however, produce scaffolds that rely upon noncovalent polymer interactions, such as chain

entanglements or hydrophobic interactions, for their mechanical integrity. Fewer studies have investigated systems were the polymer is covalently crosslinked around a porogen.

We have developed tissue engineering materials based upon the polymer poly(propylene fumarate) (PPF). PPF's repeating unit contains one carbon-carbon double bond that allows for covalent crosslinking of the polymer as well as two ester groups that allow hydrolytic degradation of the polymer. PPF is a viscous liquid at room temperature, requiring crosslinking of its fumarate groups in order to form a solid with mechanical integrity. As a crosslinked solid, PPF has been shown to be both biocompatible and bioresorbable [51]. Previous works have crosslinked PPF using a crosslinking monomer N-vinyl pyrrolidinone (NVP), the thermal initiator benzoyl peroxide (BP), and the accelerator N,N-dimethyl-p-toluidine (DMT) [54,73]. We have recently reported the photocrosslinking of PPF using only the photoinitiator bis(2,4,6-trimethylbenzoyl) phenylphosphine oxide (BAPO) and long wavelength ultraviolet (UV) light, eliminating the need for a crosslinking monomer and an accelerator.

The goal of this study was to produce and characterize porous PPF scaffolds constructed by a photocrosslinking/porogen leaching technique. Such scaffolds differ significantly from most porogen based scaffolds as they contain a covalently crosslinked polymer network and rely upon a photoinitiated process for crosslinking. To our knowledge, few investigations have produced a photocrosslinked polymer scaffold and there has been little characterization of this process [12]. We demonstrate here that PPF can be photocrosslinked in the presence of a salt porogen and ask the following questions. (a) How does porogen content affect the photoinitiated crosslinking of a polymer? (b) Can a photocrosslinking/porogen leaching technique be used to produce a

scaffold whose porosity is both controllable and interconnected? (c) What are the mechanical properties of a polymer scaffold produced by a photocrosslinking /porogen leaching technique?

MATERIALS AND METHODS

Poly(Propylene Fumarate) Synthesis

Poly(propylene fumarate) was synthesized following a two step procedure. Briefly, 1 mole of diethyl fumarate (Acros Organics, Pittsburgh, PA, USA) and 3 moles of 1,2 propanediol (Acros Organics) were reacted using 0.01 moles $ZnCl_2$ (Fisher Chemicals, Pittsburgh, PA, USA) as a catalyst. The reaction produced bis(hydroxypropyl) fumarate as the main product and ethanol as a byproduct. The bis(hydroxypropyl) fumarate was then transesterified, producing poly(propylene fumarate) and 1,2 propanediol as a byproduct. The PPF polymer was then purified. PPF dissolved in methylene chloride (Fisher Chemicals) was first washed with acid (5 wt% HCl in H_2O) to remove the catalyst and then purified with two washes each of both water and brine. The organic phase was dried with sodium sulfate and then the drying agent was removed by vacuum filtration. The organic solvent was removed from the PPF by rotary evaporation followed by vacuum drying. The PPF synthesized for this study had a number average molecular weight (M_n) of 2200, a weight average molecular weight (M_w) of 3600, and a polydispersity index of 1.6. The final purified product was a clear, light yellow, viscous liquid.

Gel Permeation Chromatography

The molecular weight distribution of the PPF was determined by gel permeation chromatography (GPC). The GPC system includes an HPLC pump (Waters, Model 510,

Milford, MA, USA), an autosampler (Waters, Model 717), a chromatography column (Waters, Styragel HR 4E, 7.8 x 300 mm column [50 - 100,000 Da range]), and a differential refractometer (Waters, Model 410). The solvent, degassed chloroform, was run at 1.0 mL/min for sample measurement. Polystyrene standards (500, 2630, 5970, and 9100 Da) were used to obtain a calibration curve for calculating molecular weight distributions.

PPF Scaffold Photocrosslinking

Poly(propylene fumarate) was crosslinked with ultraviolet light using the photoinitiator bis(2,4,6-trimethylbenzoyl) phenylphosphine oxide (BAPO, Ciba Specialty Chemicals, Tarrytown, NY, USA). 1.0 g BAPO was dissolved in 10 mL methylene chloride. The uncrosslinked PPF solution was warmed in an oven at approximately 60°C (allowing the viscous polymer to become fluid) and then mixed with the BAPO solution (0.05 mL BAPO solution/g PPF) to achieve an initiator content of 0.5 wt%. Solid PPF samples were prepared by simply pouring the PPF/BAPO solution into cylindrical glass vials (6.5 mm x 40 mm), which were then heated (60°C) and centrifuged (5 minutes at 3000 rpm) to remove any bubbles. The porous PPF samples were prepared by first mixing the PPF/BAPO solution with the proper amount of NaCl (300 - 500 μm crystal size) to achieve the final porogen content. The resulting mixture ranged from a viscous fluid (70 wt% NaCl) to a stiff paste (90 wt% NaCl). The mixture was then packed into a glass vial.

The ultraviolet light source used was an Ultralum (Paramount, CA, USA) ultraviolet light box. This UV box device is outfitted with four 15W, long wavelength UV bulbs and its interior reflects UV light. The total light emission covers a range of UV

wavelengths, with a peak at 365 nm (320 – 405 nm) and an intensity of approximately 2 mW/cm^2 at 10 cm. BAPO absorbs wavelengths below 400 nm, with a general increase in absorption as the wavelength decreases to 200 nm. All of the samples were exposed to ultraviolet light for 30 minutes at a distance of approximately 10 cm. Samples were placed on their sides in a petri dish that was elevated from the floor of the UV box. This configuration allows the incident light to penetrate the sample radially from all sides.

Crosslinked samples (Figure 5.1) were removed from the vials by breaking the glass. Porous samples were leached for three days in water, which was changed daily, to remove the NaCl porogen. These samples were dried, first with an absorbent cloth and then with 24 hours of vacuum drying, and finally were stored under vacuum.

Measurement of Photocrosslinking Reaction Temperature

The temperature of a variety of samples during ultraviolet light exposure was measured using a wire thermocouple system. The following samples were first prepared in 6.5 mm diameter glass vials: (A) 100 wt% PPF, (B) PPF with 0.5 wt% of the BAPO photoinitiator, (C) 70 wt% NaCl and 30 wt% of PPF containing 0.5 wt% of the photoinitiator, (D) 80 wt% NaCl and 20 wt% of PPF containing 0.5 wt% of the photoinitiator, (E) 90 wt% NaCl and 10 wt% of PPF containing 0.5 wt% of the photoinitiator, and (F) 100 wt% NaCl. A 0.025 mm diameter, Teflon insulated wire thermocouple (Omega Engineering, Stamford, CT, USA) was then inserted into the sample. While the thermocouple tip was kept at least 10 mm from the end of the glass vial as well as away from the side of the glass cylinder, no radial position was specified. This setup was then placed within the UV box. Initial sample temperature was 23±1°C. Temperature was then recorded at 15 Hz using an InstruNet data acquisition box and

software program (Nordisk Transducer Teknik, Hadsund, Denmark) for 4000 s. Ultraviolet light exposure lasted from t = 100 s to t = 1900 s only, with the remainder of the experiment occurring in the dark. Each sample type was run in triplicate.

Measurement of Ultraviolet Light Transmission Through PPF Composites

This study was initiated to determine whether UV light could penetrate NaCl as well as PPF/NaCl composites. Five sample types were investigated: (A) 100 wt% PPF, (B) 70 wt% NaCl and 30 wt% of PPF, (C) 80 wt% NaCl and 20 wt% of PPF, (D) 90 wt% NaCl and 10 wt% of PPF, and (E) 100 wt% NaCl. Ultraviolet light intensity was measured using a photometer (International Light, Model IL1400A, Newburyport, MA, USA) outfitted with a UV detector (International Light, Model XR340A) that senses light between approximately 300 and 500 nm. Each sample was placed in a 13 mm diameter cylinder above the 14 mm diameter UV detector; the sample chamber was separated from the detector by a thin glass slide whose UV absorbance was minimal. As location (in all three directions), temperature, and time all effect the light intensity recorded by the detector, fixed values were picked for each to minimize differences. The detector was located in the center of the UV box, 10.5 mm from the light source; all experiments were begun with the temperature within the box at 24±1°C; and ultraviolet light intensity was recorded after 30 min of exposure. The intensity of UV light transmitted through each of these sample types was recorded as a function of sample thickness.

Fourier Transform Infrared Spectroscopy

Fourier transform infrared (FTIR) spectroscopy was performed using a model 552 Nicolet 500 spectrophotometer (Nicolet, Madison, WI). Spectra were obtained from samples mixed with KBr and pressed, under vacuum, into pellets. Sixteen scans were

taken of each sample at a resolution of 4 cm^{-1}. Two types of PPF samples were obtained from a crosslinked PPF cylinder: interior samples were extracted from the inner most 0.5 mm of the cylinder while exterior samples were obtained from the outer most 0.5 mm of the cylinder. The analysis inspected two regions of the FTIR spectrum: carbonyl (C=O) stretching at 1725 cm^{-1} and C=C stretching at 1640 cm^{-1}. Both absorbencies were determined relative to the valley observed at approximately 1600 cm^{-1}. The ratio of C=C to C=O height was then calculated. This analysis was performed for the interior and exterior of photocrosslinked PPF scaffolds constructed with 70, 80, and 90 wt% porogen as well as solid samples. Three similar samples were analyzed for each sample type and location; the means and standard deviations were calculated from the three spectra.

Scaffold Porosity Measurement

Scaffold porosity was measured with an Autoscan-500 mercury intrusion porosimeter (Quantachrome, Boynton Beach, FL). Sample weight varied from 0.5 to 1.0 g. After the sample was loaded into the intrusion chamber, the chamber was evacuated and then filled with mercury. Once filled, chamber pressure was increased from 0.5 to 500 psi. As pressure increased, the intruded volume of mercury was monitored. The porosimeter measurement determines the intruded volume of mercury per gram sample, which is assumed to be equal to the porous volume (V) per gram sample. The porosity, ε, is then calculated as:

$$\varepsilon = \frac{V}{V + 1/\rho} \times 100\% \qquad (1)$$

The density of PPF (ρ) was calculated by measuring the mass and volume of a solid photocrosslinked PPF cylinder and found to be 1.3 g/mL.

Scanning Electron Microscopy

Scaffold pore morphology was assessed by scanning electron microscopy (SEM). All images presented were taken from the interior of a crosslinked sample. Specifically, a 6.5 x 30 mm sample was trimmed on both ends to approximately 6.5 x 20 mm and then leached in water. After leaching, the sample was dried and again trimmed to approximately 6.5 x 5 mm. Samples were then coated with gold for 30 s at 90 mA using a CrC-100 Sputtering System (Torr International, New Windsor, NY). The samples were viewed under a JSM-5300 SEM (JEOL, Boston, MA) operated at 15-20 kV.

Measurement of Compressive Mechanical Strength

Compressive testing of photocrosslinked PPF scaffolds was conducted using an 858 Materials Testing System mechanical testing machine (MTS System Corporation, Eden Prairie, MN) outfitted with a low capacity load cell (axial capacity of 100 lb). Cylindrical samples were synthesized as described above and then cut to proper length using a diamond saw (SBT Inc., San Clemente, CA). Typical sample sizes were 6.5 mm in diameter and 13.0 mm in length, to produce a sample aspect ratio of 2:1. The porous samples were tested after three days of water leaching followed one day of vacuum drying. Force and displacement were zeroed prior to compression, with the top plate slightly above the surface of the sample. Samples were compressed at a crosshead speed of 1 mm/min while stress and strain were monitored throughout the experiment. As the porous scaffolds do not fracture but compress, the experiment was halted at 0.5 mm/mm strain. Five trials were run for each sample set. The values and errors reported for each sample are the mean values and standard deviations, respectively. Two mechanical properties were calculated: elastic modulus and compressive strength at 1% yield. The

initial slope of the stress - strain curve determined the elastic modulus of the sample. The compressive strength at 1% yield was calculated as the intersection of the stress – strain curve with a line, drawn parallel to initial slope, whose x-axis intercept is 0.01 mm/mm strain.

Statistics

Sets of data were first inspected with an F-test for treatment effects [64]. The null hypothesis (the means of each set were equal) was evaluated with a 95% confidence level ($\alpha = 0.05$). If the null hypothesis was found to be false (i.e., the means of the sets were not equal), then a Tukey's multiple comparison test was performed [64]. Tukey's test then indicated, in a pairwise fashion, the relationship between sets.

RESULTS

This study sought to characterize the photoinitiated crosslinking of the biodegradable polyester poly(propylene fumarate) in the presence of a NaCl porogen and describe the resulting porous PPF scaffolds. To first show that photocrosslinking, as opposed to a thermally initiated crosslinking, is the significant mechanism of PPF crosslinking, the temperature within the scaffolds during UV exposure was monitored. The results presented in Figure 5.2 show that the temperature within all samples remained below 45°C throughout 30 min of UV exposure. This is significantly below the 60°C used in the processing of the PPF/initiator solution (see Experimental), which is commonly done without any indication of crosslinking. Specifically, samples A (PPF only) and D (NaCl only) show the warming effect of ultraviolet light on both PPF and NaCl. The heat produced by the photoinitiated crosslinking reaction can be observed in the increase in the temperature profile from sample A to sample B, as sample B contains

the photoinitiator. Sample C, which had 80 wt% of its crosslinkable polymer replaced with the NaCl porogen, showed lower temperature profiles during UV exposure (Figure 5.2). Similar results were found with samples containing 70 wt% and 90 wt% of the NaCl porogen (data not shown). The reduction in temperature is likely due to the elimination of a portion of the photocrosslinkable polymer that produces heat as well as the presence of the inert porogen acting as a heat sink. The gross appearance of those samples containing the photoinitiator indicated that these scaffolds were crosslinked throughout their 6.5 mm diameter after 30 min of UV exposure. Ultimately, the temperatures seen within these samples during the crosslinking reaction are significantly lower than those expected to cause spontaneous thermal initiation with this system, implying that PPF crosslinking results from a photoinitiated process.

We next sought to confirm that ultraviolet light could indeed penetrate a PPF/NaCl composite to initiate PPF crosslinking photochemically. The intensity of UV light transmitted through various thicknesses of PPF/NaCl composites was therefore investigated. (It should be noted that the sample geometry in this investigation, a 13 mm diameter disc, differs from that in the others, a 6.5 mm diameter cylinder, in order to accommodate the circular geometry of the ultraviolet light detector.) The results presented in Figure 5.3A indicate that more ultraviolet light is transmitted through PPF than NaCl. For example, interpolation of the data indicate that a 2 mm thick sample of PPF transmits 1.3 mW/cm^2 UV light while a 2 mm thick sample of NaCl transmits 0.5 mW/cm^2 UV light. As expected, an increase in either sample thickness or NaCl content results in a decrease in light transmission. This relationship of decreasing intensity of

transmitted light through materials of increasing thickness follows the Beer-Lambert Law [2].

While the previous results establish the transmission of ultraviolet light through PPF/NaCl composites, they also indicate that crosslinking might be reduced in two instances due to low light intensity: the interior of all scaffolds and composites with high levels of NaCl content. The former is a typical problem identified in nearly all photoinitiated systems, namely limited light penetration of materials [2,34]. In order to investigate these effects, an infrared spectroscopic study was performed to study the photoinitiated crosslinking efficiency of PPF scaffolds. A relative level of crosslinking was determined by inspecting the carbon - carbon double bond stretching at 1640 cm^{-1} as well as the carbonyl stretching at 1725 cm^{-1}. (See Figure 5.4) It is expected that photocrosslinking would consume the carbon - carbon double bonds present within the repeating fumarate units of PPF while carbonyl groups are unchanged. As individual FTIR peak heights are concentration dependent, a ratio of C=C to C=O peak heights may indicate a level of crosslinking within a sample. Table 5.1 shows that there is no significant difference in the C=C/C=O ratio between samples taken from the interior (center 0.5 mm) and the exterior (outer 0.5 mm) of 6.5 mm diameter photocrosslinked PPF scaffolds. This result indicates that crosslinking is homogeneous throughout the samples despite the reduced levels of UV light which reach the scaffold interior. This may result from the fact that light is penetrating the samples radially from all sides (see Experimental).

Interestingly, Table 5.1 also shows that scaffolds constructed with higher levels of porogen have less C=C content and thus are crosslinked more effectively than those

scaffolds with less porogen. While counterintuitive, this result can be explained in light of the results from the ultraviolet light transmission study. Although it was shown that UV light transmission is reduced as porogen content is increased, Figure 5.3B shows that the normalized transmitted light intensity per gram of crosslinkable species (PPF) is actually increased as porogen content is increased. Therefore, while less light is transmitted though a scaffold constructed with 90 wt% NaCl, these samples show higher levels of crosslinking as there is less crosslinkable material (PPF). In addition, the reduced C=C content for solid samples (prepared without NaCl) may be the result of autoacceleration of the crosslinking reaction due to the increased reaction temperatures recorded for photoinitiated samples containing no porogen compared to the composite samples (Figure 5.2).

With some characterization of the photoinitiated crosslinking of PPF in the presence of a NaCl porogen, it was then left to describe the porosity and strength of the resulting scaffolds. Towards this effort, PPF scaffolds were constructed using 70, 80, and 90 wt% of the NaCl porogen and their porosity was measured using mercury porosimetry (Table 5.2). The pore morphology and scaffold architecture of these photocrosslinked PPF scaffolds can be seen in the SEM images presented in Figure 5.5. If the pores of the scaffold are interconnected, the mass lost during water leaching should be equal to the weight percent of the porogen included in the composite. The results in Table 5.2 show this is probably not the case for scaffolds constructed with less than 80 wt% porogen and thus these scaffolds most likely do not have fully interconnected pores. This is supported by the SEM images in Figure 5.5. Furthermore, the measured porosity corresponds to interconnected pores even though it provides an underestimate of the actual porosity for

scaffolds of pore sizes of a few hundred microns due to the limitations of mercury porosimetry [49]. Nevertheless, this porosity study has shown that highly porous scaffolds with a mostly interconnected structure may be constructed following a photocrosslinking/porogen leaching technique Finally, photocrosslinked PPF scaffolds synthesized with 70, 80, and 90 wt% porogen were subjected to compressive mechanical testing (Table 5.3). The results show the expected decline in both compressive elastic modulus and compressive yield strength with increasing porogen content (scaffold porosity).

DISCUSSION

Photoinitiated polymerization reactions have been widely studied for the production of biomaterials [58]. These processes are advantageous as they proceed at effective rates in low temperature environments, their reaction initiation and termination is somewhat controllable, and the geometry of the final product may be defined [2,34]. Furthermore, photoinitiated processes have a wide range of available light sources, which, as a result, expand the number of possible products. For example, visible blue light is commonly used in the in vivo curing of biomaterials for dental applications while lasers are utilized in the stereolithographic printing of three dimensional objects [2,34].

The success of photoinitiated biomaterials, most notably in dental field, has led to studies investigating other possible applications. We have recently reported the photoinitiated crosslinking of poly(propylene fumarate), a biodegradable polyester that has been proposed for use in bone tissue engineering. The next step in the development of this material is the construction of a porous scaffold formed from photocrosslinked PPF. These scaffolds not only address many of the requirements for a bone tissue

engineering system, but would also allow further investigations of photocrosslinked PPF, such as three dimensional degradability and biocompatibility. While the option of stereolithographic printing of scaffolds both utilizes the photoinitiation aspect of the processing and may ultimately produce more highly defined porous structures, such a technique requires significant initial testing. We, therefore, desired to characterize a simple method for the production of a porous scaffold from a photocrosslinked material. Such a technique may be generally applicable to the study of many photoinitiated materials that are being considered for tissue engineering applications.

After successful construction of photocrosslinked PPF scaffolds (Figure 5.1), we sought to address a few issues surrounding the photoinitiated crosslinking of a polymer in the presence of a porogen. First, a significant concern was that the porogen would interfere with photoinitiation process. The results have shown that the porogen does not dramatically change the temperature of a photocrosslinking PPF/NaCl composite, implying little change in the chemistry involved in the initiation of the PPF crosslinking reaction. Furthermore, while light penetration limitations that are common to photoinitiated processes are observed in this system, the porogen in effect reduces the amount of crosslinkable material so as to produce a crosslinked scaffold. However, this may be seen only in geometries similar to the one studied here, namely a 6.5 mm diameter cylinder. The results imply that larger sample geometries or systems in which ultraviolet light is exposed to only one side of the sample may suffer heterogeneous photocrosslinking due to limited light penetration. Thus, the question of the effect of a porogen upon the photocrosslinking of a surrounding polymer remains to be fully answered.

Second, we sought to investigate whether a photocrosslinking/porogen leaching strategy could be used to form a scaffold with an interconnected pore structure. As these scaffolds are meant to be used in tissue engineering applications, an interconnected pore structure is needed to allow for the ingrowth of tissue throughout the entire scaffold. The results indicate that an interconnected pore structure can be formed when a porogen content of greater than 80 wt% is used. This result is support by the SEM images presented in Figure 5.5. Similar results have been shown in the past for scaffolds of linear polymers prepared by a solvent casting technique [49].

Third, the results of the mechanical studies show that the photocrosslinked PPF scaffolds do possess significant mechanical properties, often comparable to those previously studied. For example, highly porous PLGA based scaffolds have been reported to have an approximate compressive elastic modulus of 10 - 25 MPa and compressive yield strength of 0.2 - 0.7 MPa [74]. PLLA and PLLA/hydroxyapatite based scaffolds (approximately 90% porous) have been shown to have a compressive elastic modulus of 6 - 10 MPa and a compressive yield strength of 0.2 - 0.4 MPa, though these studies were conducted with a sample aspect ratio of 0.2:1 [75]. The properties of photocrosslinked PPF scaffolds, however, are still somewhat below what would be required by a scaffold that is to be used in a bone defect, as trabecular bone has been reported to possess a compressive fracture strength of approximately 5 MPa and a compressive elastic modulus of 50 - 100 MPa [76]. Therefore there is considerable room for the advancement of the photocrosslinking/porogen leaching technique in the construction of stronger porous scaffolds.

CONCLUSIONS

We have shown that porous poly(propylene fumarate) scaffolds can be synthesized by using a photocrosslinking/porogen leaching strategy. These scaffolds were synthesized by the reaction of PPF with a photoinitiator around a NaCl porogen, which was subsequently removed by water leaching. The presence of the leachable porogen in cylindrical constructs (6.5 mm in diameter) was not found to affect the initiation of the PPF crosslinking reaction in this system. Characterization of the scaffolds, by both porosity measurements and SEM images, showed that scaffolds synthesized with 80 wt% porogen or greater contain an interconnected pore structure. We expect this UV crosslinking/porogen leaching method will prove to be a useful technique for synthesizing porous scaffolds from photoinitiated materials.

Table 5.1: The extent of PPF photocrosslinking in solid and porous scaffolds as determined by FTIR. A ratio of C=C to C=O groups was calculated by dividing the C=O stretching peak (1725 cm^{-1}) height by the C=C stretching peak (1640 cm^{-1}) height. Three samples of differing porogen content were analyzed; means and standard deviations are reported. An F-test showed no statistical difference between the interior and exterior C=C/C=O ratio for all sample types, indicating a homogeneously photocrosslinked sample. The source of differences between samples of differing porogen content is discussed in the text.

wt % NaCl at Scaffold Fabrication	Interior C=C/C=O	Exterior C=C/C=O
0%	0.32 ± 0.03	0.26 ± 0.03
70%	0.45 ± 0.02	0.43 ± 0.01
80%	0.39 ± 0.05	0.36 ± 0.02
90%	0.35 ± 0.03	0.33 ± 0.02

Table 5.2: Porosity of photocrosslinked PPF scaffolds. The wt% of porogen (NaCl) content at fabrication of the scaffolds should equal the percent mass lost during leaching if the scaffold's pores are interconnected; a smaller percent mass lost (70 wt% samples) indicates scaffolds whose porosity is not fully interconnected. The porosity was determined by mercury porosimetry. Means and standard deviations for three measurements are reported.

wt % NaCl at Scaffold Fabrication	vol % NaCl at Scaffold Fabrication	Percent Mass Lost During Leaching	Porosity
70%	58%	61% ± 8%	60.4% ± 4.6%
80%	70%	82% ± 1%	62.1% ± 5.8%
90%	84%	90% ± 1%	78.7% ± 1.8%

Table 5.3: Compressive mechanical strength of photocrosslinked PPF scaffolds. Elastic modulus was defined as the initial slope of the stress-strain curve; yield strength was defined as the intersection of the stress-strain curve with a line whose slope is equal to the elastic modulus and whose x-intercept is 0.01 mm/mm strain. The mean and standard deviation (n=5) are reported.

wt % NaCl at Scaffold Fabrication	Elastic Modulus (MPa)	Yield Strength (MPa)
70%	41.8 ± 15.2	1.84 ± 0.79
80%	2.3 ± 0.5	0.11 ± 0.02
90%	0.9 ± 0.3	0.05 ± 0.03

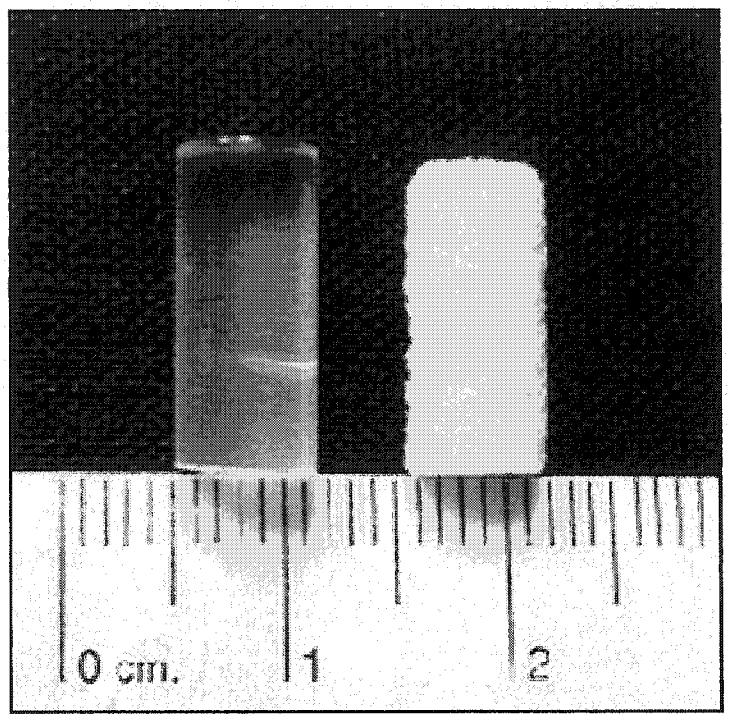

Figure 5.1: A photograph of a solid and porous photocrosslinked PPF scaffold.

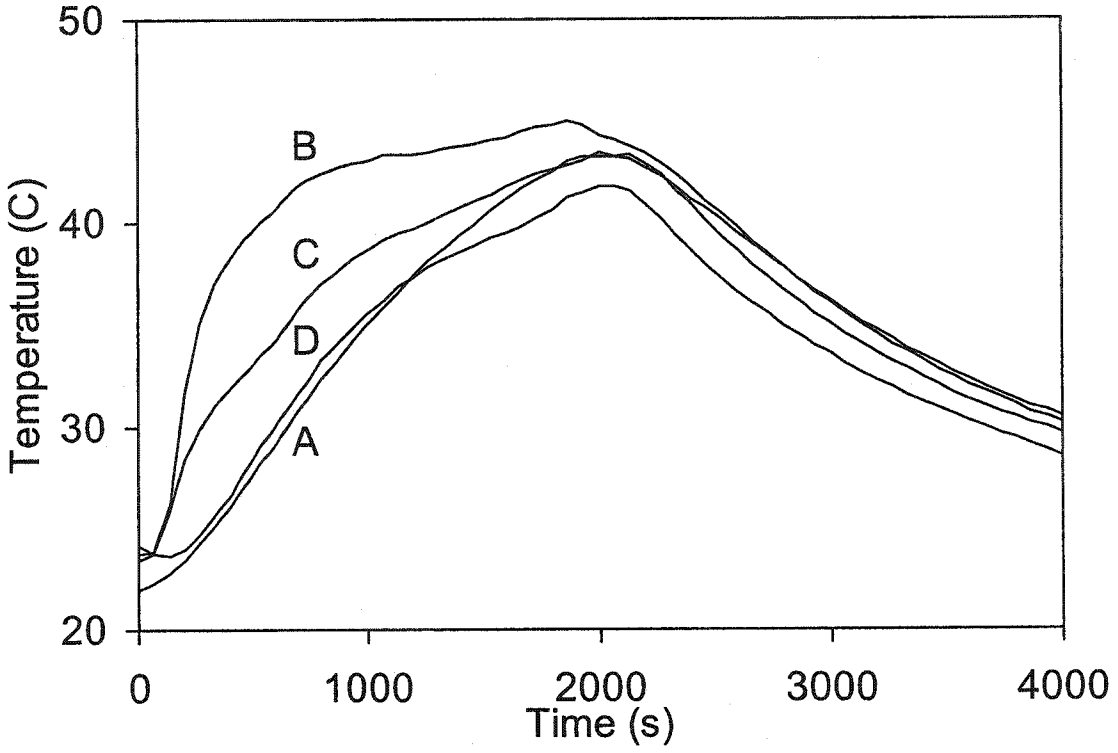

Figure 5.2: Temperature during 4000 s of ultraviolet light exposure within samples of **(A)** 100 wt% PPF, **(B)** PPF with 0.5 wt% of the BAPO photoinitiator, **(C)** 80 wt% NaCl and 20 wt% of PPF containing 0.5 wt% of the BAPO photoinitiator, and **(D)** 100 wt% NaCl. While the temperature profile increases in samples **(B)** and **(C)** due to the photoinitiated crosslinking of PPF, these temperatures remain low enough to indicate minimal thermal initiation of PPF crosslinking.

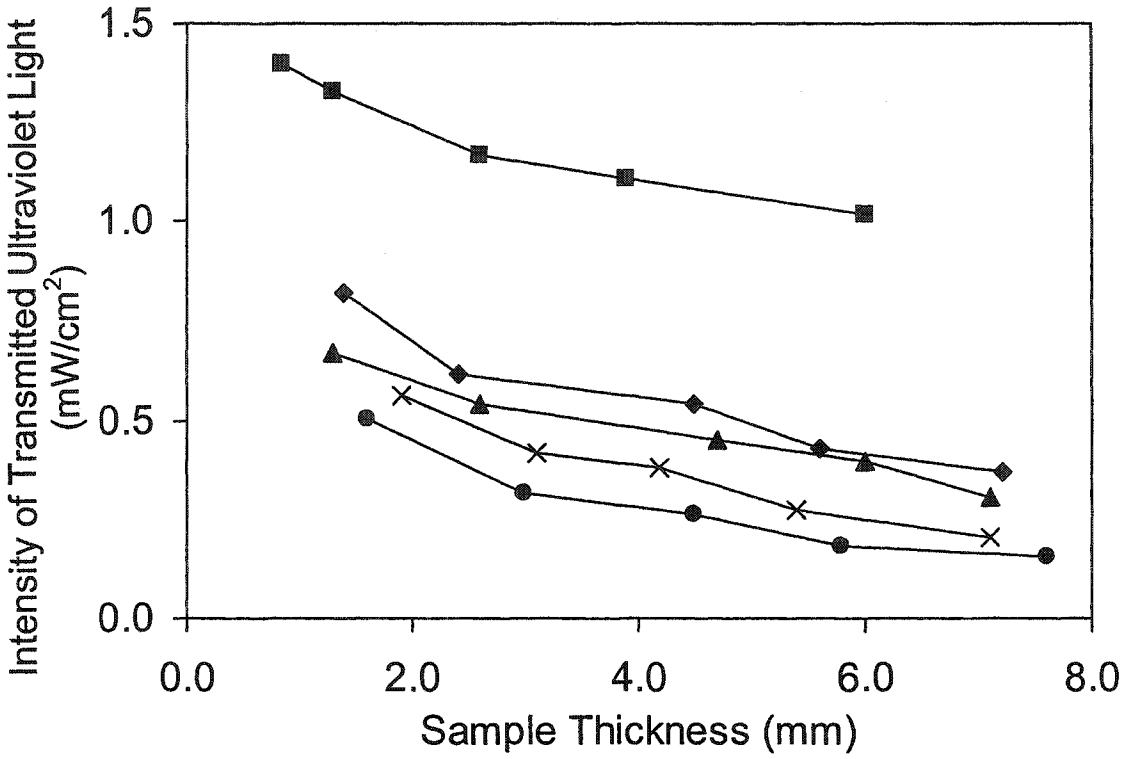

Figure 5.3 (A): The intensity of transmitted ultraviolet light through (■) 100 wt% PPF, (◆) 70 wt% NaCl/30 wt% PPF, (▲) 80 wt% NaCl/20 wt% PPF, (×) 90 wt% NaCl/10 wt% PPF, and (●) 100 wt% NaCl. While the intensity of transmitted UV light falls with increasing porogen content, the intensity per gram of PPF increases with increasing porogen content. Therefore samples with high porogen content can be effectively photocrosslinked with less intense initiating light because they contain less PPF.

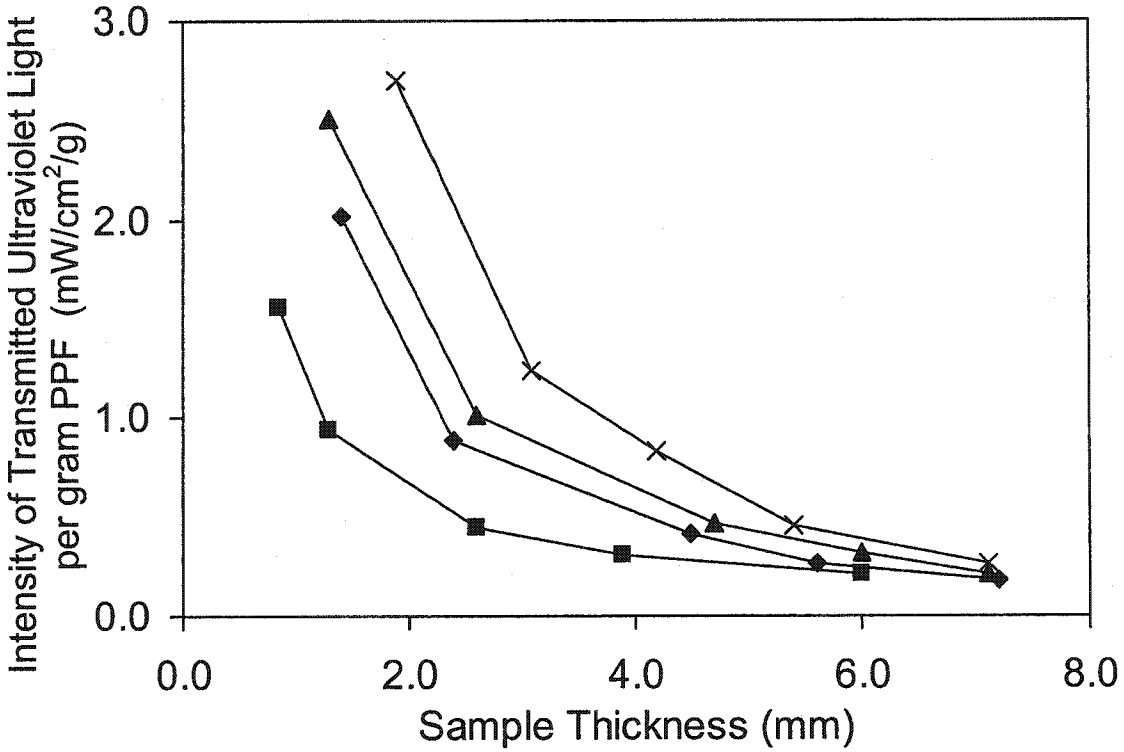

Figure 5.3 (B): The intensity of normalized transmitted ultraviolet light per gram of PPF through (■) 100 wt% PPF, (◆) 70 wt% NaCl/30 wt% PPF, (▲) 80 wt% NaCl/20 wt% PPF, (×) 90 wt% NaCl/10 wt% PPF, and (●) 100 wt% NaCl. While the intensity of transmitted UV light falls with increasing porogen content, the intensity per gram of PPF increases with increasing porogen content. Therefore samples with high porogen content can be effectively photocrosslinked with less intense initiating light because they contain less PPF.

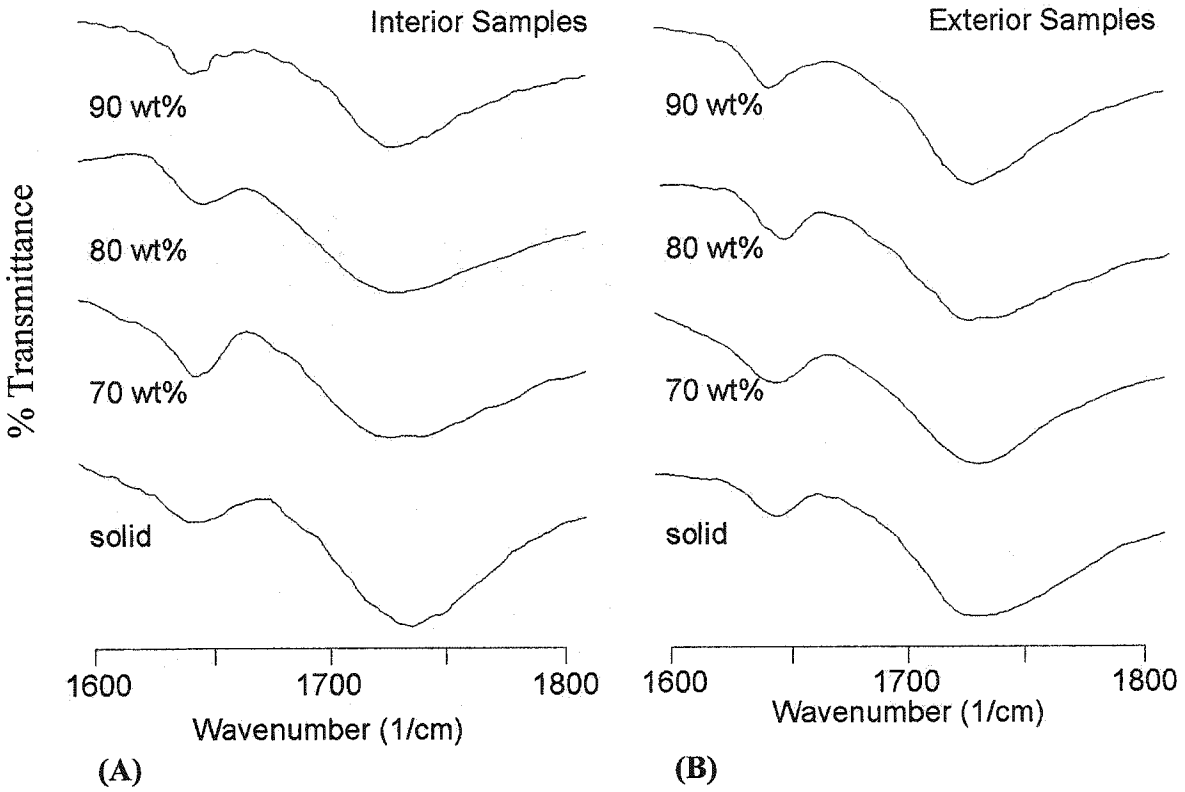

Figure 5.4: The FTIR spectrum of samples extracted from the interior **(A)** and exterior **(B)** of photocrosslinked PPF scaffolds synthesized with 70, 80, 90 wt% porogen as well as solid photocrosslinked PPF. The absorbance of carbonyl (C=O) stretching at 1725 cm^{-1} was compared to that of C=C stretching at 1640cm^{-1} to determine the level of PPF photocrosslinking. No difference was observed in the C=C/C=O levels between the interior and exterior of the samples, implying a homogeneously crosslinked scaffold. Increasing C=C/C=O levels with increasing porogen content may result from reduced crosslinkable species (PPF) in these scaffolds.

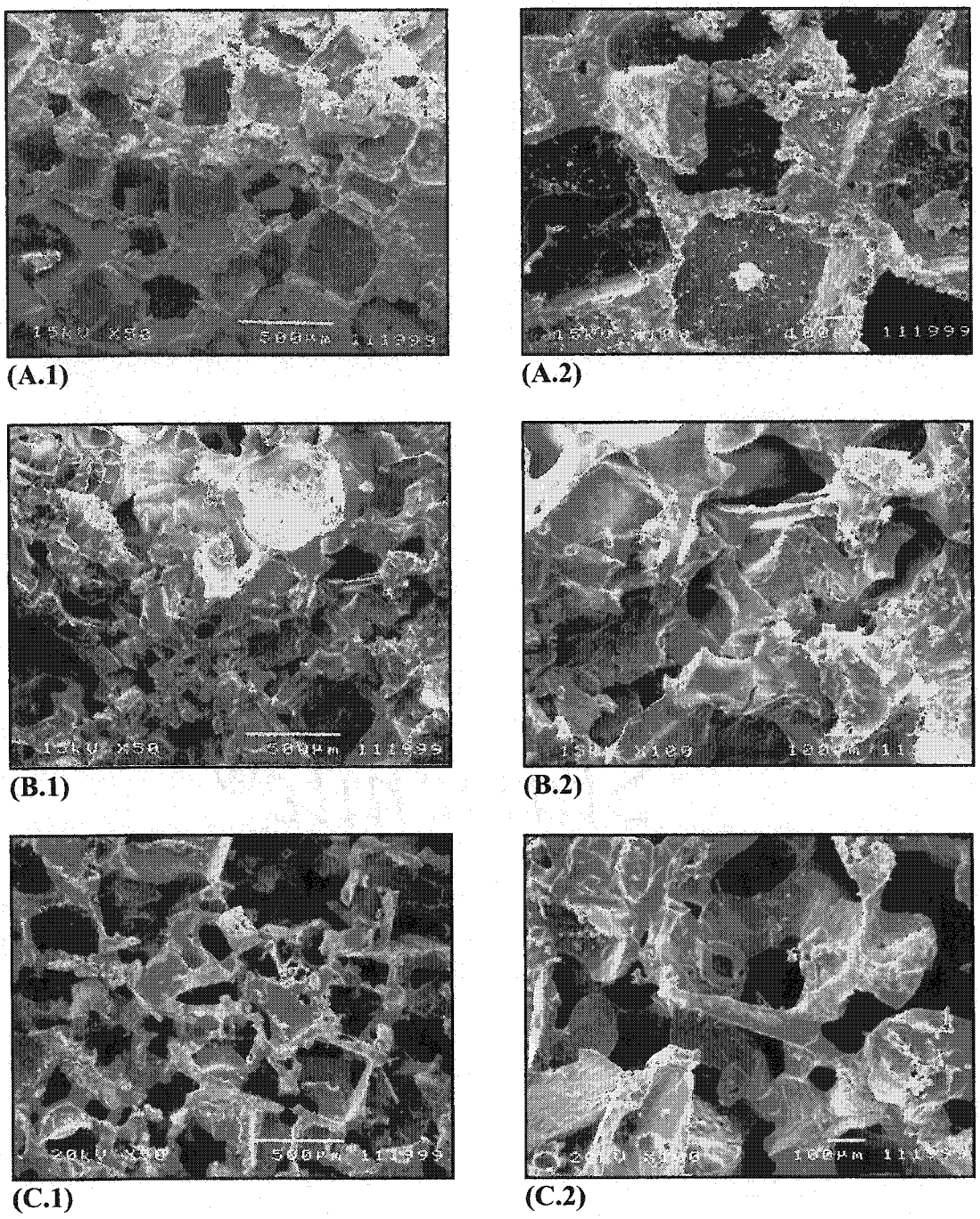

Figure 5.5: Scanning electron microscopy images of photocrosslinked PPF scaffolds. Scaffolds were constructed with 70 wt% NaCl/30 wt% PPF **(A)**, 80 wt% NaCl/20 wt% PPF **(B)**, and 90 wt% NaCl/10 wt% PPF **(C)**. A magnification of 50 times was used for the images on the left **(1)** and a magnification of 100 times was used for the images on the right **(2)**. Increasing the NaCl porogen content results in larger scaffold porosity, with an interconnected pore structure evident in samples with 80 wt% porogen and greater.

CHAPTER VI

IN VITRO DEGRADATION OF PHOTOCROSSLINKED POLY(PROPYLENE FUMARATE) SCAFFOLDS

ABSTRACT

This study investigated the *in vitro* degradation of both solid PPF networks and porous PPF scaffolds in 0.01 M phosphate buffered-saline (pH 7.4) at 37°C over the course of 32 weeks. Three formulations of scaffolds of differing porosity and pore size were constructed by varying porogen size and content. The effects of pore size and pore volume on scaffold mass, geometry, porosity, mechanical properties, and water absorption were then examined. Throughout the study, the solid networks and porous scaffolds exhibited continual mass loss and slight change in length. Porogen content appeared to have the greatest effect upon physical degradation. For example, scaffolds initially fabricated with 80wt% porogen content lost approximately 30% of their initial PPF content, while scaffolds fabricated with 70wt% porogen content lost approximately 18%. For all scaffold formulations, water absorption capacity, porosity, and compressive modulus were retained at fairly constant values upon completion of porogen leaching. These results indicate the potential of photocrosslinked PPF scaffolds in tissue engineering applications which require maintenance of scaffold structure, strength, and porosity during degradation.

INTRODUCTION

Recent tissue engineering research has focused on designing polymer scaffolds to provide temporary structural support and to promote cell growth in defective or degenerative tissues [77,78]. These three dimensional, porous structures may be coated with bioactive compounds, and then implanted into a tissue defect to facilitate the ingrowth of cells from surrounding tissue. Alternatively, scaffolds may be seeded with cells prior to implantation to promote cell migration and the growth of cells within the composite. As tissue growth occurs, the polymer matrix degrades, replacing the defect with healthy tissue [79,80].

To be considered for tissue engineering applications, polymer scaffolds must be biocompatible to avoid inflammatory response from host tissue and to provide a suitable substrate for cell attachment and proliferation. Additionally, porosity and pore size should be sufficient for the transport of cells and nutrients through the material. The composite should possess mechanical properties similar to the native tissue and provide structural strength to prevent pore collapse during the ingrowth of new tissue. Furthermore, since polymer scaffolds serve a temporary purpose, the composite material should biodegrade into nontoxic products that can be eliminated from the body through natural pathways. Ideally, polymer scaffolds would degrade at the rate of tissue ingrowth to allow for maintenance of scaffold porosity, structure, and mechanical integrity in the initial stages of tissue formation [77,81].

Recent investigations have demonstrated the potential of the aliphatic polyester poly(propylene fumarate) (PPF) in constructing degradable scaffolds which meet the design criteria for tissue engineering [51,54,73]. PPF's repeating unit contains one

unsaturated bond that permits covalent crosslinking and two ester groups that allow for hydrolysis of the polymer into the principle, non-toxic degradation products of fumaric acid and propylene glycol [82]. Previous investigations have shown thermally crosslinked PPF to be biocompatible and biodegradable [51,73]. However, photocrosslinking techniques have the advantage of greater temporal and spatial control of polymerization and greater flexibility during scaffold implantation than chemical crosslinking methods [33]. Therefore, we have recently reported the photocrosslinking of PPF using the photoiniatior bis(2,4,6-trimethylbenzoyl) phenylphosphine oxide (BAPO) and long wavelength ultraviolet (UV) light [60]. Using this photocrosslinking technique with the incorporation of a porogen, PPF scaffolds with an interconnected pore network and promising mechanical properties have been reproducibly fabricated [60]. To further assess the usefulness of this material in tissue engineering applications, a detailed examination of the physical and chemical structure of scaffolds during long-term degradation is required.

Previous studies have analyzed the *in vitro* degradation of PPF thermally crosslinked with the monomer N-vinyl pyrrolidinone (NVP), initiator benzoyl peroxide (BP), and accelerator N,N-dimethyl-p-toluidine (DMT) [73]. Since thermally crosslinked scaffolds possess a different composition than photocrosslinked scaffolds, the degradation behavior of these and photocrosslinked scaffolds can be expected to differ. This study examined changes in scaffold mass, geometry, porosity, mechanical properties, and water absorption throughout 32 weeks of *in vitro* degradation to address the following questions: (1) How does the incorporation of a pore network to photocrosslinked PPF composites effect material degradation? (2) How does degradation

alter scaffold structure? (3) How does pore size and/or pore volume effect scaffold degradation?

MATERIALS AND METHODS

Poly(Propylene Fumarate) Synthesis

Poly(propylene fumarate) was synthesized by a two step procedure [62]. In the first step, 1 mole of diethyl fumarate (DEF) (Acros Organics, NJ, USA) and 3 moles of 1,2 propanediol (PG) (Acros Organics) were reacted using 0.01 moles of the catalyst $ZnCl_2$ (Fisher Chemicals, Fair Lawn, NJ, USA). As the reaction stoichiometry calls for a 1:2 mole ratio of DEF to PG, excess PG was used to drive the reaction to completion. The reaction was run for approximately eight hours under a nitrogen blanket and at atmospheric pressure, producing bis(hydroxypropyl) fumarate as the main product and ethanol as a byproduct. The vapor temperature was maintained at approximately 10°C above the boiling point of ethanol (78°C) in order to remove the byproduct by distillation. In the second step, bis(hydroxypropyl) fumarate was transesterified at low pressure (<1mm Hg) producing poly(propylene fumarate) (PPF) and the byproduct 1,2 propanediol (PG). The vapor temperature was maintained at about 10°C above the boiling point of PG at 1 mm Hg (48°C) to remove the byproduct by distillation. The reaction was run until the product had the desired molecular weight as determined by gel permeation chromatography. For purification, poly(propylene fumarate) was dissolved in methylene chloride (Fisher Chemicals). The PPF was first washed with acid (5 wt% HCl in H_2O) to remove the catalyst, and then purified with two washes each of both water and brine. The organic phase was dried with sodium sulfate and then the drying agent was removed by vacuum filtration. The organic solvent was removed from the PPF by rotary

evaporation followed by vacuum drying. The final purified PPF was a clear viscous liquid of number average molecular weight (M_n) 1650 and polydispersity index (PI) of 1.48, as determined by gel permeation chromatography.

Gel Permeation Chromatography

The molecular weight distribution of PPF was determined by gel permeation chromatography (GPC). The GPC system includes an HPLC pump (Waters, Model 510, Milford, MA, USA), an autosampler (Waters, Model 717), a chromatography column (Waters, Styragel HR 4E, 7.8 x 300 mm column [50 - 100,000 Da range]), and a differential refractometer (Waters, Model 410). The solvent, degassed chloroform, was run at 1.0 mL/min for sample measurement. Polystyrene standards (500, 2630, 5970, and 9100 Da) were used to obtain a calibration curve for calculating molecular weight distribution.

Formulation of Photocrosslinked PPF Scaffolds

Three porous, poly(propylene fumarate) scaffold formulations were fabricated for this study by altering the weight percent and size of porogen in the scaffold composition. As shown in Table 6.1, scaffolds of 70wt% 300-500 μm NaCl (70Ps), 80wt% 300-500 μm NaCl (80Ps), and 80wt% 600-800 μm NaCl (80Pl) were formulated. Additionally, solid PPF networks were prepared as the experimental control group. Both the porous and solid samples were fabricated using a photocrosslinking technique employing the photoinitiator bis(2,4,6-trimethylbenzoyl) phenylphosphine oxide (BAPO, Ciba Specialty Chemicals, Terrytown, NY, USA) and ultraviolet light. The photoinitiator solution was obtained by dissolving 1.0g BAPO in 10 mL methylene chloride. PPF was warmed in a water bath (allowing the viscous polymer to become fluid) and then mixed with the

BAPO photoinitiator solution (0.050 mL BAPO solution/g PPF). Solid PPF networks were prepared by simply pouring the PPF/BAPO solution into cylindrical glass vials (6.5 mm x 40 mm), which were then heated (50°C) and centrifuged (5 minutes at 3000 rpm) to remove any bubbles. The porous PPF samples were prepared by first mixing the PPF/BAPO solution with the desired amount and size of NaCl porogen. This mixture was then packed into glass vials (6.5 mm x 40 mm).

Both the solid and porous samples were then exposed to ultraviolet light for 30 minutes at a distance of approximately 15 cm. Samples were placed on their sides, allowing the incident light to penetrate radially. The ultraviolet light source used was an Ultralum (Paramount, CA) ultraviolet light box outfitted with four 15W long wavelength UV bulbs. The total light emission covers a range of UV wavelengths (320 – 405 nm), with a peak at 365 nm and an intensity of 4 mW/cm^2 at 15 cm. BAPO absorbs wavelengths below 400 nm, with a general increase in absorption as the wavelength decreases to 200 nm (Ciba Specialty Chemicals).

Crosslinked units (6.5 mm x 40 mm) were removed from the vials by breaking the glass. Samples were cut from the interior (approximately 10 mm from the edges) of the photocrosslinked units and then trimmed to a length approximately twice their diameter (6.5 mm x 12.4 mm). The samples' initial mass (M_i) and length (L_i) were recorded.

In Vitro Degradation

The PPF scaffolds and solid networks were placed in sealed 20 mL vials containing 0.01 M, pH 7.4 phosphate-buffered saline (PBS). The samples were stored on a shaker table (75 rpm) at 37°C, while pH was monitored. During the initial 48 hours, the PBS solution was changed every eight hours. The PBS solution was then changed daily

for the remainder of the first week and changed weekly thereafter. At each time point (days 1, 3 and weeks 1, 2, 3, 6, 9, 12, 18, 32), five samples of each formulation were removed from PBS and immediately used for wet, compressive mechanical testing. Additional samples of each formulation were removed from PBS and wet mass (M_w) was immediately measured. These samples were vacuumed dried for 48 hours, and then dry mass (M_d) and length (L_d) were recorded prior to further analysis.

Changes in mass, dimension, and water absorption of the porous scaffolds and solid networks were monitored at each time point. Analysis of total mass degradation was performed by calculating the percent mass remaining (P_M) in each sample according to the formula,

$$P_M = \frac{M_d}{M_i} \times 100\%. \quad (1)$$

Significant initial mass loss was expected for porous formulations due to leaching of the water soluble porogen. Since this study was concerned with examining the extent of PPF loss in porous scaffolds, the percent of PPF remaining (P_P) was determined for each formulation by normalizing P_M by the initial PPF content (C_p = g PPF/g total) as shown below,

$$P_P = \frac{P_M}{C_p} \times 100\%. \quad (2)$$

These calculations were based on the assumption that initial scaffold mass loss was attributed solely to leaching of the water soluble porogen. Thus, calculations of P_P were performed for time points after which cumulative mass loss was found to equal initial salt content and the remaining scaffold was assumed to be composed only of PPF and its

degradation products. Changes in the length of the samples (P_L) were calculated by the following formula,

$$P_L = \frac{L_d}{L_i} \times 100\%. \quad (3)$$

Water absorption (A_w) of the samples was defined by the following equation,

$$A_W = \frac{M_w - M_d}{M_d} \times 100\,\%. \quad (4)$$

Scanning Electron Microscopy

At each time point, pore morphology of the porous scaffolds was imaged by scanning electron microscopy (SEM). The images presented are taken of the exterior cross-sectional surface of a scaffold after removal from PBS and subsequent vacuum drying. Samples were coated with gold for 30 s at 90 mA using a CrC-100 Sputtering System (Torr International, New Windsor, NY). The top surface of the samples was viewed under a JSM-5300 SEM (JEOL, Boston, MA) operated at 15-20 kV.

Scaffold Porosity Measurement

Mercury porosimetry was used to examine scaffold porosity (ε) at each time point. Scaffold porosity was measured with an Autoscan-500 mercury intrusion porosimeter (Quantachrome, Boynton Beach, FL). Each sample was loaded into the intrusion chamber, and then the chamber was evacuated to 0.2 psi. Mercury was loaded into the chamber to 0.5 psi and intruded into the sample with pressure increasing from 0.5 to 500 psi. The intruded volume of mercury and pressure were monitored during each run. The porosimeter measurement determines the intruded volume of mercury per gram

sample, which is assumed to be equal to the porous volume (V_{por}) per gram sample. Porosity (ε) is determined by the equation shown below:

$$\varepsilon = \frac{V_{por}}{V_{por} + 1/\rho} \times 100\% . \quad (5)$$

where ρ is the sample density. In calculating ρ, initial mass loss is assumed to be due solely to the effects of salt leaching, so that mass loss exceeding a sample's theoretical salt content is attributed only to PPF degradation. Accordingly, NaCl content (C_s = g NaCl/g total), NaCl density (ρ_s = 2.17 g/mL), PPF content (C_p = g PPF/g total), and PPF density (ρ_p = 1.28 g/mL) can be used to calculate sample density (ρ) from the equation

$$\rho = \frac{C_s + C_p}{(C_s/\rho_s) + (C_p/\rho_p)} . \quad (6)$$

Porosity measurements from mercury porosimetry were compared with the theoretical porosity values for each scaffold formulation. Theoretical porosity (ε_T) is calculated from the equation,

$$\varepsilon_T = \frac{(C_s/\rho_s)}{(C_s/\rho_s) + (C_p/\rho_p)} \times 100\% . \quad (7)$$

Theoretical porosity assumes that the polymer/porogen mixture is a homogenous mixture and that all of the porogen, but none of the polymer is removed with leaching.

Compressive Mechanical Testing

Compressive testing of the PPF samples at each time point was conducted using an 858 Materials Testing System mechanical testing machine (MTS System Corporation, Eden Prairie, MN). Throughout the study, mechanical testing of solid networks employed a high capacity load cell (axial capacity of 2200 lb). Prior to placing the

samples in PBS, the high capacity load cell was used to analyze the unleached scaffolds at day 0. However, subsequent mechanical testing of porous scaffolds was performed with a low capacity load cell (axial capacity of 100 lb) due to the effects of salt leaching on scaffold mechanical strength. Both the solid and porous samples were tested wet, immediately after removal from PBS. Force and displacement were zeroed prior to compression, with the top plate slightly above the surface of each sample. Samples were compressed at a crosshead speed of 1 mm/min while stress and strain were monitored throughout the experiment. For the solid samples, the experiment was halted when the sample fractured. For the porous samples, which do not fracture but compress, the experiment was halted at 0.4 mm/mm strain. Compressive modulus, compressive strength at 1% yield, and fracture strength were measured to characterize the mechanical strength of the solid networks. The initial slope of the stress - strain curve determined the compressive modulus of each sample. The compressive strength at 1% yield was calculated as the intersection of the stress – strain curve with a line, drawn parallel to initial slope, whose x-axis intercept is 0.01 mm/mm strain. For porous scaffolds, which do not fracture upon compression, only compressive modulus was calculated.

Statistics

The measurement values and errors reported are the mean values and standard deviations, respectively. All sets of data were first inspected with an F-test for treatment effects [64]. The null hypothesis (the means of each set were equal) was evaluated with a 95% confidence level ($\alpha = 0.05$). If the null hypothesis was found to be false (i.e., the means of the sets were not equal), then a Tukey's multiple comparison test was

performed [64]. Tukey's test then indicated, in a pairwise fashion, the relationship between sets.

RESULTS

Throughout the 32 week study, the scaffolds and solid networks generally maintained their cylindrical shape, while exhibiting mass loss, length change, and water absorption. SEM images in Figure 6.1 indicate the retention of pore size and shape of the scaffolds over 32 weeks. Figure 6.2 presents photographs of the solid networks throughout the degradation study. For the solid samples, significant cracks became evident at week 1, and slight discoloration appeared by week 12. At week 32, the cracks within the solid networks had widened, and a yellow discoloration became apparent. Images of the porous samples display porogen loss at the early stages of the study while some deterioration of scaffold shape is noted in later times. The porous scaffolds also displayed a slight yellowish discoloration by week 32.

The mass loss for both the solid and porous samples is presented in Figure 6.3. The three porous scaffold formulations exhibited similar mass loss profiles (Figure 6.3A). Initially, a dramatic decrease in mass, comparable to the samples' initial salt content, was observed. The 80Ps and 80Pl scaffolds lost approximately 80% of their initial mass by day 3, indicating nearly complete salt leaching. The 70Ps scaffolds, however, required 1-3 weeks for a mass loss equivalent to initial salt content, suggesting the isolation of pores within the network of these scaffolds. Mass loss beyond the initial salt content was measured for each of the three porous formulations. The percent PPF remaining at 32 weeks for the 70Ps, 80Ps, and 80Pl scaffold formulations (Figure 6.3B) was 82.1% ±

3.1%, 72.5% ± 3.9%, and 68.9% ± 8.2%, respectively. In contrast, the percent mass remaining for the solid PPF networks after 32 weeks was 86.6% ± 0.3%.

Throughout the 32 week study, a slight decrease in length (Figure 6.4) was measured for the three porous formulations and the solid networks, with the 80Pl scaffolds displaying the largest length change. Increasing water absorption and porosity accompanied decreasing compressive modulus during the initial period of salt leaching for all porous formulations (Figure 6.5 - 6.7A). Upon completion of porogen leaching, water absorption, porosity, and compressive modulus appeared to remain constant. For each formulation, the initial changes were found to correspond to salt leaching, as the 80Ps and 80Pl scaffolds exhibited a more rapid alteration in scaffold properties than the 70Ps scaffolds.

As expected, the porosity of 80Ps and 80Pl formulations was greater than the porosity of the 70Ps scaffolds at each time point, since these formulations were fabricated with a higher initial porogen content. Once the NaCl porogen had been leached, the 80Ps and 80Pl scaffold formulations attained a porosity of approximately 65%, while the 70Ps scaffolds exhibited a porosity of approximately 57%. These values correlate with the expected theoretical porosity of each formulation, 70% for 80Ps and 80Pl scaffolds and 58% for 70Ps scaffolds.

The extent of mass, length, and water absorption changes within the solid networks was significantly less than the changes observed with the porous scaffolds. Unlike the porous scaffolds which exhibited an initial decrease in compressive modulus, an increase in the compressive modulus of solid networks (Figure 6.7B) from 106.6 ± 13.3 MPa to 290.1 ± 29.8 MPa was seen over the initial 6 weeks of the study. The solid

networks' compressive strength at 1% yield (Figure 6.7C) followed a similar trend, increasing over the initial 6 weeks from 10.5 ± 1.9 MPa to 18.6 ± 3.6 MPa and then remaining constant. At day zero, the fracture strength of the solid networks was measured to be 87.0 ± 11.7 MPa. However at week 1, a sharp decrease in fracture strength (Figure 6.7D) occurred coincident with the appearance of axial cracks within these samples.

DISCUSSION

This study examined the *in vitro* degradation upon a novel material, photocrosslinked PPF. We first investigated the effects of porosity upon degradation by comparing degrading solid PPF networks to degrading porous PPF scaffolds. The results indicate that increased porosity results in quicker PPF loss (Figure 6.3B). A previous study found similar results with the *in vitro* degradation of porous poly(L-lactic acid) (PLLA) foams, where total mass loss was shown to increase with increasing foam porosity [83]. The results of both studies suggest the importance of porosity on scaffold degradation. The increase in surface area of the highly porous scaffolds exposes more of the polymer to the surrounding fluids. Furthermore, fluid transport from the exterior to the interior of a scaffold may also be facilitated by the presence of an interconnected pore network. This work suggests that the combined effects of increased surface area and increased fluid transport may significantly increase the rate of polymer degradation.

The results from the mechanical testing of the solid PPF samples provide a clearer understanding of the physical and chemical behavior of degrading photocrosslinked PPF. For the first six weeks of the study, the solid PPF samples showed an increase in compressive modulus and compressive strength (Figure 6.7B and 6.7C), while the

fracture strength fell (Figure 6.7D). This decrease in fracture strength is likely attributable to the cracks that coincidentally became apparent in these samples. The increase in both compressive modulus and compressive strength, while unexpected, may be a result of spontaneous, additional crosslinking of the PPF chains. While continued crosslinking may also occur in the porous samples, their decrease in mechanical properties due to porogen leaching most likely overshadows this effect.

The changes in scaffold mass, geometry, porosity, water absorption, and mechanical properties were studied next to assess the alteration of scaffold structure during degradation. Continuous scaffold degradation was evident from measured changes in scaffold properties throughout the 32 week study. Initially, distinct mass loss, a decrease in compressive modulus, and an increase in both porosity and water absorbance of the scaffolds resulted from the effects of porogen leaching. However, mass loss in excess of initial porogen content continued throughout the 32 week study, accompanied by slight length reduction and discoloration. While continuous mass loss was observed, scaffolds appeared to retain their cylindrical shape and relatively constant compressive modulus, porosity, and water absorbency after completion of porogen leaching.

For tissue engineering applications, scaffolds should retain their volume, structure, and mechanical stability long enough to ensure sufficient tissue formation within the matrix [79,81]. Comparison of the results of this study and a study by Peter et al. suggest that mechanical properties of photocrosslinked PPF scaffolds can be retained for longer time periods than similar scaffolds which were crosslinked with a thermal initiator [73]. The modulus of thermally crosslinked scaffolds, formulated with PPF,

NVP, NaCl and BP in a mass ratio of 1:1:1:0.05, was reduced essentially to zero by 12 weeks [73]. Incorporation of β-TCP to thermally crosslinked PPF scaffolds resulted in a longer retention period for scaffold modulus [73]. In comparison, photocrosslinked scaffolds fabricated, with PPF, NaCl, and BAPO in a mass ratio of 1:2.33:0.005, retained an compressive modulus of approximately 35 MPa for 32 weeks. While previous investigations into PPF degradation have not examined changes in scaffold porosity, this study has shown that photocrosslinked PPF networks can also retain constant porosity for 32 weeks of *in vitro* degradation.

The effects of pore size and volume upon degradation were analyzed by studying the degradation of different scaffold formulations. The results indicate that pore volume, rather than pore size, has a significant impact on the physical degradation of the photocrosslinked PPF composites. For example, the 80Ps and 80Pl scaffolds, both constructed with 80wt% NaCl porogen, displayed greater changes in mass, length, and water absorption than the 70Ps scaffolds which were constructed with 70wt% NaCl porogen. However, no statistical difference between the 80Ps (which were constructed with 300-500 μm NaCl porogen) and the 80Pl (which were constructed with 600-800 μm NaCl porogen) was apparent from the 32 week values of mass loss, PPF loss, length change, and absorption. A possible explanation for this effect may be related to fluid transport within the scaffolds. Those scaffolds with low initial porogen content (70Ps) may not possess sufficient porosity to form an interconnected pore network, thereby reducing polymer degradation. The SEM images of the 70Ps scaffolds do in fact show the isolation of individual pores within these scaffolds. Therefore, the lack of pore interconnectivity may reduce the fluid transport within the scaffolds and thus decrease

PPF degradation. The results from the extreme case of zero pore volume, namely the solid PPF samples, also support this concept.

Though pore volume appears to have a significant impact on the extent of physical degradation, results of this study also indicate that pore size may influence a scaffold's ability to retain mechanical properties. The compressive modulus of leached 70Ps and 80Ps scaffolds remained fairly constant throughout the 32 week study at values of approximately 35.0 MPa and 3.9 MPa, respectively. Leached 80Pl scaffolds, which were formulated with a larger porogen size of 600-800 μm, maintained an compressive modulus of approximately 0.6 MPa until week 18 but had little mechanical integrity at week 32. These results indicate that pore size may influence changes in scaffold mechanics during degradation, with increased pore size reducing compressive modulus.

Attempts were made to also characterize scaffold degradation by monitoring its change in chemical composition over time. For example, the degradation of scaffolds fabricated from uncrosslinked, linear polymers has been previously monitored using gel permeation chromatography, showing the shortening of the polymer chains over time [83]. However, this method of characterization is not possible with crosslinked polymers as they are, by definition, not soluble in solvents. To circumvent this, solid state ^{13}C nuclear magnetic resonance spectroscopy and Fourier transfer infrared spectroscopy were employed to monitor the hydrolysis of ester groups within the PPF backbone into carboxylic acids. Both methods, however, were found to be inadequate as these acids could not be sufficiently distinguished from their corresponding esters. Further work is required to develop accurate chemical assays for the hydrolysis of crosslinked polymers.

Finally, while we have demonstrated that photocrosslinked PPF can be used to construct scaffolds which retain mechanical properties and porosity for 18-32 weeks *in vitro*, previous work has indicated that shorter *in vivo* retention times may be expected. For instance, thermally crosslinked PPF scaffolds formulated without β-TCP, exhibited an compressive modulus above 50 MPa for approximately 9 weeks, but lacked sufficient mechanical integrity for testing after 4 days of *in vivo* degradation [51,73]. Therefore, further studies are also necessary to analyze the response of photocrosslinked PPF scaffolds to *in vivo* degradation.

CONCLUSIONS

This study investigated the *in vitro* degradation of both solid PPF networks and porous PPF scaffolds in phosphate buffered-saline (pH = 7.4, 37°C) over the course of 32 weeks. Various scaffold morphologies were investigated by fabricating scaffolds with different porogen content and porogen sizes. The effects of pore size and pore volume on scaffold mass, geometry, porosity, mechanical properties, and water absorption were then examined. The results show that both scaffold pore size and pore volume influence degradation, specifically scaffold mass loss, length reduction, and water absorption. However, throughout the degradation study, scaffold mechanical properties were generally retained. The results indicate that porogen size and content could be selected to formulate photocrosslinked PPF scaffolds with a degradation rate, porosity, and mechanical properties that match target values for a specific tissue defect. This flexibility in scaffold design supports the potential of photocrosslinked PPF as a composite material for tissue engineering.

Table 6.1: The three photocrosslinked PPF scaffold formulations that were examined in this *in vitro* study. The scaffolds differ in their PPF content, porogen content, and porogen size.

Scaffold Class	PPF wt% at Fabrication	NaCl wt% at Fabrication	NaCl size (μm)
70Ps	30	70	300 - 500
80Ps	20	80	300 - 500
80Pl	20	80	600 - 800

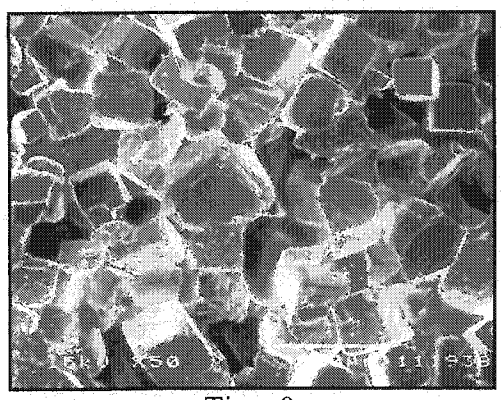
Time 0

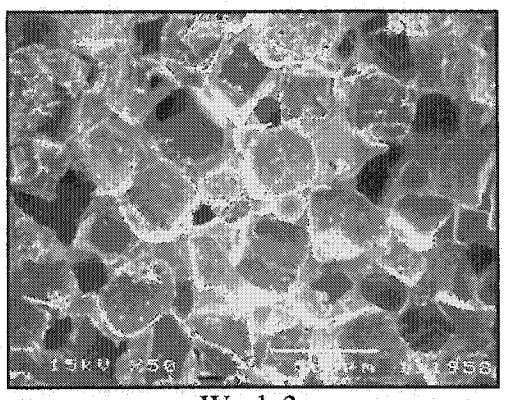
Week 3

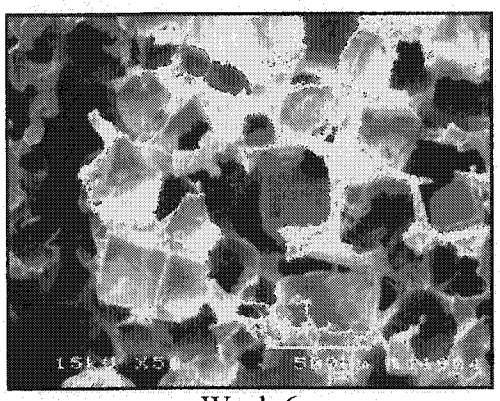
Week 6

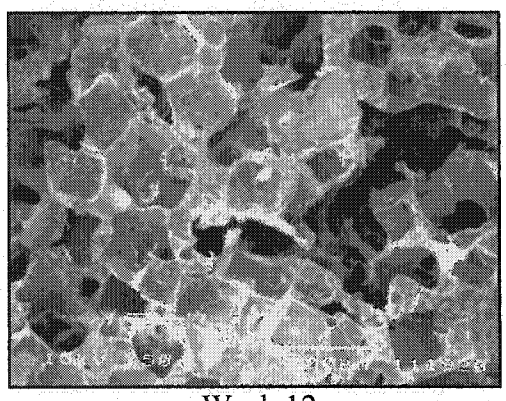
Week 12

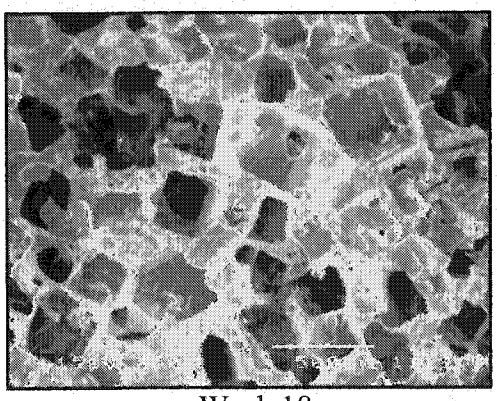
Week 18

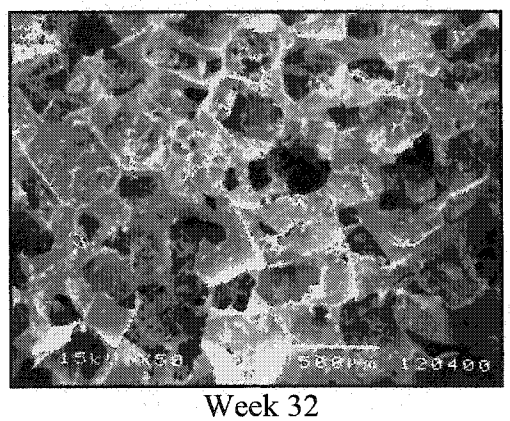
Week 32

Figure 6.1: Scanning electron micrographs of photocrosslinked PPF scaffolds at indicated time points. Micrographs of 80Ps scaffolds exhibit a well defined, interconnected pore network at all time points. Week 1 images confirm completion of salt leaching. By week 6, the polymer material exhibits evidence of degradation.

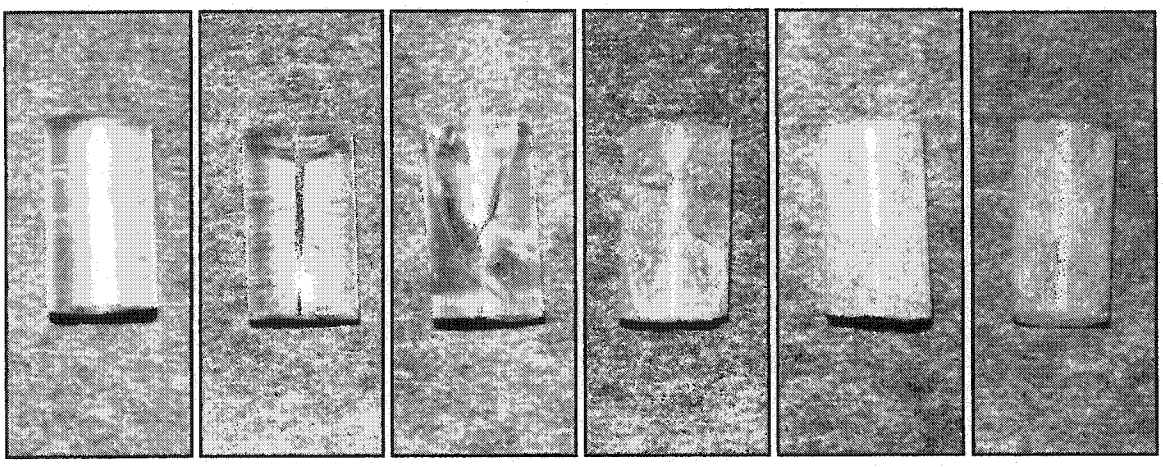

Figure 6.2: Photographs of solid PPF networks at indicated time points. The samples initially appear as clear solid units, and then show axial cracks at week 1 and slight discoloration at week 12. Both cracking and discoloration continued through week 32.

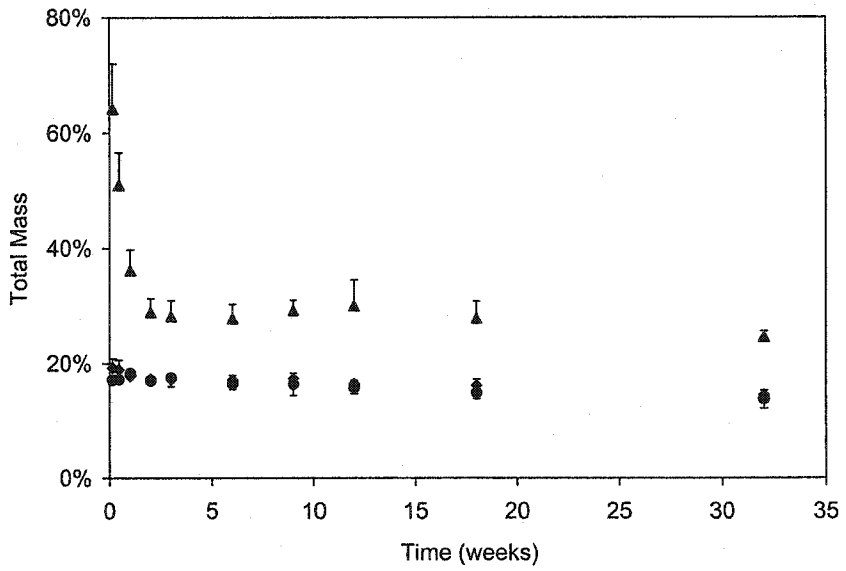

(A)

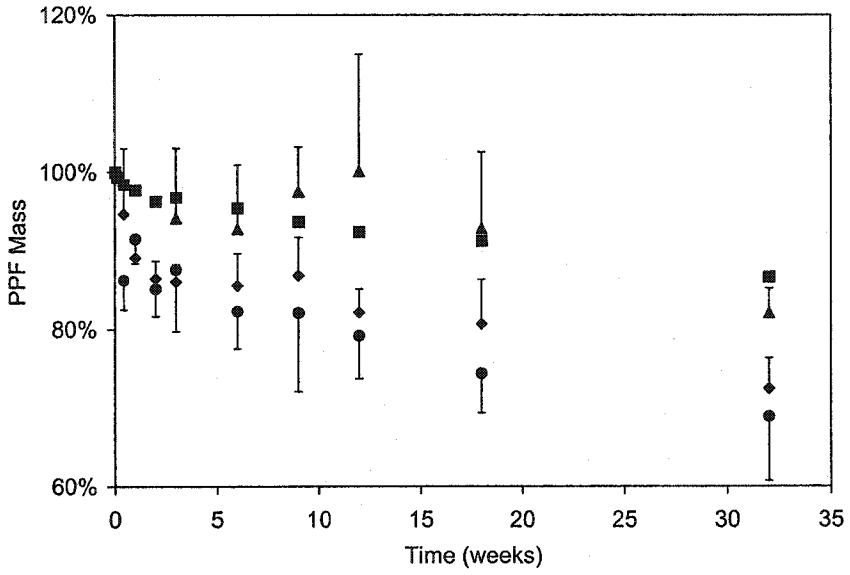

(B)

Figure 6.3: Sample mass loss during *in vitro* degradation. **(A)** Percent mass remaining for PPF scaffolds of (▲) 70Ps, (◆) 80Ps, and (●) 80Pl formulations. **(B)** Percent PPF remaining for (■) solid PPF networks and for porous scaffolds of (▲) 70Ps, (◆) 80Ps, and (●) 80Pl formulations. At week 32, no difference was observed between the percent PPF remaining in the solid networks and 70Ps scaffolds. Additionally, no difference was measured in the PPF loss at 32 weeks for the 80Ps and 80Pl formulations. However, PPF loss in both the 80Ps and 80Pl formulations was found to be greater than the solid and 70Ps scaffolds, suggesting that increased pore volume and an interconnected pore network may increase the extent of PPF degradation.

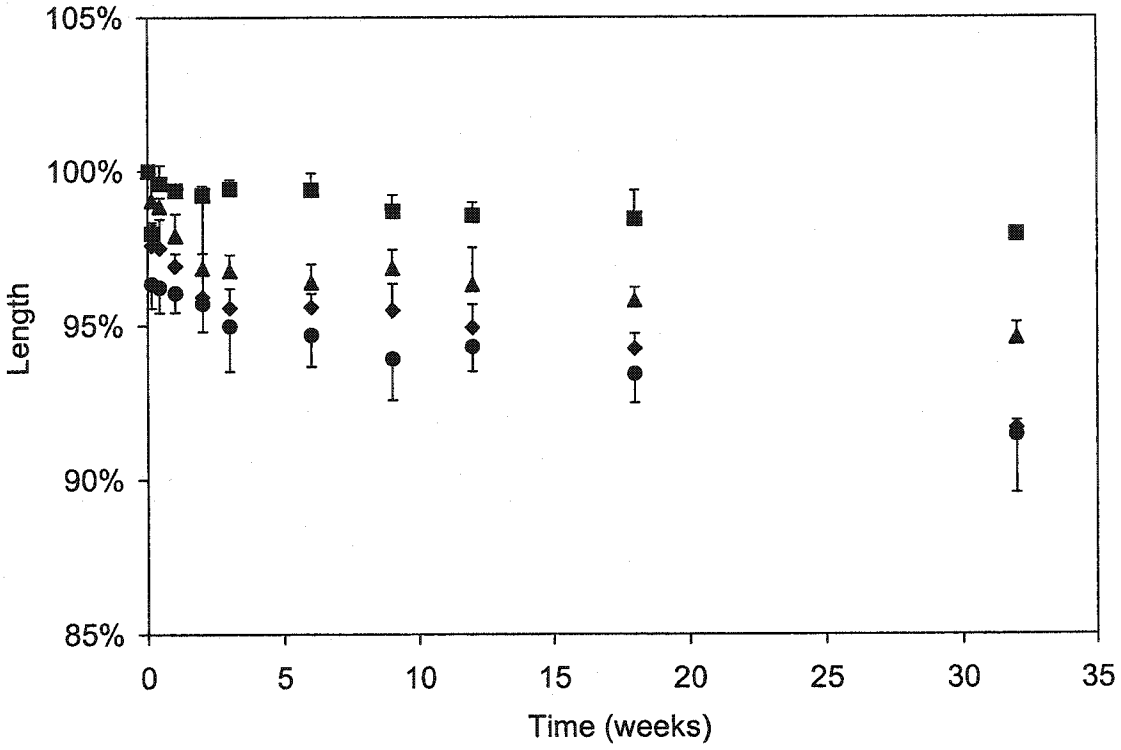

Figure 6.4: Sample length change during *in vitro* degradation. Percent length remaining in (■) solid PPF networks and in porous scaffolds of (▲) 70Ps, (◆) 80Ps, and (●) 80Pl formulations. At week 32, the 80Ps and 80Pl formulations exhibited the greatest change in length, followed by the 70Ps scaffolds and solid networks, respectively. No difference in length change was observed between the 80Ps and 80Pl formulations, suggesting that pore volume, rather than pore size, may significantly effect dimensional changes in degrading scaffolds.

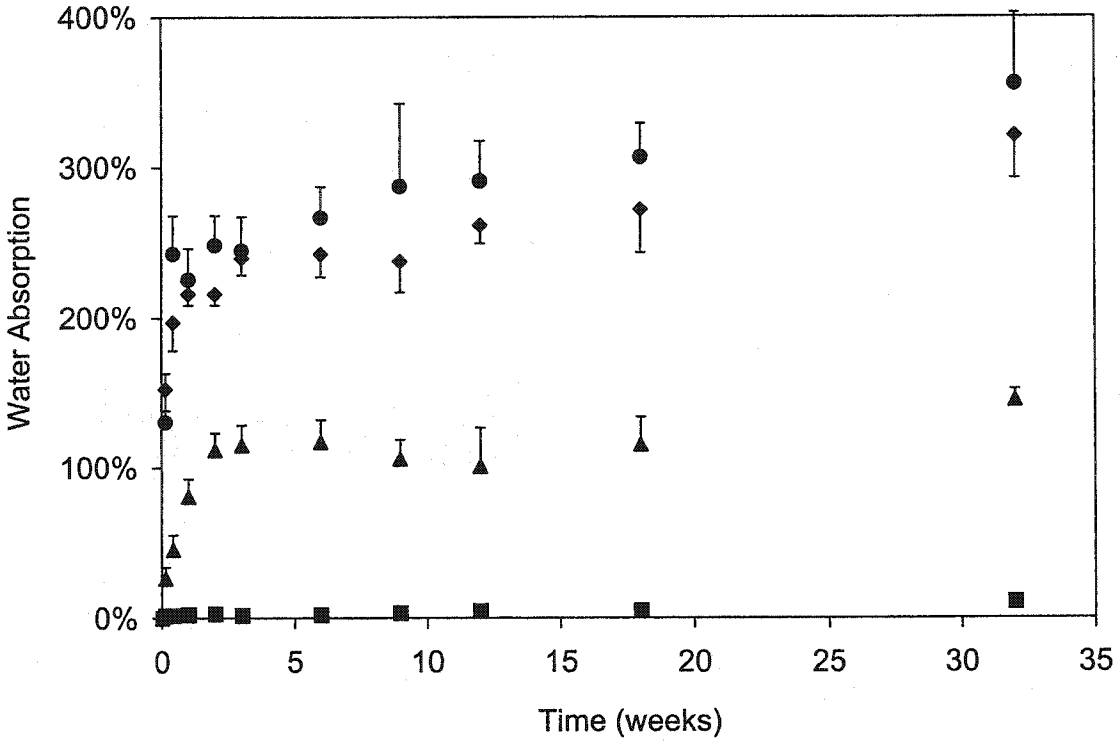

Figure 6.5: Sample water absorption during *in vitro* degradation. Water absorption in (■) solid PPF networks and in porous scaffolds of (▲) 70Ps, (◆) 80Ps, and (●) 80Pl formulations. At week 32, the 80Ps and 80Pl formulations exhibited the greatest water absorption, followed by the 70Ps scaffolds and solid networks, respectively. No difference in absorbency was observed between the 80Ps and 80Pl formulations.

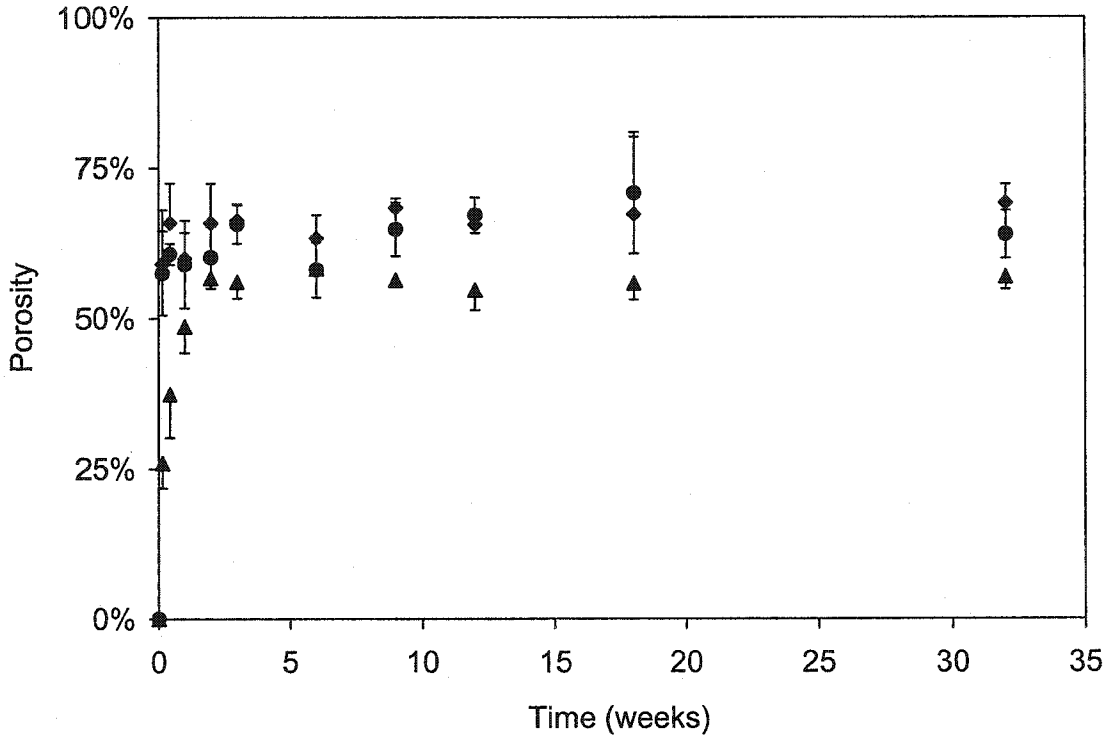

Figure 6.6: Scaffold porosity during *in vitro* degradation. Porosity for scaffolds of (▲) 70Ps, (◆) 80Ps, and (●) 80Pl, as determined by mercury porosimetry, was maintained after complete porogen leaching, with 80Ps and 80Pl scaffolds exhibiting higher porosities than the 70Ps scaffolds.

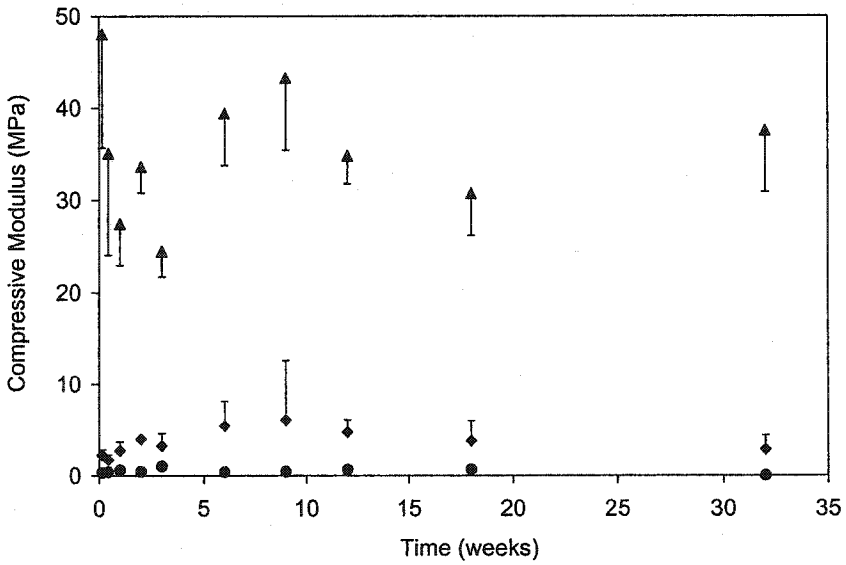
Compressive Modulus (MPa)
50
40
30
20
10
0
0
5
10
15
20
25
30
35
Time (weeks)

(A)

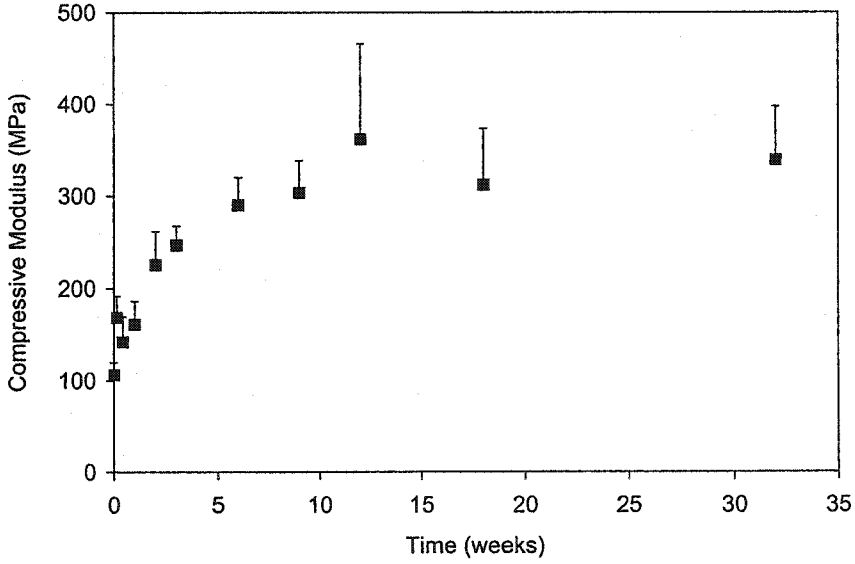
Compressive Modulus (MPa)
500
400
300
200
100
0
0
5
10
15
20
25
30
35
Time (weeks)

(B)

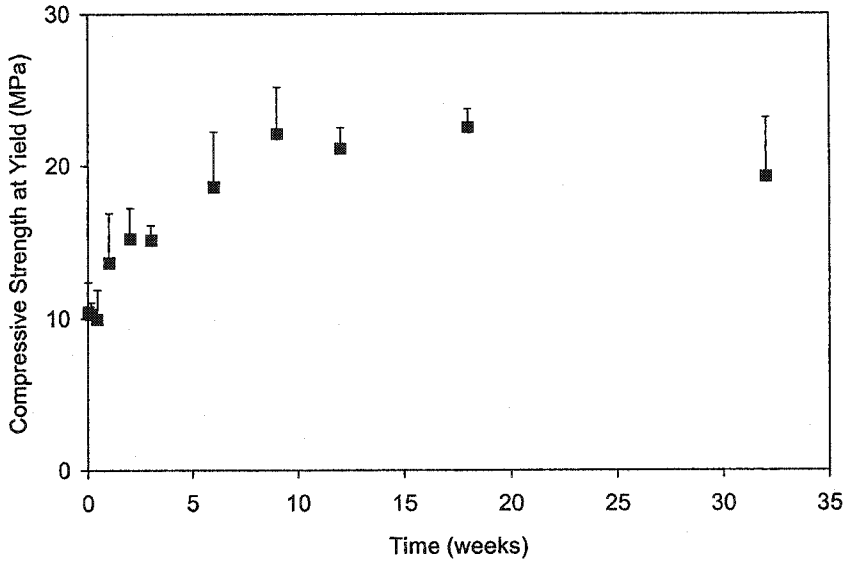

(C)

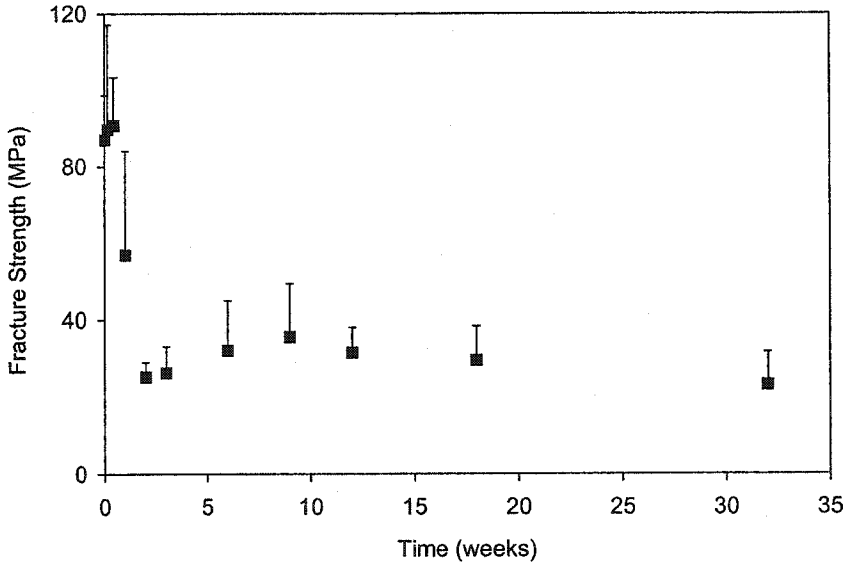

(D)

Figure 6.7: Sample mechanical properties during *in vitro* degradation. **(A)** Following an initial period of salt leaching, the compressive modulus for porous scaffolds of (▲) 70Ps, (◆) 80Ps, and (●) 80Pl was maintained at approximate values of 35.0 MPa, 3.9 MPa, and 0.6 MPa, respectively. **(B/C)** Compressive modulus and compressive strength at 1% yield of (■) solid PPF networks increased over the first 6 weeks and then remained constant through week 32. **(D)** A distinct decrease in fracture strength of (■) solid PPF networks corresponded with the appearance of cracks at week 1.

CHAPTER VII

PHOTOCROSSLINKING CHARACTERISTICS AND MECHANICAL PROPERTIES OF DIETHYL FUMARATE/POLY(PROPYLENE FUMARATE) BIOMATERIALS[†]

ABSTRACT

The development of tissue engineered materials for the treatment of large bone defects would provide attractive alternatives to the autografts, allografts, non-degradable polymers, ceramics, and metals that are currently used in clinical settings. To this end, poly(propylene fumarate) (PPF), a viscous polyester synthesized from diethyl fumarate (DEF), has been studied for use as an engineered bone graft. We have investigated the photocrosslinking of PPF dissolved in its precursor, DEF, using the photoinitiator bis(2,4,6-trimethylbenzoyl) phenylphosphine oxide (BAPO) and low levels of ultraviolet light exposure. A three factor, 2x2x4 factorial design was developed, studying the effects of PPF number average molecular weight, BAPO initiator content, and DEF content upon photocrosslinking characteristics and mechanical properties. Uncured DEF/PPF solution viscosity fell over three orders of magnitude as DEF content was increased from 0 to 75%. The exothermic photocrosslinking reaction released low levels of heat, with no more than 160 J/g released from any formulation tested. As a result, the maximum photocrosslinking temperature remained below 47°C for all samples. Both sol fraction and swelling degree generally increased with increasing DEF content. Compressive

[†] This chapter was published as the following article: Fisher JP, Dean D, Mikos AG. Photocrosslinking characteristics and mechanical properties of diethyl fumarate/poly(propylene fumarate) biomaterials. Biomaterials. 2002; 23: 4333-4343.

mechanical properties were within the range of trabecular bone, with the strongest samples possessing an elastic modulus of 195.3 ± 17.5 MPa and a fracture strength of 68.8 ± 9.4 MPa. Finally, the results indicate that PPF crosslinking was facilitated at low DEF precursor concentrations, but hindered at higher precursor concentrations. These novel DEF/PPF solutions may be preferred over pure PPF as the basis for an engineered bone graft because they (1) exhibit reduced viscosity and thus are easily handled, (2) form polymer networks with compressive strength at fracture suitable for consideration for trabecular bone replacement, and (3) may be readily fabricated into solids with a wide range of structures.

INTRODUCTION

Injectable, degradable biomaterials used within a tissue engineering strategy hope to quickly become viable devices for the treatment large bone defects [84]. These biomaterials may be formed from either ceramics or synthetic polymers, so long as they degrade by natural biological pathways into biocompatible products [84-88]. A principle advantage to injectable biomaterials lies in their ability to completely fill the irregularly shaped bone defects that often arise clinically. Other advantages include their ease of use, allowance of minimally invasive surgical procedures, and ability to act as a carrier of cells or bioactive agents. The development of an injectable, in situ polymerizable biomaterial, however, requires the consideration of a number of material characteristics that are not often evaluated for other biomaterials, including uncured solution viscosity and heat evolution during curing.

We have recently investigated photocrosslinked poly(propylene fumarate) (PPF) as a possible basis for an engineered bone graft. PPF contains a repeating fumarate unit

that is comprised of one carbon - carbon double bond and two ester groups. The carbon - carbon double bond allows the viscous PPF polymer to be crosslinked into a solid, while each ester group allows PPF to degrade, via ester hydrolysis, into biocompatible fragments [82]. Photocrosslinked PPF has been formed into scaffolds and shown in a rabbit cranial defect model to elicit a mild tissue response as well as facilitate bone formation when loaded with transforming growth factor beta 1 (TGF-β1) [59-61]. A photocrosslinkable biomaterial such as this PPF-based system may be suitable both for treatments that prefer a prefabricated implant and treatments that prefer an injectable biomaterial that is cured by light, either during or after its injection [58].

At high PPF molecular weights, however, the polymer becomes quite viscous, inhibiting its handling properties and, by definition, markedly reduces its ability to flow. This viscous nature of PPF has repercussions for both injectable and prefabrication processes. We desired to create a PPF system that possesses a significantly reduced viscosity, while still retaining the advantageous characteristics of fumarate-based biomaterials. To this end, we have developed a class of biomaterials that are formed by the photocrosslinking of the PPF polymer dissolved within diethyl fumarate (DEF), the diester precursor from which PPF is synthesized. DEF was chosen because it contains the crosslinkable carbon - carbon double bond that is present within PPF and thus should be able to participate in the crosslinking reaction. Furthermore, DEF should not significantly alter the biomaterial properties of the purely PPF materials investigated previously.

The goal of this study was to characterize the photocrosslinking characteristics and mechanical properties of DEF/PPF biomaterials as determined by three factors: PPF

molecular weight, BAPO photoinitiator content, and DEF content. We would like to study the effects of these factors upon (1) uncured DEF/PPF solution viscosity, (2) DEF/PPF photocrosslinking reaction extent as measured by heat evolution, sol fraction, as well as swelling degree, and (3) cured DEF/PPF mechanical properties. Definition of the DEF/PPF photocrosslinking characteristics and mechanical properties will help to realize the potential of these novel fumarate-based biomaterials as well as describe the crosslinking of a polymer/polymer precursor system.

MATERIALS AND METHODS

Experimental design

A three factor, factorial design was devised. The three factors investigated were (1) poly(propylene fumarate) number average molecular weight (PPF M_n), (2) bis(2,4,6 trimethylbenzoyl) phenylphosphine oxide content (mg BAPO/g (DEF+PPF)), and (3) diethyl fumarate content (g DEF/g PPF). The first two factors were both investigated at two levels, while the third factor, diethyl fumarate content, was investigated at four levels. Thus a 2x2x4 design, comprised 16 formulations, was investigated; Table 7.1 presents the composition of all formulations.

Poly(propylene fumarate) synthesis

Poly(propylene fumarate) was synthesized following a two step procedure [62]. First, 1 mole of diethyl fumarate (Acros Organics, Pittsburgh, Pa) and 3 moles of 1,2 propanediol (Acros Organics) were reacted using 0.01 moles $ZnCl_2$ (Fisher Chemicals, Fair Lawn, NJ) as a catalyst and 0.002 moles hydroquinone (Acros Organics) as a radical inhibitor. The reaction was run under a nitrogen blanket, producing bis(hydroxypropyl) fumarate as the main product and ethanol as a byproduct. Second, the

bis(hydroxypropyl) fumarate was transesterified, producing poly(propylene fumarate) and 1,2 propanediol as a byproduct. Since the number average molecular weight (M_n) of PPF generally increases with increasing transesterification temperature and time, the reaction was run until the product had the desired molecular weight as determined by gel permeation chromatography. The PPF product was dissolved in methylene chloride (Fisher Chemicals) for purification. PPF was first washed with acid (5 wt% HCl in H_2O) to remove $ZnCl_2$ and then purified with two washes each of both pure water and brine. The organic phase was then dried with sodium sulfate. Next, the PPF was precipitated in ethyl ether twice to remove the hydroquinone. The excess ether was then decanted. The remaining solvents were finally removed from the PPF by rotary evaporation followed by vacuum drying. M_n typically rises after purification as lower molecular weight chains are removed by the aqueous washes. The final product is a clear, light yellow viscous liquid. Two PPF samples were synthesized: a short chain sample (M_n = 1260, P.I. = 1.4, and average number of double bonds per PPF chain = 7.6) and long chain sample (M_n = 2260, P.I. = 1.7, and average number of double bonds per PPF chain = 14.0).

Gel permeation chromatography

The molecular weight distributions of PPF were determined by gel permeation chromatography (GPC). The GPC system includes an HPLC pump (Waters, Model 510, Milford, MA), an autosampler (Waters, Model 717), a chromatography column (Waters, Styragel HR 4E, 7.8 x 300 mm column [50 – 100,000 Da range]), and a differential refractometer (Waters, Model 410). The solvent, degassed chloroform, was run at 1.0 ml/min for sample measurement. Polystyrene standards (500, 2630, 5970, and 18100 Da) were used to obtain a calibration curve for calculating molecular weight distributions.

Each sample type was run in triplicate; the reported values for M_n and P.I. are the mean values.

DEF/PPF photocrosslinking

The diethyl fumarate/poly(propylene fumarate) formulations were crosslinked with ultraviolet light using the photoinitiator bis(2,4,6-trimethylbenzoyl) phenylphosphine oxide (BAPO, Ciba Specialty Chemicals, Tarrytown, NY) (Figure 7.1). For the formulations that did not contain DEF, BAPO was first dissolved in methylene chloride (0.05 ml/g PPF). The uncrosslinked PPF solution was warmed to approximately 50°C, allowing the viscous polymer to become fluid, and then mixed with the BAPO solution to achieve the appropriate initiator content. For the formulations that did contain DEF, the appropriate amount of BAPO initiator was first dissolved into DEF and then the corresponding amount of PPF was mixed into the DEF/BAPO solution. The final solution was poured into a cylindrical glass vial (6.5 mm x 40 mm). Vials were then centrifuged (5 min at 3000 rpm) if the final solution was viscous enough to retain air bubbles. The samples were photocrosslinked using an Ultralum (Paramount, CA) ultraviolet light box. This UV box is outfitted with four 15W, long wavelength UV bulbs and its interior reflects UV light. The total light emission covers a range of UV wavelengths (320 - 405 nm), with a peak at 365 nm and an intensity of approximately 2 mW/cm^2 at 10 cm. The BAPO photoinitiator absorbs wavelengths below 400 nm, with a general increase in absorption as the wavelength decreases to 200 nm. All of the samples were exposed to ultraviolet light for 30 minutes at a distance of approximately 10 cm. Samples were placed on their sides in a Pyrex petri dish that was elevated from the floor

of the UV box. This configuration allows the incident light to penetrate the cylindrical samples radially from all sides.

Differential photocalorimetry

Differential photocalorimetry (DPC) was performed using a differential scanning calorimeter (Model 2920, TA Instruments, New Castle, Delaware) fitted with a DPC module (Model DSC2910, TA Instruments). The UV light (200 W Hg lamp whose characteristic wavelengths include 313, 366, 405 and 435 nm) was corrected for any uneven distribution over both the sample and reference in the chamber. The reference was a previously cured sample of photocrosslinked DEF/PPF whose formulation was identical to the test sample. Heat flux was measured during UV exposure under isothermal conditions and after chamber equilibration at 37°C. The heat release due to UV initiated crosslinking was calculated as the area beneath the heat flux curve with a baseline drawn coincident with the plateau region between 5 and 30 min. Each sample type was run in triplicate; the reported values are the mean values and the associated errors are the standard deviations.

Photocrosslinking reaction temperature

The interior temperature of DEF/PPF samples during ultraviolet light exposure was measured using a wire thermocouple. Uncured samples were first prepared in 6.5 mm diameter glass vials as previously described. A 0.025 mm diameter, Teflon insulated wire thermocouple (Omega Engineering, Stamford, CT) was then inserted into the sample. The thermocouple tip was kept at least 10 mm from the end of the glass vial as well as away from the side of the glass cylinder, but no radial position was specified. The sample with thermocouple was then placed within the UV box. Initial sample

temperature was 23±2°C. Temperature was then recorded at 1 Hz for 4000 s using an InstruNet data acquisition box and software program (Nordisk Transducer Teknik, Hadsund, Denmark). Ultraviolet light exposure lasted from 100 to 1900 s only, with the remainder of the experiment occurring in the dark. The maximum reaction temperature was defined as the local maximum temperature between approximately 200 and 800 s. The time to maximum reaction temperature was defined as the time from the ignition of the UV light (t = 100 s) to the time at which the maximum reaction temperature was recorded. Each sample type was run in triplicate; the reported values are the mean values and the associated errors are the standard deviations.

Rheometry

The solution viscosity was determined using a rheometer (Model AR1000, TA Instruments). Due to the wide range of viscosities that were to be tested, a modified parallel plate system was utilized so that all sample types could be tested in the same manner. The sample solution was placed into a Teflon mold (10 mm diameter and 15 mm depth) positioned on the temperature controlled plate of the rheometer. The temperature was set at 37°C. An 8 mm diameter, cylindrical parallel plate geometry was lowered into approximately 0.5 ml of the sample contained within the mold. A continuous flow program, with shear strain held at 10 Pa, was run for 300 s and viscosity was monitored throughout the experiment. The value recorded for a single run was the average value over the final 200 s of the experiment. Each sample type was run in triplicate; the reported values are the mean values and the associated errors are the standard deviations.

Sol fraction

A study of the DEF/PPF construct sol fraction was performed using photocrosslinked cylinders, approximately 0.5 g in weight, whose fabrication was described previously. A photocrosslinked sample was weighed (W_i) and placed into 20 ml of methylene chloride, as both PPF and DEF are soluble in this organic solvent but crosslinked DEF/PPF networks are not. Vials containing the samples in methylene chloride were capped and then stirred at 75 rpm for approximately 160 hrs. Samples, most of which had crumbled, were then removed from the solvent by pouring the mixture through a weighed filter paper (W_p). The filter paper containing the sample was dried for 1 hr at 60°C and then weighed again (W_{p+s}). The sol fraction of the sample was then calculated using the formula:

$$\text{Sol Fraction (Cylinder)} = \frac{W_i - (W_{p+s} - W_p)}{W_i} \times 100\%. \qquad (1)$$

Each sample type was run five times; the reported values are the mean values and the associated errors are the standard deviations.

Degree of swelling

Degree of swelling and sol fraction of all DEF/PPF constructs was also investigated using photocrosslinked flat sheets, approximately 0.25 g in weight and 1.5 mm in thickness. The formulations were poured into a rubber gasket mold, sealed between two glass plates, and then crosslinked by exposure to 30 min of ultraviolet light. A photocrosslinked sample was weighed (W_i) and placed into capped vials containing 20 ml of toluene for 24 hours. Toluene was used in this study as PPF swells only moderately in this solvent and thus the samples retain their three dimensional structure

throughout the experiment. The samples were removed from the toluene, blotted dry with weigh paper, and then weighed (W_s). Finally, the samples were left in a fume hood to dry overnight and subsequently weighed (W_d). The degree of swelling was calculated using the formula:

$$\text{Swelling Degree} = \frac{W_s - W_d}{W_s}. \quad (2)$$

The sol fraction was calculated using the formula:

$$\text{Sol Fraction (Sheet)} = \frac{W_i - W_d}{W_i} \times 100\%. \quad (3)$$

Each sample type was run five times; the reported values are the mean values and the associated errors are the standard deviations.

Compressive mechanical testing

Compressive testing of DEF/PPF constructs were conducted using a mechanical testing system (Model 858, MTS System Corporation, Eden Prairie, MN). Cylindrical samples were synthesized as described previously and then cut to proper length; typical sample sizes were 6.5 mm in diameter and 13.0 mm in length. Force and displacement were zeroed prior to compression, with the top plate slightly above the surface of the sample. Samples were compressed at a crosshead speed of 1 mm/min while stress and strain were monitored throughout the experiment. The experiment was halted after sample fracture. The initial slope of the stress - strain curve determined the elastic modulus of the sample. Compressive strength at fracture was defined as the stress required to fracture the material. Each sample type was run five times; the reported values are the mean values and the associated errors are the standard deviations.

Statistics

The results of the 2x2x4 factorial design were inspected by an analysis of variance (ANOVA) [89]. As three factors were investigated, a total of seven treatments were possible: 3 main factor effects, 3 two factor interaction effects, and 1 three factor interaction effect. (For example, in a study of factors A, B, and C, the main effects are A, B, and C, the two factor interaction effects are AB, AC, and BC, and the three factor interaction is ABC.) An F value, F critical value, and p value were then calculated for each of the seven treatments; p values are indicated. A significance level of 95% (α = 0.05) was chosen, thus a treatment with a p value less than 0.05 is considered to be significant determinant of the response. While all treatments were investigated in this manner, only the main effects were discussed in this work.

RESULTS

Solution viscosity

The viscosities of the uncured DEF/PPF solutions were found to fall over three orders of magnitude, from 5940 to 2 Pa s, as DEF content is increased from 0 to 75% (Figure 7.2). Analysis of the results from the factorial design study showed that PPF molecular weight, BAPO content, and DEF content to be statistically significant factors determining viscosity, though BAPO content was found to be a weak factor. Increases in PPF molecular weight and decreases in DEF content act to increase uncured DEF/PPF solution viscosity.

Heat release during photocrosslinking

The heat flux produced from the photocrosslinking reaction during 30 min of ultraviolet light exposure was measured using a differential photocalorimeter. A typical

heat flux curve is presented in Figure 7.3. Heat release varied between 41.9 and 158.4 J/g, with the greatest values found in those formulations containing 25 - 50 % DEF content (Figure 7.4A). Results of the factorial design indicated that PPF molecular weight, BAPO content, and DEF content all have statistically significant effects upon heat release during the photocrosslinking reaction. Maximum heat release occurs between 28 and 53 s after initiation of ultraviolet light exposure (Figure 7.4B). Statistical analysis of the results show that BAPO content and DEF content had a statistically significant effect upon the time to maximum heat release.

Photocrosslinking reaction temperature

Interior temperatures of DEF/PPF samples during and after the photocrosslinking reaction were monitored using a wire thermocouple. The results show that a local maximum temperature exists in early experimental times for formulations containing DEF, but not in formulations containing only PPF (Figure 7.5). This first local peak likely reflects the exothermic photocrosslinking reaction. The second local peak at 1900 s, found in all samples, is due to the warming effects of the ultraviolet light, as the fall in sample temperature occurs immediately following the cessation of UV light exposure at 1900 s (Figure 7.5). Since the interest of this work lies in the photocrosslinking reaction, not the heating effects of UV light, the samples containing only PPF were not considered in the further analyses.

The results show that formulations containing 50 % DEF generally present the highest maximum reaction temperatures (Figure 7.6A). Analysis of the factorial design further indicates that DEF content is the significant factor determining the maximum reaction temperature. The amount of time required to achieve maximum reaction

temperature was also noted in these experiments (Figure 7.6B). The time to maximum reaction temperature varied from 352 to 768 s and found to be determined by PPF molecular weight, BAPO initiator content, and DEF content.

Sol fraction

The results show that a significant fraction of all photocrosslinked DEF/PPF cylinders are soluble in the methylene chloride organic solvent (Figure 7.7), implying that these fractions are not contributing to the bulk, crosslinked polymer network. Figure 7.7 shows that the sol fraction for all formulations initially decreases with DEF addition, but subsequently increases when DEF content is above 25%. The smallest sol fractions, less than 30%, were found in those formulations containing high initiator content, high PPF molecular weight, and moderate (25 - 50%) DEF content. All three experimental factors, PPF molecular weight, BAPO content, and DEF content, were found to be significant in determining sol fraction.

Swelling degree

An examination of swelling degree and sol fraction was also performed using photocrosslinked flat sheets. Swelling degree was generally found to decrease with increasing PPF molecular weight, PPF content, and BAPO content (Figure 7.8A). A maximum swelling degree of 1.29 ± 0.03 was found in the formulation with low levels of PPF molecular weight, PPF content, and BAPO content, while a minimum swelling degree of 0.02 ± 0.01 was found in the formulation with high levels of PPF molecular weight, PPF content, and BAPO content. The sol fraction of photocrosslinked PPF sheets (Figure 7.8B) was generally found to follow the same trend described in the previous sol fraction study investigating photocrosslinked PPF cylinders (Figure 7.7). However, the

low penetration depth of the sheet geometry does allow for more effective photocrosslinking and thus for a given formulation the sol fraction of the sheet was lower than that of the cylinder. All three experimental factors were found to be significant in determining both swelling degree and sol fraction.

Compressive mechanical properties

The mechanical properties of the various DEF/PPF samples were assessed by compressive mechanical testing. Elastic modulus varied between 1.5 ± 0.2 and 195.3 ± 17.5 MPa, while fracture strength varied between 0.4 ± 0.1and 68.8 ± 9.4 MPa (Figures 7.9A and 7.9B). Both elastic modulus and fracture strength were generally found to be the greatest in the formulations containing 25% DEF. All three experimental factors, PPF molecular weight, BAPO content, and DEF content, were found to be significant in determining both elastic modulus and fracture strength.

DISCUSSION

The development of a synthetic, degradable biomaterial for tissue engineering applications should follow a rational progression towards a specific application, while leaving open doors for other alternatives and possibilities. We have been following such a progression in the development of photocrosslinked poly(propylene fumarate) for bone tissue engineering applications. Photocrosslinked PPF is of interest because it may allow for the prefabrication of tissue engineering scaffolds with precisely defined external dimensions as well as interior porous structure by using techniques such as stereolithography. Alternatively, photocrosslinked PPF may be suitable for injectable applications where it is cured either during or after its injection. In order to fully explore these options, a low viscosity form of photocrosslinkable PPF was desired, leading to the

development of DEF/PPF biomaterials. This work sought to characterize the crosslinking and mechanical properties of these novel DEF/PPF biomaterials.

The addition of DEF to PPF resulted in a significant reduction in viscosity, with increasing amounts of DEF lowering viscosity by over three orders of magnitude. Solution viscosity has been explored in other injectable materials proposed as bone substitutes or bone tissue engineering constructs; for example, viscosity has been controlled by the addition of calcium phosphate fillers [90]. It is also interesting to note that, similar to the system described here, clinically used bone cements of polymethylmethacrylate utilize a polymer/monomer crosslinking system that allows for injectability [91]. The advantageous feature of the PPF/DEF material is that while viscosity may be lowered with DEF addition (Figure 7.2), the mechanical strength of the crosslinked material is increased, so long as DEF content remains below 25 - 50% (Figures 7.9A and 7.9B). Thus, the addition of small amounts of DEF to PPF allows for a material with both improved handling characteristics and increased mechanical strength.

Another goal of this work was to characterize the extent of the DEF/PPF photocrosslinking reaction by investigating the reaction heat evolution as well as the sol fraction and swelling degree of the crosslinked samples. The results (Figure 7.4A) indicate that the total heat evolved during the photocrosslinking reaction is low, below 160 J/g, regardless of formulation. Figure 7.4A compares these results to the known heat of polymerization of diethyl fumarate (65 kJ/g) [65]. The results indicate that at low DEF content/high PPF content most of the DEF is involved in the photocrosslinking reaction, if it is assumed that the number of fumarate units within PPF reacted is low (< 5 fumarate

units). This seems a reasonable assumption considering the diffusional limitations restricting the PPF polymer movement as well as steric hindrances inhibiting addition to the polymer. However, at increasingly higher DEF content, Figure 7.4A suggests that significant portions of both the PPF and DEF are not involved in the photocrosslinking reaction. This is supported by the results of both sol fraction studies which show an increasing sol fraction as DEF content is increased beyond 25% (Figure 7.7 and 7.8B).

The low heat evolution is realized in the low temperatures during and after photocrosslinking. Specifically, the results indicate that no DEF/PPF formulation reaches temperatures above 47°C throughout photocrosslinking. These results are encouraging for in situ curing applications where low temperatures are required so as to minimize adverse bone tissue responses that are thought to occur at temperatures as low as 53°C [92,93]. The short times at which the maximum heat release and maximum temperatures were obtained also imply that the material cures at a clinically feasible rate, similar to polymethylmethacrylate bone cements which cure in approximately 5 - 10 min [91]. Furthermore, many prefabricated processes, such as stereolithography, would benefit from a system which crosslinks quickly and with low heat evolution [94]. Finally, since this system is photoinitiated, even quicker curing rates may be obtained by using a more intense light source, as the light source used in this work was of quite low intensity (2 mW/cm^2), though quicker rates may be associated with higher levels of heat evolution.

The mechanical properties of the crosslinked DEF/PPF biomaterials were also studied. The results indicate that an optimal DEF content of approximately 25% is needed to produce the highest elastic modulus and fracture strength. In addition to the effect of DEF content, both PPF molecular weight and BAPO content clearly effected the

final mechanical properties, with increases in either producing a stronger material. The properties of photocrosslinked DEF/PPF materials are well suited for use in a bone defect, as trabecular bone has been reported to possess a compressive fracture strength of approximately 5 MPa and a compressive elastic modulus of 50 - 100 MPa [76], though it should be noted that when materials are formed into the porous scaffolds necessary for tissue growth their mechanical strength will decrease [60].

The DEF/PPF photocrosslinking characterization also leads to a broader question: How is the crosslinking of a polymer affected by the addition of the polymer's crosslinkable precursor? The concept that has been formed is that two regimes exist: a regime of low precursor content where polymer crosslinking is facilitated and a regime of high precursor content where polymer crosslinking is hindered (Figure 7.10).

PPF is photocrosslinkable without the presence of a functional crosslinking monomer, such as DEF precursor, by forming covalent bonds between opened carbon - carbon double bonds on adjacent PPF chains. As DEF is added to PPF, crosslinking may be facilitated as polymerized DEF units bridge adjacent PPF chains, including those PPF chains which may have not reacted without the presence of the DEF precursor. Thus, the photocrosslinking of those formulations containing a small amount of the DEF precursor should involve the reaction of more fumarate carbon - carbon double bonds. The results presented earlier seem to support this concept. Solutions with 25% DEF content all release greater amounts of heat than those without DEF (Figure 7.4A), implying greater numbers of carbon - carbon double bonds involved in the photocrosslinking reaction. The swelling degree of all formulations is either constant or falls with the initial addition of DEF (Figure 7.8A), also indicating that similar or even greater numbers of double

bonds are contributing to the crosslinked network. This is realized in the constant or reduced sol fraction (Figure 7.7 and 7.8B), increased elastic modulus (Figure 7.9A), and increased fracture strength (Figure 7.9B) of these formulations.

However, as increasing amounts of the DEF precursor are added to the DEF/PPF solution, an opposing force of dissolution begins to dominate the system. Here the PPF polymer chains dissolved within the DEF precursor are separated by ever greater distances. While polymerized DEF units at lower DEF concentrations could bridge these gaps between PPF chains, at higher concentrations this becomes increasingly difficult. Thus, fewer fumarate units are involved in the photocrosslinking reaction. Again, the results described earlier seem to support concept: as DEF concentration increases from 50 to 75%, heat release upon photocrosslinking decreases (Figure 7.4A), swelling degree increases significantly (Figure 7.8A), sol fraction increases dramatically (Figure 7.7 and 7.8B), and the mechanical properties of the cured samples fall (Figure 7.9A and 7.9B). Finally, this concept is supported by the fact that without the PPF polymer, DEF alone is not photocrosslinkable into a solid under the conditions described in this work.

CONCLUSIONS

This work has investigated the photocrosslinking characteristics and material properties of a class of novel biomaterials for use as an engineered bone graft. These materials are based upon the polymer poly(propylene fumarate) and its precursor diethyl fumarate, the crosslinkable unit contained within the repeating unit of PPF. The results have shown these materials to have a low viscosity, crosslink with low levels of heat release, and possess mechanical properties similar to human trabecular bone. The results also indicate that in this polymer/polymer precursor system, crosslinking is facilitated at

low precursor concentrations but hindered at higher precursor concentrations. These novel DEF/PPF materials may be an attractive option for bone tissue engineering applications.

Table 7.1 : Outline of the three factor, 2x2x4 factorial design. The three factors investigated were poly(propylene fumarate) number average molecular weight (PPF M_n), bis(2,4,6 trimethylbenzoyl) phenylphosphine oxide content (mg BAPO/g (DEF+PPF)), and diethyl fumarate content (g DEF/g PPF). The first two factors were investigated at two levels (0 and 1), while the third factor was investigated at four levels (0, 1, 2, and 3). Thus, as indicated, 16 formulations were prepared and tested.

PPF Molecular Weight (M_n, g/mol)	BAPO Initiator Content (mg BAPO/g (DEF+PPF))	DEF Content (g DEF/g PPF)
Low (0) : 1260	Low (0) : 2.5	Low (0) : 0.00
N/A	N/A	Medium Low (1) : 0.33
N/A	N/A	Medium High (2) : 1.00
High (1) : 2260	High (1) : 5.0	High (3) : 3.00

Sample Number	PPF Molecular Weight	BAPO Initiator Content	DEF Content
1	0	0	0
2	0	0	1
3	0	0	2
4	0	0	3
5	0	1	0
6	0	1	1
7	0	1	2
8	0	1	3
9	1	0	0
10	1	0	1
11	1	0	2
12	1	0	3
13	1	1	0
14	1	1	1
15	1	1	2
16	1	1	3

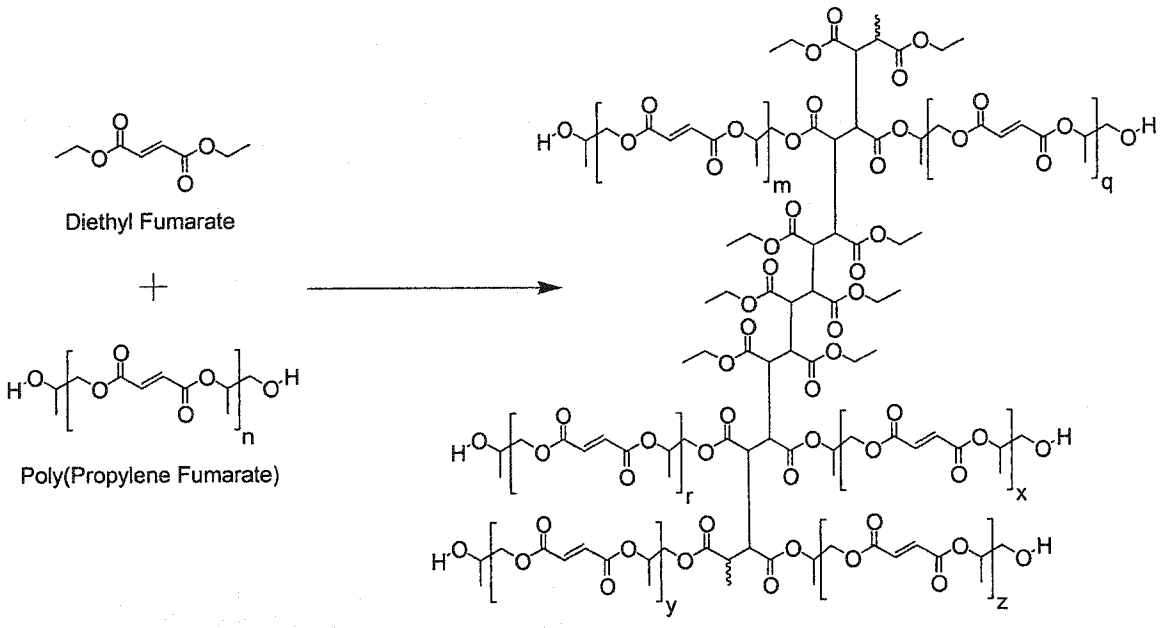

Figure 7.1 : A schematic depicting polyaddition reactions that occur between poly(propylene fumarate) and diethyl fumarate. The significant reactions depicted include the direct addition between two PPF chains as well as the crosslinking of two PPF chains by polymerized DEF.

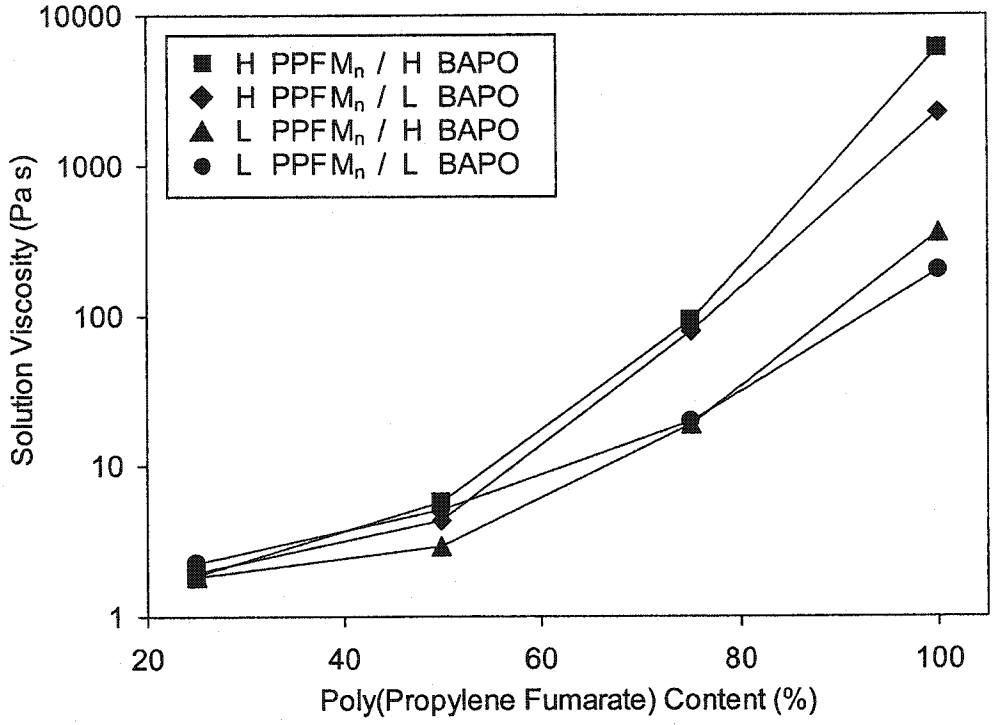

Figure 7.2 : The effect of PPF molecular weight, BAPO content, and DEF content upon the uncured solution viscosity. (See Table 7.1 for a description of sample formulations.) Note that error bars are too small to appear. All factors, PPF molecular weight ($p = 1.3 \times 10^{-8}$), BAPO content ($p = 7.2 \times 10^{-4}$), and DEF content ($p = 2.9 \times 10^{-14}$) were found to be significant in determining uncured solution viscosity.

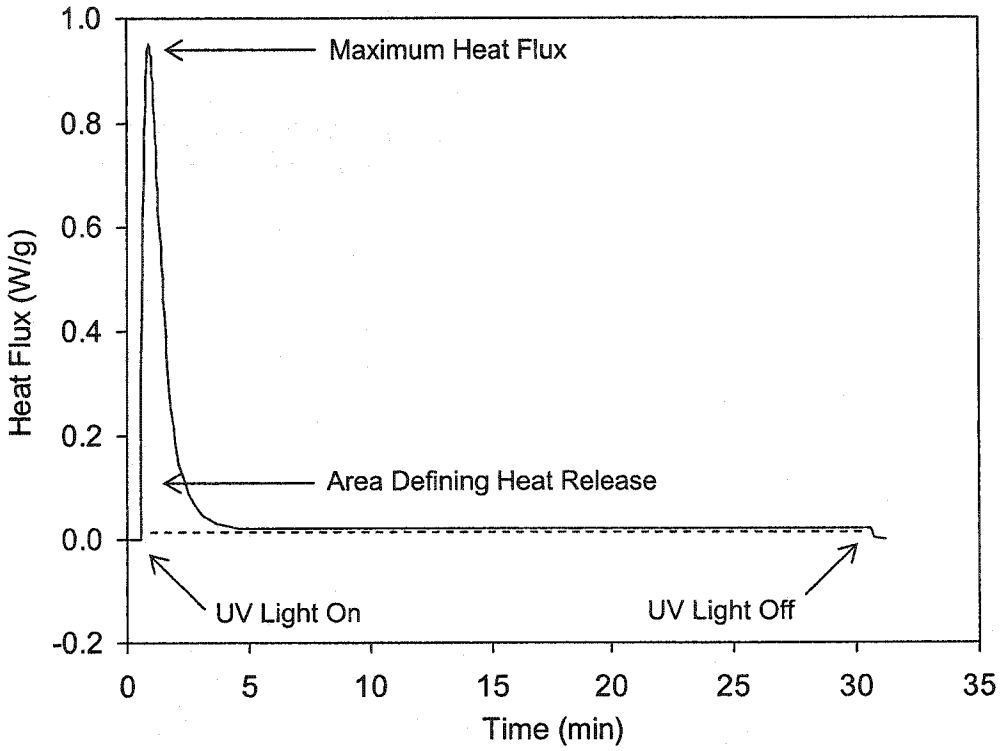

Figure 7.3 : A typical plot of heat flux from the photocrosslinking reaction of DEF/PPF; this formulation contains 1260 g/mol M_n PPF, 2.5 mg BAPO/g (PPF+DEF), and 75% DEF. Ultraviolet light exposure occurred between t = 0.5 and 30.5 min, lasting for a total of 30 min. The cumulative heat release was calculated as the area beneath the heat flux curve, with a baseline drawn coincident with the plateau region between 5 and 30 min.

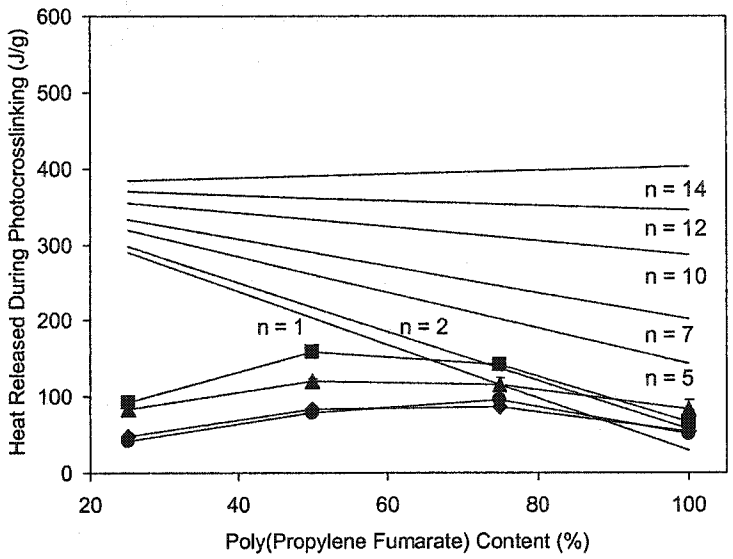

(A)

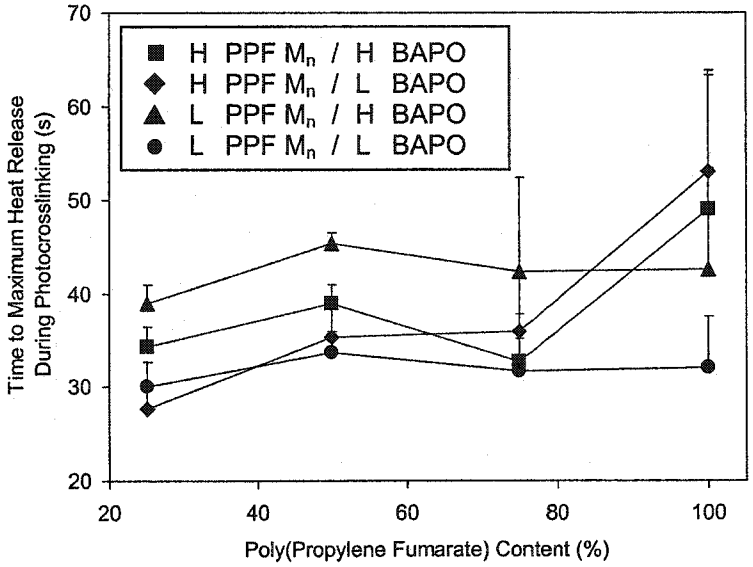

(B)

Figure 7.4 : The effect of PPF molecular weight, BAPO content, and DEF content upon the photocrosslinking reaction heat release **(A)** and the time to maximum heat release **(B)**. The heat release results **(A)** are compared to the theoretical heat evolution if all of the DEF and varying numbers of fumarate bonds within the PPF polymer (n = 1 to 14, where 14 is the theoretical number based upon a PPF M_n of 2260 g/mol) were to have reacted. PPF M_n ($p = 4.4 \times 10^{-3}$), BAPO content ($p = 1.9 \times 10^{-17}$), and DEF content ($p = 3.1 \times 10^{-17}$), were found to be significant in determining heat release. BAPO content ($p = 6.2 \times 10^{-3}$) and DEF content ($p = 1.6 \times 10^{-3}$) were found to be significant in determining the time to maximum heat release; PPF M_n ($p = 5.1 \times 10^{-1}$) was found to be an insignificant factor.

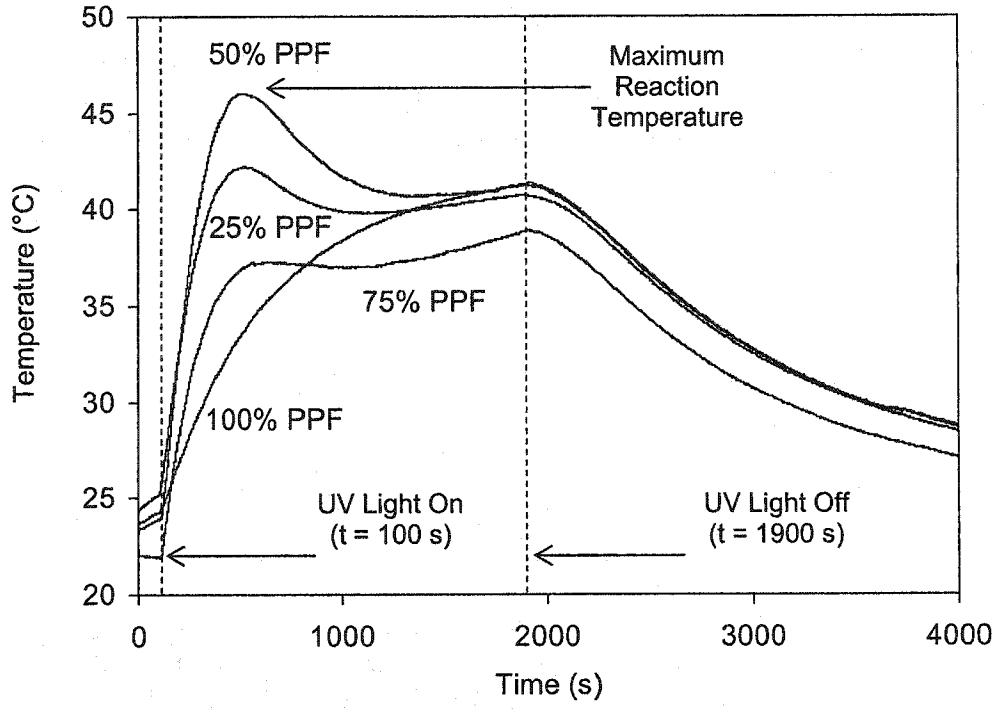

Figure 7.5 : A typical set of temperature profiles for four DEF/PPF formulations with varying DEF content (all contain 2260 g/mol M_n PPF and 2.5 mg BAPO/g (PPF+DEF)). All formulations that contain DEF were found to exhibit a local maximum temperature at approximately 500 s. This temperature was identified as the maximum reaction temperature. The time to maximum reaction temperature was defined as the time from the ignition of the UV light (t = 100 s) to the time at which the maximum reaction temperature was recorded.

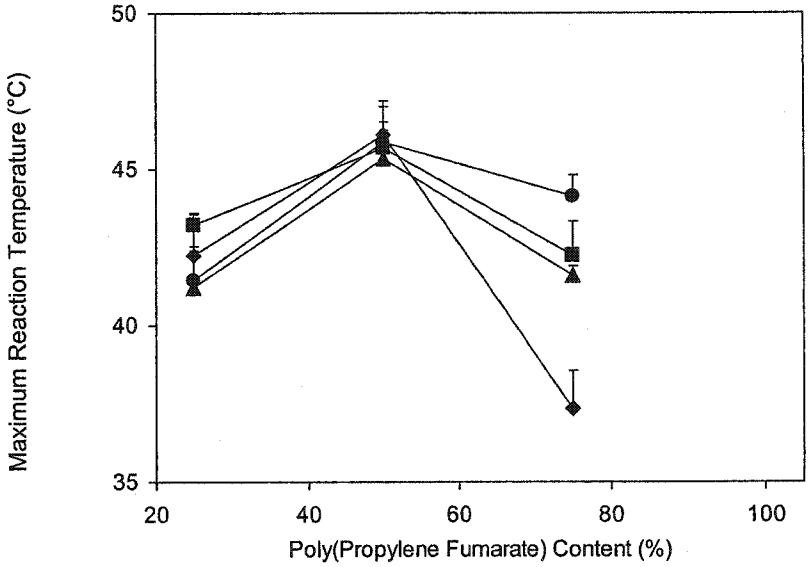

(A)

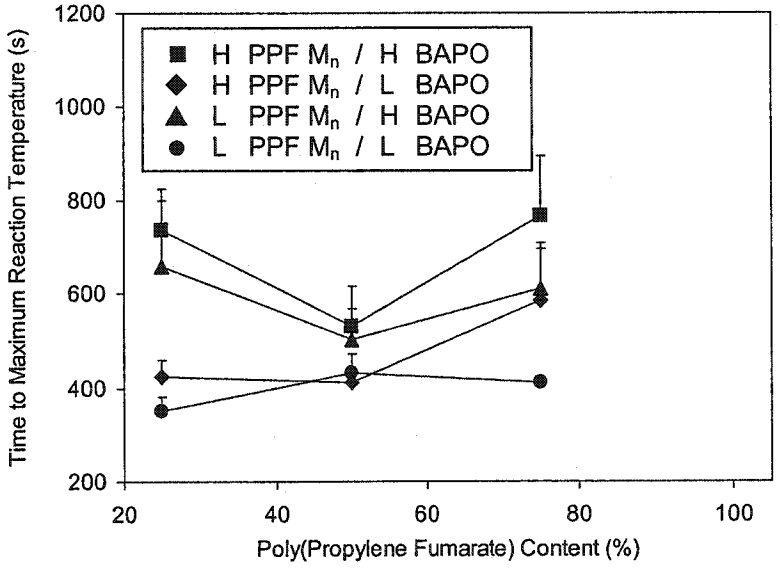

(B)

Figure 7.6 : The effect of PPF molecular weight, BAPO content, and DEF content upon the maximum reaction temperature **(A)** and the time to maximum reaction temperature **(B).** (See Table 7.1 for a description of sample formulations.) DEF content ($p = 7.7x10^{-10}$) was found to be the significant factor determining maximum reaction temperature; PPF molecular weight ($p = 2.2x10^{-1}$) and BAPO content ($p = 3.4x10^{-1}$) were found to be insignificant factors. All factors, PPF molecular weight ($p = 6.6x10^{-3}$), BAPO content ($p = 1.9x10^{-7}$), and DEF content ($p = 4.1x10^{-3}$), were found to be significant in determining the time to maximum reaction temperature.

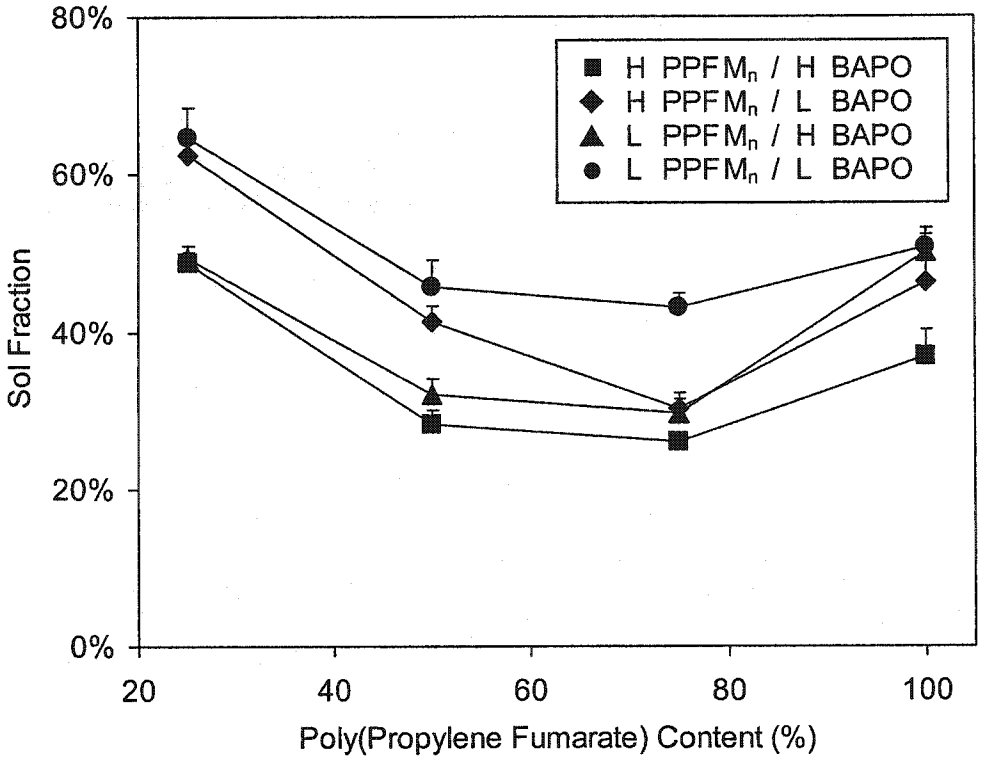

Figure 7.7 : The effect of PPF molecular weight, BAPO content, and DEF content upon the sol fraction of photocrosslinked cylinders. (See Table 7.1 for a description of sample formulations.) All factors, PPF molecular weight ($p = 1.8 \times 10^{-15}$), BAPO content ($p = 2.6 \times 10^{-28}$), and DEF content ($p = 6.2 \times 10^{-41}$), were found to be significant in determining the sample sol fraction.

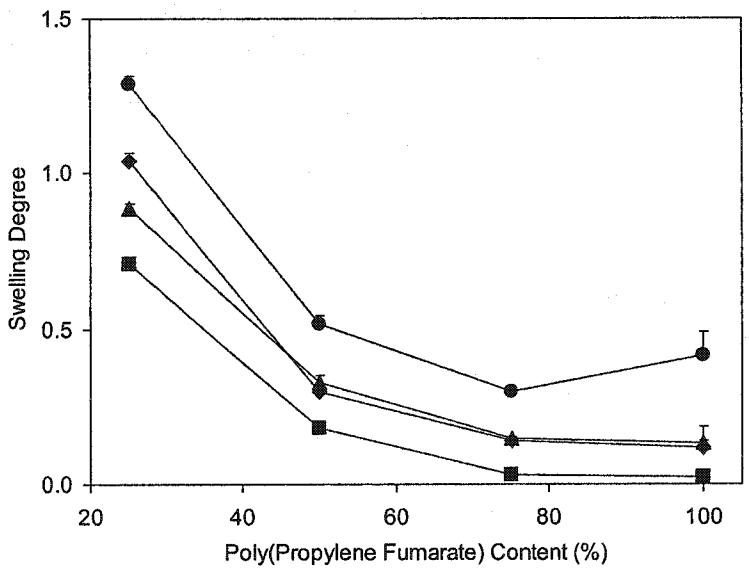

(A)

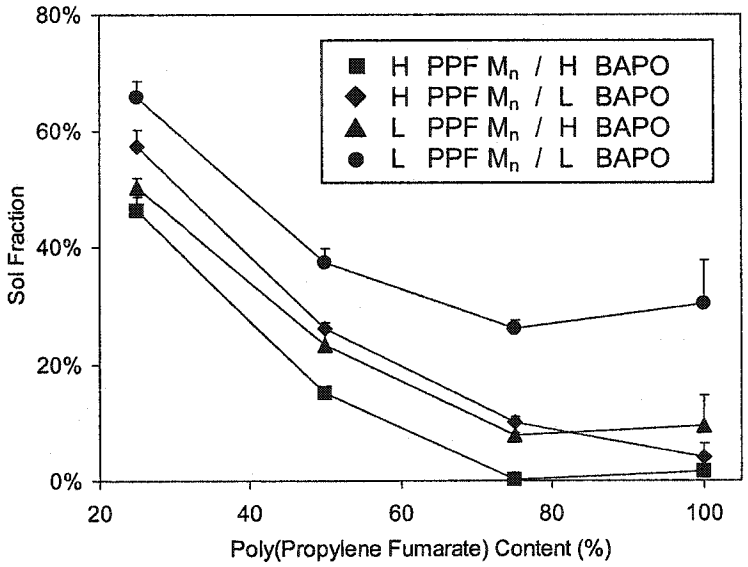

(B)

Figure 7.8 : The effect of PPF molecular weight, BAPO content, and DEF content upon the swelling degree **(A)** and sol fraction **(B)** of photocrosslinked sheets. (See Table 7.1 for a description of sample formulations.) All factors, PPF molecular weight ($p = 1.1x10^{-38}$), BAPO content ($p = 1.1x10^{-41}$), and DEF content ($p = 7.2\ x10^{-72}$), were found to be significant in determining swelling degree. Also, PPF molecular weight ($p = 9.0x10^{-43}$), BAPO content ($p = 4.5x10^{-46}$), and DEF content ($p = 3.2x10^{-72}$), were found to be significant in determining sol fraction.

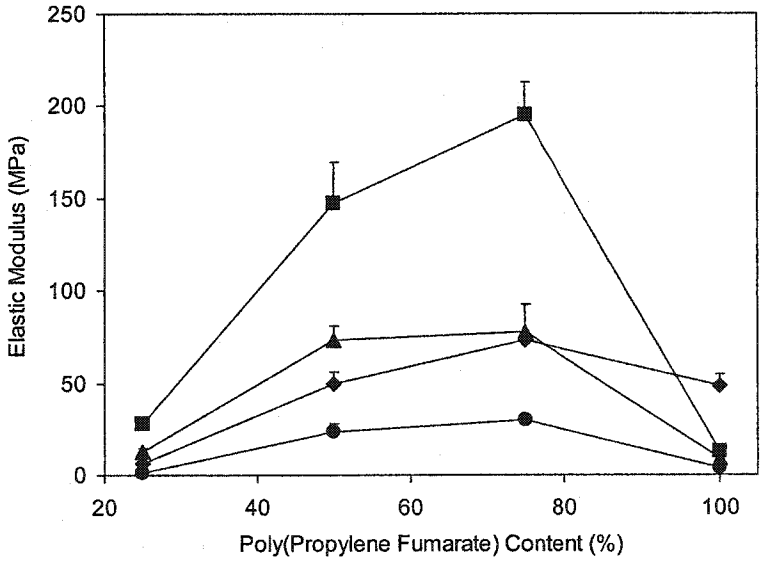

(A)

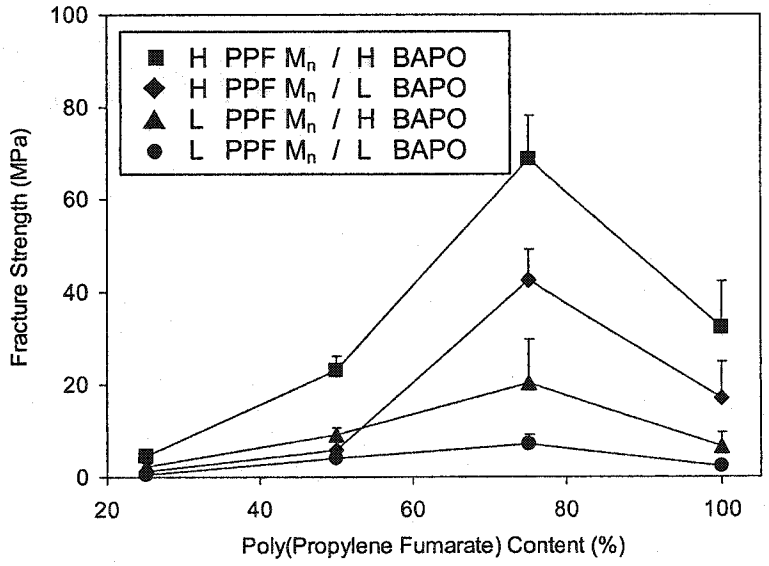

(B)

Figure 7.9 : The effect of PPF molecular weight, BAPO content, and DEF content upon photocrosslinked sample's elastic modulus **(A)** and strength at fracture **(B)**. (See Table 7.1 for a description of sample formulations.) All factors, PPF molecular weight ($p = 1.8x10^{-30}$), BAPO content ($p = 1.0x10^{-29}$), and DEF content ($p = 2.4x10^{-42}$), were found to be significant in determining elastic modulus. Similarly, PPF molecular weight ($p = 1.3x10^{-23}$), BAPO content ($p = 7.9x10^{-14}$), and DEF content ($p = 1.4x10^{-28}$), were found to be significant in determining fracture strength.

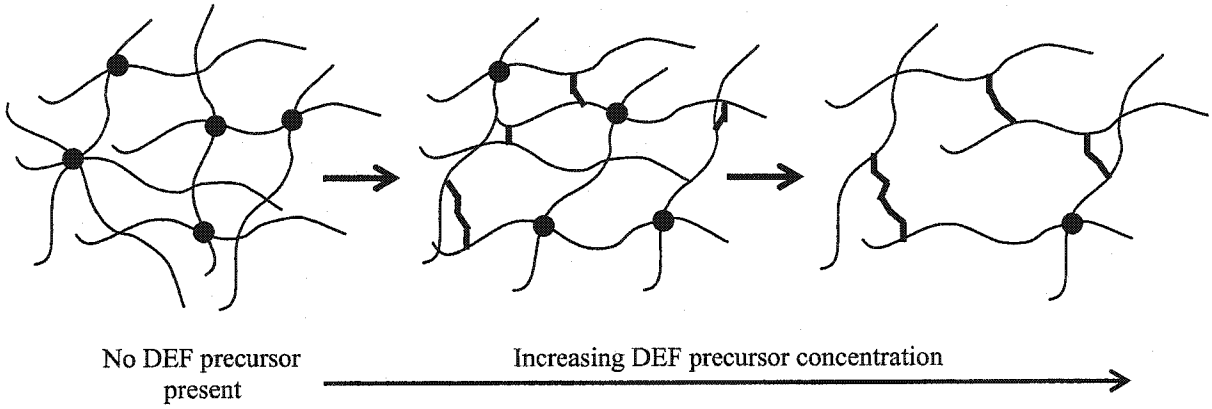

Figure 7.10 : A schematic describing how the addition of the DEF precursor to the PPF polymer may effect the structure of the formed crosslinked polymer network. (Left) Adjacent PPF polymer chains, depicted as lines, are crosslinked by covalent bonds, depicted as circles, between PPF fumarate units. (Middle) PPF polymer chains are crosslinked both by covalent bonds between their fumarate units and by bridges formed by the DEF precursor, depicted as linked bold line segments. (Right) PPF polymer chains are loosely linked both by covalent bonds between their fumarate units and DEF precursor bridges. The DEF precursor enhances crosslinking between PPF chains at low DEF concentrations, but hinders the crosslinking reaction at high DEF concentrations.

CHAPTER VIII

SOFT AND HARD TISSUE RESPONSE TO PHOTOCROSSLINKED POLY(PROPYLENE FUMARATE) SCAFFOLDS IN A RABBIT MODEL[†]

ABSTRACT

The treatment of large cranial defects may be greatly improved by the development of precisely formed bone tissue engineering scaffolds. Such scaffolds could be constructed by using ultraviolet laser stereolithography to photocrosslink a linear, biodegradable polymer into a three dimensional implant. We have previously presented a method to photocrosslink the biodegradable polyester, poly(propylene fumarate) [PPF]. In order to insure the safety and effectiveness of this technique, the soft and hard tissue response to photocrosslinked PPF scaffolds of different pore morphologies was investigated. Four classes of photocrosslinked PPF scaffolds, constructed with differing porosities (57% to 75%) and pore sizes (300 - 500 μm or 600 - 800 μm), were implanted both subcutaneously and in 6.3 mm diameter cranial defects in a rabbit model. The rabbits were sacrificed at 2 and 8 weeks and the implants were analyzed by light microscopy, histological scoring analysis, and histomorphometric analysis. Results showed the PPF scaffolds elicit a mild tissue response in both soft and hard tissues. Inflammatory cells, vascularization, and connective tissue were observed at 2 weeks; a

[†] This chapter was published as the following article: Fisher JP, Vehof JW, Dean D, van der Waerden JP, Holland TA, Mikos AG, Jansen JA. Soft and hard tissue response to photocrosslinked poly(propylene fumarate) scaffolds in a rabbit model. J Biomed Mater Res. 2002;59:547-556.181.

decrease in inflammatory cell density and a more organized connective tissue were observed at 8 weeks. Scaffold porosity and scaffold pore size were not found to significantly affect the observed tissue response. Evidence of scaffold surface degradation was noted both by histology and histomorphometric analysis. Bone ingrowth in PPF scaffolds implanted into cranial defects was less than 3% of the defect area. The results indicate that photocrosslinked PPF scaffolds are biocompatible in both soft and hard tissues and thus may be an attractive platform for bone tissue engineering.

INTRODUCTION

Critical size cranial defects may arise from surgery to correct infection, congenital abnormality, cancer, or trauma. The standard clinical treatment for these defects is the transplantation of an autologous bone graft (autograft). While an autograft is associated with no immune response, it does have the disadvantages of donor site morbidity and limited availability. Furthermore, it is possible that an autograft will not successfully vascularize in the new site, leading to its resorption and/or infection. Other treatments, such as metal or bone cement implantation, are also often used, but are associated with complications arising from their persistence. The inadequacies of the current treatments of bone defects have led us and others to investigate tissue engineering strategies.

A fundamental component of many tissue engineering strategies is a biodegradable, polymer scaffold that would act as a temporary site for cellular attachment and proliferation while slowly degrading away, eventually leaving a repaired tissue defect [77,78,95]. The development of a tissue engineered scaffold material begins with characterization of its chemical and physical properties followed by an investigation of its *in vitro* and *in vivo* mechanical strength, degradation rate, and degradation products.

Altering scaffold components and fabrication processes affects properties such as surface chemistry, degradability, and strength. Once these relationships are understood, the scaffold may be tailored to meet the needs of a given tissue. For example, scaffolds designed to function within a guided tissue regeneration strategy, where the scaffold promotes the ingrowth of tissue while providing mechanical support and stability, may be designed with local mechanical properties in mind [54,96-99]. Alternatively, scaffolds that are meant to act as carriers for growth factors or other inductive agents for bone growth may have optimized release properties [100-104]. Finally, scaffolds that are being considered as platforms for the implantation of either differentiated or progenitor cells may be altered so that their surface chemistry promotes cell attachment and proliferation [105,106]. More than likely, many of these properties must be considered in parallel during the development of a tissue engineering device.

Currently the typical biodegradable polymers that are studied for these tissue engineering applications include poly(lactic acid), poly(glycolic acid), poly(lactic-co-glycolic acid), and poly(ε - caprolactone) [78]. However, another polymer that has shown promise is poly(propylene fumarate) [PPF]. PPF is a linear polyester whose repeating unit, or mer, contains two ester groups and one unsaturated carbon - carbon double bond. Hydrolysis of the ester bonds allows PPF to degrade, and the degradation products of PPF have been shown to be primarily fumaric acid and propylene glycol [82]. Furthermore, the double bonds in PPF allow the linear polymer to be crosslinked into a solid, polymeric network. PPF, when crosslinked using a thermal initiator, has been shown to be a possible bone tissue engineering material for it is mechanically strong, biocompatible, and biodegradable [51,107]. As an alternative to thermal crosslinking,

PPF can also be crosslinked using the photoinitiator bis(2,4,6-trimethylbenzoyl) phenylphosphine oxide using relatively short and low intensity ultraviolet light exposure [60]. In the future, photocrosslinking of PPF may allow for the construction of precisely defined implants through the use of a direct or stereolithographic ultraviolet laser. A construct produced by the latter could be designed to possess a defined architecture, in terms of both external dimensions and internal porous structure, that may considerably improve its performance. Earlier investigations have characterized some of the physical properties of photocrosslinked PPF scaffolds [60]. This study sought to investigate the soft and hard tissue response to photocrosslinked PPF scaffolds and determine any effects of the scaffold pore morphology upon the tissue response.

MATERIALS AND METHODS

Poly(propylene fumarate) synthesis

Poly(propylene fumarate) was synthesized following a two step procedure. Briefly, one mole of diethyl fumarate (Acros Organics, Pittsburgh, PA, USA) and three moles of 1,2 propanediol (Acros Organics) were reacted using 0.01 moles $ZnCl_2$ (Fisher Chemicals, Pittsburgh, PA, USA) as a catalyst [60]. The reaction produced bis(hydroxypropyl) fumarate as the main product and ethanol as a byproduct. The bis(hydroxypropyl) fumarate was then transesterified, producing poly(propylene fumarate) and 1,2 propanediol as a byproduct. The PPF polymer was then purified. PPF dissolved in methylene chloride (Fisher Chemicals) was first washed with acid (5 wt% HCl in H_2O) to remove the catalyst and then purified with two washes each of both water and brine. The organic phase was dried with sodium sulfate and then the drying agent was removed by vacuum filtration. The organic solvent was removed from the PPF by

rotary evaporation followed by vacuum drying. The final purified product was a clear, light yellow, viscous liquid. PPF with a number average molecular weight (M_n) of 1700 Da and a polydispersity index (PI) of 1.6 (as determined by gel permeation chromatography) was synthesized for this study.

Preparation of PPF scaffolds

Poly(propylene fumarate) scaffolds were photocrosslinked using long wavelength ultraviolet light and the photoinitiator bis(2,4,6-trimethylbenzoyl) phenylphosphine oxide (BAPO, Ciba Specialty Chemicals, Tarrytown, NY) in the following manner. An initiator solution was first prepared by dissolving one gram of BAPO into 10 ml methylene chloride. The PPF was warmed in an oven at 60°C to soften the viscous polymer and then mixed with the initiator solution (0.05 ml/g PPF). A water soluble porogen, NaCl, was then added to the PPF mixture. Either 70 wt% of 300 - 500 μm NaCl, 80 wt% of 300 - 500 μm NaCl, 85% of 300 - 500 μm NaCl, or 80 wt% of 600 - 800 μm NaCl was added to the PPF mixture, thereby forming the four classes of PPF scaffolds studied in this work. The PPF/NaCl mixture was packed into a cylindrical polystyrene mold (6.3 mm diameter and 2.0 mm height) and then exposed to ultraviolet light for 30 min at a distance of approximately 15 cm. The UV light source was an Ultralum (Paramount, CA) ultraviolet light box outfitted with four 15W long wavelength UV bulbs. The total light emission covers a range of long UV wavelengths (320 - 405 nm), with a peak at 365 nm and an intensity of 4 mW/cm^2 at 15 cm. BAPO absorbs wavelengths below 400 nm, with a general increase in absorption as the wavelength decreases to 200 nm (Ciba Specialty Chemicals). Crosslinked samples were removed from the mold and then soaked in water for three days to remove the NaCl porogen.

These samples were dried, first with an absorbent cloth and then with 24 hours of vacuum drying. The samples were stored under nitrogen at 4°C until sterilization by ethylene oxide gas exposure (Anprolene Automatic Ventilated Sterilizer, Anderson Products, Chapel Hill, NC). 160 disc shaped scaffolds of each class were prepared. Each scaffold was approximately 6.3 mm in diameter and 2.0 mm in height. Scaffold porosity was assessed by mercury porosimetry [60]. The properties of the different scaffold classes are presented in Table 8.1.

Implant preparation

One day prior to implantation, the implants were removed from their sterile bags and prewetted with 70% ethanol in 2 ml vials under sterile conditions [108]. To remove air from the pores of the samples, a vacuum was pulled above the ethanol using a 50 ml syringe. After 20 min, the ethanol was removed and the samples were washed twice with sterilized, distilled, and de-ionized water. These samples were stored in distilled, de-ionized water under sterile conditions at 4°C until implantation.

Implantation study

Two to three month old, healthy, male New Zealand white rabbits with a weight between 2.0 and 2.9 kg were used for subcutaneous and cranial implantation study. The animals were housed separately in cages. Surgery was performed under general inhalation anesthesia. The anesthesia was induced by an intravenous injection of Hypnorm® (0.315 mg/ml fentanyl citrate and 10 mg/ml fluanisone) and atropine, while maintained by a mixture of nitrous oxide, isoflurane, and oxygen through a constant volume ventilator. To reduce the peri-operative infection risk, the rabbits received antibiotic prophylaxis (penicillin).

The animals were placed in a ventral position for the insertion of the implants. For the installation of the subcutaneous implants, the dorsum of the rabbit was first shaved, washed, and disinfected with povidone-iodine. Paravertebral, at both sides of the spinal column, four longitudinal incisions of about 1 cm were made through the full thickness of the skin. Subsequently, lateral to the incisions a subcutaneous pocket was created by blunt dissection and then the scaffolds were placed into these pockets. The skin was closed using a subcuticular Vicryl® suture.

For the cranial implants, the skull was first shaved, washed, and disinfected with povidone-iodine. A mid-sagital incision was made through the skin. The skin and subcutaneous tissue was separated from the periosteum using blunt dissection. A second longitudinal incision was made through the periosteum, which was then elevated and carefully dissected from the underlying skull bone before retraction. After exposure of the parietal calvarial bone, four full thickness skull defects were drilled (two on each side) using a 6.3 mm trephine (Merck®) drill at low rotational speed with continuous saline cooling. A cylindrical guide surrounding the trephine was used to avoid damage to the underlying dura. Each created defect received one of each of the four scaffold types. Finally, the periosteum was closed over the implant using Vicryl® sutures, and the skin was closed using a subcuticular Vicryl® suture.

A total of 160 scaffolds were implanted into 20 rabbits. All of the rabbits had one scaffold of each class (70Ps, 80Ps, 85Ps, and 80PI) implanted in both a subcutaneous pocket and a cranial defect, totaling 8 implants per rabbit. The placement of the scaffolds was varied in the following manner. The four implants in either the cranial or dorsal surgery fields were placed in a 2x2 grid, with the class of each implant noted. In each

subsequent rabbit, the positions of the scaffolds were moved one place clockwise. Thus scaffolds of each class were exposed to each of the four possible locations in both the cranial and dorsal surgery fields.

At 2 weeks after implantation, 10 rabbits were euthanized with an overdose of Nembutal® (pentobarbital). The remaining 10 rabbits were similarly euthanized 8 weeks after implantation. All implants with surrounding tissue were retrieved *en bloc*. Implants from 5 rabbits from the 2 week study and implants from 5 rabbits from the 8 week study were then randomly chosen, sectioned, and analyzed light microscopy. In this study, the Dutch and the U.S. National Institutes of Health guidelines for the care and use of laboratory animals were observed.

Light microscopy (histological scoring analysis and histomorphometric analysis)

Implants for histology were fixed in 4% phosphate buffered formaldehyde solution (pH = 7.4), dehydrated in a graded series of alcohol, and embedded in poly(methylmethacrylate). After hardening, 10 μm transverse sections were made using a modified microtome technique, with three sections obtained from each implant [109]. These sections were stained with basic fuchsin and methylene blue for evaluation by light microscopy (Leica®).

All histological sections were qualitatively analyzed using a modified histological scoring analysis (Table 8.2) [110]. The samples implanted subcutaneously were evaluated for the tissue response within the pores of the scaffold. The samples implanted into cranial defects were evaluated for the quality of the bone - implant interface as well as for the tissue response within the pores of the scaffold. Three histological sections were evaluated for each scaffold, with each section receiving a single score. The scores

of scaffolds of each class were then averaged to determine the overall score for the class; means and deviations for a class were reported.

Histomorphometric analysis was also performed on all sections to evaluate both the scaffold porosity and the quantity of newly formed bone. Three histological sections per implant were digitized at low magnification, allowing coverage of the entire PPF implant. Using a Leica® Qwin Pro image analysis system, the computer detected the areas of the PPF implant and bone. The outline of the implant area was designated as the region of interest (ROI). The image analysis program then measured the surface area of PPF (PSA), the ROI, and surface area of bone (BSA). On the basis of these data, the analysis program calculated scaffold porosity ([ROI - PSA]/ROI x 100%) and the percentage of pore area filled with bone (BSA/[ROI - PSA] x 100%).

Statistical Analysis

Sets of data were first inspected with an F-test for treatment effects [64]. The null hypothesis (the means of each set were equal) was evaluated with a 95% confidence level ($\alpha = 0.05$). If the null hypothesis was found to be false (i.e., the means of the sets were not equal), then a Tukey's multiple comparison test was performed [64]. Tukey's test then indicated, in a pairwise fashion, the relationship between sets.

RESULTS

Descriptive light microscopic evaluation

A gross light microscopical inspection of all histological sections was first performed. Figures 8.1 and 8.2 show that the PPF scaffolds could easily be recognized, appearing white with the surrounding tissue stained red and blue. Scaffold shape was

observed to be similar to its original shape at the time of implantation; only occasionally were deformations in scaffold shape noticed.

Overall, and independent of implantation period or scaffold porosity, the tissue response to the PPF material was relatively uniform. All subcutaneous implants were surrounded by a thin fibrous capsule, typically less than 5 cell layers in thickness (Figure 8.1). The capsule did not change in thickness or appearance at prolonged implantation times. Also, almost all 2 and 8 week cranial implants were surrounded by a fibrous capsule. After 8 weeks implantation, direct bone tissue-scaffold contact and ingrowth of bone inside the PPF porosity was seen in 8 of 20 scaffolds, though the amount of bone tissue ingrowth was limited (Figure 8.2).

Further, some inflammatory cells were observed inside the scaffold porosity of both subcutaneous and cranial implants (Figures 8.1 and 8.2). Inflammatory cell density ranged from diffuse to somewhat concentrated. However, no correlation between density and pore morphology, such as pore size, was observed. The inflammatory response was limited and decreased for the subcutaneous implants at 8 weeks compared with 2 weeks of implantation. Besides the presence of inflammatory cells, vascularization and connective tissue were seen in all samples. Only in some of the implants were foreign body giant cells noticed inside the porous PPF. These multinuclear cells could be associated with surface degradation of the PPF material (Figure 8.1).

Frequently, scaffolds of low porosity, notably the 70Ps class, revealed an accumulation of erythrocytes inside their pores (Figure 8.1). The amount of erythrocytes within the scaffold fell with increasing scaffold porosity and increasing implantation time.

Histological and histomorphometrical analysis

Figure 8.3A shows the data of the histological rating of interstitial characteristics of the subcutaneous implants. Statistical analysis of these data showed that no significant difference existed between the various scaffold classes ($p > 0.05$). On the other hand, a significant increase in score was noted from 2 to 8 weeks for all scaffold classes ($p < 0.05$). The increase in score reflects a reduction in inflammatory cell density, a reduction in the number of giant cells, and an increase in the vascularization of the invading tissue. Furthermore, connective tissue became more abundant and organized.

Figures 8.3B and 8.3C provide data on the evaluation of the cranial implants. Histologic rating revealed that the interstitial tissue response of the cranial implants was similar to the subcutaneous implants (Figure 8.3B). The interstitial response was similar for all materials and no increase in tissue response was observed between 2 and 8 weeks of implantation. In contrast to the subcutaneous implants, many cranial implants studied contained adipose cells within the PPF porosity. The bone-implant interface was characterized by fibrous tissue not arranged as a capsule after 2 weeks of implantation (Figure 8.3C). No significant difference existed in interface appearance between the various PPF classes. At 8 weeks of implantation, the score generally increased for all scaffold classes, but this trend was not significant ($p > 0.05$). This slight increase was mainly attributable to the presence of direct bone-implant contact (a score of 4) in 8 of 20 scaffolds.

Figures 8.4 and 8.5 show the quantification of scaffold porosity and bone area (performed by histomorphometrical analysis) within all PPF materials at both 2 and 8 weeks. The absolute values of scaffold porosity were lower than expected, ranging from

36% to 56% porous. Nevertheless, a trend of increasing scaffold porosity with increased implantation time was noted for all classes of scaffolds studied. This trend was found to be significant ($p < 0.05$) in the cases of the 85Ps scaffolds implanted subcutaneously as well as the 80Pl scaffolds implanted cranially. The percent bone growth into the defect area was low for all scaffolds studied, generally less than 3% of the defect area.

DISCUSSION

A rabbit model was used to investigate the soft and hard tissue response to photocrosslinked poly(propylene fumarate) scaffolds. Photocrosslinked PPF is a novel material that is being explored for tissue engineering applications and may be useful for the treatment of extensive loss of bone, especially in the craniofacial regions. The rabbit cranial defect was selected as the orthotopic model for this work, as it has been used widely for assessing the performance of both materials and growth factors in bone sites [101,111-116]. Previous investigations have shown a rabbit cranial defect of approximately 15 mm or greater to be of a critical size, such that it will not heal during the lifetime of the animal [117]. We chose to utilize four non-critical size, 6.3 mm diameter defects per animal in this study as they would (1) minimize experimental variation between animals, (2) reduce the number of animals needed in the study, and (3) allow a greater number of sample types to be investigated. Furthermore, the 6.3 mm diameter defects would allow the superior sagittal sinus to remain undisturbed as the four cranial defects were created bilaterally.

The soft tissue response to the scaffolds indicated that photocrosslinked PPF is a promising material for tissue engineering applications. The minimal cellular encapsulation of the PPF scaffolds implies that this material is acceptable to the host.

Vascularization, collagen matrix production, and limited amounts of foreign body giant cells were noted in the histological sections studied; the collagen matrix became more organized and foreign body giant cell density decreased with increasing implantation time. Furthermore, the histomorphometric analysis indicated a trend of increasing porosity with time, which in turn suggests the surface degradation of the PPF scaffold. Histological evidence of PPF scaffold degradation was also observed. Though the hydrolytic degradation of PPF's ester backbone is expected, the mild tissue response associated with the degrading scaffold implies that the degradation products of the photocrosslinked polymer network are themselves acceptable to the host. While previous chemical studies have shown the degradation products of PPF as primarily propylene glycol and fumaric acid [82], the *in vivo* results presented here support the characterization that these products should elicit a mild local tissue response.

The hard tissue response to photocrosslinked PPF scaffolds was similar to that found in soft tissue. In terms of bone formation, the histological evaluation as well as the histomorphometric analysis found low amounts of bone growth into the pores of the PPF scaffolds. Evidence of direct bone tissue - implant contact, however, was noted in 8 of 20 scaffolds. The results indicate that photocrosslinked PPF is bone biocompatible and, furthermore, may be an attractive polymer scaffold carrier for osteoinductive agents to promote bone regeneration in a critical size defect.

The accumulation of erythrocytes within the pores of the PPF scaffolds was an unexpected result, although the filling of the scaffolds with blood during their implantation was noted and the prewetting of the scaffolds may have facilitated the adsorption of blood cells. The effect of these accumulations, which resembled a blood

clot, upon the tissue response is unclear. It has been suggested by some that blood clots may promote bone formation in a defect and, furthermore, that the ability of a material to retain a blood clot may be critical for proper bone regeneration within a tissue engineering strategy [118,119]. Following this line of thought, Dean et al. included heparinized marrow in chemically crosslinked PPF scaffolds as well as PLGA scaffolds. Good bone ingrowth was observed in the PLGA, but no erythrocyte accumulation was observed in either sample [120]. Whang et al., in their study of poly(D,L-lactic-co-glycolic acid) scaffolds, suggested that the stabilization of hematomas by scaffolds of small pore size would significantly enhance bone regeneration through the action of the many growth factors contained within the blood and marrow [121]. Since the results presented here showed that low scaffold porosity promoted the persistence of blood clots but that these scaffolds did not possess significantly greater amount of bone ingrowth, evidence for this effect was not observed.

Beyond their effect upon erythrocyte persistence, scaffold porosity and pore size appear to have little effect upon both tissue response and bone regeneration for the samples studied in this work, namely a porosity approximately between 57% and 75% (as measured by mercury porosimetry) and a pore size of 300 - 500 μm or 600 - 800 μm. There has been a number of investigations which sought to identify the proper pore size for a tissue engineering scaffold, with results showing that pores ranging from 80 to 500 μm to be viable [122]. Previous work in rabbit cranial defects has indicated that bone ingrowth may increase over time with increasing pore size, and that pore size less than or equal to 350 μm produced the most bone ingrowth [123]. The length of that study was

considerably longer (up to 6 months), so the effect of pore size may not have been realized in the work presented here.

The values of scaffold porosity after implantation, as measured by image analysis, were lower than the porosity values measured by mercury porosimetry on scaffolds which were not implanted. For example, image analysis found scaffolds synthesized with 70 wt% to 85 wt% NaCl porogen to be 40% to 53% porous after 8 weeks of cranial implantation, whereas mercury porosimetry found similar (but not implanted) scaffolds to be 57% to 75% porous. The difference between these values is likely due to the noted scaffold deformation during implantation and scaffold morphology changes associated with poly(methylmethacrylate) embedding.

There is an abundant availability of similar studies of the biocompatibility of materials proposed for bone tissue engineering applications. The tissue response to photocrosslinked PPF scaffolds is representative of that seen in other materials, such as poly(lactic-co-glycolic acid), poly(anhydride-co-imides), poly(othro esters), and poly(ethyleneglycol terephthalate)/poly(butylene terephthalate) [96-99]. Differentiating characteristics may include the minimal fibrous encapsulation observed with photocrosslinked PPF as well as its slower degradation rate.

CONCLUSIONS

This study sought to characterize the hard and soft tissue response to photocrosslinked poly(propylene fumarate) scaffolds of differing pore morphologies. The results indicate that PPF is biocompatible within both soft and hard tissue. Minimal fibrous encapsulation of the scaffolds was found and tissue response appeared to improve with implantation time. A progressive reduction in inflammatory cell density and a

continued organization of connective tissue with the interstitial space was observed. However, tissue response was not found to vary significantly with scaffold pore size or porosity. Evidence for PPF degradation during 8 weeks of implantation was noted both histologically and histomorphometrically. The results indicate that biodegradable, photocrosslinked PPF scaffolds may be a suitable material for bone tissue engineering applications.

Table 8.1: The four classes of PPF scaffolds which were investigated in this *in vivo* study. The classes of scaffolds differ in their initial PPF and NaCl content as well as their porogen size. The porosity of each scaffold class was measured by mercury porosimetry using scaffolds which were not implanted.

Scaffold Class	Wt% NaCl	Wt% PPF	NaCl size (μm)	Porosity
70Ps	70	30	300 - 500	56.7% ± 0.8%
80Ps	80	20	300 - 500	65.8% ± 6.6%
85Ps	85	15	300 - 500	75.3% ± 3.4%
80Pl	80	20	600 - 800	60.1% ± 5.1%

Table 8.2: Histological grading scale for soft and hard tissue implants. For both the soft and hard tissue implants, the interstitial space was classified by the overall appearance of the tissue within the pores of the implant. The bone - implant interface was studied by investigating the tissue directly in contact with the perimeter as well as pores of the implant. While interface classes 0, 1, and 2 describe the entire interface quality, any significant evidence (greater than 3 identifiable instances) of the characteristics of classes 3 and 4 would warrant their assignment.

Soft Tissue Response to PPF Scaffolds / Scaffold Interstitial Space	
Fibrous, mature, not dense, resembling connective or at tissue in the non-injured regions	4
Shows blood vessels and young fibroblasts invading the spaces, few macrophages may be present	3
Shows giant cells and other inflammatory cells in abundance, but connective tissue components between	2
Dense and exclusively of inflammatory type	1
Cannot be evaluated because of infection or other factors not necessarily related to the material	0
Hard Tissue Response to PPF Scaffolds / Bone - Scaffold Interface	
Direct Bone and Implant Contact - No Soft Tissue Layer Present	4
Remodeling Lacuna with Osteoblast and/or Osteoclast	3
Localized Fibrous Tissue not Arranged as a Capsule	2
Fibrous Tissue Capsule	1
Inflammation	0
Hard Tissue Response to PPF Scaffolds / Scaffold Interstitial Space	
Mature Bone and Differentiation of Bone Marrow	4
Bone Formation	3
Fibrous Connective Tissue - Collagen Fibers at Interface	2
Fibrous Connective Tissue - Cellular and Vascular Components	1
Implant Cannot be Evaluated	0

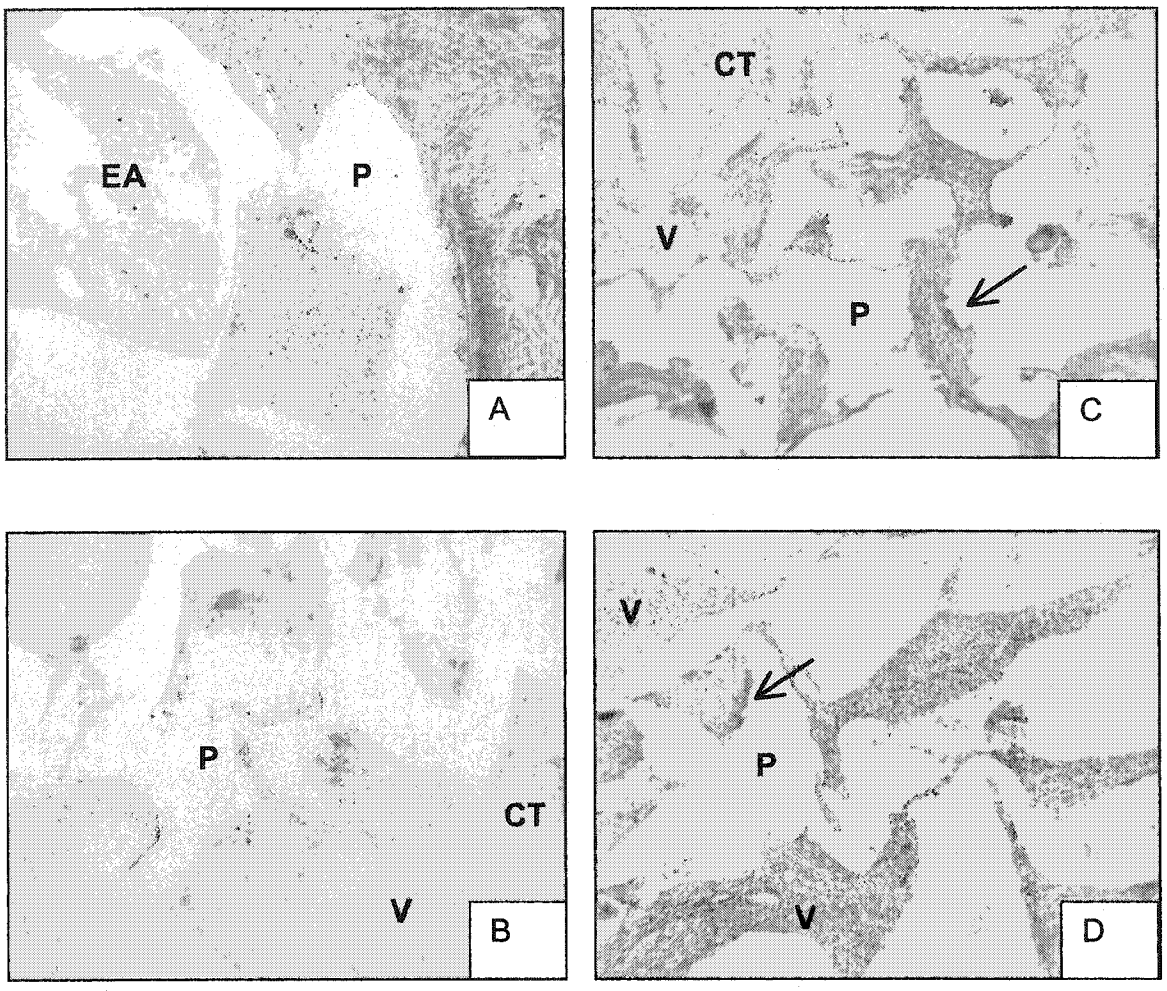

Figure 8.1: Histological sections of PPF scaffolds implanted subcutaneously. Scaffold classes 70Ps (A), 80Ps (B), 85Ps (C), and 80Pl (D) after 8 weeks of implantation are presented in 9x magnification. The PPF scaffold (P) appears in all images as white areas. Evidence of erythrocyte accumulation (EA) is clearly visible in the 70Ps class of scaffolds. Vascularization (V) and connective tissue (CT) can be observed in scaffold classes 80Ps, 85Ps, and 80Pl. Arrows indicate possible histological observations of PPF degradation by multinuclear cells. In these four examples, the 80Ps and 85Ps classes exhibit a diffuse cell density while a more dense cell population is observed in the 80Pl class.

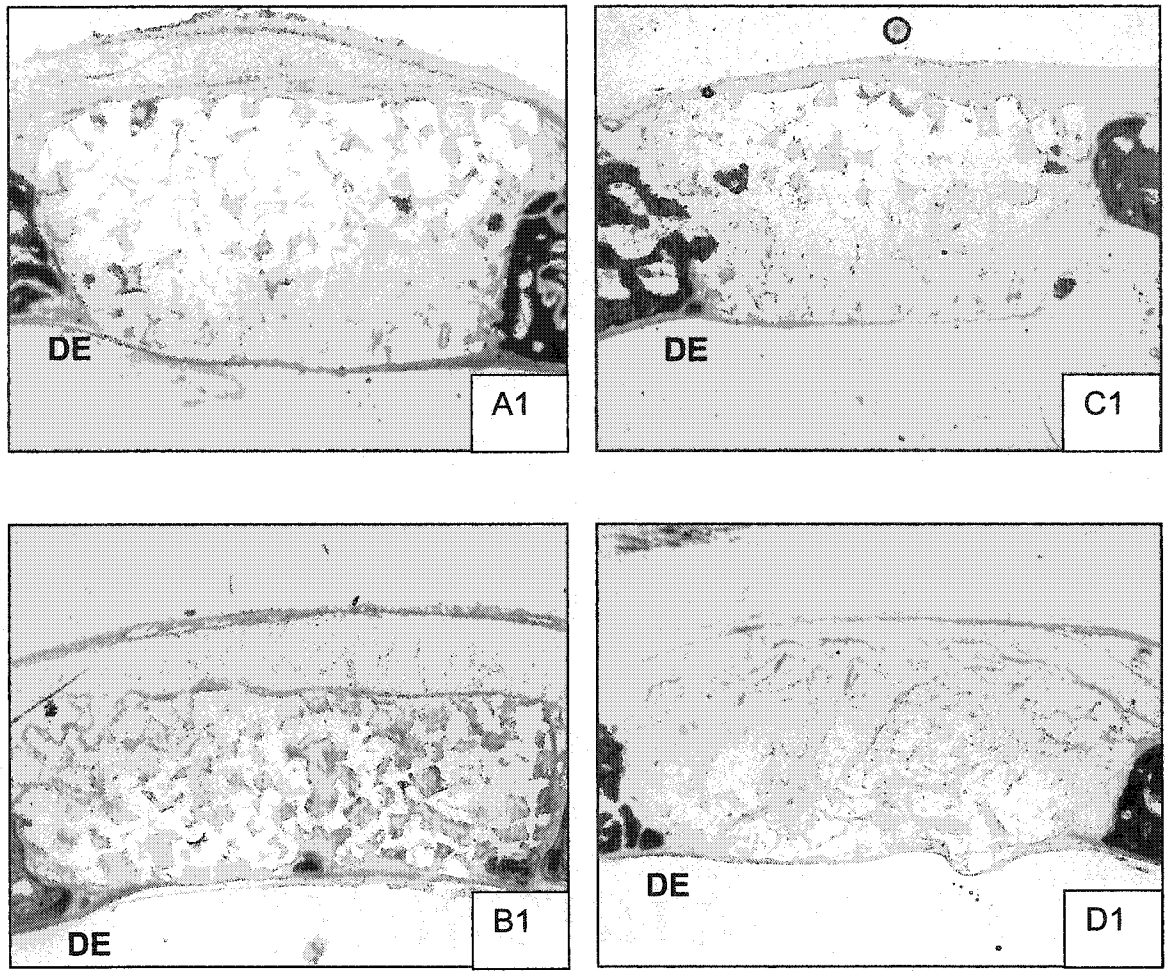

Figure 8.2: Histological sections of PPF scaffolds implanted in cranial defects. Scaffold classes 70Ps (A1), 80Ps (B1), 85Ps (C1), and 80Pl (D1) after 8 weeks of implantation are presented in low (1.4x) magnification. The PPF scaffold (P) appears in all images as white areas and the original defect edge (DE) can be seen in the low magnification images (1). Bone-like tissue (BT) appears in red and direct bone - implant contact (BIC) can be observed in the 85Ps scaffold class. Vasculature (V), connective tissue (CT), adipose cells (AC), and inflammatory cells (IC) are indicated.

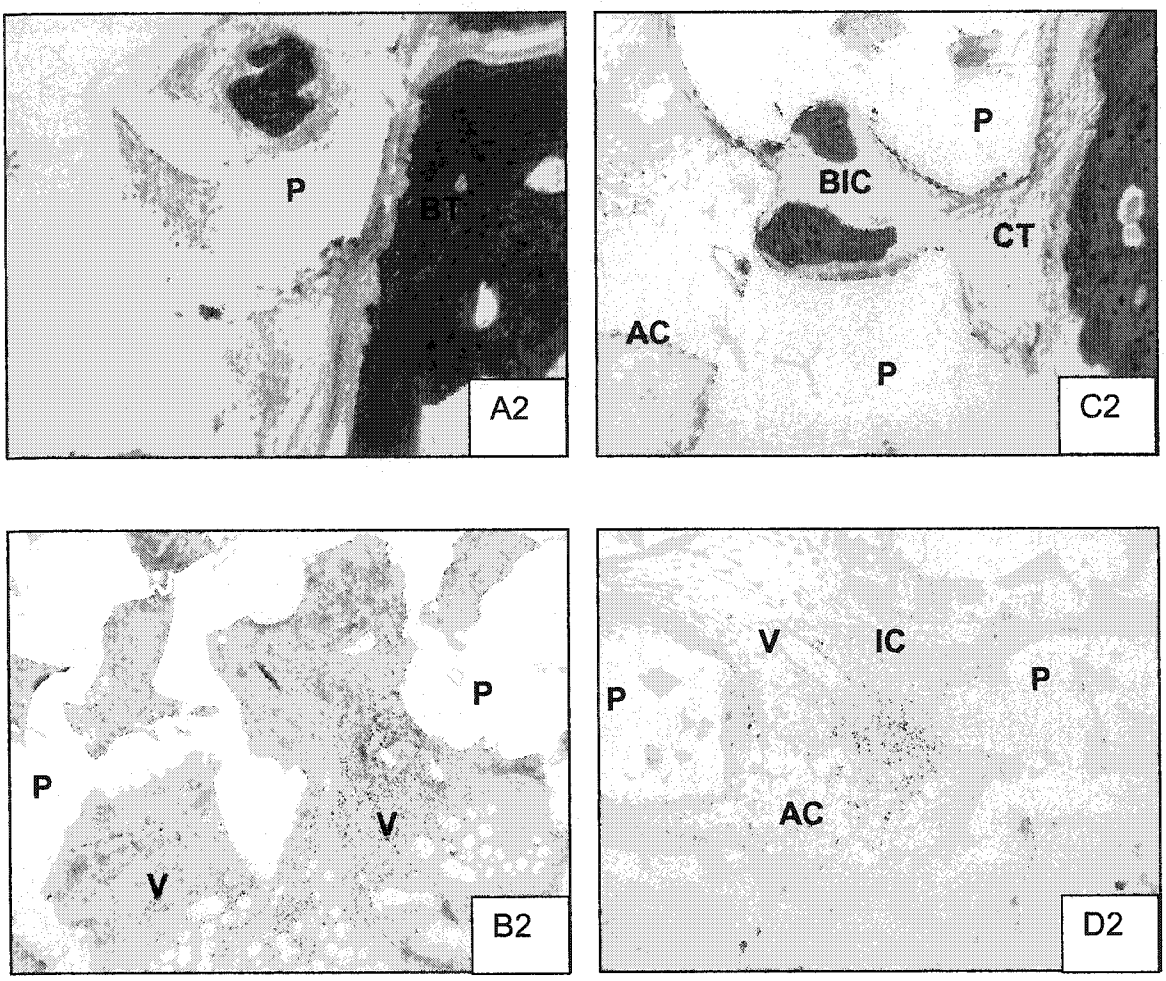

Figure 8.2 (cont.) : Histological sections of PPF scaffolds implanted in cranial defects. Scaffold classes 70Ps (A2), 80Ps (B2), 85Ps (C2), and 80Pl (D2) after 8 weeks of implantation are presented in high (9x) magnification. The PPF scaffold (P) appears in all images as white areas and the original defect edge (DE) can be seen in the low magnification images (1). Bone-like tissue (BT) appears in red and direct bone - implant contact (BIC) can be observed in the 85Ps scaffold class. Vasculature (V), connective tissue (CT), adipose cells (AC), and inflammatory cells (IC) are indicated.

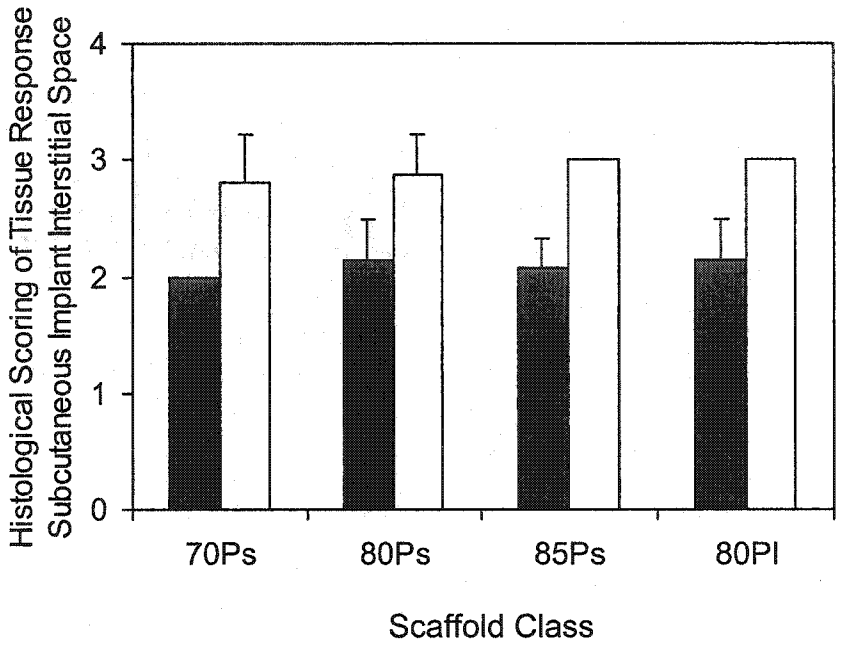

(A)

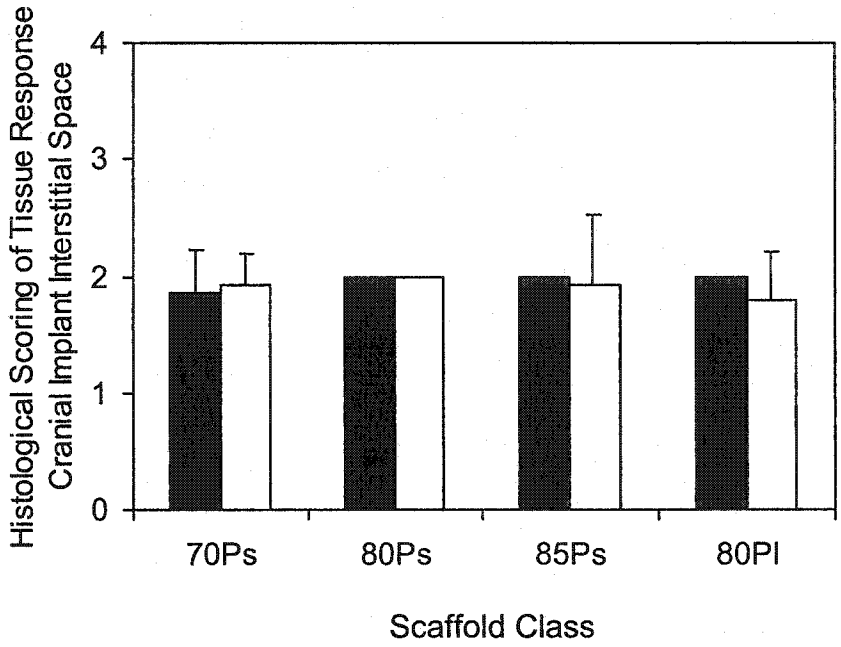

(B)

Figure 8.3: Histological scoring results for the soft **(A)** and hard **(B/C)** tissue response to PPF scaffolds at 2 weeks (■) and 8 weeks (□). At 2 weeks the tissue in the interstitial space for all implants was generally composed of inflammatory cells, with instances of connective tissue, notably collagen, as well as blood vessels. At 8 weeks the interstitial space became more organized with connective tissue and elongated inflammatory cells whose numbers and density were lower than that observed at 2 weeks.

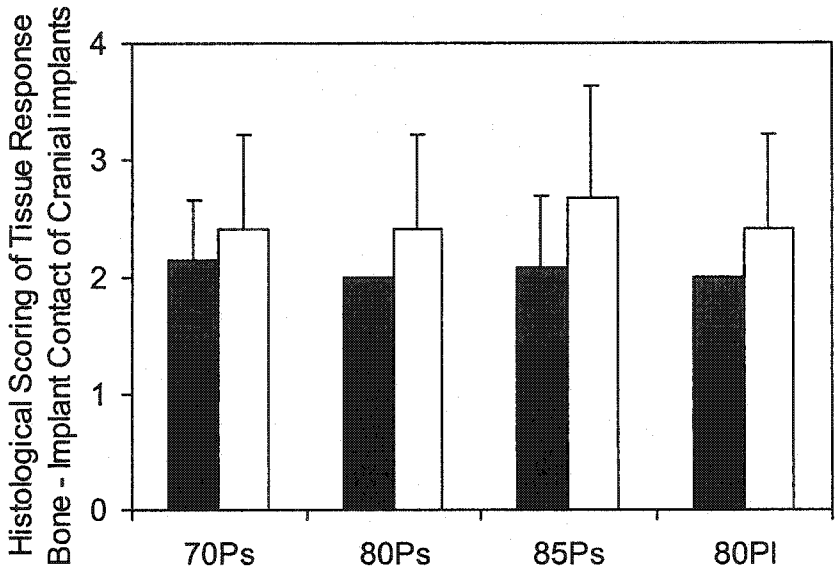

(C)

Figure 8.3: Histological scoring results for the soft **(A)** and hard **(B/C)** tissue response to PPF scaffolds at 2 weeks (■) and 8 weeks (□). The interface between the implant and the cranial defect at 2 weeks was characterized by localized fibrous tissue regardless of implant porosity, while at 8 weeks evidence of direct bone - implant contact was noted in approximately a quarter of the sections.

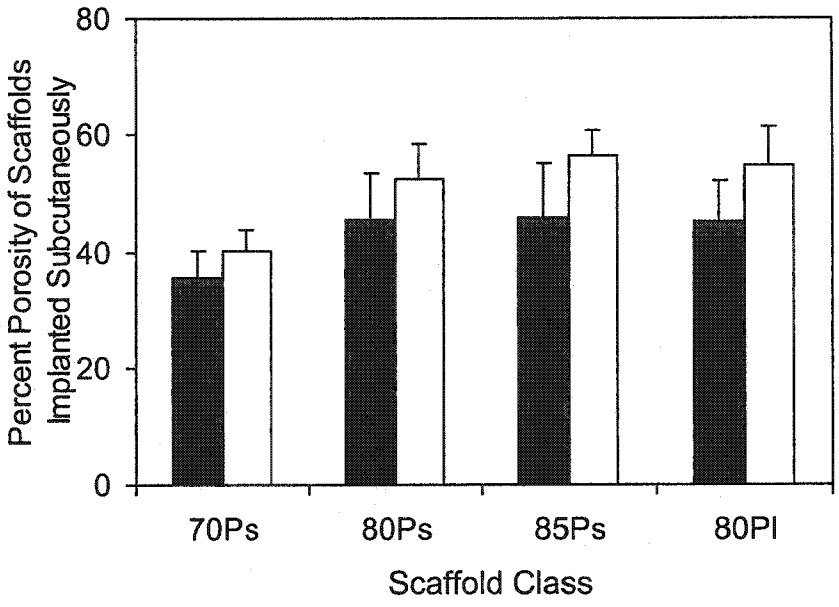

(A)

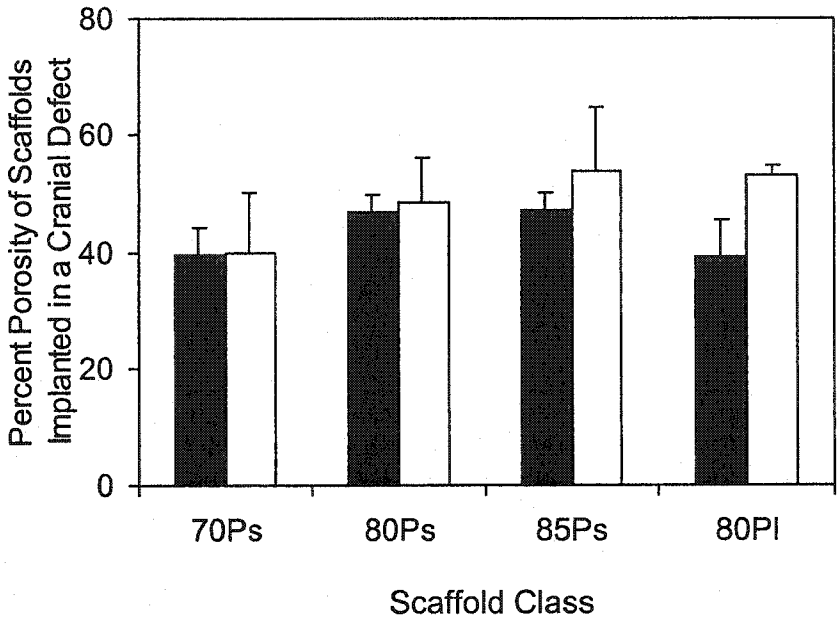

(B)

Figure 8.4: (A) The porosity at 2 weeks (■) and 8 weeks (□) of PPF scaffolds implanted subcutaneously. Porosity, as determined by image analysis, was calculated as the ratio of porous area to total implant area. A general trend of increasing porosity from 2 to 8 weeks was observed for all implants, with a statistically significant increase in implant class 85Ps. **(B)** The porosity at 2 weeks (■) and 8 weeks (□) of PPF scaffolds implanted in cranial defects. Again, a general trend of increasing porosity with time was observed for all implants, with a statistically significant increase in scaffold class 80Pl. For both implantation sites **(A and B)**, the increasing porosity with implantation time indicates the degradation of the PPF scaffolds during the *in vivo* study.

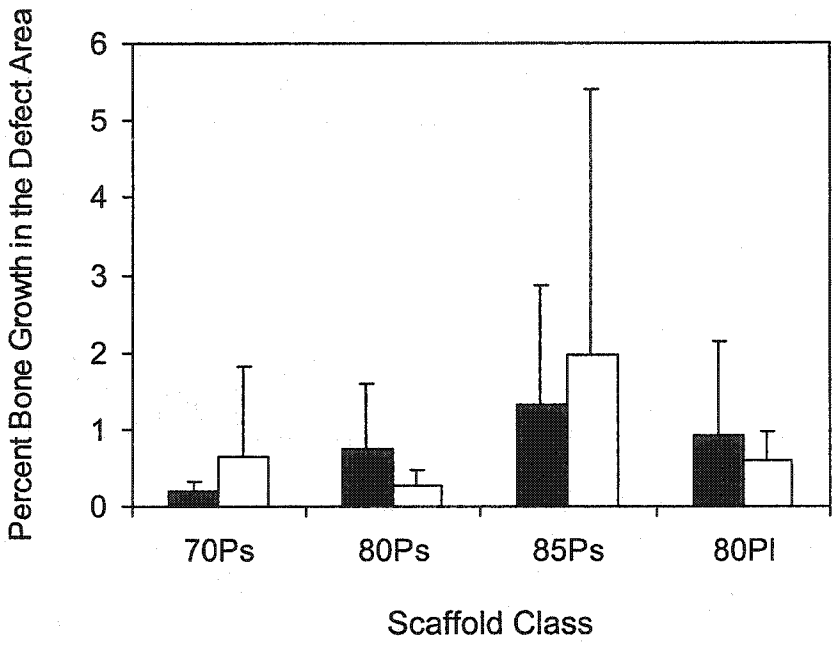

Figure 8.5: The amount of bone growth into the pores of PPF scaffolds at 2 weeks (■) and 8 weeks (□) relative to defect area. Bone ingrowth was determined by an image analysis program that determines the area of bone within the perimeter of the implant area. The results show low amounts of bone ingrowth, from less than 1% to over 2% of total defect area.

CHAPTER IX

BONE FORMATION IN TRANSFORMING GROWTH FACTOR-β1-COATED POROUS POLY(PROPYLENE FUMARATE) SCAFFOLDS[†]

ABSTRACT

This study determined the bone growth into pretreated poly(propylene fumarate) (PPF) scaffolds implanted into a sub-critical size, rabbit cranial defect. PPF scaffolds were constructed using a photocrosslinking/porogen leaching technique. These scaffolds were then either prewetted (PPF-Pw), treated with RF glow-discharge (PPF-Gd), coated with fibronectin (PPF-Fn), or coated with rhTGF-β1 (PPF-TGF-β1). One of each scaffold type was then placed into the cranium of 9 rabbits. The rabbits were sacrificed after 8 weeks, and the scaffolds were retrieved for histological analysis. The most bone formation was present in the PPF-TGF-β1 implants; the newly formed bone had a trabecular appearance together with bone marrow-like tissue. Little or no bone formation was observed in implants without rhTGF-β1. These histological findings were confirmed by image analysis. Bone surface area, bone area percentage, pore fill percentage and pore area percentage were significantly higher in the rhTGF-β1-coated implants than in the non-coated implants. No statistical difference was seen between the PPF-Fn, PPF-Pw or PPF-Gd scaffolds for these parameters. Quadruple fluorochrome labelling showed that in PPF-TGF-β1 implants bone formation mainly started in the interior of a pore and proceeded towards the scaffold. We conclude that: (1) PPF-TGF-β1scaffolds can indeed

[†] This chapter was published as the following article: Vehof JW, Fisher JP, Dean D, van der Waerden JP, Spauwen PH, Mikos AG, Jansen JA. Bone formation in transforming growth factor beta-1-coated porous poly(propylene fumarate) scaffolds. J Biomed Mater Res. 2002;60:241-251.

adequately induce bone formation in porous PPF, and (2) PPF scaffolds prepared by the photocrosslinking/ porogen leaching technique are good candidates for the creation of bone graft substitutes.

INTRODUCTION

Osteoinductive factors, like Bone Morphogentic Proteins (BMPs) or Transforming Growth Factor-βs (TGF-βs) have been used to improve the healing of bone defects. For example, BMP-2 and BMP-7 are known to induce bone formation in heterotopic as well as orthotopic sites. TGF-β1 and TGF-β2 have been shown to stimulate osteogenesis in orthotopic sites [101,124-126]. However, a prerequisite for the use of osteoinductive growth factors to regenerate bone tissue is a suitable scaffold. Scaffold materials currently under investigation are polymers or co-polymers, mainly poly(α-hydroxy acid), ceramic materials (e.g. hydroxyapatite and tricalcium phosphate), collagen, and titanium.

A recently developed scaffold material is the polyester poly(propylene fumarate) (PPF). This material has been shown to be biodegradable [51-53]. The degradation products are the non-toxic molecules fumaric acid and propylene glycol as well as excretable molecules related to the crosslinking of the polymer [82]. Another advantage of this viscous polymer is that it can be crosslinked into a solid with relatively low levels of heat release [127]. This allows PPF to be injected into a defect or fabricated into a scaffold prior to implantation [54]. In previous research, a chemical crosslinking method has been used. This crosslinking method uses the monomer N-vinyl pyrrolidone (NVP), the radical initiator benzoyl peroxide (BP), and the accelerator N,N dimethyl-p-toluidine (DMT) [127,128]. A drawback of this method is that NVP and DMT may be potentially

toxic. A photoinitiated crosslinking method has also been developed. In this method, only the photoinitiator bis(2,4,6-trimethylbenzoyl) phenylphosphine oxide (BAPO) and long wavelength ultraviolet (UV) light are used to crosslink the viscous polymer into a solid. This method eliminates the potential toxicity associated with the use of a crosslinking monomer and accelerator as well as proceeds with low levels of heat release [58,60].

Porous PPF scaffolds are prepared by photocrosslinking the PPF polymer around a water soluble porogen (NaCl). Afterwards, the composites are placed in water, allowing the soluble NaCl to dissolve and revealing a porous scaffold. Photocrosslinked PPF scaffolds have been shown to generally possess an interconnected pore structure when NaCl porogen content weight exceeds 80wt % at synthesis. Scanning electron microscopy has shown that pore morphology mostly is related to the porogen shape and content, not the photoinitiated crosslinking process [60].

Besides growth factors, another approach to improve the tissue response to biomaterials involves the use of organic coatings of proteins (e.g. collagen, laminin, fibronectin), glycoproteins, and peptides (e.g. RGD peptides) [129-131]. These organic coatings are known for their beneficial effect on cell attachment but have also been applied to modify the *in vivo* biological response [132].

Furthermore, we have to notice that PPF is a hydrophobic materials. Therefore, it is difficult to coat PPF scaffolds with osteoinductive factors and/or proteins in a controlled manner. Currently, prewetting is the standard treatment of polymeric scaffolds before their *in vitro* or *in vivo* use [108]. Physico-chemical techniques, like RF glow-discharge treatment, are also frequently used to enhance biomaterial absorption of

moisture. Therefore, RF glow discharge appears to be an appropriate technique to improve the coating process of PPF scaffolds.

The objectives of the study reported here were to investigate (a) whether PPF coated with rhTGF-β1 can induce bone formation in an orthotopic site and (b) the effect of a fibronectin coating on the bone response to porous PPF.

MATERIALS AND METHODS

Preparation of porous poly(propylene fumarate) scaffolds

PPF with a number average molecular weight (M_n) of 1700 Da and a polydispersity index (PI) of 1.6 (as determined by gel permeation chromatography) was synthesized for this study [60]. Poly(propylene fumarate) scaffolds were photocrosslinked using long wavelength ultraviolet light and the photoinitiator bis(2,4,6-trimethylbensoyl) phenylphosphine oxide (BAPO, Ciba Specialty Chemicals, Tarrytown, NY) in the following manner. One gram of BAPO was dissolved in 10 ml methylene chloride to form the initiator solution. The PPF was first warmed in an oven at 60°C to soften the viscous polymer and then mixed with the initiator solution (0.05 ml/g PPF). The leachable porogen, 80 wt% of 300 - 500 μm NaCl crystals, was subsequently added to the PPF/BAPO mixture, forming a stiff paste. This paste was packed into a cylindrical polystyrene mold (6.3 mm diameter and 2.0 mm height). The samples were then exposed to ultraviolet light for 30 min at a distance of approximately 15 cm. The UV light source was an Ultralum (Paramount, CA) ultraviolet light box outfitted with four 15W long wavelength UV bulbs. The total light emission covers a range of long UV wavelengths (320 - 405 nm), with a peak at 365 nm and an intensity of 4 mW/cm^2 at 15 cm. BAPO

absorbs wavelengths below 400 nm, with a general increase in absorption as the wavelength decreases to 200 nm (Ciba Specialty Chemicals).

Crosslinked samples were removed from the mold and then soaked in water for three days to remove the NaCl porogen. These samples were dried, first with an absorbent cloth and then with 24 hours of vacuum drying. The samples were stored under nitrogen at 4°C until sterilization by ethylene oxide gas exposure (Anprolene Automatic Ventilated Sterilizer, Anderson Products, Chapel Hill, NC). A total of 37 disc shaped implants were prepared, each approximately 6.3 mm in diameter, 2.0 mm in height, 20 mg in weight, and approximately 70% porous with a pore size of 300 - 500 μm [60].

Implant preparation

A day before implantation, nine implants were removed from their sterile bags and prewetted with 70% ethanol in 2 ml vials under sterile conditions [108]. To remove air from the pores of the samples, a vacuum was pulled above the ethanol using a 50 ml syringe. After 20 min, the ethanol was removed and the samples were washed twice with sterilized distilled, deionized water. These samples were stored in distilled, deionized water and under sterile conditions at 4°C until implantation.

An additional twenty eight PPF scaffolds were removed from their sterile bags and treated for 5 minutes with radio frequency glow discharge (Gd) (Harrick PDC-3XG, Argon, 0.15 Torr) to enhance wettability. Nine of these samples, undergoing no further treatment, were stored in vials under sterile conditions at 4°C until implantation.

Ten of these glow-discharged porous PPF implants were coated with human transforming growth factor beta, rhTGF-β1 (R&D Systems Inc. Minneapolis, Minn.,

USA), which was produced by Chinese hamster ovary (CHO) cells. The rhTGF-β1 was dissolved in sterile 4 mM HCl containing 1 mg/ml bovine serum albumin (BSA). A dose of 30 µl of the HCl solution, containing 2 µg of rhTGF-β1, was applied to each of the 10 PPF implants. The constructs were subsequently lyophilized and then stored under sterile conditions at 4°C until implantation.

Finally, the last nine glow discharged porous PPF scaffolds were coated with human plasma fibronectin. Lyophilized human plasma fibronectin (Sigma Aldrich Chemie b.v., Zwijndrecht, the Netherlands) was dissolved in PBS at a concentration of 100 µg/ml. A dose of 40 µl of the PBS solution, containing 4 µg of fibronectin (concentration is 100 µgr/ml), was added to each PPF implant. The constructs were subsequently lyophilized and then stored under sterile conditions at 4°C until implantation.

The doses of TGF-β1 and fibronection were selected on basis of previously performed studies [126,129].

In vitro rhTGF-β1 release

The *in vitro* release of rhTGF-β1 from a coated PPF scaffold was measured with a commercially available enzyme-linked, immunosorbent assay (ELISA) kit (Promega® Benelux b.v., Leiden, the Netherlands). One of the rhTGF-β1 coated implants was placed in a 24-well-plate with 2 ml of minimal essential medium (α-MEM, Gibco BRL, Life Technologies b.v., Breda, the Netherlands) containing 10% FCS and gentamycin. The 24-well-plate was placed in an incubator (humidified atmosphere of 95% air and 5% CO_2 at 37°C). Two 50 µl samples were extracted at 15 min, 30 min, 1 h, 2 h, 4 h, 24 h, and 1 week. Subsequent to each of these extractions, 100 µl α-MEM solution was added to

replace the lost volume. Samples were kept at 4°C until the time of measurement. The duplicate samples were prepared and diluted. The ELISA test was then performed according to the Promega® protocol. The absorption was read using a microplate reader set at a wavelength of 450 nm. All measurements were corrected for the dilution that had occurred during sampling.

Experimental animal study

For implantation, nine healthy, skeletally mature, male New Zealand white rabbits with a weight between 2.0 and 2.9 kg were used. The animals were housed separately in cages. Surgery was performed under general inhalation anesthesia. The anesthesia was induced by an intravenous injection of Hypnorm® (0.315 mg/ml fentanyl citrate and 10 mg/ml fluanisone) and atropine, while maintained by a mixture of nitrous oxide, isoflurane, and oxygen through a constant volume ventilator. To reduce the peri-operative infection risk, the rabbits received antibiotic prophylaxis (penicillin).

The animals were placed in a ventral position for the insertion of the implants. The dorsum of the skull was shaved, washed, and disinfected with povidone-iodine. A mid-sagital incision was made through the skin. The skin and subcutaneous tissue were separated from the periosteum using blunt dissection. A second longitudinal incision was made through the periosteum, which was then elevated and carefully dissected from the underlying skull bone (Figure 9.1A) before retraction. After exposure of the parietal calvarial bone, four full thickness skull defects were drilled (two on each side) using a 6.3 mm trephine (Merck®) drill at low rotational speed with continuous saline cooling (Figure 9.1B). A cylindrical guide surrounding the trephine was used to avoid damage to the underlying dura. Subsequently, one of each of the four scaffold types was inserted

(Figure 9.1C), the periosteum was closed over the implant using 3-0 Vicryl® sutures, and the skin was closed using a subcuticular Vicryl® suture.

A total of 36 scaffolds were implanted: 9 prewetted PPF scaffolds (PPF-Pw), 9 glow discharge only treated PPF scaffolds (PPF-Gd), 9 glow discharge treated PPF scaffolds coated with rhTGF-β1 (PPF-TGF-β1), and 9 glow discharge treated PPF scaffolds coated with fibronectin (PPF-Fn). The PPF-Pw scaffolds were used as a general control since in our group pre-wetting is the standard treatment of PPF scaffolds before experimental use [108]. The PPF-Gd scaffolds were used as a control for the TGF-β1 coated specimens. All rabbits received one implant of each scaffold type. A statistical randomization scheme was used to locate the scaffolds so that the cranial anatomy would not affect the outcome.

Additionally, six rabbits received quadruple fluorochrome labeling. The fluorochrome labels tetracycline (yellow), alizarin-complexone (red), calcein (green), and tetracycline (yellow) were subcutaneously administered at 1, 3, 5, and 7 weeks postoperatively, respectively. The treatment dose was 25 mg/kg body weight for all labels.

At 8 weeks postimplantation, euthanasia was performed with an overdose of Nembutal® (pentobarbital). The implants with surrounding cranial tissue were retrieved *en bloc* and prepared for light microscopy. In this study, the Dutch and the U.S. National Institutes of Health guidelines for the care and use of laboratory animals were observed.

Light microscopy (subjective and histomorphometry)

Implants for histology were fixed in 4% phosphate buffered formaldehyde solution (pH = 7.4), dehydrated in a graded series of alcohol, and embedded in

methylmethacrylate. After polymerization, 10 μm transverse sections were made using a modified microtome technique [109]. These sections were stained with basic fuchsin and methylene blue for evaluation by light microscopy (Leica®).

In appropriate implants, two additional sections of 30 μm were made for fluorochrome labeling analysis. These sections were left unstained and examined with a fluorescence microscope (Leica®) equipped with an excitation filter of 470 - 490 nm.

With the help of light- and fluorescence microscopy, the tissue response to the different implants was fully described. In addition, image analysis was performed on all sections to evaluate the quantity of newly formed bone. Specifically, three histological sections per implant were digitized at low magnification, allowing coverage of the entire PPF implant (Figure 9.2A). Using a Leica® Qwin Pro image analysis system, the computer detected the areas of the PPF implant and bone. The outline of the implant area was then designated as the region of interest (ROI). The image analysis program then measured the surface area of PPF (PSA) (Figure 9.2B), area of the ROI (Figure 9.2C), and surface area of bone (BSA) (Figure 9.2D). The analysis program then calculated the percent of pore area ([ROI - PSA]/ROI), the percent of bone area (BSA/ROI), and percent of pore fill (BSA/[ROI - PSA]).

Statistical analysis

Statistical analysis was performed using a paired t-test. Nine repetitions were performed for all *in vivo* studied and all data are reported as means and standard deviations.

RESULTS

In vitro TGF-β1 release

The results of the TGF-β1 release are depicted in Figure 9.3. A rapid release was observed during the first 2 hr, during which almost 55% of the total dose of TGF-β1 was released. Following this initial peak, a decline in the level of TGF-β1 occurred at 4 hr. After 1 wk, the entire theoretical initial 2 μg dose was observed to have been released.

Experimental animal study

During the experiment all rabbits remained in good health and did not show any wound complications. At the end of the 8 wk study, all 36 implants were retrieved. At explantation, no inflammatory signs or adverse tissue reaction could be seen. For some of the PPF-TGF-β1 implants, bone formation could already be observed macroscopically on the internal (dural) surface.

Light microscopy, subjective

Analysis of the sections via light microscopy revealed various levels of bone formation at 8 weeks post-implantation. For all implants, the defect edge was still visible. In all specimens, some inflammatory cells were seen.

In all non-TGF-β1 coated implants (PPF-Pw, PPF-Gd, PPF-Fn), very limited bone growth inside the pores of the PPF scaffold could be observed (Figure 9.4A). Bone had grown from the edge of the former defect up to the PPF scaffold (Figure 9.4B). An intervening fibrous capsule was present in between the newly formed bone and PPF scaffold. In addition, an organized fibrous capsule was present covering the top and bottom of the PPF. Inside the PPF, some inflammatory cells, fibroblasts and small blood vessels were seen. Also, no signs of microfragmentation could be observed

histologically. Subjective light microscopical analysis revealed no differences in histological appearance and bone ingrowth between PPF-Gd, PPF-Fn and PPF-Pw implants.

On the other hand, in all PPF-TGF-β1 implants bone formation had occurred. In five PPF-TGF-β1 implants extensive bone formation had occurred (10%-25% of the original graft volume) (Table 9.1, Figure 9.4E). In these implants the bone had a trabecular appearance together with haemopoetic bone marrow-like tissue (Figure 9.4F). Bone was present throughout and surrounding the implant in close contact with the PPF pore surface without an intervening fibrous tissue layer. In some areas active bone formation could be observed with osteoblast-like cells and osteoid. Almost no PPF degradation was seen histologically. Occasionally multinucleated giant cells in contact with the PPF were observed. In the other four PPF-TGF-β1 implants bone formation was limited (1%-6%) (Table 9.1, Figure 9.4C). The bone also had a trabecular appearance. Less haemopoetic bone marrow-like tissue was present (Figure 9.4D). In addition, some inflammatory cells were present. Where bone formation was not present within the scaffold, fibrous tissue ingrowth could be observed.

Fluorochrome labeling

The fluorochrome labels were clearly visible. In the non-TGF-β1 coated implants, the accumulation sequence of the labels revealed that some initial bone formation had occurred starting at the wound edges up to the PPF scaffold (Figure 9.5A, 9.5B). In the PPF-TGF-β1 implants, bone formation was observed throughout the porous foam interior. Indeed, bone formation appeared to proceed from the interior of the pore towards the PPF scaffold (Figure 9.5C, 9.5D).

Light microscopy, image analysis

The results of the histomorphometrical measurements show that the TGF-β1 treated implants present an average bone surface area of 1.72 mm^2, whereas in the non-TGF-β1 treated implants the average was 0.06 - 0.07 mm^2 (Figure 9.6A). Furthermore, bone filled approximately 11 % of the defect area for the TGF-β1 treated implants but less than 0.5 % of the defect area for the non-TGF-β1 treated implants (Figure 9.6B). Average pore fill percentage was approximately 16 % for the TGF-β1 treated implants and below 1 % for the non-TGF-β1 treated implants (Figure 9.6C). The pore area percentage of total scaffold volume was approximately 66% for the TGF-β1 treated implants and 53 - 56% for the non-TGF-β1 treated implants (Figure 9.6D).

Statistical evaluation, using a paired t-test, revealed significant differences between PPF-Gd and PPF-TGF-β1 implants for bone surface area ($p<0.005$), bone area percentage ($p<0.005$), pore fill percentage ($p<0.005$) and pore area percentage ($p<0.005$) (Figure 9.6). No significant differences were observed between the PPF-Gd and PPF-Fn, and PPF-Gd and PPF-Pw implants for any parameter (Figure 9.6).

DISCUSSION

In our *in vitro* release study we found a burst effect during the first 2 hr in which almost 55% of the TGF-β1 had been released. This initial burst release was followed by a slow completion of TGF-β1 release by the end of week 1. Although this experiment does not provide data about the activity of the released TGF-β1, our results suggest that the same release profile will occur *in situ*. The observed burst release of TGF-β1 also corroborates previous work studying the growth factor release from titanium fiber mesh implants [126]. The initial phase of rapid protein loss is thought to be related to protein

properties, especially solubility, rather than scaffold properties [133,134]. Furthermore, in the present study total release was higher after 1 week than in our titanium mesh experiment. This may be attributable to the lower affinity of the PPF implants for TGF-β1 [134]. We also note that Figure 9.3 shows a total release of approximately 112 +/- 5% (mean +/- SD), which is indicative of the error involved with the measurement.

We have previously demonstrated that the experimental design used is not a critical size defect model [126]. However, the purpose of this study was to evaluate the general tissue response to TGF-β1 and fibronectin adsorbed onto PPF scaffolds and non-treated PPF scaffolds. In view of this, our histological findings confirm that PPF is biocompatible with host bone in a rabbit animal model. There were slightly more inflammatory cells than are observed in the earlier titanium fiber mesh study, but this is to be expected for a biodegradable material [126]. However, histological observations found only a minimal sign of degradation. The polymer maintained its porous structure throughout the 8 week study. Chemically crosslinked PPF has been shown to degrade within days *in vivo* in a rat intramuscular site [51]. Furthermore, in a proximal tibial rat model, progressive replacement by bone had occurred by 5 weeks [135]. Both of these works, however, studied a PPF composite containing both a NaCl porogen and ß-tricalcium phosphate. Consequently, full degradation characteristics of photocrosslinked PPF remain to be investigated over a longer time span.

The application of a fibronectin coating did not modify the tissue response to a PPF scaffold by 8 weeks. Though fibronectin has been proven to enhance osteoblast-like cell adhesion and *in vivo* bone formation by osteogenic cell-loaded scaffolds, it does not further enhance the biological response in a porous PPF scaffold material [129]. On the

other hand, no adverse effects were observed. Future experiments have to prove the osteogenic properties of fibronectin coated porous PPF scaffolds loaded with osteogenic cells.

The bone stimulative effect of rhTGF-β1 in combination with a porous carrier is in agreement with the results of several other studies [101,124-126,136-140]. The amount of bone formation within our scaffolds was variable. Five scaffolds with adsorbed TGF-β1 showed significant amounts of bone, while four implants showed less. Comparison of the findings with our similarly designed titanium fiber mesh study reveals that more bone occurred in the titanium fiber mesh with less inter-implant variation [126]. In the present study average total bone surface area was 1.72 mm^2 per implant. In the titanium study the total bone surface area was approximately 2.74 mm^2 per implant. Two explanations can be given for these findings. First, coating difficulties caused by a relatively low affinity of TGF-β1 for PPF could have resulted in a suboptimal amount of TGF-β1 at the time of implantation. Although, the implants were treated with Gd to enhance adsorption, we know that a shadow effect exists, which prevents the Gd treatment to reach the surface of the inner pores. Second, a low affinity of TGF-β1 for PPF can lead to insufficient retention of the TGF-β1 after implantation. Unfortunately, no exact information is currently available about this phenomenon. For other osteoinductive growth factors, like BMPs, carrier-protein affinity has been more thoroughly studied [133,134,141]. The *in vivo* osteoinductive activity was found to be positively correlated with the amount of protein retained at the site. Higher retention yields a higher osteoinductive activity. Supposedly, if less growth factor is retained, a higher dose is needed for the same osteoinductive response. In view of this, due to

coating difficulties or protein retention, the remaining dose on some of our implants might have been below the optimal osteoinductive level [101,142,143].

Image analysis revealed a higher pore area percentage for the TGF-β1 coated scaffolds (66%) than for non-coated specimens (53 - 56%). Several possible explanations can be given for this observation. A possible explanation is the reduced compression of the implanted PPF-TGF-β1 foams (and thus reduced porosity decrease) because of the mechanical reinforcement of the foams due to increased bone formation. Another explanation is the reduced contraction of the implanted PPF-TGF-β1 foams due to decreased fibrovascular tissue growth [144]. Alternatively, it may have occured due to the image analysis measuring technique which is based on color differences between the various structures. In general, the color difference between PPF and fibrous tissue is smaller than the difference between bone tissue and PPF. This may have resulted in a measurement error.

Further, fluorescent labeling revealed that in the TGF-β1 coated scaffolds the process of bone formation had proceeded in a centrifugal manner, starting in the middle of the pores and growing towards the surface of the scaffold. We have also observed this type of bone formation in titanium scaffolds loaded with TGF-β1, BMPs, or osteogenic cells [126,145,146]. Only for bioactive scaffold materials, so-called bonding osteogenesis, i.e. bone formation starting at the surface area and proceeding away from the surface, can occur [147].

Despite the favorable effect of TGF-β1 on bone healing, we have to notice that there is still some concern about the safety of this growth factor for use in humans [148-150]. For example, a recent clinical trial has demonstrated that systemic administration

of TGF-β2 can lead to a reversible decline in renal function [151]. Nevertheless, this observation does not prove a causal connection between local administration of low doses of TGF-β1, as occurs for bone regenerative applications, and adverse effects. Nevertheless, it is important that a therapeutic index is established for TGF-β1, allowing a rational approach for safe delivery and dosage of this growth factor in local therapeutic use.

CONCLUSIONS

Photocrosslinked PPF is biocompatible with host bone and shows minimal histological evidence of degradation during an 8 week experimental period. On the other hand, the osteoconductive properties of porous PPF are limited in the model used. Additionally, fibronectin coating as applied in this study does not modify the bone response to these PPF scaffolds *in vivo*. TGF-β1 did induce significant bone formation in these porous PPF scaffolds. These results indicate that porous PPF combined with an appropriate growth factor carrier is a good candidate for the creation of osteoinductive bone graft substitutes.

Table 9.1: Histomorphometrical Analysis of PPF-TGF-β1 Implants

Implant Number	Bone Area %
1	0.9
2	16.6
3	5.7
4	4.2
5	6.3
6	12.9
7	24.3
8	10.8
9	19.5

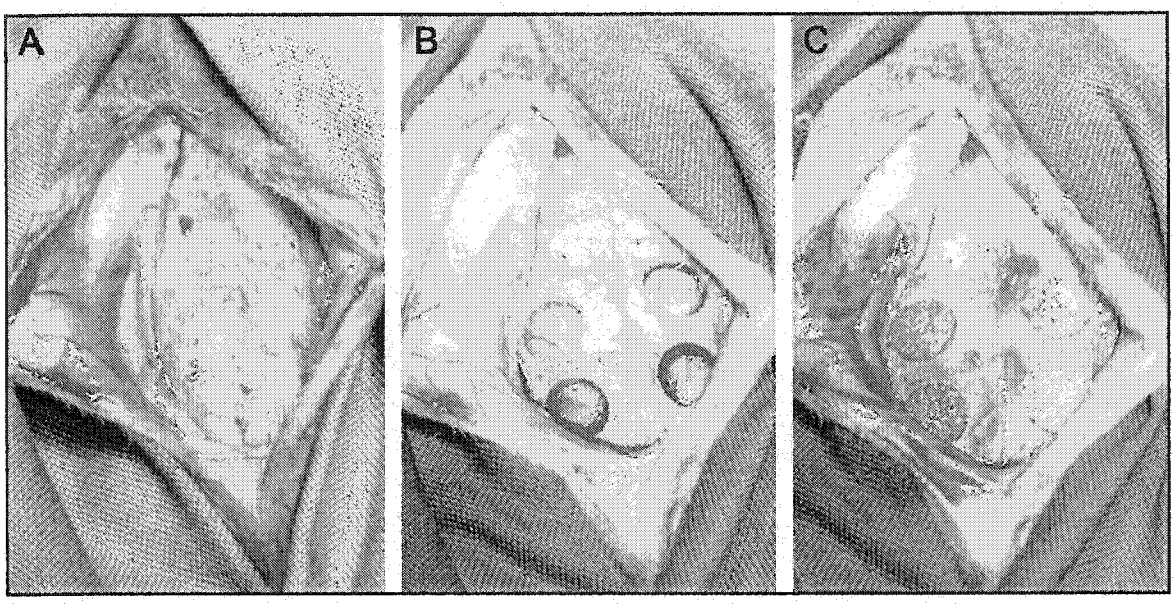

Figure 9.1: (A) Exposure of the skull bone. **(B)** Four cranial defects. **(C)** Inserted porous PPF scaffolds.

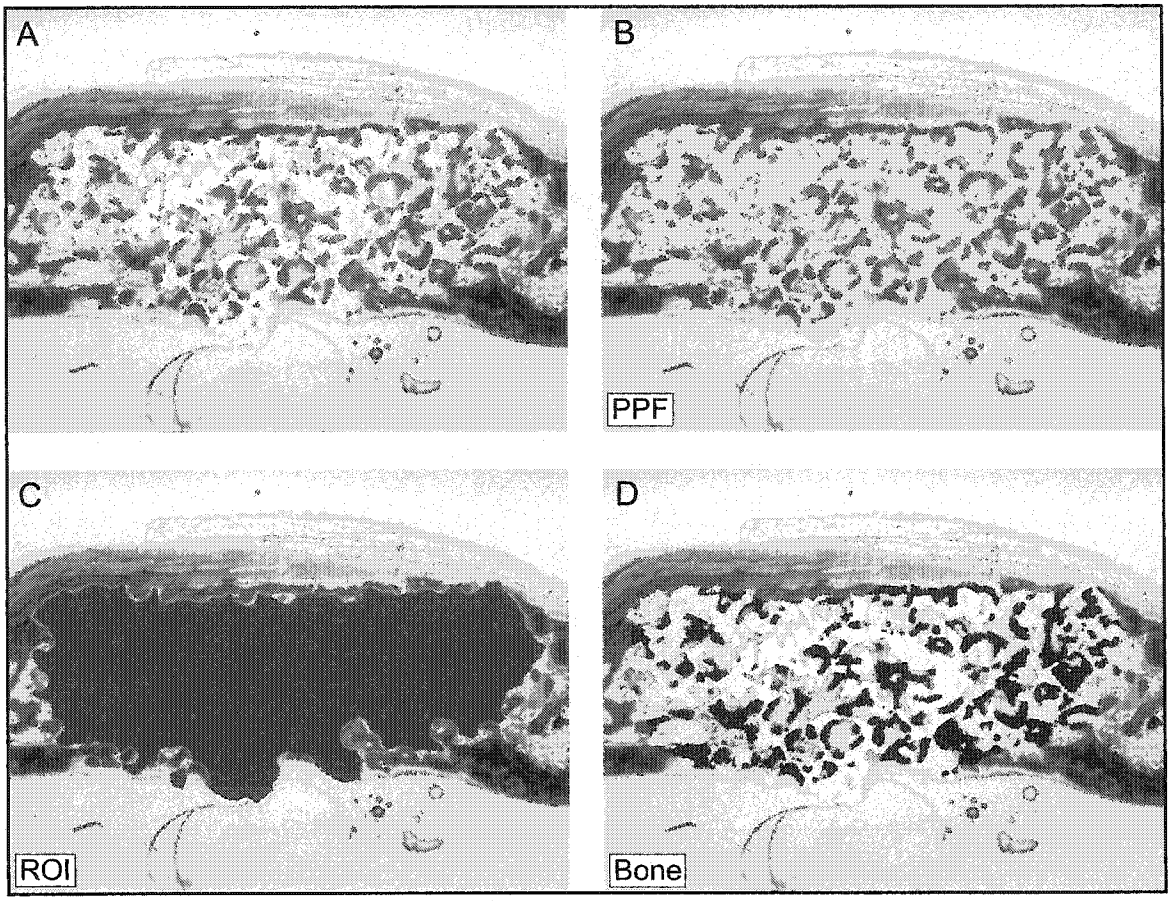

Figure 9.2: Image analysis procedure. **(A)** Three histological sections per implant were digitalyzed at low magnification, allowing coverage of the entire PPF implant. **(B)** The computer detected and measured the area of the PPF. **(C)** The outline of the PPF area was then designated as the region of interest (ROI). **(D)** The computer detected and measured the area of bone within the ROI (bone surface area). From these areas, the analysis program calculated the pore area percentage, the bone area percentage and pore fill percentage.

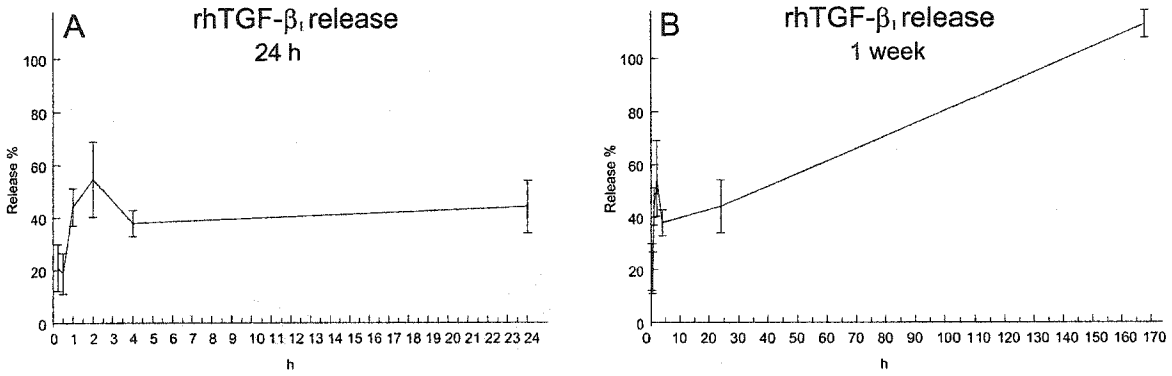

Figure 9.3: Graph showing *in vitro* rhTGF-β1 release. A burst release can be seen in which most of the rhTGF-β1 was released by 2 h **(A)**, followed by a slow release up to 1 week (data shown are mean +/- standard deviation (SD)) **(B)**.

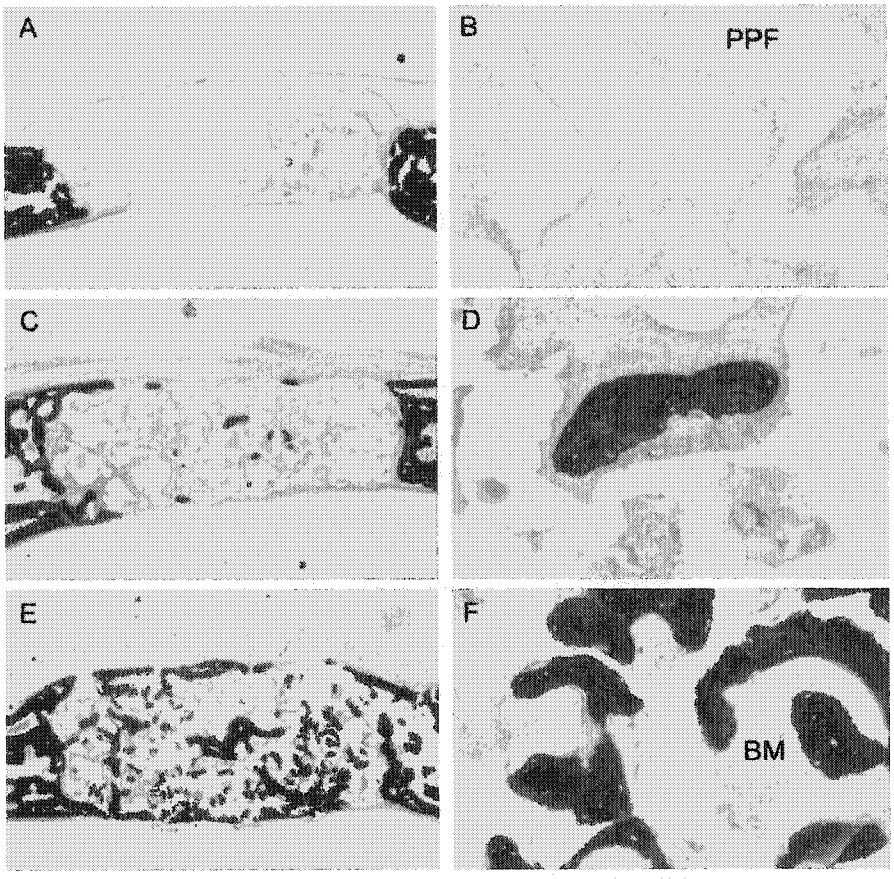

Figure 9.4: **(A)** Undecalcified section of a non-coated porous PPF scaffold at 8 weeks postimplantation (original magnification x2.5). Bone has grown up to the external edge of the PPF scaffold. Only very limited penetration of bone can be observed inside the PPF scaffold. The outside of the PPF is surrounded by a small fibrous capsule. PPF-Fn, PPF-Gd and PPF-Pw show a similar histological image. **(B)** Undecalcified section of a non-coated porous PPF scaffold at higher magnification. The porous spaces of the scaffold are filled with fibrous tissue and capillaries. Some inflammatory cells (multinucleated giant cells) are seen (original magnification x20). **(C)** Undecalcified section of a porous PPF scaffold coated with TGF-β1. A limited amount of bone is present throughout the porous PPF space (original magnification x2.5). **(D)** Undecalcified section of a porous PPF scaffold coated with TGF-β1. Some bone formation is present. Less bone marrow-like tissue can be observed compared with Figure 9.4F (original magnification x20). **(E)** Undecalcified section of a porous PPF scaffold coated with TGF-β1. Bone is present throughout the porous PPF space. The bone has a trabecular appearance and is present in close contact with the PPF surface without an intervening fibrous tissue layer (original magnification x2.5). **(F)** Undecalcified section of a porous PPF scaffold coated with TGF-β1. Some bone is present. The formed bone has a trabecular appearance and is present in close contact with the PPF surface without an intervening fibrous tissue layer. In addition, hemopoietic bone marrow-like tissue (BM) appears to be present (original magnification x20).

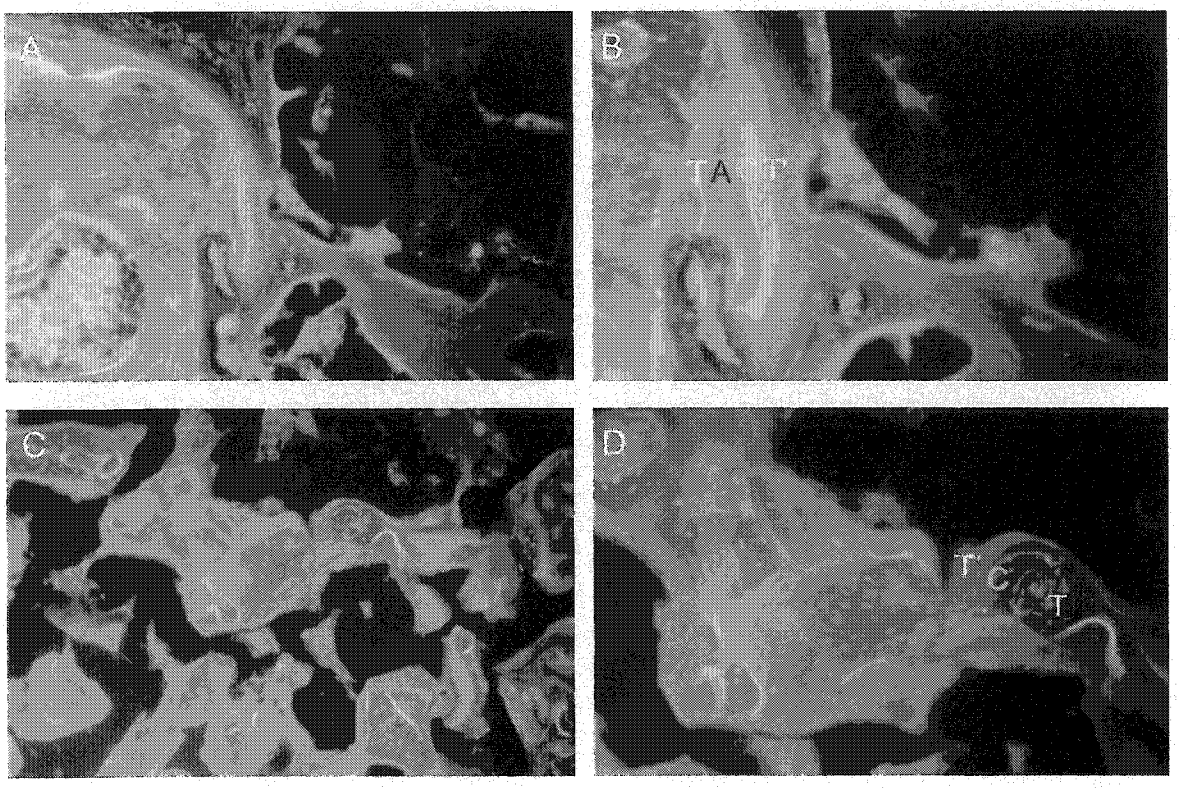

Figure 9.5: (A) Nonstained undecalcified section of a non-coated porous PPF scaffold viewed with a fluorescence microscope. Some initial bone bone guidance has occurred from the former defect edge up to the edge of the PPF scaffold (original magnification x10). A similar result was observed in the PPF-Gd, PPF-Pw and PPF-Fn implants. **(B)** Nonstained undecalcified section of a of a non-coated porous PPF scaffold. In PPF-Gd, PPF-Pw and PPF-Fn implants, the accumulation sequence of the various labels, T = tetracylin (yellow, 1 week), A = alizarin-complexon (red, 3 weeks), C = calcein (green, 5 weeks) and T' = tetracylin (yellow, 7 weeks) label, indicate that some initial bone guidance has occurred, starting from the former defect edge up to the PPF scaffold edge (original magnification x20). **(C)** Nonstained undecalcified section of a porous PPF scaffold coated with rhTGF-β1. This section is viewed with a fluorescence microscope. We observe bone formation starting within the porous space (original magnification x10). **(D)** Nonstained undecalcified section of a porous PPF scaffold coated with rhTGF-β1. The accumulation sequence of the labels T = tetracylin (yellow, 1 week), A = alizarin-complexon (red, 3 weeks), C = calcein (green, 5 weeks) and T' = tetracylin (yellow, 7 weeks) label (see Figure 9.5B) indicates that bone formation has started in the center of the porous space and has grown towards the scaffold (original magnification x20).

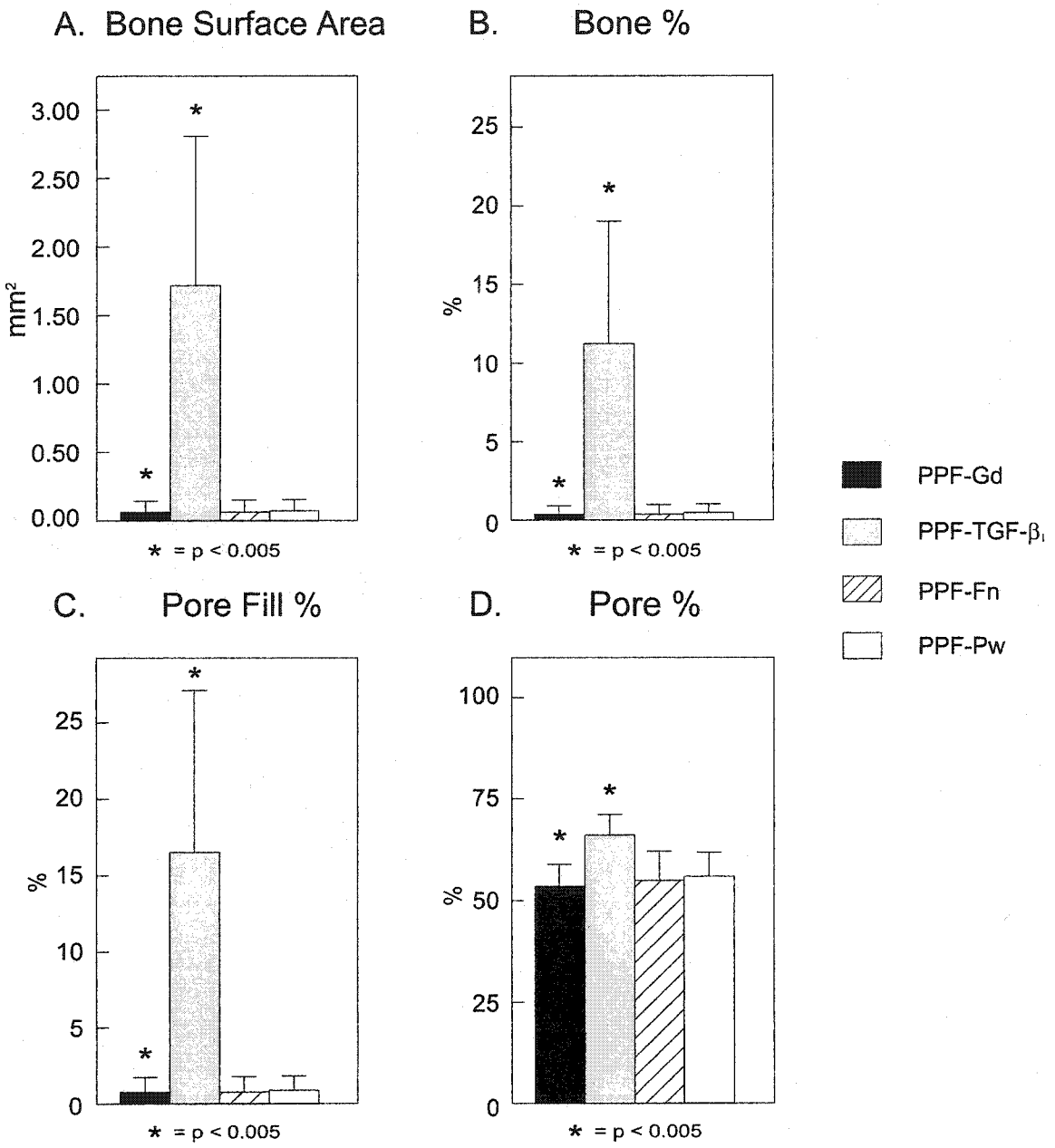

Figure 9.6: **(A)** The bone surface area and **(B)** bone area % and **(C)** pore fill % and **(D)** pore area %. In addition, the results of the paired *t*-test comparing PPF-Gd with the other implant types are shown. Significant differences between PPF-Gd and PPF-TGF-β1 (*) are marked. No significant difference was found between PPF-Gd and the other noncoated implants for any parameter ($p > 0.05$) (data shown are mean +/- SD).

CHAPTER X

THE EFFECT OF BIOMATERIAL PROPERTIES ON BONE FORMATION AS CHARACTERIZED BY HISTOMORPHOMETRICAL ANALYSIS OF WOUND HEALING AND GROWTH FACTOR LOCALIZATION IN A RABBIT TOOTH EXTRACTION SOCKET MODEL

ABSTRACT

In this work we seek to understand the effect of biomaterial properties upon the localization of molecular signals, specifically osteogenic and angiogenic growth factors, within healing bone tissue. To this end, healing bone within a rabbit incisor extraction socket, a subcritical size defect, was investigated as it allows for study of bone formation without significant soft tissue invasion. Four incisor teeth, two each from the mandible and maxilla, were removed from each subject. One tooth socket was left as an empty control, while the remaining three were filled with crosslinked polymer networks formed from either the hydrophobic polymer poly(propylene fumarate) (PPF), the hydrophilic oligomer oligo(poly(ethylene glycol) fumarate) (OPF), or PPF coated with transforming growth factor-β1 (PPF+TGF). All polymer networks were fabricated in the form of a fine particulate (500 – 700 μm) to facilitate filling of the defect. At five different time points (4 days as well as 1, 2, 4, and 8 weeks) bone specimens containing the tooth sockets were removed. The bone healing process was analyzed by histomorphometrical analysis of hematoxylin and eosin stained sections. Using immunohistochemical staining techniques, sections were also assayed for the presence of the angiogenic factors FGF-2 and VEGF as well as the osteogenic factors PDGF-A, TGF-β1, and BMP-2. It was hypothesized that a hydrophobic biomaterial such as PPF will not significantly alter bone

formation within a tooth extraction socket. This hypothesis was supported by the histomorphometrical results. Furthermore, these results indicate that the negative control, networks of OPF, tend to inhibit bone formation, while the positive control, PPF+TGF, did not significantly increase bone formation. Immunohistochemical results reflect molecular signaling indicative of the early invasion of platelets, the vascularization of wound healing tissue, the differentiation of migrating progenitor cells, and the formation and remodeling of bone tissue. The effect of biomaterial properties on bone formation most closely parallel the FGF-2 localization results, indicating its critical role in the initial phases of wound healing to facilitate later bone formation.

INTRODUCTION

Bone formation may be characterized by the following steps: accumulation of progenitor cells, differentiation of progenitor cells to osteoblasts, secretion of extracellular matrix by osteoblasts, mineralization of extracellular matrix, maturation of osteoblasts to osteocytes, remodeling of immature woven bone to mature lamellar bone, and resorption and replacement of lamellar bone [152]. The result of this process is a highly organized tissue with diverse cellular and matrix components. The cellular component is derived from a mesenchymal cell line, including progenitor cells, osteoblasts, and osteocytes, and a hematopoietic cell line, including progenitor cells, monocytes, and osteoclasts [153]. The matrix component includes organically derived molecules, most notably collagen type I, as well as the inorganic ions such as calcium, phosphorous, sodium, and magnesium [153]. While these major components have been generally recognized in bone formation, the controlling and determining factors of this process, however, are less well understood.

Growth factors are produced and excreted by cells to elicit a specific response, whether acting in a autocrine, endocrine, or paracrine fashion, and thus have been widely investigated for their role in controlling many physiological processes, including bone formation [154,155]. In bone tissue growth factors are mostly produced by osteoblasts, though small amounts may also be sequestered from the surrounding serum [155]. Once produced, the various bone related growth factors are often retained within the extracellular matrix during bone formation, to be released upon remodeling or injury to the bone tissue [155,156]. These factors then proceed to initiate and control healing by regulating mesenchymal stem cell differentiation, osteoblast and osteoclast metabolism, and endothelial cell proliferation and migration [155-157]. Two large groups of factors intimately involved in bone formation are angiogenic factors, which facilitate the formation and maintenance of a vascularized bed that is required for bone growth and remodeling, and osteogenic factors, which initiate the formation of bone itself by directing processes such as progenitor cell differentiation and extracellular matrix production.

The growth factors fibroblastic growth factor-2 (FGF-2), also known as basic FGF (bFGF), and vascular endothelial growth factor (VEGF) have been widely investigated as angiogenic factors. FGF-2, generally involved in angiogenesis and mesenchymal mitogenesis, has been identified in the early stages of fracture healing [158-160]. Furthermore, it has been shown to be expressed by osteoblasts present in the later stages of healing as well as in bone remodeling [160]. While it is well known to promote neovascularization during bone healing, it has also been shown to have a proliferative effect on osteoblasts that form bone [155,160]. In contrast, VEGF acts

mainly within bone formation by promoting angiogenesis through induction of the proliferation and migration of endothelial cells [157]. It has also has been shown to induce neovascularization, critical in bone formation, by the recruitment of progenitor endothelial cells from the circulation [161]. Recent work has shown VEGF to stimulate vessel network formation, elongation, and branching within an environment that is lacking nutrients and oxygen [162].

Osteogenic factors involved in bone formation include platelet derived growth factor-A (PDGF-A), transforming growth factor-β (TGF-β), and bone morphogenetic protein-2 (BMP-2). PDGF-A is secreted mainly by platelets during the early phases of fracture healing and has been identified at fracture sites in both mice and humans [154]. PDGF-A has been demonstrated to be mitogenic for mesenchymal derived cells in general, and osteoblasts in specific [154,155]. TGF-β, on the other hand, is concentrated in bone, platelets, and cartilage since osteoblastic cells are a major source for the TGF-β that is found within bone [154,163]. TGF-β has been localized both in the early fracture healing period and during endochondral ossification [164-167]. This factor is believed to be involved in the regulation of a wide range of processes, including the stimulation of mesenchymal cells, inhibition of ectodermal cells, and autocrine modulation of bone forming cells [155,163]. Supporting its role in bone formation, osteoblasts have been found to be highly enriched with TGF-β receptors [163]. Nevertheless, the effects of TGF-β are generally thought to be diverse and thus difficult to describe with precision. In contrast, BMP-2, as well as other bone morphogenetic proteins, are known to be growth factors that can stimulate mesenchymal stem cell differentiation to osteoblasts

[155,168,169]. Thus the critical role of BMP-2 within bone formation, and particularly to maintain osteoblastic cells, has been vigorously investigated [155,168,169].

Significant work has been undertaken to describe the actions of growth factors throughout bone formation. After injury, TGF-β and PDGF-A are released early in the healing phase as they are expressed by platelets and released by extracellular matrix [155,156,170]. These factors act to recruit progenitor cells and osteoblasts from the surrounding tissue as well as initiate the differentiation of the progenitor cells. Also released early within the healing phase, BMP-2 further initiates the progenitor cell differentiation towards an osteoblastic lineage [155]. Later in the healing response, the recruited and newly differentiated osteoblasts continue to express these and other factors, including FGF. These factors act to maintain healing and, in the case of FGF and VEGF, create the vascularization critical for bone tissue.

A possible approach for the healing of critical size bone defects or the quickening of bone repair is to deliver exogenous growth factors. This strategy, the controlled release of growth factors by an implantable, degradable biomaterial construct, has been extensively explored in fields such as drug delivery and tissue engineering. One complicating factor, however, within these strategies is the effect of the biomaterial itself upon healing, and specifically upon endogenous localization of those factors which are critical to healing. This study seeks to understand the effects of biomaterial properties upon bone healing by histomorphometrical analysis of bone formation visualized by hematoxylin and eosin staining and growth factor localization visualized by immunohistochemical staining. (The term localization is used here to describe the presence of a growth factor and does not indicate anything about its expression, release,

or uptake.) The experimental model used within this study was the healing bone within a rabbit incisor extraction socket, which is a subcritical size defect. This model was chosen primarily because it allows for study of bone healing without significant soft tissue invasion.

It was hypothesized that a hydrophobic biomaterial would not significantly alter bone formation within a subcritical size, tooth extraction socket defect. A hydrophobic material should allow for the significant adsorption and retention of proteins *in vivo*, as they typically adsorb to hydrophobic surfaces, and thus cell adhesion [171-174]. Alternatively, a hydrophilic material may prevent protein adsorption and cell adhesion [171-174]. To examine this hypothesis, we have chosen two degradable biomaterials which possess a related molecular structure, but differ significantly in their hydrophobic and hydrophilic balance. Both materials are polyesters of fumaric acid. A polyester of fumaric acid and propylene glycol, poly(propylene fumarate) (PPF) is a hydrophobic polymer. Alternatively, when polymerized with the hydrophilic polymer poly(ethylene glycol) (PEG), the resulting oligomer, oligo(poly(ethylene glycol) fumarate) (OPF), is hydrophilic. Thus, these two polymers allow for the investigation of hydrophobic and hydrophilic effects, without a dramatic change in molecular structure. Specifically within this study, the experimental group investigated was a hydrophobic, crosslinked polymer network formed from PPF. The negative control was a hydrophilic hydrogel formed from OPF. The positive control was PPF coated with TGF-β1 (PPF+TGF), which has previously been shown to be biocompatible and osteoconductive in a subcritical size cranial defect [59,61]. (All of the biomaterials were implanted in the form of a dry

particulate.) Finally, a fourth incisor socket was left as an empty control to compare to normal bone healing within an extraction socket.

For the purposes of this work, a hydrophobic material is defined as a material that exhibits a large contact angle, whereas a hydrophilic material exhibits a small contact angle. PPF has been previously shown to possess a water contact angle of 60.1° [175]. Additionally, crosslinked PPF has been shown *in vitro* to support marrow stromal cell adhesion at levels similar to tissue culture polystyrene [176]. In contrast, copolymers of PPF and PEG have been shown to possess water contact angles between 20° and 30°, with increasing PEG (hydrophilic) content resulting in a decrease in the water contact angle [177]. OPF hydrogels, in the absence of any tethered adhesion peptide sequences, have been shown to prevent marrow stromal cell adhesion *in vitro* [178].

Materials and Methods

Study design

This study utilizes the tooth extraction socket of a New Zealand White rabbit as the experimental model. This species was selected as the animal model based on an examination of dental anatomy, eating habits, and ability to withstand surgical procedures. The dental formula of these animals is: Incisors 4/4, Canines 0/0, Premolars 3/2, and Molars 3/3. All animals were males, weighing between 2.5 and 3.0 kg.

Twenty-five rabbits were divided into 5 groups, each of 5 animals. After extraction of the four incisor teeth, each animal received three different biomaterial implants, which were in the form of powder, in the following manner. The right mandible incisor socket was left empty as a control; the left mandible incisor socket was filled with 0.03 - 0.05 g of dried, crosslinked oligo(poly(ethylene glycol) fumarate)

networks; the left maxilla incisor socket was filled with 0.03 - 0.05 g of crosslinked poly(propylene fumarate) networks; the right maxilla incisor socket was filled with 0.03 - 0.05 g of crosslinked PPF networks coated with transforming growth factor-β1 (3.33 μg TGF-β1/g PPF). All animal groups received the same set of biomaterials, but were euthanized at 4 days, 1 week, 2 weeks, 4 weeks, or 8 weeks after biomaterial implantation.

Poly(propylene fumarate) synthesis

Poly(propylene fumarate) was synthesized by a two step procedure [62]. Briefly, one mole of diethyl fumarate (Acros Organics, Pittsburgh, PA, USA) and three moles of 1,2 propanediol (Acros Organics) were reacted using 0.01 moles $ZnCl_2$ (Fisher Chemicals, Pittsburgh, PA, USA) as a catalyst and 0.002 moles of hydroquinone (Acros Organics) as a radical inhibitor. The PPF polymer was then purified by acidic water, pure water, and brine washes, followed by precipitation in ethyl ether. The purified product has a number average molecular weight (M_n) of 2360 and a polydispersity index (PI) of 1.69, as determined by gel permeation chromatography using polystyrene standards.

Poly(propylene fumarate) particulate fabrication

The PPF polymer was fabricated into a powder by a photocrosslinking technique [60]. First, a solution of the photoinitiator bis(2,4,6-trimethylbenzoyl) phenylphosphine oxide (BAPO, Ciba Specialty Chemicals, Tarrytown, NY) in methylene chloride (1 g/10 ml) was mixed into the PPF polymer (0.05 ml/g PPF). A NaCl porogen (80 wt%) was then added to this PPF mixture. The resulting paste was packed into a glass mold and exposed to ultraviolet light (4 mW/cm^2) for 30 minutes. The crosslinked samples were

removed from the mold and then soaked in water for three days to remove the NaCl porogen. The samples were dried, first with an absorbent cloth and then by vacuum drying. The dried samples were then ground into a powder with a mortar and pestle. The resulting powder was sieved and the particles between 500 and 700 μm collected. The crosslinked PPF powder was sterilized by ethylene oxide gas exposure (Anprolene Automatic Ventilated Sterilizer, Anderson Products, Chapel Hill, NC) and stored at 4°C until implantation.

Poly(propylene fumarate) with transforming growth factor-β1 particulate fabrication

The PPF+TGF-β1 scaffolds were fabricated by coating TGF-β1 onto the surface of the PPF powder [59]. TGF-β1 (R&D Systems, Minneapolis, MN) was first reconstituted in a 4 mM HCl solution containing 1 mg/ml bovine serum albumin at a concentration of 3 μg/ml. This solution was then applied to sterilized PPF particulates at a concentration of 3.33 μg TGF-β1/g PPF. The powder was left to sit for 30 min, allowing the TGF-β1 to adsorb to the PPF, and then lyophilized overnight. The PPF+TGF-β1 powder was stored at 4°C until implantation.

Oligo(poly(ethylene glycol) fumarate) synthesis

Oligo(poly(ethylene glycol) fumarate) was synthesized by a one step reaction [179]. One mole of dried, 3350 Da poly(ethylene glycol) (PEG, Aldrich, Milwaukee, WI, USA) was first dissolved in 500 ml of anhydrous methylene chloride. Next, 0.9 mole of fumaryl chloride (Acros Organics) and 1.8 moles of triethylamine (Aldrich) were added drop wise over the course of 3 hours to the stirring PEG solution. The drop wise addition occurred while the reaction vessel was kept in an ice bath in order to reduce reaction temperature. The reaction was then allowed to proceed overnight at room

temperature. The methylene chloride solvent was then removed by rotoevaporation and the reaction products dissolved in ethyl acetate. The triethylamine hydrochloride salt by-product was removed by filtration, allowing the OPF product to be recovered. Finally, the OPF was purified by recrystallization in ethyl acetate twice, dried with ethyl ether, and vacuum dried.

Oligo(poly(ethylene glycol) fumarate) particulate fabrication

Oligo(poly(ethylene glycol) fumarate) was fabricated into a dry powder by a thermal crosslinking technique. To accomplish this, 5.0 g OPF was first dissolved into 12 ml H_2O. A water soluble initiator solution, consisting of 1.5 ml of an ammonium persulfate (APS, Aldrich) solution (1.14 g APS in 5 ml H2O) and 1.5 ml of an ascorbic acid (AA, Sigma, St. Louis, MO, USA) solution (0.88 g AA in 5 ml H2O), was then added to the OPF solution to initiate crosslinking. A circular, hydrogel disk (12 cm diameter x 0.5 cm thick) was fabricated by combining the initiator and OPF solution at 60°C for 30 min. The crosslinked hydrogel was then leached in water for one day to remove any unreacted components. The hydrogel was then dried, first by air and then by vacuum drying. The dried, crosslinked OPF hydrogel was then broken into small (< 2 cm^2) pieces, frozen in liquid nitrogen, and ground into a powder with a mortar and pestle. The resulting powder was sieved and the particles between 500 and 700 μm collected. The crosslinked OPF particles were sterilized by ethylene oxide gas exposure (Anprolene Automatic Ventilated Sterilizer) and stored at 4°C until implantation.

Animal model and surgery

The animals were anesthetized prior to tooth extraction with an oro-endotracheal intubation technique, using isoflurane as the pharmacological agent. The four incisor

teeth were then extracted atraumatically using dental elevators. After material implantation, each tooth socket was closed with 1-2 degradable sutures. All surgical procedures were carried out by a single operator. An intra-operative and post-operative dose of the antibiotic benzathine penicillin and two post-operative doses of analgesics were given 12 hours apart. The animals were fed a soft diet for 72 hours following extraction of teeth, followed by a regular diet. Food and water (via water bottle) were given liberally. Animals were weighed every other day for 10 days following extractions. All procedures were undertaken following a protocol submitted to and approved by the Animal Welfare Committee of the University of Texas Health Science Center at Houston.

Euthanasia and tissue harvest

At the proper time, subject animals were sedated and euthanized following an approved protocol. Briefly, a dose of a ketamine, acepromazine cocktail was first given for deep sedation. After sedation, an intravenous injection of an overdose of a pentobarbital preparation was given to euthanize the animal. Maxilla and mandible bone specimens were then dissected using a scalpel. Using a surgical saw, the bone specimens were first sectioned into right and left halves and then removed. This method allows the retrieval of the four extraction sockets, contained within the left and right maxilla as well as the left and right mandible, from each animal.

Tissue fixation, decalcification, embedding, and sectioning

The harvested tissues were immediately placed into 50 ml of freshly prepared paraformaldehyde-lysine-phosphate (PLP) fixative solution (pH 7.4) for 6 hours on a shaker table (75 rpm). Samples were removed from the PLP fixative, rinsed 5 times in

PBS (0.01 M, pH 7.4), and then left in PBS overnight on a shaker table. A 5% formic acid solution was used as the decalcifying agent. Samples were removed from the PBS and placed into the 5% formic acid decalcifying solution on a shaker table for 4 days. (Note that the decalcifying step should also soften the implanted biomaterials, by acid catalyzed ester hydrolysis, and thus facilitate sectioning.) Samples were removed from the 5% formic acid solution, rinsed 5 times in PBS, and then left in PBS overnight on a shaker table. The samples were removed from the PBS, cut in half parallel to the frontal plane (noting the proximal and distal ends), and then placed, freshly cut side down, into plastic molds filled with O.C.T. compound. The samples embedded in O.C.T. were frozen with dry ice and stored at -20°C until sectioning. Frozen sections were cut on a cryostat at 10 μm thickness and placed on albumin-coated glass microscope slides. Serial sections were taken from the freshly cut end and then stored at -20°C.

Immunohistochemistry

Tissue sections were immunostained using an Biogenex automated stainer (Biogenex i6000 Automated Immunostaining System, San Ramon, CA). The slides were prepared by encircling the sections with a hydrophobic ink. The slides were first incubated in 95% ethanol (300 μl) for 3 min and then rinsed with distilled water (3 ml). Next, the endogenous peroxidase activity was blocked with a H_2O_2/CH_3OH solution (300 μl) incubation for 1 hr and then rinsed twice with immunohistochemical (IHC) buffer (3 ml). Random secondary antibody binding was then blocked with a normal blocking serum (300 μl) incubation for 1 hr. (The normal blocking serum was from the same species as the secondary antibody to be used later.) The primary antibody (300 μl) was then bound for 2 hr and followed by two rinses of IHC buffer (3 ml). The slides were

then incubated in a biotinylated secondary antibody (300 µl) for 1 hr, followed by two rinses of IHC buffer (3 ml). The ABC reagent (300 µl) was then bound for 1 hr, followed by two rinses of IHC buffer (3 ml). Next, the slides were incubated in a DAB developing reagent (300 µl) for 10 min, followed by a distilled water (3 ml) rinse. The slides were then stained with hematoxylin (300 µl) for 8 min, rinsed with distilled water (3 ml), and clarified with acid alcohol (300 µl) for 3 min. Finally, the slides were rinsed twice with distilled water (3 ml) and then dehydrated with 2 x 95% ethanol (300 µl for 3 min) and 2 x 100% ethanol (300 µl for 3 min) rinses. Subsequently, the slides were rinsed in xylene and mounted. Negative controls were obtained by incubating the sections with 0.01M PBS in place of the primary antibody. A final group of sections undergo conventional hematoxylin and eosin staining.

Immunohistochemical reagents

PLP fixative: The PLP fixative solution consists of 300 ml lysine phosphate buffer, 100 ml paraformaldehyde solution, and 0.025 M sodium m-periodate. The lysine phosphate buffer was a solution of 0.01 M dibasic sodium phosphate added to 0.2 M L-lysine HCl until a pH 7.4 has been obtained. The paraformaldehyde solution was formed from 8 g paraformaldehyde dissolved, with heat (50-60°C), in 100 ml distilled water with 1 g NaOH; once cooled, 5.4 g dextrose was added.

H_2O_2/CH_3OH solution: The H_2O_2/CH_3OH solution consists of 50 ml of 30% H_2O_2 in 200 ml CH_3OH.

IHC buffer: The IHC buffer solution consists of 0.1 M PBS with 0.5 wt% Tween.

Normal blocking serum solution: The normal serum blocking solution was purchased as a portion of the Vectastain® Elite® ABC Kit (Vector Laboratories,

Burlingame, CA). Stock normal blocking serum (150 µl) was added to 10 ml of 0.1 M PBS. The reagent was used the same day it was prepared.

Primary antibody solution: The following antibodies were used: anti-TGF-β1 (goat polyclonal antibody, sc-146-G, Santa Cruz Biotechnology), anti-PDGF-A (mouse monoclonal antibody, sc-9974, Santa Cruz Biotechnology), anti-FGF-2 (goat polyclonal antibody, sc-79-G, Santa Cruz Biotechnology), anti-VEGF (mouse monoclonal antibody, 05-443, Upstate Biotechnology), and anti-BMP-2 (goat polyclonal antibody, sc-6895, Santa Cruz Biotechnology). All antibodies were used at a dilution of 2 µg primary antibody in 1 ml 0.1 M PBS. The mouse monoclonal antibodies were used in conjunction with an anti-mouse ABC kit. Similarly, the goat polyclonal antibodies were used in conjunction with an anti-goat ABC kit. The diluted antibody solutions were used the same day they were prepared. The antibodies and associated reagent kits have been verified for use in the rabbit tooth extraction socket model in previous studies [180-182].

Biotinylated secondary antibody reagent: The biotinylated secondary antibody was purchased from Vector Laboratories as a portion of the Vectastain® Elite® ABC Kit. Stock normal blocking serum (150 µl) and stock biotinylated antibody (50 µl) was added to 10 ml of 0.1 M PBS. The reagent was used the same day it was prepared.

Avidin-biotin complex reagent: The ABC reagent was purchased from Vector Laboratories as a portion of the Vectastain® Elite® ABC Kit. Stock reagent A (100 µl) and stock reagent B (100 µl) were added to 10 ml of 0.1 M PBS. The reagent was used the same day it was prepared.

3,3'-Diaminobenzidine developing reagent: The DAB reagent was purchased from Vector Laboratories as DAB Substrate Kit. Stock buffer solution (168 µl), stock

DAB solution (256 µl), and stock H_2O_2 solution (160 µl) were added to 10 ml of 0.1 M PBS. The reagent was used the same day it was prepared.

Image Acquisition

Sections stained with hematoxylin and eosin, used to assess the amount of bone formation, were imaged in the following manner with a light microscope (Eclipse E600, Nikon, Melville, NY) outfitted with a CCD video camera (DXC-950P, Sony, New York, NY) Using light microscopy at a magnification of 4x, the approximate center of the extraction socket lumen was first determined. Three digital images, centered and evenly distributed on a single axis, were then taken from within the lumen of the tooth extraction socket at a magnification of 10x using brightfield microscopy (See Figure 10.1A). The procedure was repeated for a second section, thus obtaining 6 total images for each animal. Depending upon the number of animal subjects (See Table 10.1), the total number of images per data point varied from 18 (n = 3) to 30 (n = 5). If, due to sectioning, staining, or mounting artifacts, a histological section was not acceptable for imaging, the source of the artifact was recorded and another section was imaged. Rules for the removal of a section from analysis were determined prior to imaging. Sections stained immunohistochemically were imaged in a similar manner, however images were obtained at a magnification of 20x, thus altering the imaged field size and the spacing between images (See Figure 10.1B).

Histomorphometry

Histomorphometric analysis was performed using IPLab 3.5® image analysis software (Scanalytics, Fairfax, VA). The brightfield images described in the previous section were a composite of three 8-bit monochromatic channels (Red, Green, and Blue),

resulting in a 24-bit color image. In addition, the Red, Green, and Blue channels of brightfield images can be normalized by the sum of the three channels. For example, 8-bit RN values can be calculated from the 24-bit images according to:

$$RN = \frac{255 * Red}{Red + Green + Blue} \quad (1)$$

where Red, Green, and Blue were the pixel values of the three monochromatic channels. Selection of calcified tissue from the hematoxylin and eosin stained sockets was performed by combined thresholding of the Red and RN pixel values from the brightfield images. This procedure resulted in some non-specific selection; so, it was followed by interactive (J.P.F.) correction of selected areas using the "paintbrush" and "region of interest" tools in IPLab. The number of pixels selected as positive was divided by the total image size for a measurement of the percentage of bone area. The average trabecular size was determined by considering each continuous area of bone in a section as a trabecula. The size of each trabecula in an image was determined and divided by the total number in the image to give the average size. Bone measurement calculations were automated in IPLab.

Although absolute protein levels cannot be determined from immunohistochemical stains, a correlation has been shown between immunohistochemical staining and protein levels measured by Western blot analysis [183-185] and enzyme immunoassays [186-189]. Staining levels were determined from 24-bit images of DAB-stained tissue, as described previously [180,182]. Briefly, images were converted to 8-bit BN images according to the following equation:

$$BN = \frac{255 * Blue}{Red + Green + Blue} \quad (2)$$

BN images allow automatic delineation of DAB tissue from hematoxylin background [180]. Threshold values were set after examining preliminary images and held constant for analysis of all images. The area selected as DAB positive was then divided by the total image area to give the percent area of stain. Analysis of DAB-stained samples was completely automated in IPLab without the need for interactive correction.

Statistical analysis

Sets of data were first inspected with an F-test for treatment [190]. The null hypothesis, that the means of each set were equal, was evaluated with a 90% confidence level ($\alpha = 0.10$); a 90% confidence level was used within this work to differentiate treatment effects which were associated with variability. If the null hypothesis was found to be false, indicating that the means of the different experimental treatment sets were not equal, then Tukey's multiple comparison test was performed. Tukey's multiple comparison test then indicates, in a pair wise fashion, the relationship between the different sets.

RESULTS

Experimental animal study

The biomaterials were implanted without complications. The PPF containing samples remained intact throughout implantation while the OPF samples, as expected, swelled significantly upon contact with the aqueous wound environment. All animals remained in good health throughout the study, with visual inspection of their wounds showing complete and healthy soft tissue covering the extraction sockets after 2 weeks. All bone specimens were retrieved at their prescribed time points and no signs of an adverse tissue response were noted. All specimens were fixed, decalcified, embedded

and sectioned for analysis. The decalcification process was thought to not only dissolve the calcium and phosphate minerals, but also initiate degradation of the polyester biomaterials used within this study so as to facilitate sectioning of the samples. It should be indicated, however, that sectioning of hard tissue samples containing biomaterials was often difficult due to the differences in hardness within the sample.

Light microscopy of H&E stained empty control group

Microscopic investigation of the empty control samples clearly shows the process of healing and bone formation within the tooth extraction socket (Figure 10.2). Four days after extraction, the center of the socket lumen contains remnants of the fibrin network associated with the initial blood clot formation, while the outer rim of the socket lumen has been invaded by inflammatory cells. By 1 week, the inner fibrin network has been taken up by inflammatory cells, producing a socket with an apparently uniform composition. Two weeks after tooth extraction bone formation has begun in the outer periphery of the socket, but the center of the lumen generally remains composed of soft tissue. The formation of bone was characterized by many distinct trabecula that were typically small in size. After four weeks of healing, bone filled the socket, though some radial dependency can still be noted. The bone trabecula are larger in size, but fewer in number than at 2 weeks. Eight weeks after extraction the bone within the cortical shell of the mandible has remodeled into large trabecula that uniformly, but sparsely, fill the area.

In 3 instances (twice in 4 week samples and once in an 8 week sample) the formation of new tooth tissue was identified by light microscopy. Proper characterization of this tissue was difficult, but its location, dense H&E staining, disorganized matrix, and acellular composition indicated that it was most likely cementum. The formation of this

tissue could have been the result of the incomplete removal of the incisor and/or its associated root pulp. As this study was focused solely upon bone formation, these samples were excluded from the study. See Table 10.1 for an itemization of the number of repeats within each time point for the empty control group

Light microscopy of H&E stained experimental, positive control, and negative control groups

The sockets filled with PPF, OPF, and PPF+TGF follow the same overall course of tissue formation outlined above for the empty control group. Within these groups, 6 instances of tooth tissue formation were identified: an OPF sample at 2 weeks, a PPF sample at 4 and 8 weeks, and a PPF+TGF sample at 2, 4, and 8 weeks. These samples were also excluded from the study. See Table 10.1 for an itemization of the number of repeats within each time point for the experimental groups.

A limitation of this study was observed. Although the sockets were filled with the biomaterial to capacity, as determined by the implanting surgeon, and the amount implanted was found to be generally consistent, this procedure did not result in a standardized packing of the biomaterial within the socket. While this should have little impact upon the study of the effects of biomaterial properties upon bone formation, it is necessary to point out that an individual histological section from the groups containing an implant does not always contain the biomaterial. Thus results described below should not be interpreted with the concept that the implanted biomaterial would, by definition, reduce the area available for immunohistochemical stain or bone formation.

Bone formation: histomorphometry of H&E staining

The results from the study of the total area of bone as well as the average trabecular size are presented in Figure 10.3. Figure 10.3A shows for the empty control the expected increase in bone tissue from day 0 to approximately 2 weeks after incisor removal. Following this period of bone formation was a period of remodeling during which the size of the individual trabecula increases, but the total amount of bone remains constant as the number of trabeculae decrease (See Figure 10.3B).

The two groups containing the hydrophobic poly(propylene fumarate) polymer, PPF and PPF+TGF, show a nearly identical trend in bone formation as the empty control, though both groups do show a significantly greater amount of bone than the empty control 1 week after extraction. No significant difference was observed between the two PPF containing groups. The negative control group containing the hydrophilic oligomer oligo(poly(ethylene glycol) fumarate) shows a statistically significant reduction in bone formation compared to the empty control and the two PPF containing groups.

Growth factor localization: histomorphometry of immunohistochemical staining

The two angiogenic factors investigated in this study, fibroblastic growth factor-2 (Figure 10.4A) and vascular endothelial growth factor (Figure 10.4B), show differing trends in localization over time (Figures 10.5 and 10.6). FGF-2 was initially high in its localization in all groups except the OPF negative control, and then reaches a relatively constant level from 2 to 8 weeks after extraction. In contrast, VEGF localization was generally constant, with a slight trend in increasing localization over time for all groups. The only significant difference in localization between the experimental and control groups was the low level of FGF-2 localization associated with the OPF filled sockets in

the 4 day and 1 week time points, when compared to the empty control and the PPF filled sockets.

The three osteogenic factors investigated in this study, platelet derived growth factor-A (Figure 10.4C), transforming growth factor-β1 (Figure 10.4D), and bone morphogenetic protein-2 (Figure 10.4E), also showed differing trends in localization over time (Figures 10.7, 10.8, and 10.9). A dramatic peak in PDGF-A localization was observed at 1 week after extraction for all groups, after which PDGF-A localization remains generally constant. TGF-β1 localization shows a mild increase from 4 days through 2 weeks after extraction, after which it also remains mostly constant. BMP-2, in contrast, shows a trend of increasing localization throughout the study, that was particularly evident in the OPF and PPF filled sockets. Beyond changes over time, there was little difference between the experimental and the control groups for all three of the osteogenic growth factors investigated.

DISCUSSION

The incisor extraction socket of a rabbit was used to investigate the effects of biomaterial properties upon bone formation, studied at both a microscopic and a molecular level. The critical aspect of this work is that while previous works have investigated the expression of growth factors during bone formation, we present here one of the first examples how tissue engineering scaffolds may affect bone tissue healing in a subcritical size defect.

In order to investigate the molecular aspects of healing, we have chosen to analyze our results using quantitative histomorphometry with immunohistochemical staining. This is an alternative approach to the qualitative scoring of

immunohistochemically stained sections that is often performed. It should be noted that care must be taken with three critical experimental aspects: immunohistochemical staining, image acquisition, and image analysis. These techniques must be performed precisely. Using this approach, previous studies with the tooth extraction socket model have shown quantitative immunohistochemistry to be valid [180-182]. Furthermore, other works have shown that quantitative evaluation of immunohistochemical staining to be an appropriate approach for studies similar to the one we describe here [162,187,191,192]. Nevertheless, it should be emphasized that the interpretation of the quantities of immunohistochemically stained area should be undertaken prudently. For example, while the trends and comparisons made between groups are valid, the absolute values themselves should not be interpreted as absolute measures of growth factor concentrations.

The overall trends of the results indicate a few significant trends. Bone formation occurs rapidly within the extraction socket; at 2 weeks the extraction socket has generally formed the amount of bone that it will retain (Figure 10.3A). After this point, the remodeling of bone was the major event occurring, as evidenced by the increasing size of the socket's trabecula. In terms of the growth factors, the angiogenic factor FGF-2 appears to play a critical part in early wound healing, reflecting its role in initiating the vascularization of the wound bed and differentiating invading progenitor cells (Figure 10.5). The trend of VEGF localization indicates it may be more significant in the expansion and maintenance of the vessel network, though this is speculation (Figure 10.6). The initial release of platelet derived growth factor-A from wound healing platelets correlates with the results and appears to be invariant with biomaterial properties

(Figure 10.7). The trend of increased TGF-β1 localization at the early time points may reflect the proliferation and high activity of the bone forming cells that are thought to be a significant source of TGF-β1 (Figure 10.8). Finally, the slow rise of BMP-2 localization over the course of the study parallels its role in the maintenance of a proliferating and active bone cell population (Figure 10.9). As a whole, the observed trends agree with current theories about the role of these angiogenic and osteogenic factors in bone formation.

In terms of the effects of biomaterial properties, our hypothesis was that a hydrophobic biomaterial will not significantly alter bone formation within a tooth extraction socket. The bone tissue formation results seem to support this hypothesis (Figure 10.3A). The percent area of bone was similar between the experimental PPF group and the empty control in all cases, except at 1 week where the PPF group had significantly greater bone formation. This result may be attributed to the stabilizing and retaining effects of the hydrophobic PPF upon those factors critical to bone tissue healing. The results of the immunohistochemical study limitedly support this interpretation, as staining for only the angiogenic factor FGF-2 at the 4 day time point shows a significantly higher localization for the experimental PPF group over the empty control (Figure 10.5). Nevertheless, retention of FGF-2, as discussed below, may be a significant factor in facilitating early bone tissue healing.

The positive control, the poly(propylene fumarate) particles coated with TGF-β1, did not show a significant increase in bone formation (Figure 10.3), angiogenic factor localization (Figures 10.5 and 10.6), or osteogenic factor localization (Figures 10.7 –

10.9) over the experimental PPF group. We speculate that the source of this result lies in the low amount of TGF-β1 delivered (approximately 0.15 μg) to each socket.

As the results from the experimental group seem to support the hypothesis that a hydrophobic biomaterial would not significantly alter bone formation due to its ability to stabilize protein adsorption; the alternative case should also be considered. It has been previously shown that hydrophilic surfaces, and specifically poly(ethylene glycol) surfaces, prevent protein adsorption [174]; this has been suggested to result from low interfacial energy, entropic forces, or favorable water-polymer interactions [171-174]. Thus the case of a hydrophilic surface was considered in the negative control, a hydrogel formed from the degradable oligomer oligo(poly(ethylene glycol) fumarate. The results did show a significant decrease in bone formation when compared to the empty control and the two PPF containing groups (Figure 10.3). Furthermore, the OPF showed a significant reduction in FGF-2 localization at the 4 day and 1 week time points, when compared the other groups. As was seen in the experimental PPF group, the results indicate a significant role of initial FGF-2 localization in bone formation. In specific, initially low levels of FGF-2 (in the case of the OPF group) localization appear to correlate with limited amounts of later bone formation, while initially high levels of FGF-2 localization (in the case of the PPF group) appear to correlate with increased bone formation. Beyond FGF-2, the OPF negative control showed significantly lower localization than the other groups in only the initial time points for PDGF-A.

Previous studies of the efficacy of a PPF scaffold for facilitating bone healing in a subcritical size, cranial defect showed minimal bone formation in PPF scaffold and a significant increase in bone formation for a PPF scaffold coated with TGF-β1 [59]. The

differing results between these studies reflect the significant variance in responses that can be observed even within subcritical size defects.

Finally, a similar study of growth factor localization, specifically PDGF-A, TGF-β1, and BMP-2, within the healing tooth extraction socket and in the absence of biomaterial implantation has been recently reported [182]. In this work, a general trend was observed: low growth factor localization through 4 weeks after tooth extraction, followed by a significant increase in localization at 8, 12, and 16 weeks after extraction. The work presented here displays the modulation of these trends by biomaterial implantation. Further differences between the previous work and the empty control socket within this study may be attributed to the further development of the methods used to analyze the immunohistochemical staining, most notably the standardization of the image acquisition procedure.

CONCLUSIONS

This work investigates the effects of a degradable biomaterial upon wound healing and bone formation within a tooth extraction socket. The results present a clear process of bone formation for 2 weeks after tooth extraction, followed by remodeling of the immature bone. Furthermore, the implantation of a hydrophobic, degradable biomaterial did not significantly alter this process, while a hydrophilic, degradable biomaterial significantly reduced bone formation. The results of the immunohistochemical study of angiogenic and osteogenic factors reflect the current theories of wound healing and bone formation: early invasion of platelets and inflammatory cells, vascularization of the wound healing tissue, differentiation of migrating progenitor cells, formation of bone tissue, maintenance of bone tissue

vascularization, and remodeling of bone tissue. The effect of biomaterial's surface properties upon bone formation most closely parallel the FGF-2 localization results, indicating its critical role in the initial phases of wound healing to facilitate later bone formation.

TABLE 10.1: Itemization of the number of repeats for the experimental and control groups within each time point.

		4 day	1 Week	2 Week	4 Week	8 Week
Empty	(Empty control)	n = 5	n = 5	n = 5	n = 3	n = 4
OPF	(Negative control)	n = 5	n = 5	n = 4	n = 5	n = 5
PPF	(Experimental)	n = 5	n = 5	n = 5	n = 4	n = 4
PPF+TGF	(Positive control)	n = 5	n = 5	n = 4	n = 4	n = 4

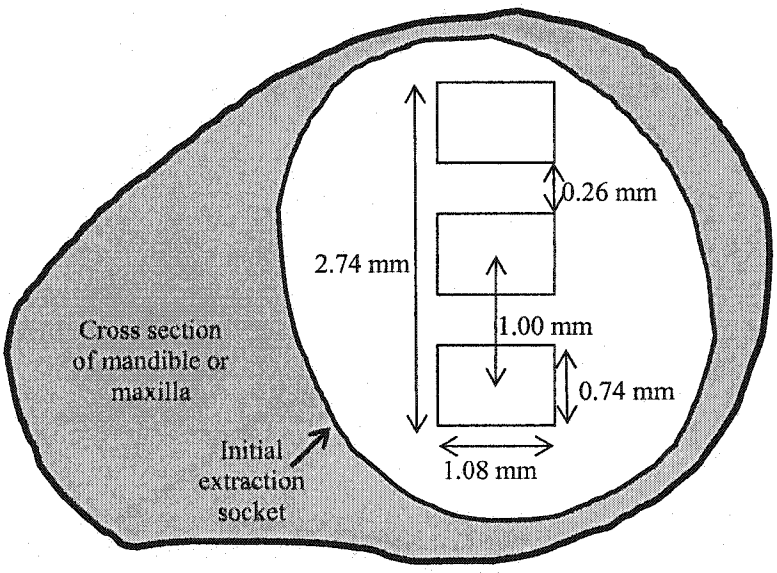

(A)

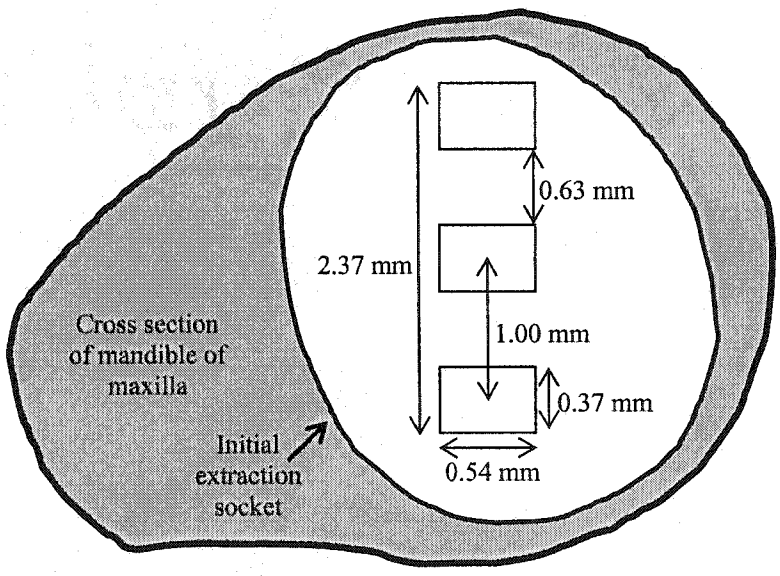

(B)

FIGURE 10.1: Schematic depiciting a typical histological section and the areas imaged for histomorphometrical analysis of bone formation **(A)** and immunohistochemical staining **(B)**.

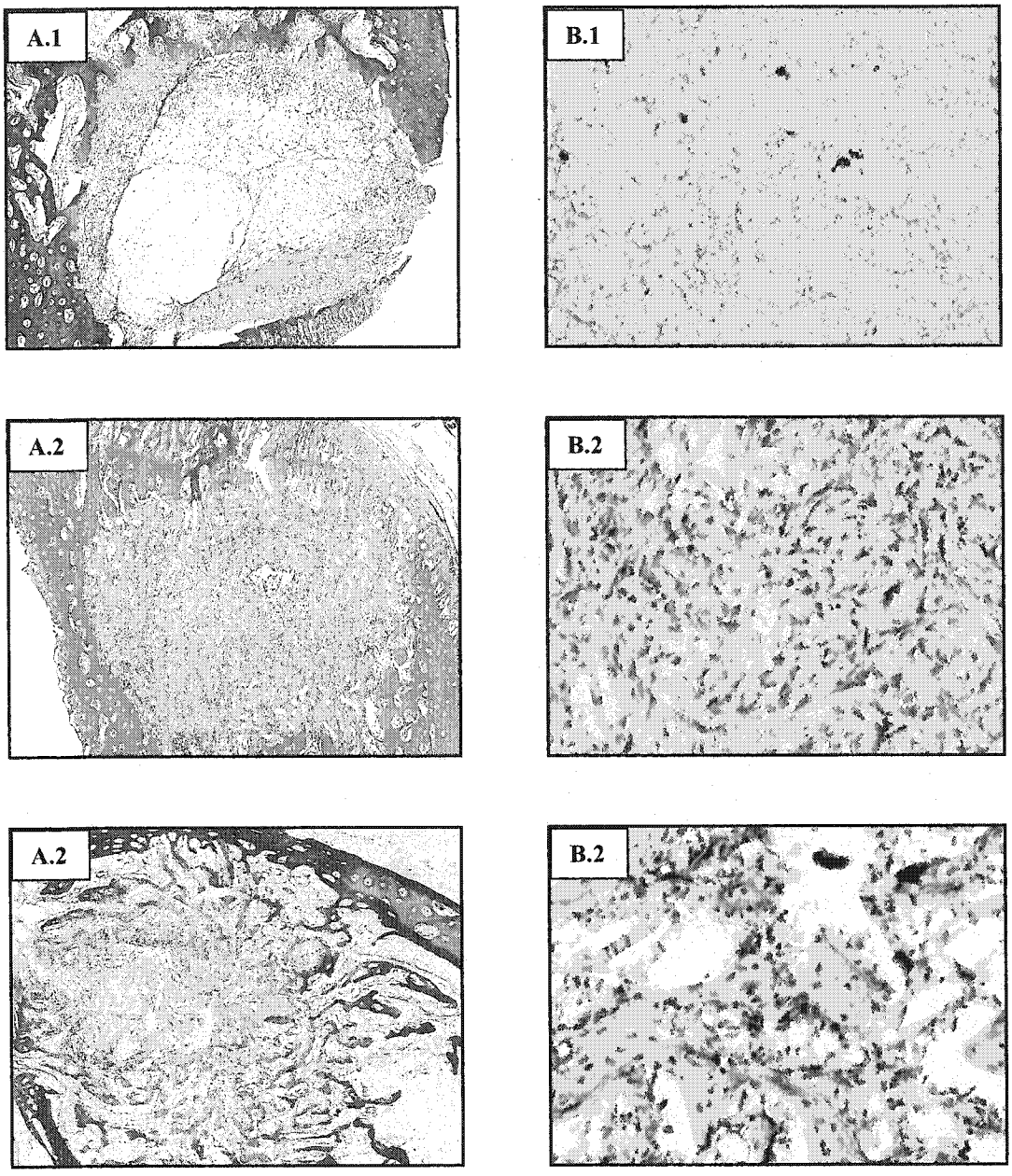

FIGURE 10.2: Light microscopy images of empty control sockets stained with hematoxylin and eosin at 4x magnification **(A)** or for FGF-2 at 20x magnification **(B)** at 4 days **(1)**, 1 week **(2)**, and 2 weeks **(3)** after tooth extraction. The H&E sections display the radial invasion of inflammatory cells followed by bone formation, while the corresponding FGF-2 stained sections show the localizationof the growth factor corresponding with wound healing and then bone formation.

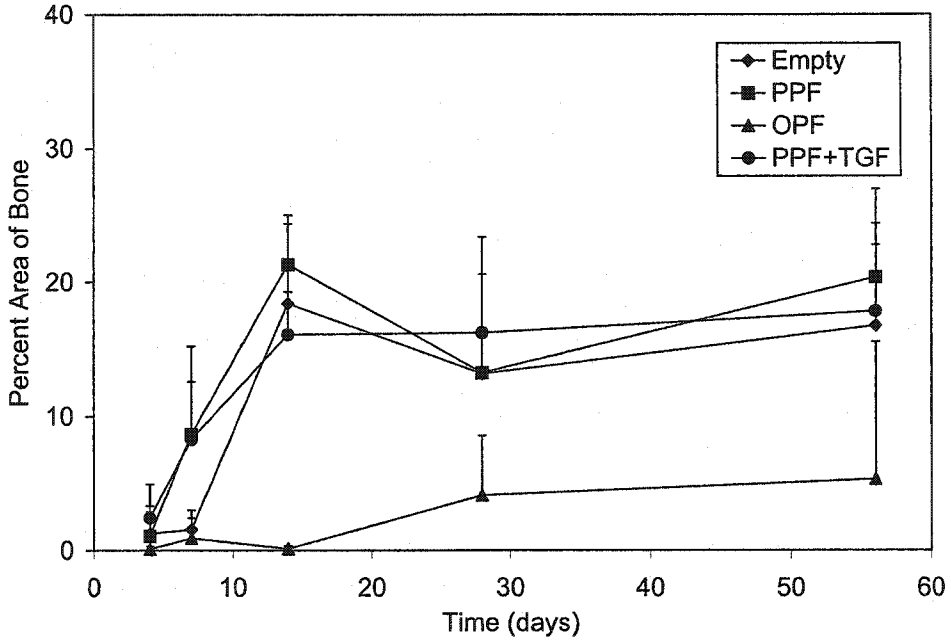

(A)

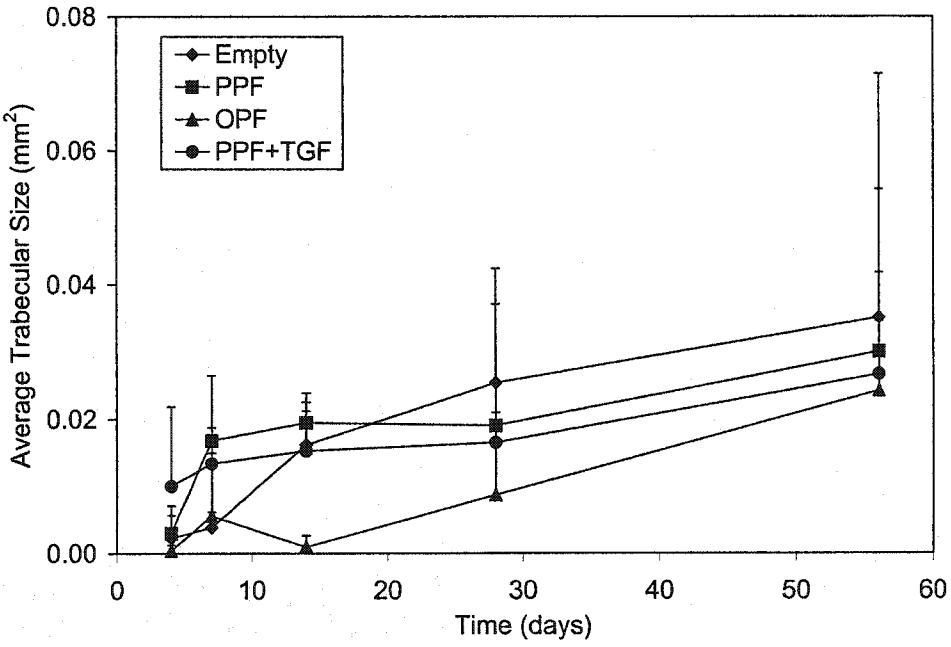

(B)

FIGURE 10.3: The percent area of bone **(A)** and the average trabecular size **(B)** for the experimental (PPF), negative control (OPF), positive control (PPF+TGF), and empty control (Empty) groups. For clarity, error bars are (+) standard deviation only. The number of subjects for each time point and group are listed in Table 10.1.

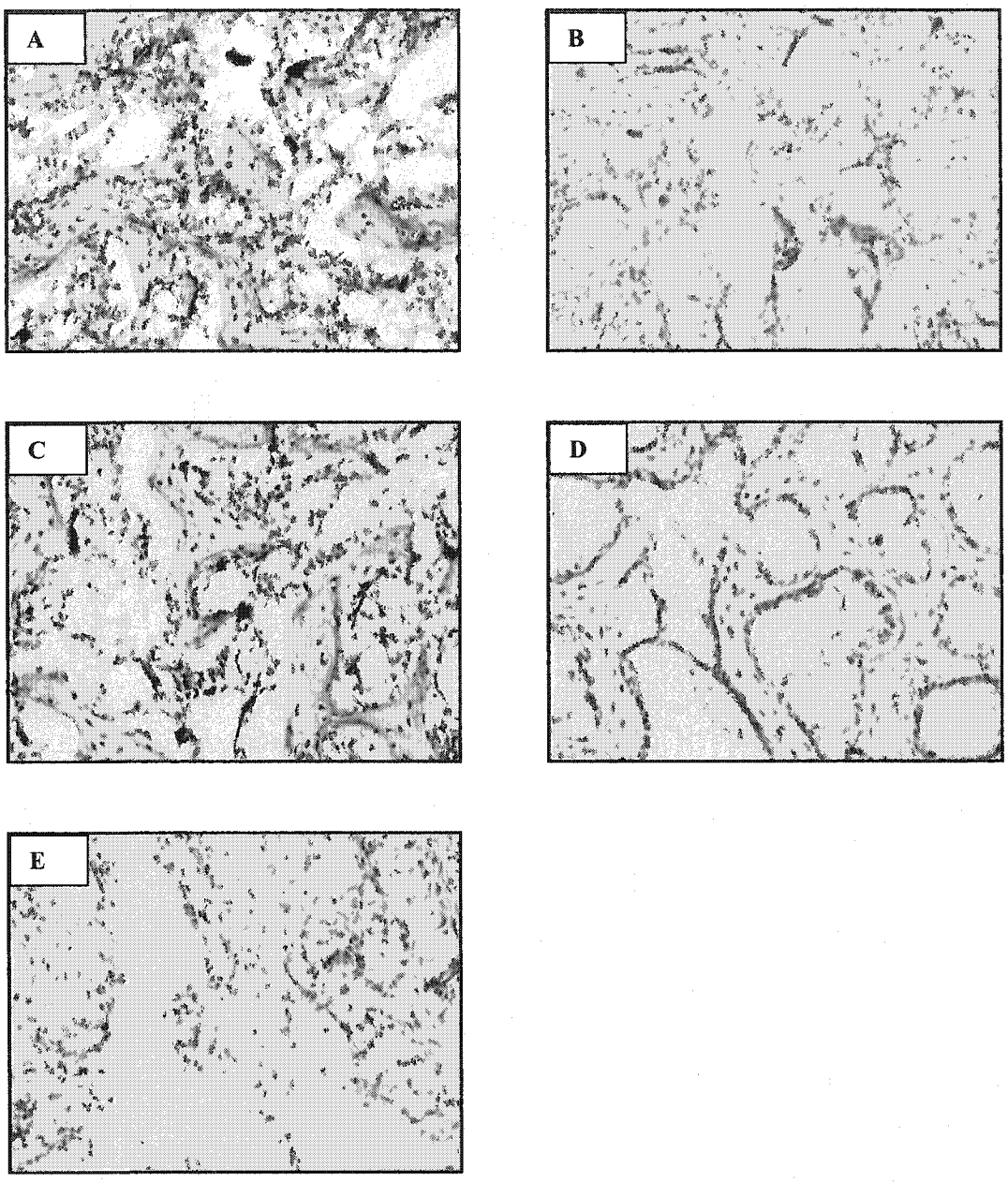

FIGURE 10.4: Light microscopy images (20x magnification) of empty control sockets stained immunohistochemically for the growth factors FGF-2 **(A)**, VEGF **(B)**, PDGF-A **(C)**, TGF-β1 **(D)**, and BMP-2 **(E)**. The images, taken two weeks after tooth extraction, depict the differing staining patterns of the growth factors within the developing bone tissue.

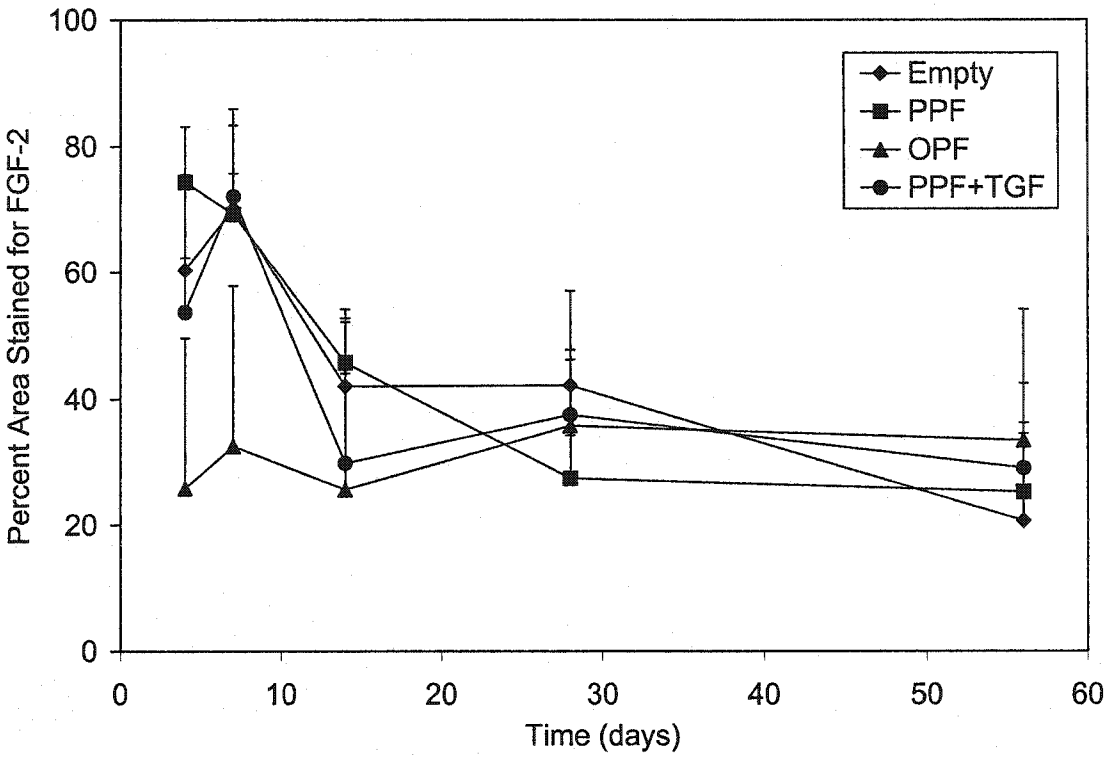

FIGURE 10.5: The percent area immunohistochemically stained for FGF-2 for the experimental (PPF), negative control (OPF), positive control (PPF+TGF), and empty control (Empty) groups. For clarity, error bars are (+) standard deviation only. The number of subjects for each time point and group are listed in Table 10.1.

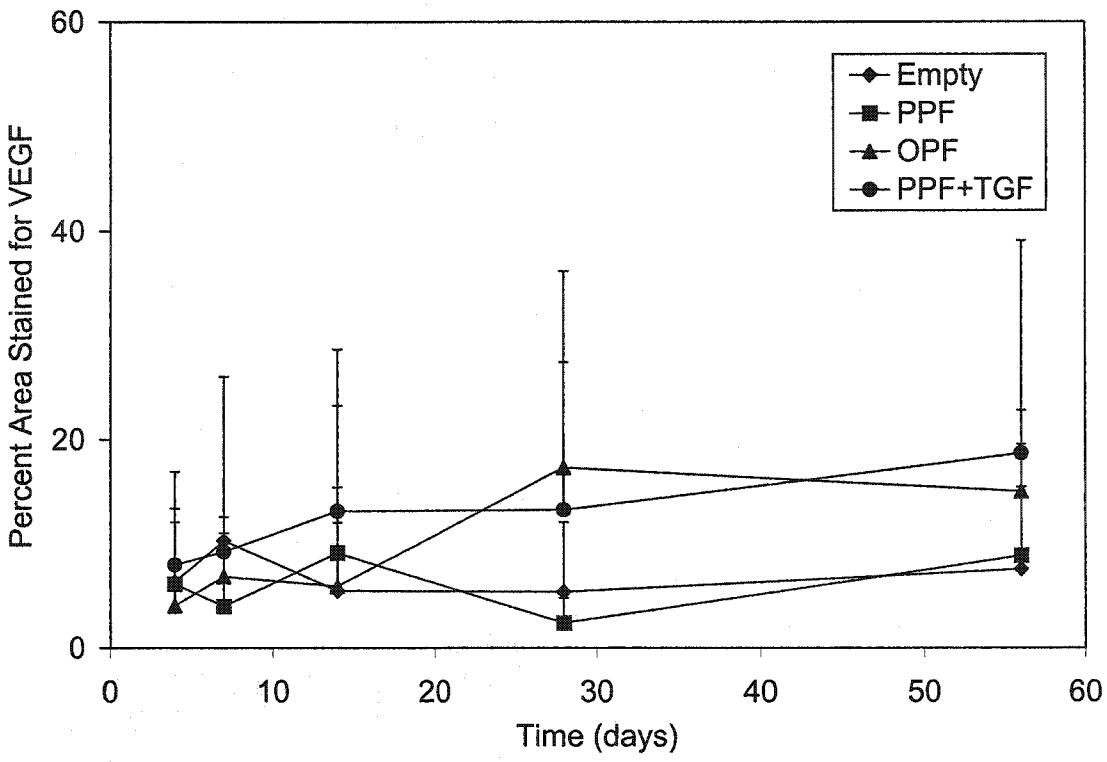

FIGURE 10.6: The percent area immunohistochemically stained for VEGF for the experimental (PPF), negative control (OPF), positive control (PPF+TGF), and empty control (Empty) groups. For clarity, error bars are (+) standard deviation only. The number of subjects for each time point and group are listed in Table 10.1.

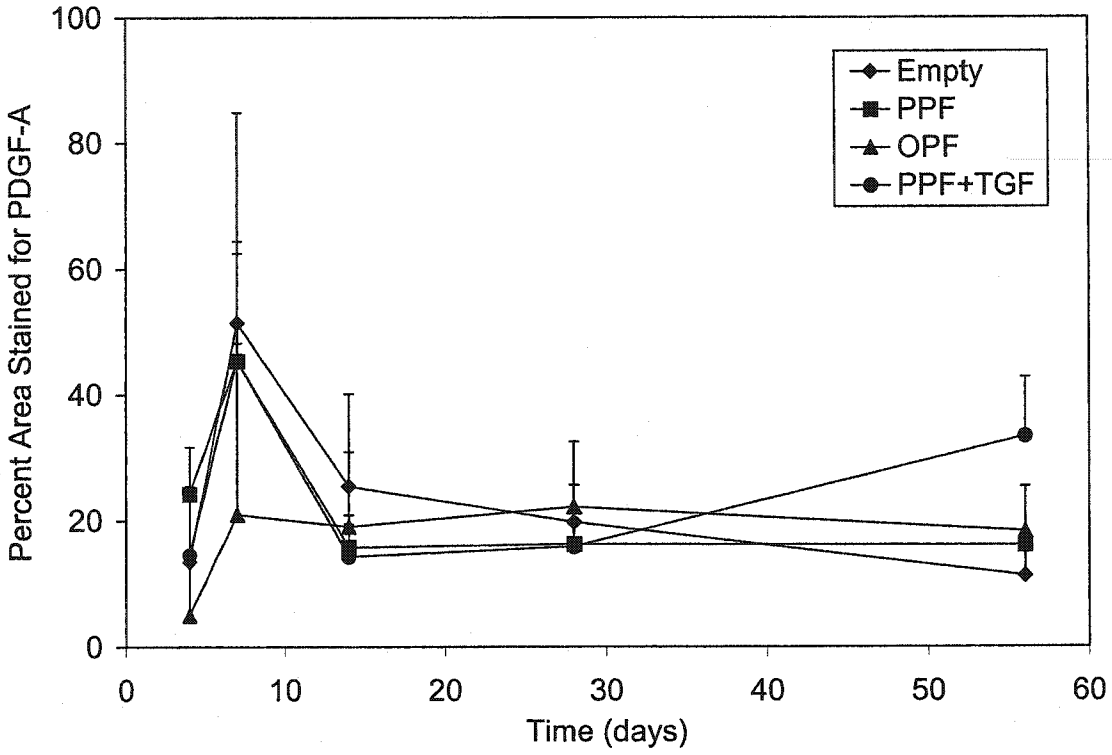

FIGURE 10.7: The percent area immunohistochemically stained for PDGF-A for the experimental (PPF), negative control (OPF), positive control (PPF+TGF), and empty control (Empty) groups. For clarity, error bars are (+) standard deviation only. The number of subjects for each time point and group are listed in Table 10.1.

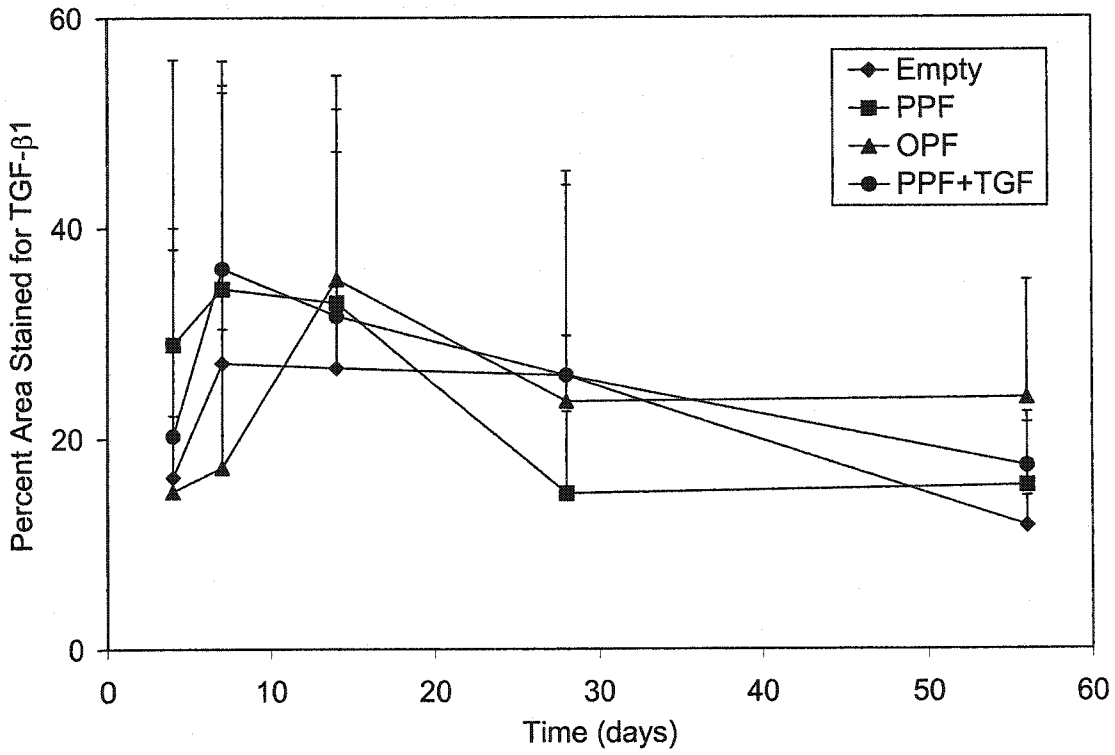

FIGURE 10.8: The percent area immunohistochemically stained for TGF-β1 for the experimental (PPF), negative control (OPF), positive control (PPF+TGF), and empty control (Empty) groups. For clarity, error bars are (+) standard deviation only. The number of subjects for each time point and group are listed in Table 10.1.

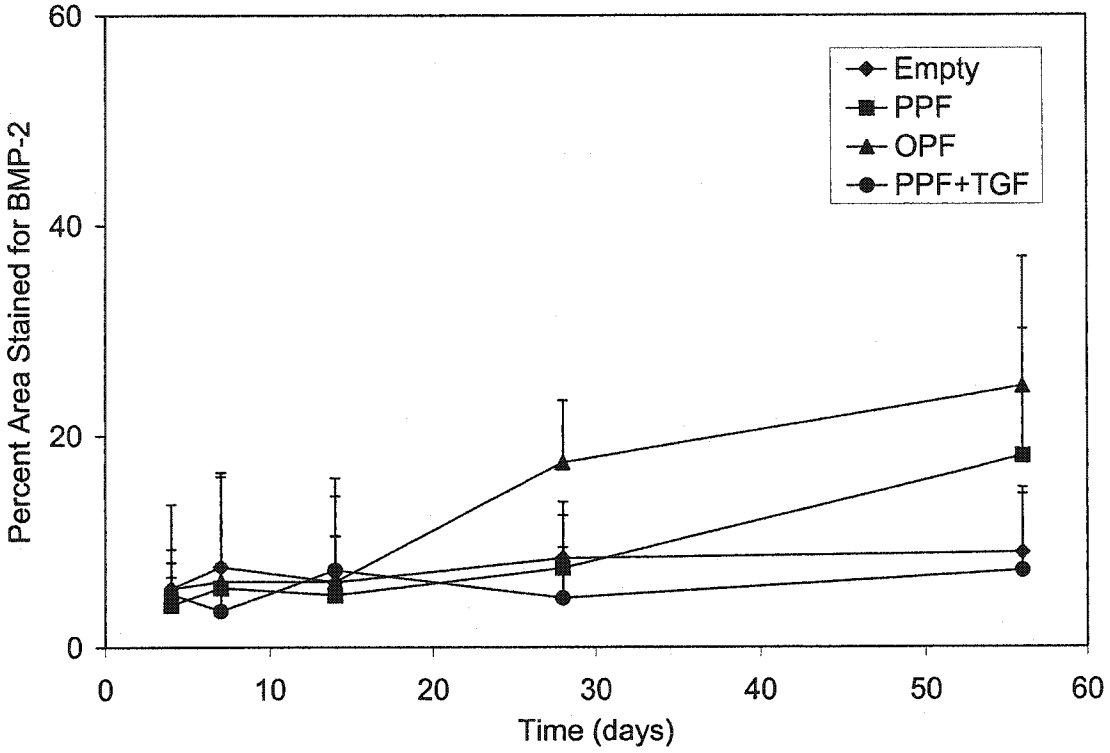

FIGURE 10.9: The percent area immunohistochemically stained for BMP-2 for the experimental (PPF), negative control (OPF), positive control (PPF+TGF), and empty control (Empty) groups. For clarity, error bars are (+) standard deviation only. The number of subjects for each time point and group are listed in Table 10.1.

CHAPTER XI

SUMMARY

The overall goal of this work was to develop and characterize a photocrosslinkable, degradable polymer for use in the fabrication of tissue engineering scaffolds. The first objective in this work was to develop a photocrosslinkable system for poly(propylene fumarate). Initial studies showed that the photoinitiator bis(2,4,6-trimethylbenzoyl) phenylphosphine oxide (BAPO) could effectively crosslink PPF upon low level ultraviolet light irradiation without the use of a crosslinking monomer. This biodegradable material, BAPO initiated photocrosslinked PPF, was then rigorously investigated throughout the remainder of this work.

The second objective of this work was to characterize the mechanism by which PPF is photocrosslinked as well as the final network structure of the crosslinked PPF polymer. By contrasting the fumarate conversion and bulk properties of BAPO crosslinked PPF with those of a monoacylphosphine oxide crosslinked PPF, it was concluded that a single phosphinoyl radical derived from BAPO was primarily responsible for the photoinitiated crosslinking of PPF. Furthermore, this knowledge of the crosslinking mechanism allowed for a determination of the general network structure of BAPO initiated, photocrosslinked PPF.

The third objective of this work was to fabricate the PPF photocrosslinkable material into porous scaffold using a porogen leaching technique and characterize the

effects of porogen inclusion upon the photocrosslinking mechanism. It was demonstrated that porous poly(propylene fumarate) scaffolds can be synthesized by using a photocrosslinking/porogen leaching strategy. These scaffolds were synthesized by the reaction of PPF with a photoinitiator around a NaCl porogen, which was subsequently removed by water leaching. The presence of the leachable porogen in cylindrical constructs (6.5 mm in diameter) was not found to affect the initiation of the PPF crosslinking reaction in this system. Characterization of the scaffolds, by both porosity measurements and SEM images, showed that the scaffolds synthesized with 80 wt% porogen or greater contained an interconnected pore structure.

The fourth objective of this work was to describe the *in vitro* degradation of photocrosslinked PPF scaffolds and to determine the effects of pore inclusion, pore size, and pore volume upon degradation. Thus, an *in vitro* degradation study of both solid PPF networks and porous PPF scaffolds in phosphate buffered-saline (pH = 7.4, 37°C) was performed over the course of 32 weeks. The results show that scaffold pore size and pore volume influence degradation, specifically scaffold mass loss, length reduction, and water absorption. However, throughout the degradation study, scaffold mechanical properties were generally retained. The results indicate that porogen size and content could be selected to formulate photocrosslinked PPF scaffolds with a degradation rate, porosity, and mechanical properties that match target values for a specific tissue defect. This flexibility in scaffold design supports the potential of photocrosslinked PPF as a composite material for tissue engineering.

The fifth objective of this work was to modify the PPF photocrosslinking strategy so that scaffold fabrication techniques which require the uncured PPF solution to be fluid

are feasible. A novel material was developed which was based upon poly(propylene fumarate) and its precursor diethyl fumarate (DEF), the crosslinkable unit contained within the repeating unit of PPF. Characterization studies demonstrated that these materials have a low viscosity, crosslink with low levels of heat release, and possess mechanical properties similar to human trabecular bone. These studies also indicated that in this polymer/polymer precursor system, crosslinking is facilitated at low precursor concentrations but hindered at higher precursor concentrations. These novel DEF/PPF materials may be an attractive option for bone tissue engineering applications.

The sixth objective of this work was to investigate the soft and hard tissue response to photocrosslinked PPF scaffolds and determine any effects of the scaffold pore morphology upon the tissue response. Thus, four classes of photocrosslinked PPF scaffolds, constructed with differing porosities (57% to 75%) and pore sizes (300 - 500 μm or 600 - 800 μm), were implanted both subcutaneously and in 6.3 mm diameter cranial defects in a rabbit model. The results of this *in vivo* study indicated that PPF is biocompatible within both soft and hard tissue. Minimal fibrous encapsulation of the scaffolds was found and tissue response appeared to improve with implantation time. A progressive reduction in inflammatory cell density and a continued organization of connective tissue with the interstitial space was observed. However, tissue response was not found to vary significantly with scaffold pore size or porosity. Evidence for PPF degradation after 8 weeks of implantation was noted both histologically and histomorphometrically.

The seventh objective of this work was to investigate whether photocrosslinked PPF scaffolds may act as a carrier for an adsorbed protein in order to promote bone

formation. Thus, the bone growth into pretreated PPF scaffolds implanted into a sub-critical size, rabbit cranial defect was examined. The results of this *in vivo* study indicated that a fibronectin coating, as applied in this study, does not modify the bone response to these PPF scaffolds. On the other hand, rhTGF-β1 did induce significant bone formation in these porous PPF scaffolds. These results indicate that porous PPF combined with an appropriate growth factor carrier is a good candidate for the creation of osteoinductive bone graft substitutes.

Finally, the eight objective of this work is to determine the effect of the photocrosslinked PPF scaffolds upon bone formation as assessed by histomorphometrical analysis of wound healing and growth factor localization. Thus, an *in vivo* study of the effects of a degradable biomaterial upon wound healing and bone formation within a tooth extraction socket was undertaken. The results presented a clear process of bone formation for 2 weeks after tooth extraction, followed by remodeling of the immature bone. Furthermore, the implantation of the hydrophobic and degradable PPF biomaterial did not significantly alter this process, while the negative control group, a hydrophilic, degradable biomaterial, significantly reduced bone formation. The results of the immunohistochemical study of angiogenic and osteogenic factors reflect the current theories of wound healing and bone formation: early invasion of platelets and inflammatory cells, vascularization of the wound healing tissue, differentiation of migrating progenitor cells, formation of bone tissue, maintenance of bone tissue vascularization, and remodeling of bone tissue. The effect of biomaterial's surface properties upon bone formation most closely parallel the FGF-2 localization results,

indicating its critical role in the initial phases of wound healing to facilitate later bone formation.

These studies has shown that photocrosslinked poly(propylene fumarate) has great potential as the basis for tissue engineering scaffolds. Furthermore, this work has shown that the development of a tissue engineering scaffold may be guided by a rigorous procedure beginning with the characterization of its chemical and physical properties, followed by an investigation of its *in vitro* and *in vivo* mechanical strength, degradation rate, and tissue response.

CHAPTER XII

LITERATURE CITED

1. Wayne RP. Principles and applications of photochemistry. Oxford: Oxford University Press; 1988.

2. Rabek JF. Mechanisms of photophysical processes and photochemical reactions in polymers : theory and applications. New York: Wiley; 1987.

3. Calvert JG, Pitts JN. Photochemistry. New York,: Wiley; 1966.

4. Silverstein RM, Bassler GC, Morrill TC. Spectrometric identification of organic compounds (5th ed). New York: Wiley; 1991.

5. Odian GG. Principles of polymerization (3rd ed). New York: Wiley; 1991.

6. Fouassier J-P. Photoinitiation, photopolymerization, and photocuring : fundamentals and applications. Munich: Hanser; 1995.

7. Kubota H, Fukuda A. Photopolymerization synthesis of poly(N-isopropylacrylamide) hydrogels. J Appl Polym Sci. 1997;65:1313-1318.

8. Lai YC, Quinn ET. The effects of initiator and diluent on the photopolymerization of 2-hydroxyethyl methacrylate and on properties of hydrogels obtained. In: Peiffer RW, ed. ACS Symposium Series: Photopolymerization: Fundamentals and applications. Vol. 673. Washington, D. C.: American Chemical Society; 1997:35-50.

9. Lai YC. Effects of crosslinkers on photocopolymerization of N-vinylpyrrolidone and methacrylates to give hydrogels. J Appl Polym Sci. 1997;66:1475-1484.

10. John G, Morita M. Synthesis and characterization of photo-crosslinked netwroks based on L-lactide/serine copolymers. Macromolecules. 1999;32:1853-1858.

11. Kim BS, Hrkach JS, Langer R. Biodegradable photo-crosslinked poly(ether-ester) networks for lubricious coatings. Biomaterials. 2000;21:259-265.

12. Burkoth AK, Burdick J, Anseth KS. Surface and bulk modifications to photocrosslinked polyanhydrides to control degradation behavior. J Biomed Mater Res. 2000;51:352-359.

13. Bruining MJ, Edelbroek-Hoogendoorn PS, Blaauwgeers HG, Mooy CM, Hendrikse FH, Koole LH. New biodegradable networks of poly(N-vinylpyrrolidinone) designed for controlled nonburst degradation in the vitreous body. J Biomed Mater Res. 1999;47:189-197.

14. Guggenberger R, Lechner G, Weinmann W. Bisacylphosphine oxides as photoinitiators in dental materials. Polym Preprints. 1997;38:105.

15. Ono K, Saito Y, Yura H, Ishikawa K, Kurita A, Akaike T, Ishihara M. Photocrosslinkable chitosan as a biological adhesive. J Biomed Mater Res. 2000;49:289-295.

16. Ahn KD, Chung CM, Kim YH. Synthesis and photopolymerization of multifunctional methacrylates derived from Bis-GMA for dental applications. J Appl Polym Sci. 1999;71:2033-2037.

17. Andreopoulos FM, Beckman EJ, Russell AJ. Light-induced tailoring of PEG-hydrogel properties. Biomaterials. 1998;19:1343-1352.

18. Andreopoulos FM, Deible CR, Stauffer MT, Weber SG, Wagner WR, Beckman EJ, Russell AJ. Photoscissable hydrogel synthesis via rapid photopolymerization of novel PEG-based polymers in the absence of photoinitiators. J Am Chem Soc. 1996;118:6235-6240.

19. Scott RA, Peppas NA. Highly crosslinked, PEG-containing copolymers for sustained solute delivery. Biomaterials. 1999;20:1371-1380.

20. Han DK, Hubbell JA. Synthesis of polymer network scaffolds from L-lactide and poly(ethylene glycol) and their interaction with cells. Macromolecules. 1997;30:6077-6083.

21. Hill-West JL, Chowdhury SM, Slepian MJ, Hubbell JA. Inhibition of thrombosis and intimal thickening by in situ photopolymerization of thin hydrogel barriers. Proc Natl Acad Sci U S A. 1994;91:5967-5971.

22. Hill-West JL, Dunn RC, Hubbell JA. Local release of fibrinolytic agents for adhesion prevention. J Surg Res. 1995;59:759-763.

23. West JL, Hubbell JA. Separation of the arterial wall from blood contact using hydrogel barriers reduces intimal thickening after balloon injury in the rat: the roles of medial and luminal factors in arterial healing. Proc Natl Acad Sci U S A. 1996;93:13188-13193.

24. Chowdhury SM, Hubbell JA. Adhesion prevention with ancrod released via a tissue-adherent hydrogel. J Surg Res. 1996;61:58-64.

25. An Y, Hubbell JA. Intraarterial protein delivery via intimally-adherent bilayer hydrogels. J Control Release. 2000;64:205-215.

26. Lu S, Anseth KS. Photopolymerization of multilaminated poly(HEMA) hydrogels for controlled release. J Control Release. 1999;57:291-300.

27. Matsuda T, Mizutani M, Arnold SC. Molecular design of photocurable liquid biodegradable copolymers. 1. Synthesis and photocuring characteristics. Macromolecules. 2000;33:795-800.

28. Gursel I, Balcik C, Arica Y, Akkus O, Akkas N, Hasirci V. Synthesis and mechanical properties of interpenetrating networks of polyhydroxybutyrate-co-hydroxyvalerate and polyhydroxyethyl methacrylate. Biomaterials. 1998;19:1137-1143.

29. Cook WD. Thermal aspects of the kinetics of dimethacrylate photopolymerization. Polymer. 1992;33:2152-2161.

30. Maffezzoli A, Della Pietra A, Rengo S, Nicolais L, Valletta G. Photopolymerization of dental composite matrices. Biomaterials. 1994;15:1221-1228.

31. Venhoven BA, de Gee AJ, Davidson CL. Light initiation of dental resins: dynamics of the polymerization. Biomaterials. 1996;17:2313-2318.

32. Chung CM, Kim JG, Choi JH. Synthesis and photopolymerization of dicarboxylic acid dimethacrylates and their application as dental monomers. J Appl Polym Sci. 2000;77:1802-1808.

33. Anseth KS, Shastri VR, Langer R. Photopolymerizable degradable polyanhydrides with osteocompatibility. Nat Biotechnol. 1999;17:156-159.

34. Anseth KS, Svaldi DC, Laurencin CT, Langer R. Photopolymerization of novel degradable networks for orthopedic applications. In: Peiffer RW, ed. ACS Symposium Series: Photopolymerization: Fundamentals and applications. Vol. 673. Washington, D. C.: American Chemical Society; 1997:182-202.

35. Young JS, Gonzales KD, Anseth KS. Photopolymers in orthopedics: characterization of novel crosslinked polyanhydrides. Biomaterials. 2000;21:1181-1188.

36. Muggli DS, Burkoth AK, Keyser SA, Lee HR, Anseth KS. Reaction behavior of biodegradable, photo-cross-linkable polyanhydrides. Macromolecules. 1998;31:4120-4125.

37. Muggli DS, Burkoth AK, Anseth KS. Crosslinked polyanhydrides for use in orthopedic applications: degradation behavior and mechanics. J Biomed Mater Res. 1999;46:271-278.

38. D'Urso PS, Earwaker WJ, Barker TM, Redmond MJ, Thompson RG, Effeney DJ, Tomlinson FH. Custom cranioplasty using stereolithography and acrylic. Br J Plast Surg. 2000;53:200-204.

39. Fallahi B, Foroutan M, Motavalli S, Dujovny M, Limaye S. Computer-aided manufacturing of implants for the repair of large cranial defects: an improvement of the stereolithography technique. Neurol Res. 1999;21:281-286.

40. Eufinger H, Wehmoller M, Scholz M, Harders A, Machtens E. Reconstruction of an extreme frontal and frontobasal defect by microvascular tissue transfer and a prefabricated titanium implant. Plast Reconstr Surg. 1999;104:198-203.

41. Bryant SJ, Nuttelman CR, Anseth KS. Cytocompatibility of UV and visible light photoinitiating systems on cultured NIH/3T3 fibroblasts in vitro. J Biomater Sci Polym Ed. 2000;11:439-457.

42. Orban JM, Faucher KM, Dluhy RA, Chaikof EL. Cytomimetic biomaterials. 4. In-situ photopolymerization of phospholipids on an alkylated surface. Macromolecules. 2000;33:4205-4212.

43. Nakayama Y, Miyamura M, Hirano Y, Goto K, Matsuda T. Preparation of poly(ethylene glycol)-polystyrene block copolymers using photochemistry of dithiocarbamate as a reduced cell-adhesive coating material. Biomaterials. 1999;20:963-970.

44. Hern DL, Hubbell JA. Incorporation of adhesion peptides into nonadhesive hydrogels useful for tissue resurfacing. J Biomed Mater Res. 1998;39:266-276.

45. Elisseeff J, Anseth K, Sims D, McIntosh W, Randolph M, Langer R. Transdermal photopolymerization for minimally invasive implantation. Proc Natl Acad Sci U S A. 1999;96:3104-3107.

46. Elisseeff J, McIntosh W, Anseth K, Riley S, Ragan P, Langer R. Photoencapsulation of chondrocytes in poly(ethylene oxide)-based semi-interpenetrating networks. J Biomed Mater Res. 2000;51:164-171.

47. Cruise GM, Hegre OD, Scharp DS, Hubbell JA. A sensitivity study of the key parameters in the interfacial photopolymerization of poly(ethylene glycol) diacrylate upon porcine islets. Biotechnol Bioeng. 1998;57:655-665.

48. Cruise GM, Scharp DS, Hubbell JA. Characterization of permeability and network structure of interfacially photopolymerized poly(ethylene glycol) diacrylate hydrogels. Biomaterials. 1998;19:1287-1294.

49. Mikos AG, Thorsen AJ, Czerwonka LA, Bao Y, Langer R, Winslow DN, Vacanti JP. Preparation and characterization of poly(L-lactic acid) foams. Polymer. 1994;35:1068-1077.

50. Behravesh E, Yasko AW, Engel PS, Mikos AG. Synthetic biodegradable polymers for orthopaedic applications. Clin Orthop. 1999:S118-129.

51. Peter SJ, Miller ST, Zhu G, Yasko AW, Mikos AG. In vivo degradation of a poly(propylene fumarate)/beta-tricalcium phosphate injectable composite scaffold. J Biomed Mater Res. 1998;41:1-7.

52. Gresser JD, Hsu SH, Nagaoka H, Lyons CM, Nieratko DP, Wise DL, Barabino GA, Trantolo DJ. Analysis of a vinyl pyrrolidone/poly(propylene fumarate) resorbable bone cement. J Biomed Mater Res. 1995;29:1241-1247.

53. Lewandrowski KU, Gresser JD, Wise DL, Trantol DJ. Bioresorbable bone graft substitutes of different osteoconductivities: a histologic evaluation of osteointegration of poly(propylene glycol-co-fumaric acid)-based cement implants in rats. Biomaterials. 2000;21:757-764.

54. Peter SJ, Kim P, Yasko AW, Yaszemski MJ, Mikos AG. Crosslinking characteristics of an injectable poly(propylene fumarate)/beta-tricalcium phosphate paste and mechanical properties of the crosslinked composite for use as a biodegradable bone cement. J Biomed Mater Res. 1999;44:314-321.

55. Gatlik I, Rzadek P, Gescheidt G, Rist G, Hellrung B, Wirz J, Dietliker K, Kunz M, Wolf JP. Structure-reactivity relationships in radical reactions: A novel method for the simultaneous determination of absolute rate constants and structural features. J Am Chem Soc. 1999;121:8332-8336.

56. Jockusch S, Turro NJ. Phosphinoyl radicals: Structure and reactivity. A laser flash photolysis and time-resolved ESR investigation. J Am Chem Soc. 1998;120:11773-11777.

57. Kolczak U, Rist G, Dietliker K, Wirz J. Reaction mechanism of monoacyl- and bisacylphosphine oxide photoinitiators studied by ^{31}P-, ^{13}C, and ^{1}H-CIDNP and ESR. J Am Chem Soc. 1996;118:6477-6489.

58. Fisher JP, Dean D, Engel PS, Mikos AG. Photoinitiated polymerization of biomaterials. Annu Rev Mater Res. 2001;31:171-181.

59. Vehof JW, Fisher JP, Dean D, van der Waerden JP, Spauwen PH, Mikos AG, Jansen JA. Bone formation in transforming growth factor beta-1-coated porous poly(propylene fumarate) scaffolds. J Biomed Mater Res. 2002;60:241-251.

60. Fisher JP, Holland TA, Dean D, Engel PS, Mikos AG. Synthesis and properties of photocross-linked poly(propylene fumarate) scaffolds. J Biomater Sci Polym Ed. 2001;12:673-687.

61. Fisher JP, Vehof JW, Dean D, van der Waerden JP, Holland TA, Mikos AG, Jansen JA. Soft and hard tissue response to photocrosslinked poly(propylene fumarate) scaffolds in a rabbit model. J Biomed Mater Res. 2002;59:547-556.

62. Shung AK, Timmer MD, Jo S, Engel PS, Mikos AG. Kinetics of poly(propylene fumarate) synthesis by step polymerization of diethyl fumarate and propylene glycol using zinc chloride as a catalyst. J Biomater Sci Polym Ed. 2002;13:95-108.

63. Timmer M, Jo S, Wang C, Ambrose CG, Mikos AG. Characterization of the Cross-Linked Structure of Fumarate-Based Degradable Polymer Networks. Macromolecules. 2002;35:4373-4379.

64. Hogg RV, Ledolter J. Applied statistics for engineers and physical scientists (2nd ed). New York: Macmillan; 1992.

65. Brandrup J, Immergut EH. Polymer handbook (3rd ed). New York: Wiley; 1989.

66. Han DK, Park KD, Hubbell JA, Kim YH. Surface characteristics and biocompatibility of lactide-based poly(ethylene glycol) scaffolds for tissue engineering. J Biomater Sci Polym Ed. 1998;9:667-680.

67. Nam YS, Yoon JJ, Park TG. A novel fabrication method of macroporous biodegradable polymer scaffolds using gas foaming salt as a porogen additive. J Biomed Mater Res. 2000;53:1-7.

68. Patrick CW, Mikos AG, McIntire LV. Frontiers in tissue engineering (1st ed). Oxford, U.K.: Pergamon; 1998.

69. Holy CE, Shoichet MS, Davies JE. Engineering three-dimensional bone tissue in vitro using biodegradable scaffolds: investigating initial cell-seeding density and culture period. J Biomed Mater Res. 2000;51:376-382.

70. Perka C, Schultz O, Spitzer RS, Lindenhayn K, Burmester GR, Sittinger M. Segmental bone repair by tissue-engineered periosteal cell transplants with bioresorbable fleece and fibrin scaffolds in rabbits. Biomaterials. 2000;21:1145-1153.

71. Marra KG, Szem JW, Kumta PN, DiMilla PA, Weiss LE. In vitro analysis of biodegradable polymer blend/hydroxyapatite composites for bone tissue engineering. J Biomed Mater Res. 1999;47:324-335.

72. Whang K, Tsai DC, Nam EK, Aitken M, Sprague SM, Patel PK, Healy KE. Ectopic bone formation via rhBMP-2 delivery from porous bioabsorbable polymer scaffolds. J Biomed Mater Res. 1998;42:491-499.

73. Peter SJ, Nolley JA, Widmer MS, Merwin JE, Yaszemski MJ, Yasko AW, Engel PS, Mikos AG. In vitro degradation of a poly(propylene fumarate)/β-tricalcium phosphate composite orthopaedic scaffold. Tissue Eng. 1997;3:207-215.

74. Thomson RC, Yaszemski MJ, Powers JM, Mikos AG. Hydroxyapatite fiber reinforced poly(alpha-hydroxy ester) foams for bone regeneration. Biomaterials. 1998;19:1935-1943.

75. Zhang R, Ma PX. Poly(alpha-hydroxyl acids)/hydroxyapatite porous composites for bone-tissue engineering. I. Preparation and morphology. J Biomed Mater Res. 1999;44:446-455.

76. Athanasiou KA, Zhu C, Lanctot DR, Agrawal CM, Wang X. Fundamentals of biomechanics in tissue engineering of bone. Tissue Eng. 2000;6:361-381.

77. Hutmacher DW. Scaffolds in tissue engineering bone and cartilage. Biomaterials. 2000;21:2529-2543.

78. An YH, Woolf SK, Friedman RJ. Pre-clinical in vivo evaluation of orthopaedic bioabsorbable devices. Biomaterials. 2000;21:2635-2652.

79. Burg KJ, Porter S, Kellam JF. Biomaterial developments for bone tissue engineering. Biomaterials. 2000;21:2347-2359.

80. Widmer MS, Mikos AG. Fabrication of biodegradable polymer scaffolds. In: McIntire LV, ed. Frontiers in tissue engineering (1st ed). Oxford, U.K.: Pergamon; 1998:107-120.

81. Middleton JC, Tipton AJ. Synthetic biodegradable polymers as orthopedic devices. Biomaterials. 2000;21:2335-2346.

82. He S, Timmer M, Yaszemski MJ, Yasko AW, Engel PS, Mikos AG. Synthesis of biodegradable poly(propylene fumarate) networks with poly(propylene fumarate)-diacrylate macromers as crosslinking agents and characterization of their degradation products. Polymer. 2000;42:1251-1260.

83. Lu L, Peter SJ, Lyman MD, Lai HL, Leite SM, Tamada JA, Vacanti JP, Langer R, Mikos AG. In vitro degradation of porous poly(L-lactic acid) foams. Biomaterials. 2000;21:1595-1605.

84. Temenoff JS, Mikos AG. Injectable biodegradable materials for orthopedic tissue engineering. Biomaterials. 2000;21:2405-2412.

85. Lee KY, Alsberg E, Mooney DJ. Degradable and injectable poly(aldehyde guluronate) hydrogels for bone tissue engineering. J Biomed Mater Res. 2001;56:228-233.

86. Gauthier O, Bouler JM, Weiss P, Bosco J, Daculsi G, Aguado E. Kinetic study of bone ingrowth and ceramic resorption associated with the implantation of different injectable calcium-phosphate bone substitutes. J Biomed Mater Res. 1999;47:28-35.

87. Frankenburg EP, Goldstein SA, Bauer TW, Harris SA, Poser RD. Biomechanical and histological evaluation of a calcium phosphate cement. J Bone Joint Surg Am. 1998;80:1112-1124.

88. Iooss P, Le Ray AM, Grimandi G, Daculsi G, Merle C. A new injectable bone substitute combining poly(epsilon-caprolactone) microparticles with biphasic calcium phosphate granules. Biomaterials. 2001;22:2785-2794.

89. Neter J, Wasserman W, Kutner MH. Applied linear statistical models : regression, analysis of variance, and experimental designs (2nd ed). Homewood, Ill.: R.D. Irwin; 1985.

90. Grimandi G, Weiss P, Millot F, Daculsi G. In vitro evaluation of a new injectable calcium phosphate material. J Biomed Mater Res. 1998;39:660-666.

91. Kèuhn KD. Bone cements : up-to-date comparison of physical and chemical properties of commercial materials. Berlin: Springer; 2000.

92. Eriksson A, Albrektsson T, Grane B, McQueen D. Thermal injury to bone. A vital-microscopic description of heat effects. Int J Oral Surg. 1982;11:115-121.

93. Wilcox CW, Wilwerding TM, Watson P, Morris JT. Use of electrosurgery and lasers in the presence of dental implants. Int J Oral Maxillofac Implants. 2001;16:578-582.

94. Jacobs PF. Stereolithography and other RP&M technologies: from rapid prototyping to rapid tooling. New York: American Society of Manufacturing Engineers Press; 1996.

95. Temenoff JS, Lu L, Mikos AG. Bone-tissue engineering using synthetic biodegradable polymer scaffolds. In: Davies JE, ed. Bone engineering. Toronto: em squared incorporated; 2000:454-461.

96. Solheim E, Sudmann B, Bang G, Sudmann E. Biocompatibility and effect on osteogenesis of poly(ortho ester) compared to poly(DL-lactic acid). J Biomed Mater Res. 2000;49:257-263.

97. van der Elst M, Klein CP, de Blieck-Hogervorst JM, Patka P, Haarman HJ. Bone tissue response to biodegradable polymers used for intra medullary fracture fixation: a long-term in vivo study in sheep femora. Biomaterials. 1999;20:121-128.

98. Ibim SM, Uhrich KE, Bronson R, El-Amin SF, Langer RS, Laurencin CT. Poly(anhydride-co-imides): in vivo biocompatibility in a rat model. Biomaterials. 1998;19:941-951.

99. Jansen JA, de Ruijter JE, Janssen PT, Paquay YG. Histological evaluation of a biodegradable Polyactive/hydroxyapatite membrane. Biomaterials. 1995;16:819-827.

100. Koempel JA, Patt BS, O'Grady K, Wozney J, Toriumi DM. The effect of recombinant human bone morphogenetic protein-2 on the integration of porous hydroxyapatite implants with bone. J Biomed Mater Res. 1998;41:359-363.

101. Beck LS, Amento EP, Xu Y, Deguzman L, Lee WP, Nguyen T, Gillett NA. TGF-beta 1 induces bone closure of skull defects: temporal dynamics of bone formation in defects exposed to rhTGF-beta 1. J Bone Miner Res. 1993;8:753-761.

102. Boyan BD, Lohmann CH, Somers A, Niederauer GG, Wozney JM, Dean DD, Carnes DL, Jr., Schwartz Z. Potential of porous poly-D,L-lactide-co-glycolide particles as a carrier for recombinant human bone morphogenetic protein-2 during osteoinduction in vivo. J Biomed Mater Res. 1999;46:51-59.

103. Lu L, Stamatas GN, Mikos AG. Controlled release of transforming growth factor beta1 from biodegradable polymer microparticles. J Biomed Mater Res. 2000;50:440-451.

104. Peter SJ, Lu L, Kim DJ, Stamatas GN, Miller MJ, Yaszemski MJ, Mikos AG. Effects of transforming growth factor beta1 released from biodegradable polymer microparticles on marrow stromal osteoblasts cultured on poly(propylene fumarate) substrates. J Biomed Mater Res. 2000;50:452-462.

105. Ishaug-Riley SL, Crane GM, Gurlek A, Miller MJ, Yasko AW, Yaszemski MJ, Mikos AG. Ectopic bone formation by marrow stromal osteoblast transplantation using poly(DL-lactic-co-glycolic acid) foams implanted into the rat mesentery. J Biomed Mater Res. 1997;36:1-8.

106. Shea LD, Wang D, Franceschi RT, Mooney DJ. Engineered bone development from a pre-osteoblast cell line on three-dimensional scaffolds. Tissue Eng. 2000;6:605-617.

107. Yaszemski MJ, Payne RG, Hayes WC, Langer R, Mikos AG. In vitro degradation of a poly(propylene fumarate)-based composite material. Biomaterials. 1996;17:2127-2130.

108. Mikos AG, Lyman MD, Freed LE, Langer R. Wetting of poly(L-lactic acid) and poly(DL-lactic-co-glycolic acid) foams for tissue culture. Biomaterials. 1994;15:55-58.

109. van der Lubbe HB, Klein CP, de Groot K. A simple method for preparing thin (10 μm) histological sections of undecalcified plastic embedded bone with implants. Stain Technol. 1988;63:171-176.

110. Jansen JA, Dhert WJ, van der Waerden JP, von Recum AF. Semi-quantitative and qualitative histologic analysis method for the evaluation of implant biocompatibility. J Invest Surg. 1994;7:123-134.

111. Hong L, Tabata Y, Yamamoto M, Miyamoto S, Yamada K, Hashimoto N, Ikada Y. Comparison of bone regeneration in a rabbit skull defect by recombinant human BMP-2 incorporated in biodegradable hydrogel and in solution. J Biomater Sci Polym Ed. 1998;9:1001-1014.

112. Ashby ER, Rudkin GH, Ishida K, Miller TA. Evaluation of a novel osteogenic factor, bone cell stimulating substance, in a rabbit cranial defect model. Plast Reconstr Surg. 1996;98:420-426.

113. Levy FE, Hollinger JO, Szachowicz EH. Effect of a bioresorbable film on regeneration of cranial bone. Plast Reconstr Surg. 1994;93:307-312.

114. Miller TA, Ishida K, Kobayashi M, Wollman JS, Turk AE, Holmes RE. The induction of bone by an osteogenic protein and the conduction of bone by porous hydroxyapatite: a laboratory study in the rabbit. Plast Reconstr Surg. 1991;87:87-95.

115. Valdevit A, Turegun M, Kambic H, Siemionow M, Zins J. Cranial defect repair using e-PTFE: part I. Evaluation of bone stiffness. J Biomed Mater Res. 2000;53:62-66.

116. Hammerle CH, Schmid J, Lang NP, Olah AJ. Temporal dynamics of healing in rabbit cranial defects using guided bone regeneration. J Oral Maxillofac Surg. 1995;53:167-174.

117. Schmitz JP, Hollinger JO. The critical size defect as an experimental model for craniomandibulofacial nonunions. Clin Orthop. 1986:299-308.

118. Davies JE, Hosseini MM. Histodynamics of endosseous wound healing. In: Davies JE, ed. Bone engineering. Toronto: em squared incorporated; 2000:1-14.

119. Marx RE. Platelet concentrate: A strategy for accelerating and improving bone regeneration. In: Davies JE, ed. Bone engineering. Toronto: em squared incorporated; 2000:447-453.

120. Dean D, Topham NS, Rimnac C, Mikos AG, Goldberg DP, Jepsen K, Redtfeldt R, Liu Q, Pennington D, Ratcheson R. Osseointegration of preformed

polymethylmethacrylate craniofacial prostheses coated with bone marrow-impregnated poly (DL-lactic-co-glycolic acid) foam. Plast Reconstr Surg. 1999;104:705-712.

121. Whang K, Healy KE, Elenz DR, Nam EK, Tsai DC, Thomas CH, Nuber GW, Glorieux FH, Travers R, Sprague SM. Engineering bone regeneration with bioabsorbable scaffolds with novel microarchitecture. Tissue Eng. 1999;5:35-51.

122. Baksh D, Davies JE. Design strategies for 3-dimensional in vitro bone growth in tissue-engineering scaffolds. In: Davies JE, ed. Bone engineering. Toronto: em squared incorporated; 2000:488-495.

123. Robinson BP, Hollinger JO, Szachowicz EH, Brekke J. Calvarial bone repair with porous D,L-polylactide. Otolaryngol Head Neck Surg. 1995;112:707-713.

124. Arnaud E, Morieux C, Wybier M, de Vernejoul MC. Potentiation of transforming growth factor (TGF-beta 1) by natural coral and fibrin in a rabbit cranioplasty model. Calcif Tissue Int. 1994;54:493-498.

125. Moxham JP, Kibblewhite DJ, Bruce AG, Rigley T, Gillespy T, 3rd, Lane J. Transforming growth factor-beta 1 in a guanidine-extracted demineralized bone matrix carrier rapidly closes a rabbit critical calvarial defect. J Otolaryngol. 1996;25:82-87.

126. Vehof JW, Haus MT, de Ruijter AE, Spauwen PH, Jansen JA. Bone formation in transforming growth factor beta-I-loaded titanium fiber mesh implants. Clin Oral Implants Res. 2002;13:94-102.

127. Peter SJ, Suggs LJ, Yaszemski MJ, Engel PS, Mikos AG. Synthesis of poly(propylene fumarate) by acylation of propylene glycol in the presence of a proton scavenger. J Biomater Sci Polym Ed. 1999;10:363-373.

128. Peter SJ, Yaszemski MJ, Suggs LJ, Payne RG, Langer R, Hayes WC, Unroe MR, Alemany LB, Engel PS, Mikos AG. Characterization of partially saturated poly(propylene fumarate) for orthopaedic application. J Biomater Sci Polym Ed. 1997;8:893-904.

129. Dennis JE, Caplan AI. Porous ceramic vehicles for rat-marrow-derived (Rattus norvegicus) osteogenic cell delivery: effects of pre-treatment with fibronectin or laminin. J Oral Implantol. 1993;19:106-115; discussion 136-107.

130. Kornu R, Maloney WJ, Kelly MA, Smith RL. Osteoblast adhesion to orthopaedic implant alloys: effects of cell adhesion molecules and diamond-like carbon coating. J Orthop Res. 1996;14:871-877.

131. Healy KE, Rezania A, Stile RA. Designing biomaterials to direct biological responses. Ann N Y Acad Sci. 1999;875:24-35.

132. Schaffner P, Meyer J, Dard M, Nies B, Verrier S, Kessler H, Kantlehner M. Induced tissue integration of bone implants by coating with bone selective RGD-peptides in vitro and in vivo studies. J Mater Sci Mater Med. 1999;10:837-839.

133. Uludag H, D'Augusta D, Golden J, Li J, Timony G, Riedel R, Wozney JM. Implantation of recombinant human bone morphogenetic proteins with biomaterial carriers: A correlation between protein pharmacokinetics and osteoinduction in the rat ectopic model. J Biomed Mater Res. 2000;50:227-238.

134. Uludag H, D'Augusta D, Palmer R, Timony G, Wozney J. Characterization of rhBMP-2 pharmacokinetics implanted with biomaterial carriers in the rat ectopic model. J Biomed Mater Res. 1999;46:193-202.

135. Yaszemski MJ, Payne RG, Hayes WC, Langer R, Aufemorte TB, Mikos AG. The ingrowth of new bone tissue and initial mechanical properties of a degrading polymeric composite scaffold. Tissue Eng. 1995;1:41-52.

136. Gombotz WR, Pankey SC, Bouchard LS, Phan DH, Puolakkainen PA. Stimulation of bone healing by transforming growth factor-beta 1 released from polymeric or ceramic implants. J Appl Biomater. 1994;5:141-150.

137. Lind M, Overgaard S, Nguyen T, Ongpipattanakul B, Bunger C, Soballe K. Transforming growth factor-beta stimulates bone ongrowth. Hydroxyapatite-coated implants studied in dogs. Acta Orthop Scand. 1996;67:611-616.

138. McKinney L, Hollinger JO. A bone regeneration study: transforming growth factor-beta 1 and its delivery. J Craniofac Surg. 1996;7:36-45.

139. Sumner DR, Turner TM, Purchio AF, Gombotz WR, Urban RM, Galante JO. Enhancement of bone ingrowth by transforming growth factor-beta. J Bone Joint Surg Am. 1995;77:1135-1147.

140. Zellin G, Beck S, Hardwick R, Linde A. Opposite effects of recombinant human transforming growth factor-beta 1 on bone regeneration in vivo: effects of exclusion of periosteal cells by microporous membrane. Bone. 1998;22:613-620.

141. Hollinger JO, Uludag H, Winn SR. Sustained release emphasizing recombinant human bone morphogenetic protein-2. Adv Drug Deliv Rev. 1998;31:303-318.

142. Heckman JD, Ehler W, Brooks BP, Aufdemorte TB, Lohmann CH, Morgan T, Boyan BD. Bone morphogenetic protein but not transforming growth factor-beta enhances bone formation in canine diaphyseal nonunions implanted with a biodegradable composite polymer. J Bone Joint Surg Am. 1999;81:1717-1729.

143. Blom EJ, Klein-Nulend J, Klein CP, Kurashina K, van Waas MA, Burger EH. Transforming growth factor-beta1 incorporated during setting in calcium phosphate cement stimulates bone cell differentiation in vitro. J Biomed Mater Res. 2000;50:67-74.

144. Goldstein AS, Zhu G, Morris GE, Meszlenyi RK, Mikos AG. Effect of osteoblastic culture conditions on the structure of poly(DL-lactic-co-glycolic acid) foam scaffolds. Tissue Eng. 1999;5:421-434.

145. Vehof JW, Spauwen PH, Jansen JA. Bone formation in calcium-phosphate-coated titanium mesh. Biomaterials. 2000;21:2003-2009.

146. Vehof JW, Mahmood J, Takita H, van't Hof MA, Kuboki Y, Spauwen PH, Jansen JA. Ectopic bone formation in titanium mesh loaded with bone morphogenetic protein and coated with calcium phosphate. Plast Reconstr Surg. 2001;108:434-443.

147. Kuboki Y, Takita H, Kobayashi D, Tsuruga E, Inoue M, Murata M, Nagai N, Dohi Y, Ohgushi H. BMP-induced osteogenesis on the surface of hydroxyapatite with geometrically feasible and nonfeasible structures: topology of osteogenesis. J Biomed Mater Res. 1998;39:190-199.

148. Clouthier DE, Comerford SA, Hammer RE. Hepatic fibrosis, glomerulosclerosis, and a lipodystrophy-like syndrome in PEPCK-TGF-beta1 transgenic mice. J Clin Invest. 1997;100:2697-2713.

149. Kopp JB, Factor VM, Mozes M, Nagy P, Sanderson N, Bottinger EP, Klotman PE, Thorgeirsson SS. Transgenic mice with increased plasma levels of TGF-beta 1 develop progressive renal disease. Lab Invest. 1996;74:991-1003.

150. Ledbetter S, Kurtzberg L, Doyle S, Pratt BM. Renal fibrosis in mice treated with human recombinant transforming growth factor-beta2. Kidney Int. 2000;58:2367-2376.

151. Calabresi PA, Fields NS, Maloni HW, Hanham A, Carlino J, Moore J, Levin MC, Dhib-Jalbut S, Tranquill LR, Austin H, McFarland HF, Racke MK. Phase 1 trial of transforming growth factor beta 2 in chronic progressive MS. Neurology. 1998;51:289-292.

152. Buckwalter JA, Glimcher MJ, Cooper RR, Recker R. Bone biology. Part II: Formation, form, modeling, remodeling, and regulation of cell function. J Bone Joint Surg Am. 1995;77-A:1276-1289.

153. Buckwalter JA, Glimcher MJ, Cooper RR, Recker R. Bone biology. Part I: Structure, blood supply, cells, matrix, and mineralization. J Bone Joint Surg Am. 1995;77-A:1256-1275.

154. Lieberman JR, Daluiski A, Einhorn TA. The role of growth factors in the repair of bone. Biology and clinical applications. J Bone Joint Surg Am. 2002;84-A:1032-1044.

155. Lind M. Growth factors: possible new clinical tools. A review. Acta Orthop Scand. 1996;67:407-417.

156. Canalis E, McCarthy T, Centrella M. Growth factors and the regulation of bone remodeling. J Clin Invest. 1988;81:277-281.

157. Carmeliet P. Mechanisms of angiogenesis and arteriogenesis. Nat Med. 2000;6:389-395.

158. Friesel RE, Maciag T. Molecular mechanisms of angiogenesis: fibroblast growth factor signal transduction. Faseb J. 1995;9:919-925.

159. Wang JS. Basic fibroblast growth factor for stimulation of bone formation in osteoinductive or conductive implants. Acta Orthop Scand Suppl. 1996;269:1-33.

160. Canalis E, Centrella M, McCarthy T. Effects of basic fibroblast growth factor on bone formation in vitro. J Clin Invest. 1988;81:1572-1577.

161. Toi M, Matsumoto T, Bando H. Vascular endothelial growth factor: its prognostic, predictive, and therapeutic implications. Lancet Oncol. 2001;2:667-673.

162. Helmlinger G, Endo M, Ferrara N, Hlatky L, Jain RK. Formation of endothelial cell networks. Nature. 2000;405:139-141.

163. Robey PG, Young MF, Flanders KC, Roche NS, Kondaiah P, Reddi AH, Termine JD, Sporn MB, Roberts AB. Osteoblasts synthesize and respond to transforming growth factor-type beta (TGF-beta) in vitro. J Cell Biol. 1987;105:457-463.

164. Joyce ME, Jingushi S, Bolander ME. Transforming growth factor-beta in the regulation of fracture repair. Orthop Clin North Am. 1990;21:199-209.

165. Bolander ME. Regulation of fracture repair by growth factors. Proc Soc Exp Biol Med. 1992;200:165-170.

166. Bourque WT, Gross M, Hall BK. Expression of four growth factors during fracture repair. Int J Dev Biol. 1993;37:573-579.

167. Rosier RN, O'Keefe RJ, Hicks DG. The potential role of transforming growth factor beta in fracture healing. Clin Orthop. 1998:S294-300.

168. Yamaguchi A, Katagiri T, Ikeda T, Wozney JM, Rosen V, Wang EA, Kahn AJ, Suda T, Yoshiki S. Recombinant human bone morphogenetic protein-2 stimulates osteoblastic maturation and inhibits myogenic differentiation in vitro. J Cell Biol. 1991;113:681-687.

169. Urist MR, DeLange RJ, Finerman GA. Bone cell differentiation and growth factors. Science. 1983;220:680-686.

170. Centrella M, McCarthy TL, Canalis E. Effects of transforming growth factors on bone cells. Connect Tissue Res. 1989;20:267-275.

171. Gombotz WR, Guanghui W, Horbett TA, Hoffman AS. Protein adsorption to poly(ethylene oxide) surfaces. J Biomed Mater Res. 1991;25:1547-1562.

172. Jeon SI, Lee JH, Andrade JD, DeGennes PG. Protein-surface interactions in the presence of poly(ethylene oxide)-I. Simplified theory. J Colloid Interface Sci. 1991;142:149-158.

173. Prime KL, Whitesides GM. Adsorption of proteins onto surfaces containing end-attached oligo(ethyleneoxide): a model system using self-assembled monolayers. J Am Chem Soc. 1991;115:10714-10721.

174. Park JH, Bae YH. Hydrogels based on poly(ethylene oxide) and poly(tetramethylene oxide) or poly(dimethyl siloxane): synthesis, characterization, in vitro protein adsorption and platelet adhesion. Biomaterials. 2002;23:1797-1808.

175. Jo S, Shin H, Mikos AG. Modification of oligo(poly(ethylene glycol) fumarate) macromer with a GRGD peptide for the preparation of functionalized polymer networks. Biomacromolecules. 2001;2:255-261.

176. Payne RG, McGonigle JS, Yaszemski MJ, Yasko AW, Mikos AG. Development of an injectable, in situ crosslinkable, degradable polymeric carrier for osteogenic cell populations. Part 2. Viability of encapsulated marrow stromal osteoblasts cultured on crosslinking poly(propylene fumarate). Biomaterials. 2002;23:4373-4380.

177. Tanahashi K, Mikos AG. Cell adhesion on poly(propylene fumarate-*co*-ethylene glycol) hydrogels. J Biomed Mater Res. 2002;62:558-566.

178. Shin H, Jo S, Mikos AG. Modulation of marrow stromal osteoblast adhesion on biomimetic oligo[poly(ethylene glycol) fumarate] hydrogels modified with Arg-Gly-Asp peptides and a poly(ethyleneglycol) spacer. J Biomed Mater Res. 2002;61:169-179.

179. Jo S, Shin H, Shung AK, Fisher JP, Mikos AG. Synthesis and characterization of oligo(poly(ethylene glycol) fumarate) macromer. Macromolecules. 2001;34:2839-2844.

180. Brey EM, Lalani Z, Johnston C, Wong ME, McIntire LV, Duke PJ, Patrick CW. Automated image analysis of immunohistochemical staining with DAB-labeled antigens. J Histochem Cytochem. 2002:Submitted.

181. Lalani Z, Wong MEK, Brey EM, Johnston C, Mikos AG, Duke PJ, Montufar-Solis D. The development of an animal model, tissue processing, and immunohistochemical

techniques for the molecular analysis of wound healing in a tooth extraction socket. Oral Surg Oral Med Oral Pathol Oral Radiol Endod. 2002:Submitted.

182. Lalani Z, Wong MEK, Brey EM, Mikos AG, Duke PJ. Spatial and temporal localization of TGF-β1, BMP-2, and PDGF-A in healing tooth extraction sockets in a rabbit model. J Oral Maxillofac Surg. 2002:In Press.

183. Venter DJ, Tuzi NL, Kumar S, Gullick WJ. Overexpression of the c-erbB-2 oncoprotein in human breast carcinomas: immunohistological assessment correlates with gene amplification.PG. Lancet. 1987;2.

184. Podhajsky RJ, Bidanset DJ, Caterson B, Blight AR. A quantitative immunohistochemical study of the cellular response to crush injury in optic nerve.PG - 153-61. Exp Neurol. 1997;143.

185. Dias P, Chen B, Dilday B, Palmer H, Hosoi H, Singh S, Wu C, Li X, Thompson J, Parham D, Qualman S, Houghton P. Strong immunostaining for myogenin in rhabdomyosarcoma is significantly associated with tumors of the alveolar subclass.PG - 399-408. Am J Pathol. 2000;156.

186. Aasmundstad TA, Haugen OA, Johannesen E, Hoe AL, Kvinnsland S. Oestrogen receptor analysis: correlation between enzyme immunoassay and immunohistochemical methods.PG - 125-9. J Clin Pathol. 1992;45.

187. Lehr HA, Mankoff DA, Corwin D, Santeusanio G, Gown AM. Application of photoshop-based image analysis to quantification of hormone receptor expression in breast cancer. J Histochem Cytochem. 1997;45:1559-1565.

188. Bhatnagar J, Tewari HB, Bhatnagar M, Austin GE. Comparison of carcinoembryonic antigen in tissue and serum with grade and stage of colon cancer.PG - 2181-7. Anticancer Res. 1999;19.

189. Simone NL, Remaley AT, Charboneau L, Petricoin EF, 3rd, Glickman JW, Emmert-Buck MR, Fleisher TA, Liotta LA. Sensitive immunoassay of tissue cell proteins procured by laser capture microdissection.PG - 445-52. Am J Pathol. 2000;156.

190. Daly LE, Bourke GJ. Interpretation and uses of medical statistics (5th ed). Oxford: Blackwell Science Ltd.; 2000.

191. Seidal T, Balaton AJ, Battifora H. Interpretation and quantification of immunostains. Am J Surg Pathol. 2001;25:1204-1207.

192. Yao W, Godfrey DA. Vesicular acetylcholine transporter in the rat cochlear nucleus: an immunohistochemical study. J Histochem Cytochem. 1999;47:83-90.